Higher Moments Measurement of Net-Kaon Multiplicity Distribution in the Search for the QCD Critical Point

Submitted in partial fulfillment of the requirements
for the degree of
Doctor of Philosophy

by

Amal Sarkar
(Roll No. 09412601)

Supervisor
Prof. Raghava Varma

Department of Physics
INDIAN INSTITUTE OF TECHNOLOGY, BOMBAY, INDIA
December, 2015

Dedicated To

My Parents

&

My Supervisor

Thesis Approval

Thesis entitled **"Higher Moments Measurement of Net-Kaon Multiplicity Distribution in the Search for the QCD Critical Point"** by **Amal Sarkar** is approved for the degree of Doctor of Philosophy.

Examiners

(1) Ajit M. Srivastava

(2)

Supervisor

Raghavarne

Chairman

Amey Mehta

Date : December 3, 2015

Place : Mumbai

Declaration

I declare that this written submission represents my ideas in my own words and where others' ideas or words have been included, I have adequately cited and referenced the original sources. I also declare that I have adhered to all principles of academic honesty and integrity and have not misrepresented or fabricated or falsified any idea/data/fact/source in my submission. I understand that any violation of the above will be cause disciplinary action by the Institute and can also evoke penal action from the sources which have thus not been properly cited or from whom proper permission has not been taken when needed.

Amal Sarkar

Roll No. 09412601

Date : 27/12/2015

Place : IIT Bombay, Mumbai

Abstract

The Relativistic Heavy-Ion Collider (RHIC), at Brookhaven National Laboratory (BNL), with its beam energy scan (BES) program by colliding heavy-ions has covered a wide range of baryonic chemical potential (μ_B) to map the QCD phase diagram. Lattice QCD calculations at finite temperature and baryon chemical potential $\mu_B \approx 0$ suggest a crossover between hadronic to quarks and gluons degrees of freedom. Several QCD based calculations find the quark-hadron phase transition to be of the first order at large μ_B. The point in the QCD phase plane (T vs μ_B) where the first order line ends and phase transition becomes continuous is called the QCD critical point (CP). Current theoretical calculations are highly uncertain about location of the critical point because of numerical challenges in computing. At the critical point long range correlation and fluctuation arise at all length scales. Such properties of state open several possibilities for experimental signatures. These distinct experimental observables can be used to discover the QCD critical point.

The correlation length (ξ) and the magnitude of the fluctuations of the conserved quantities (net-baryon, net-strangeness and net-charge) diverge at the critical point but because of the finite size and time slowing down effects in the heavy ion collisions, ξ takes values in the range of $2 - 3$fm. Higher non Gaussian moments such as skewness, S ($\propto \xi^{4.5}$), and kurtosis, $\kappa(\propto \xi^{7})$ of these conserved quantities can provide much better handle in location of CP as they are much more sensitive than variance ($\propto \xi^{2}$) to the correlation length. As these higher order moments are system size or volume dependent moment products, such as, S$\sigma(\propto \xi^{2.5})$ and $\kappa\sigma^2(\propto \xi^{5})$ can be constructed to cancel out the volume dependency.

QCD-based models and Lattice calculations show that moments of net-conserved (baryons (B), strangeness (S) and charge (Q)) distributions are related to its con-

served number susceptibilities ($\chi_x = \frac{\langle(\Delta N_x)^2\rangle}{VT}$; where, x represents B, S and Q, & V is the volume). Volume independent moment products Sσ and $\kappa\sigma^2$ are the ratio of third ($\chi_x^{(3)}$) to second $\chi_x^{(2)}$ order and fourth $\chi_x^{(4)}$ to second $\chi_x^{(2)}$ order susceptibilities. Close to the critical point, QCD based models predict the distributions of the conserved quantities to be non-Gaussian. The susceptibilities diverge causing Sσ and $\kappa\sigma^2$ to fluctuate near the critical point. Experimentally measuring conserved quantum numbers on an event-by-event basis is very difficult. Hence, net proton, kaons and pions can serve as proxy for baryon, strangeness and charge conservation respectively. We calculate event-by-event the net-kaon multiplicity ($\Delta N_K = N_{K^+} - N_{K^-}$) to obtain the net-kaon distribution. Simulations carried out in this work demonstrate that net-kaon multiplicity can be taken to be a proxy for net strangeness to a reasonably good approximation.

In this Thesis, we report the measurement of the moments of the net-kaon multiplicity distributions as a function of baryon chemical potential which was varied from 410 to 20 MeV by changing the $\sqrt{s_{NN}}$ from 7.7, 11.5, 19.6, 27, 39, 62.4 to 200 GeV in $Au + Au$ collisions by the STAR experiment at RHIC. The measurements of these higher moments of ΔN_K multiplicity distributions was carried out at mid-rapidity ($|\eta| < 0.5$) in $0.2 < p < 1.6$ GeV/c in $Au + Au$ collisions. Higher moments such as Mean (M), Variance (σ^2), Skewness (S) and kurtosis (κ) of the net-kaon (ΔN_K) multiplicity distributions as a function of collision centrality are presented. As these higher moments are system size dependent different combination of moment product such as $S\sigma$ and $\kappa\sigma^2$ have been calculated (to cancel out the dependence on the volume) as a function of collision centrality and energy. QCD based calculations expect a non-monotonic dependence of these moment products near the critical point. Various methods have been used to calculate the statistical errors for this analysis. The systematic have been studied for the experimental acceptance used to select the data sample. The detector efficiency correction method have been developed and implemented in the results. The experimental results have been compared with different baselines and Monte Carlo simulated model which do not include the critical point for non-critical baseline.

We observe deviation from the Poissonian behaviour for $S\sigma$ and $\kappa\sigma^2$ at 19.6 GeV and 27 GeV. This indicates that we are very near the critical point. Presently we are analyzing the behaviour at center of mass energy of 14 GeV to further confirm our results. To confirm the discovery of critical point we would need much larger statistics which would be undertaken in the Beam Energy Scan Program-II of RHIC.

Keywords : QGP, Phase transition, Critical Point, Higher Moments.

Contents

List of Figures

List of Tables

Chapter 1

Introduction

"Nature has a great simplicity and therefore a great beauty"

– Richard P. Feynman

Mankind since time immemorial has tried to investigate the origin of the universe and to find the basic building blocks of the matter. These quests have driven mankind to develop a scientific approach to understand the secrets of the nature. The cosmologists in conjunction with astrophysicists propounded the **Big Bang** theory which pertains to beginning of the universe. This cosmological model answers the physical conditions prevailing at the early stages of the universe and its large scale evolution of the universe in which we now live. However, the question whether the universe is a closed or open still remains unanswered.

The beginning of the time according to the **Big Bang** theory is taken to be singularity when the energy density was infinite. As the universe evolved, the state of the matter was very hot and extremely dense. Due to the immensity of the high energy it consisted of ultra-relativistic particles. During this stage all the forces, namely the strong, electromagnetic weak and the gravitational forces were unified and manifested as a single force. According to the **Big Bang** theory the universe started expanding 13.798 ± 0.037 billion years ago. Gravitation decoupled first and the other three which are based on the fundamental principles of local gauge invariance were still coupled. As the universe cooled further, the elec-

troweak symmetry was spontaneously broken. It is assumed that each stage of symmetry break down was associated with a phase transition, very much similar to what is the subject of investigation of this thesis. Due to the space-time expansion the universe cooled down and the value of the energy density reduced. The universe during these stages consisted of a sea of quarks and gluons, as well as other elementary particles. The quark-gluon plasma is mixture or soup of quarks and gluons. Then the universe further cooled down to the complex and composite particles. At later stages, the universe started accelerating due to the dark energy.

The physicists would like to understand from the very large or ultimate in terms of size like our universe to the very small again to the ultimate which is the basic building blocks of which we all are made up off. The understanding of this scale from fraction of a Fermi to 28×10^9 pc is the success of modern science. This has been made possible by technological advances which has resulted in man probing the heart of matter to the structure of universe. The technological marvel that the large hadron collider at CERN is has provided the final confirmation to the **Standard Model** which gives the ultimate building blocks of matter and the interactions that govern them. In conjunction with the theoretical physics, the modern particle physics experiments developed the **Standard Model** for a better understanding to the building blocks of matter or elementary particles and their interaction [5]. The theory of **Standard Model** gives a comprehensive understanding of all known subatomic particles and described the electromagnetic, weak and strong interaction among them.

1.1 The Standard Model

Experimentalists and theoreticians from all over the world have collaboratively developed the **Standard Model**. This model is an amalgamation of all the experimental and theoretical work and hence it would be safe to say that this formally came into being at the beginning of the last quarter of the 20^{th} century. The formu-

lation of this model has been finalized by the experimental proof of existence of **quarks** (mid-1970), **top quarks** (1995), **tau neutrino** (2000) and recently the **Higgs boson** (2013). Till now the **Standard Model** is able to explain everything except gravity. Because of its ability to explaining almost all physical phenomena and experimental results it is often referred to as the "**Theory of almost everything**".

As mentioned earlier, in nature the elementary particles can interact amongst themselves in four fundamental ways, i.e. the **Electromagnetic**, **Strong**, **Weak** and **Gravitational**. The basic feature underlying the model is that they obey gauge invariance and this leads to the fact that these interaction take place via photon for electromagnetic, gluon for strong, $W^{\pm}$ and Z^0 for weak and graviton for the gravitational interaction respectively. So far, the Standard Model is able to explain the first three fundamental interaction but unable to describe the gravitational interaction.

The Standard Model is comprised with 17 elementary particles shown in the Figure 1.1 which explain all physics phenomena. Some of these elementary particles have multiple "**color**s" . Among these particles the matter particles broadly classified as fermions which have quarks and leptons and the force carrying particles, like the photons, gluons and W and Z which are bosonsic in nature and hence integral spin particles.

Quarks are the mass carrying elementary particles and the basic building blocks of nucleons of an atom. The existence of quarks was conformed by the Deep Inelastic Scattering (DIS) in 1968 at the Stanford Linear Accelerator (SLAC)[6, 7]. There are six quarks in the Standard Model namely **up(u), down(d), charm(c), strange(s), top(t)** and **bottom(b)**. Each of these quarks and their antiparticles contain a fraction of integer charge and mass in the range of 1.5 MeV/c^2 to 173.34 GeV/c^2. By combining two or three quarks one creates larger sub-atomic particles like **Mesons** and **Baryons** respectively. In the Standard Model the only elementary particles that undertakes all kind of fundamental interaction via all kind of fundamental forces are the quarks. Using the color based logic the **Quantum Chromodynamics** (QCD) applies a color to each of these quarks. Due to the

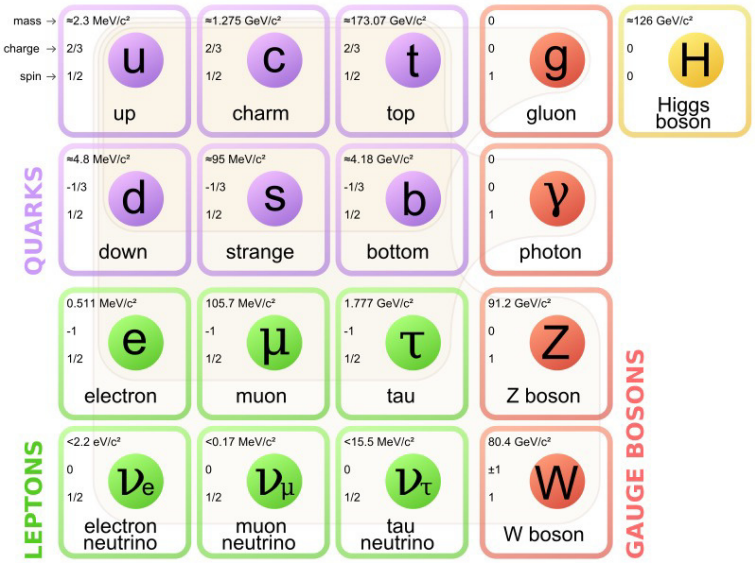

Figure 1.1: (Color online) The **Standard Model** of the elementary particles with quarks, leptons, gauge boson and Higgs boson.

color confinement it is not possible to observe any isolated quark or one says one only observes color singlet states. Since color can take three quantum numbers, red blue and green, in nature we observe a meson (a composite particle of a colored quark and an anti-colored quark) or a baryon (a composite particle of three quarks having colors red blue and green).

Leptons are the group of particles in the Standard Model which also like quarks have half-integer spin (spin 1/2) [8]. By the specification of charge there are two categories of leptons. Charged leptons are known as the electron-like and the neutral leptons are know as the neutrinos. The electron-like leptons contain a integer charge with value one and mass in the range of 0.511 MeV/c^2 to 1.777 GeV/c^2. The neutrinos contain zero charge and mass within the range of zero to several MeV/c^2. By the formation of "flavour" there are six flavours of leptons which can be divided into three generation. These three generations are: the electron (e^-) and electron neutrino (ν_e); muon (μ) and muonic neutrino (ν_μ); tau (τ) and tau neutrino (ν_τ). The leptons does not take part in the strong interaction but experience other two fundamental interactions, namely electromagnetic and weak. As quarks and leptons are half integral spin particles they obey the Fermi

statistics and are collectively referred to as fermions [9].

Bosons are the force carrying particles in the Standard Model with integral spin [10]. In quantum mechanics bosons are those particle which follows the Bose-Einstein statistics. The most important characteristic of bosons is that they can share the same quantum state and their number does not restrict them to share the same state. In this category the fundamental particles are **photon (γ)**, **gluon (g)**, **W**, **Z**, **Higgs (H^0)** and **graviton**. The graviton is expected to describe the fundamental theory of quantum gravity. The first four bosons are the force carrying **gauge boson**. Each of these boson carry a specific type of force like strong nuclear force, electromagnetic force, weak nuclear force.

Although the constituent building blocks of matter and their interaction of the universe is described in the **Standard Model**, it is incomplete because of its inability to explain the theory of gravitation as described in the general theory of relativity. Moreover, the **Standard Model** does not contain any dark matter particle and is therefore unable to explain the physics of dark energy. In addition, though the Standard Model is theoretically self-consistent, it is also incomplete due to several unsolved puzzles like neutrino oscillation (their non-zero masses), CP problem and hierarchy problem.

Due to the fact that the quarks are not possible to be observed experimentally for the color confinement it is very challenging to understand the theory of strong interaction. The interaction between quarks and gluon take place via strong interaction and described by Quantum Chromodynamics.

1.2 Strong interaction and Quantum Chromodynamics (QCD)

The matter in the universe is build with atoms with the nucleus at its centre. The nucleus consists of nucleons which in turn is made up of quarks and gluons. These fundamental particles are strongly interacting particles and bound to each other by the strong force which has a short range force. If the interaction goes

through strong interaction then the reaction obeys all the symmetries of nature. The symmetries of nature are expressed mathematically in terms of conservation laws, like momentum-energy, angular momentum, charge, baryon number, lepton flavour etc.. The theory of strong interaction between quarks and gluons is known as Quantum Chromodynamics (QCD) [12]. ıThe gluons as they carry the color quantum quantum can interact with each other, which makes QCD a non-abelian **gauge theory**. As gluons carry eight colors, the theory has **SU(3)** symmetry [12, 13]. QCD Lagrangian for a single flavour quark can be expressed as,

$$\mathcal{L}_{QCD} = \bar{\psi}_i\Big(i(\gamma^\mu D_\mu)_{ij} - m\delta_{ij}\Big)\psi_j - \frac{1}{4}G^a_{\mu\nu}G^{\mu\nu}_a \tag{1.1}$$

where $\mathcal{L}_{QCD}$ is the gauge invariant QCD Lagrangian for the stronAg interaction, ψ_i is the quark field of the SU(3) gauge group, γ^μ are the **Dirac matrices** also known as the **gamma matrices**, D_μ is the gauge covariant derivative, $G^a_{\mu\nu}$ is the gauge invariant strength tensor of the gluon field and given by,

$$G^a_{\mu\nu} = \partial_\mu \mathcal{A}^a_\nu - \partial_\nu \mathcal{A}^a_\mu + g f^{abc}\mathcal{A}^b_\mu \mathcal{A}^c_\nu \tag{1.2}$$

where $\mathcal{A}^a_\mu(x)$ are the space-time gluon field and f^{abc} are the SU(3) structure constant. m and g are constants which control the mass and coupling constant. The strength of interactions between partons are determined by these coupling constants. The loop variable of this Lagrangian known as the **Wilson Loop** play most important role to separate different forms of QCD to distinguish the confined and de-confined states.

Analogous to Quantum Electrodynamics (QED) charges, QCD separate the fundamental particles by **color charges**. In **1964** the color charge was first proposed by **Oscar W .Greenberg** to explain the coexistence of quarks inside the hadrons. All six different types of quarks are divided into three generations of color charges. The color charges is a fundamental property of strongly interacting quarks and gluons and have three color charges which as mentioned before are red, green and blue. For the conservation of the color charges in pair produc-

tion and particle annihilation the anti-particles should have the anti-color charge for each associated particle with a color charge. The mixture of all the three colors or a color with its anti color is called **colorless** or zero color charge.

1.3 Confinement and Asymptotic freedom

Colored charged particles like quarks and gluons cannot be observed directly. They are always confined within hadrons and this phenomena is known as the **confinement** or the **color confinement**. This does not come from QCD but is an additional constraint on the theory based on the experimental observation that only color singlet states are observed. One way to understand confinement is to examine the behaviour of QCD coupling constant α_s, as a function of momentum transfer Q^2. This coupling decreases as the momentum transfer increases. The coupling constant also known as the running coupling const (α_s) determines the strength with which partons (quarks and gluons) interact and its dependence on Q^2 is given by

$$Q^2 \frac{\partial \alpha_s(Q^2)}{\partial Q^2} = \beta\Big(\alpha_s(Q^2)\Big) \tag{1.3}$$

the function β is given as,

$$\beta(\alpha_s(Q^2)) = -\beta_0 \alpha_s^2(Q^2) - \beta_1 \alpha_s^3(Q^2) - \beta_2 \alpha_s^4(Q^2) - \beta_3 \alpha_s^5(Q^2) + \mathcal{O}(6) \tag{1.4}$$

where,

$$\begin{aligned} \beta_0 &= \frac{33 - 2N_f}{12\pi} \\ \beta_1 &= \frac{153 - 19N_f}{24\pi^2} \\ \beta_2 &= \frac{77139 - 15099N_F + 325N_f^2}{3456\pi^3} \end{aligned} \tag{1.5}$$

The details of β function calculation and its higher order terms can be found in the Ref. [14]. Here N_f represent the number of active quark flavours at the energy scale Q.

In one loop approximation (neglecting β_1 and higher order terms) the solution

of the Equation 1.3 is,

$$\begin{aligned}\alpha_s(Q^2) &= \frac{\alpha_s(\mu^2)}{1+\alpha_s(\mu^2)\beta_0 \ln\frac{Q^2}{\mu^2}} \\ &= \frac{\alpha_s(\mu^2)}{1+\alpha_s(\mu^2)\left(\frac{33-2N_f}{12\pi}\right)\ln\frac{Q^2}{\mu^2}}\end{aligned} \tag{1.6}$$

where, μ is a QCD scale parameter. Equation 1.6 gives the relation between two α_s values measured at two different scales Q^2 and μ^2. For a smaller Q^2 value the $\alpha_s(Q^2)$ has a larger value. For $Q^2 \leq \mathcal{O}$ (1 GeV) and $N_f = 2...5$ and $\alpha_s(\mu^2 = M_{Z^0}^2) = 0.12$, the value of $\alpha_s(Q^2)$ becomes more than unity which implies that perturbative calculation is not applicable. In addition, the quarks and gluons get confined inside the hadrons and hence one does not observed colored particles in nature.

In Figure 1.2 the coupling constant or the running coupling constant is shown as a function of the momentum transfer measured from different experiments. Both the theoretical and experimental results shows asymptotic variation with the energy. For events involving high momentum transfer, as α_s is small, QCD is a calculable tool. However, for reactions with low moment transfer, Q^2 small, α_s becomes larger than one. The contribution of next to leading order term is larger than the leading order, next to next to leading order term becomes larger than next to leading order and so on. The theory diverges, and hence in such cases one either uses effective field theories where the degrees of freedom are not quarks and gluons but baryons and mesons or one performs the calculations using Lattice QCD (LQCD). Lattice QCD is quantum chromodynamics formulated on a discrete Euclidean space time grid. In its formulation no new parameters or field variables are introduced and therefore as a consequence LQCD retains all the symmetries of QCD. The discreteness of the space-time lattice acts as a non- perturbative regularization scheme. At finite values of the lattice spacing **a**, an automatic momentum cutoff at $\frac{\pi}{a}$ is in built in the theory preventing it from divergences. Not only that, renormalized physical quantities allows us to calcu-

late all the quantities as for perturbative QCD in the limit of $a \to 0$. LQCD can also therefore be used to address issues like the mechanism for confinement and chiral symmetry breaking which as mentioned before are the two properties that characterize QCD. In recent times LQCD has been widely used to calculate the equilibrium properties of QCD at finite temperature. As mentioned later, these studies are important for the work done in this thesis.

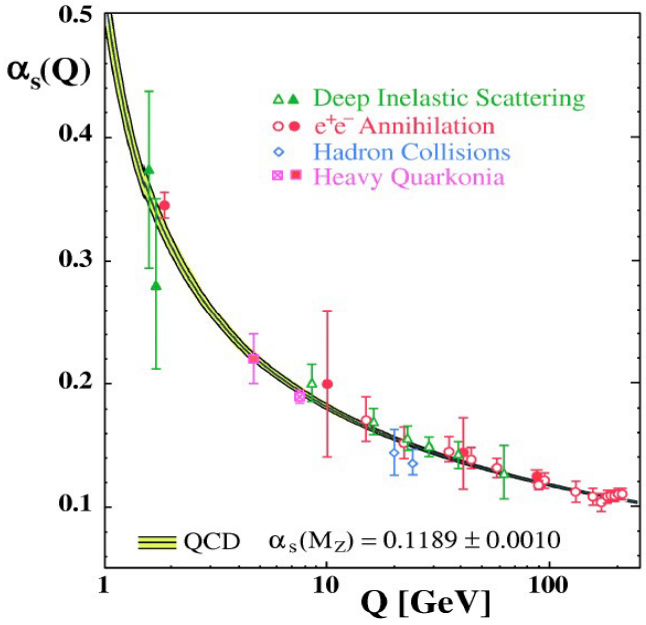

Figure 1.2: (Color online) A summary of coupling constant measurement from different experiments and theoretical calculations as a function of the energy scale (momentum transfer) Q. The figure is taken from Ref.[15].

If $N_f < 17$, β_0 becomes positive and for larger Q^2 value $\alpha_s(Q^2)$ decreases asymptotically to zero. In this condition the coupling strength between the quarks and gluon becomes negligible and they becomes free asymptotically. From the Figure 1.2, it is also observed that at very high momentum transfer (or high energy) the coupling strength decreases asymptotically. This phenomena is known as the **Asymptotic Freedom**. This is one of the revolutionary discovery in science for which Frank Wilczek, David Gross and David Politzer were honored with the Nobel prize in 2004.

The discovery of asymptotic freedom suggests that at very high momentum

transfer, quarks and gluons will no longer be confined inside a hadron. Under this condition the quarks and gluons becomes free and the hadronic matter transforms to the QCD matter. In such a state there are no hadronic degrees of freedom or QCD confinement and the color degrees of freedom govern the physical processes. This new state of QCD matter is called the **Quark Gluon Plasma (QGP)**. In addition, also at very high baryon density, the hadrons are expected to overlap and the distance between two quarks from two different hadrons becomes much less than the diameter of the hadrons. In such conditions the coupling strength between those two quarks become negligible due to the smaller value of the coupling constant. Under this condition the quarks and gluons become free to form QGP. According to the **Big Bang** theory, during its evolution, the universe reached the QGP state just few micro seconds (10^{-6} s) after the Big Bang. In a way one can say that the discovery of the asymptotic freedom motivates experimentalists to study the state of early universe by creating the new state of matter in heavy ion collision experiments where the quarks and gluons are almost free. However, it must be pointed out that with the present day accelerators, it is not possible to reach a state of matter where quarks and gluons are weakly interacting.

1.3.1 The Quark Gluon Plasma and Heavy Ion Collisions

Quark Gluon Plasma is a state of matter with quarks and gluons in extreme conditions. The QGP is a mixture or soup of quarks and gluons bound very weakly and free to move. In this state the quarks and gluons are no more confined within hadrons. In QGP color degrees of freedom play the role instead of the hadronic degrees of freedom. Using Equation 1.6 the running coupling const can be written as,

$$\alpha_s(Q^2) = \frac{4\pi}{\left(11 - \frac{2}{3}N_f\right) ln(\frac{Q^2}{\Lambda^2})} \tag{1.7}$$

where,

$$\Lambda^2 = \frac{\mu^2}{e^{1/(\beta_0 \alpha_s(\mu^2))}} \tag{1.8}$$

is a dimensional scaling parameter identical to the energy scale Q when $\alpha_s(Q^2) \rightarrow \infty$. The typical value of Λ is few hundred MeVs and for Q^2 much greater than Λ^2 the value of $\alpha_s(Q^2)$ becomes very small hence the coupling strength between the quarks and gluons reduces. Under such a condition by applying very high energy it is possible to form the so called **QGP** sate of matter. Also, in the condition of very high baryon density where they overlap with each other it is possible to form the QGP state. It is expected that at energy scales larger than several hundred MeVs. At sufficiently high temperatures, QGP state with quarks and gluons should behaves like an ideal gas, more like a perfect fluid with negligible viscosity.

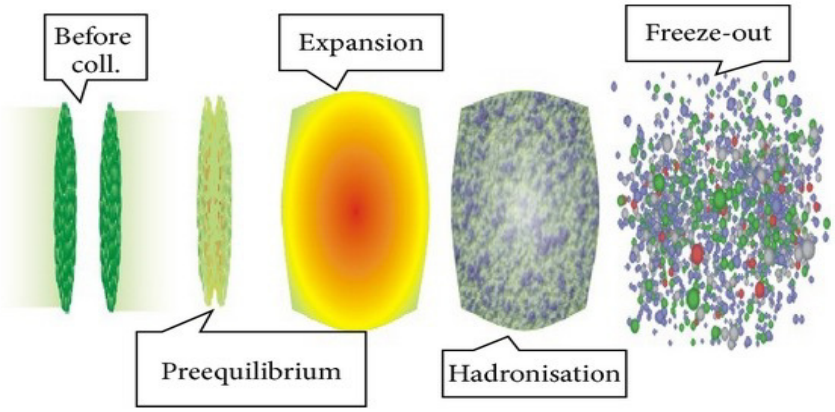

Figure 1.3: (Color online) Evolution of heavy ion collision.

The behavior of matter under extreme conditions of temperature and/or density has been of interest to physicists now for more than half a century. Fermi, way back in 1950's first initiated the question about the possibilities of new states of matter at very large pressure and temperature[16]. Almost simultaneously, Pomeranchuk[17] reasoned that hadrons, known to be most dense system, should have a limiting temperature and density. About a decade later, Hagedron proposed limiting temperature of strongly interacting matter[18]. QCD was firmly established as the correct theory of strong interactions, with the discovery of the asymptotic freedom [19][20] and the infrared slavery [22][23]. Being asymp-

totically free, at sufficiently high temperatures and density QCD predicts a deconfined system of weakly interacting quarks and gluons called Quark Gluon Plasma. However, experimental results at RHIC and now at LHC have established that the fire ball formed in these ultra relativistic heavy ion collisions is strongly interacting. At sufficiently high temperatures ($\sim$600 MeV), QGP would certainly obey the asymptotic freedom and would be weakly interacting. However, in the temperature range accessible with the present day accelerators (100-300 MeV) it is not.

Additional motivation to collide two ultra relativistic heavy ions comes from the fact that the Big Bang theory predicts that the universe, few micro seconds after the singularity existed in the quark gluon plasma state. The hope of going back in time and studying the nature of the early universe by creating the QGP state in the laboratory also has motivated scientists from all over the world to build powerful accelerators for **Heavy Ion Collisions**. These accelerators collide two oppositely directed massive ions with relativistic speed to create the QGP state or the state of early universe. The two principal heavy ion colliders, namely Relativistic Heavy Ion Collider at Brookhaven National Laboratories, Upton New York or LHC, CERN, Geneva collide gold-gold or lead-lead ions with velocity almost equal to that of light. The collision between two Lorentz contracted nuclei containing hundreds of protons and neutrons produce a medium of very high energy and baryon density. Under this condition everything melts into a soup of quarks and gluons. The size of this system as been measured to be of the order of few Fermis. The region of overlap is also often called the fireball. As the fireball cools down, the quarks and gluons recombine to form hadrons. These hadrons are ordinary matter and is often termed as hadron gas. This hadron gas continues to expands as the particles interact amongst themselves. In this evolution of the fireball from its formation to the time when the interaction between the hadrons ceases one can locate to milestone configurations termed the chemical freeze-out and the kinetic freeze-out. After a certain time during the evolution of the fireball the inelastic interaction between particles stops and hence the particle produc-

tion also freezes This phenomena is called chemical freeze-out after which the number of particles produced (as a result of expansion of this system of quarks and gluons) becomes fixed. The kinetic freeze-out takes place when the elastic scattering also stops between the particles. The final state interaction between the produced particles ceases and these are particles which are observed asymptotically by the detectors. Lattice QCD calculation and few theoretical approach strongly supported the phenomena of QGP formation. The lattice QCD calculation observed a abrupt change in the energy density and in pressure as a function of temperature which is a indication of transition between two phases.

In the heavy ion collision experiments detector are installed in the crossing points of opposite directed ion beams. These detectors measure the particles streaming into them from the collision after the freeze-out. Many advance detectors can carefully measure the particle spectra, multiplicity, momentum, types etc.. From these measured produced particles it may be possible to study whether they contains the information of the early state or not.

In the year 1971 the first heavy ion collisions were undertaken in the Bevatron at the Lawrence Berkeley National Laboratory (LBNL), Berkeley, USA. The particle accelerator HILAC was converted to accelerate heavy ion which carried by a transport line to the Bevatron with the energy range of 1-2 GeV per nucleon. At the same time there was other accelerators for the nuclear researches, started increasing the energy scales such as in JINR in Dubna, USSR, NSLC/MSU in Michigan, USA and GSI, in Darmstadt, Germany. Later on in the 80's the Super Proton Synchrotron (SPS) at European Organization for Nuclear Research (CERN) and Alternating Gradient Synchrotron (AGS) at Brookhaven Nation Laboratory (BNL) were started injecting heavy ions. The Relativistic Heavy Ion Collider (RHIC) at BNL is one of the most successful heavy ion collider ever build. RHIC has started the heavy ion collision experiments in the year 2000 and it can accelerates heavy ions up to 200 GeV and protons up to 500 GeV. In the year 2009 the Large Hadron Collider (LHC) at CERN started its $Pb + Pb$ collisions at 2.7 TeV, LHC can accelerates proton up to 7 TeV. Till date RHIC and LHC are

very successful running heavy ion collider and looking for future upgrades.

1.4 Experimental Observables for the QGP Signature

There have been a number of measurements which strongly indicate the formation of QGP at RHIC. The hadronic degrees of freedom fail to explain these measurements.

Particle Spectra and Ratios

The information of the fireball produced in the heavy ion collisions is carried by the bulk properties of the medium. Therefore to get information about the system produced in these collisions one needs information of the different stages of freeze-out. During the freeze-out first chemical freeze-out occurs then the kinetic freeze-out. By fitting the identified particles transverse momentum (p_T) spectra the chemical and kinetic freeze-out parameters can be extracted.

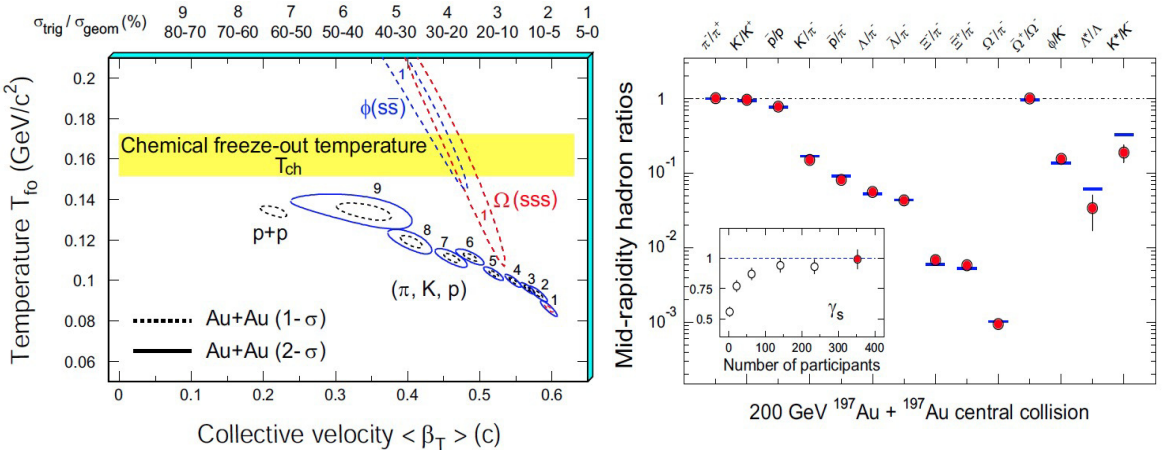

Figure 1.4: (Color online) (Left panel) Variation of T_{fo} as a function of average radial flow ($< \beta >$) extracted from the fitting of radial and thermal flow of produced hadrons in $Au + Au$ collisions at 200 GeV. (Right panel) Ratio of p_T integrated hadrons in top central $Au + Au$ collisions at mid-rapidity. The horizontal bars are the statistical model fits to the ratio of the measured yield [24].

The left panel of Figure 1.4 shows the extracted T_{fo} as a function of $< \beta >$, the average radial flow. The data fitted with the statistical thermal model shows a chemical freeze-out at $T_{ch} = 160 \pm 4\ MeV$ and $\mu_B = 24 \pm 4\ MeV$ [24]. The kinetic freeze-out can be estimated in the same way by fitting to the hadronic spectra.

The right panel of the Figure 1.4 shows the low p_T integrated particle yield measured by the STAR experiment at 200 GeV in $Au + Au$ collisions. The measured yields are fitted with the thermal model which shows good agreements except for short lived resonance particles like Λ^* and K^*. This has been explained that there is more re-scattering due to the larger system formed after the chemical freeze-out. The centrality dependent of yield ration (γ_s) shows a saturated value towards the central collision implying that there is saturation in the strange sector [24].

Jet Quenching

The fragmentation of energetic patrons or Jets are the symbol of QCD hard scattering and are therefore calculable by perturbative QCD. In the higher transverse momentum ($p_T \geq 5.0\ GeV$) region the particle production is predicted to take place by these hard processes [25]. The dijets are always produced in the opposite direction and the possibility of the origin to be at the center of the fireball is very low. Hence, the inner and outer side jets will travel different path length in the hot dense medium and will lose different amount of energy due to the interaction. This phenomena is known as the jet-quenching which can be studied as a probe for the signature of QGP formation in the heavy ion collisions.

In experimental measurements the jet-quenching phenomena is described by the nuclear modification factor. In heavy ion experiments for a collisions of $A+B$ the modification factor with respect to $p + p$ collision is defined as,

$$R_{AB}(p_T) = \frac{d^2N_{AB}/dp_T d\eta}{T_{AB} d^2\sigma_{pp}/dp_T d\eta} \tag{1.9}$$

where, $T_{AB} = \langle N_{bin} \rangle / \sigma_{inel}^{pp}$ takes into account the collision geometry, which is cal-

culated from Glauber Model [26] and $\langle N_{bin} \rangle$ is the number of binary collisions. This modification factor is expected to be equal to one in the absence of effects like Gluon-saturation, Shadowing and Cronin effect or for particle not undergoing strong interaction.

In Figure 1.5 the modification factor and two particles azimuthal distribution are shown as a function of p_T and $\Delta\phi$ for different collision systems [27]. The left panel shows a strong suppression in the central $Au + Au$ systems relative to the $d + Au$ system in the higher p_T region at $\sqrt{s_{NN}} = 200\ GeV$. This indicates that the suppression is due to the final state interaction and not for that of initial state effects which further indicate a hot and dense medium must be produced in this central $Au + Au$ collisions. The production of high p_T particles is suppressed due to partronic energy loss in the dense medium.

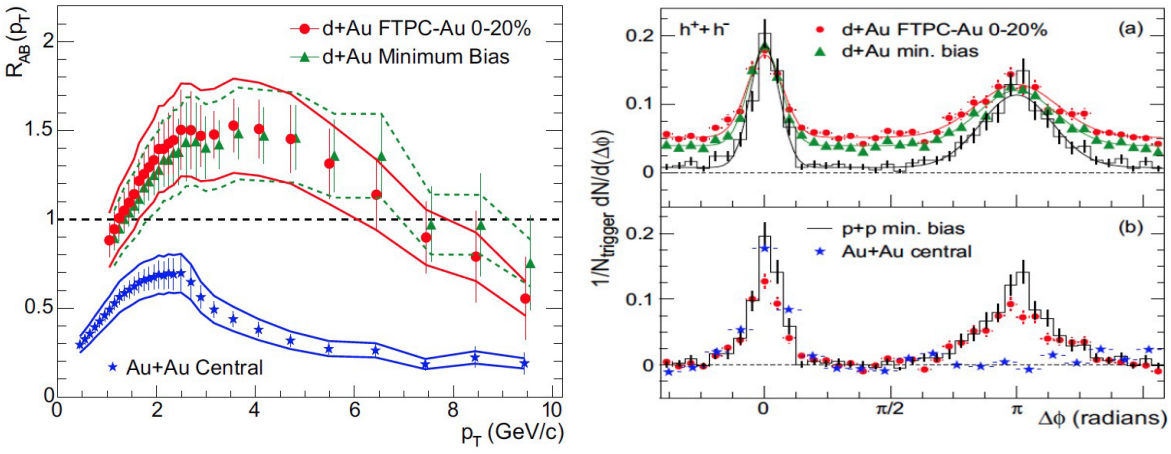

Figure 1.5: (Color online) Left panel: the nuclear modification factor R_{AB} as a function of p_T for $Au + Au$ and $d + Au$ collision systems at 200 GeV. Right panel: (a) two particle azimuthal distributions for $p + p$, $d + Au$ at 200 GeV and (b) comparison of two particle azimuthal distribution of $Au + Au$, $d + Au$ central collisions and $p + p$ minimum bias systems [27].

The right panel shows the two particle azimuthal distribution for different collision systems which illustrate the phenomena of jet-quenching. The azimuthal distribution of associated hadrons ($p_T^{trigger} > p_T^{associate} > 2\ GeV$) with respect to a trigger hadron ($4 < p_T^{trigger} < 6\ GeV$) shows an enhancement in the near side

($\Delta\phi \sim 0$) with respect to the away side ($\Delta\phi \sim \pi$) of the jet produce in the three colliding systems. The away side jet ($\Delta\phi \sim \pi$) of the $Au + Au$ central collision system suppressed completely due to the jet-quenching phenomenon.

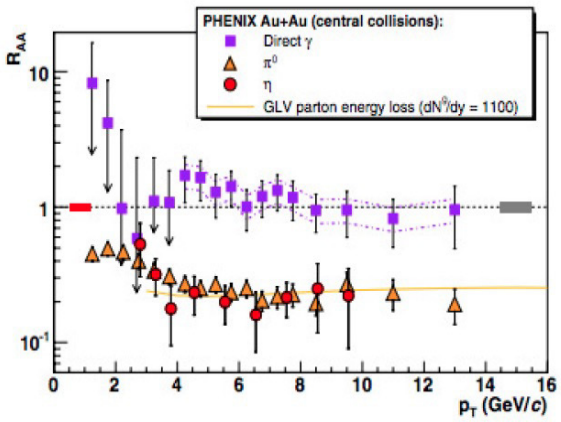

Figure 1.6: (Color online) $R_{AA}(p_T)$ for π^0, η and direct photons γ at 200 GeV central of mass energy in the $Au + Au$ collision system at RHIC [28].

In Figure 1.6 the modification factor for π^0, η and direct photon γ are shown as a function of transverse momentum at 200 GeV $Au + Au$ central collision [28]. It is observed that the charge neutral mesons π^0 and η shows a strong suppression in the high p_T region while direct photons does not show any suppression. This effect is interpreted as the partons interact strongly with the medium while the photons interacts through electromagnetic interaction. This comprehensive study strongly indicates the formation of QGP matter in the central $Au + Au$ collision of top RHIC energy.

Elliptic Flow

As mentioned before, when the two Lorentz contracted nuclei collide they produce a fire ball that has spatial anisotropy. The spatial anisotropy is reflected in the momentum anisotropy which gets mirrored in the azimuthal distribution of the produced particles. This distribution when Fourier decomposed, because of the symmetry of the system formed results in the absence of sine terms. The coefficients of the cos terms give various flow terms for instance the constant term is

called the directed flow [29], the coefficient of $\cos 2\phi$ is called the **elliptic flow** [30]. In the heavy ion collisions the impact parameter and the beam direction define a plain known as the reaction plain which changes with every collision. The elliptic flow (v_2) is the azimuthal anisotropy of the emitted particle in the momentum space with respect to the reaction plain. Elliptic flow is a strong and fundamental observable it not only gives an estimate of the nuclear equation of state but the constituent quark scaling observed for all the particles in mid p_T region is an indication that the system was collective and QGP was formed in these collisions.

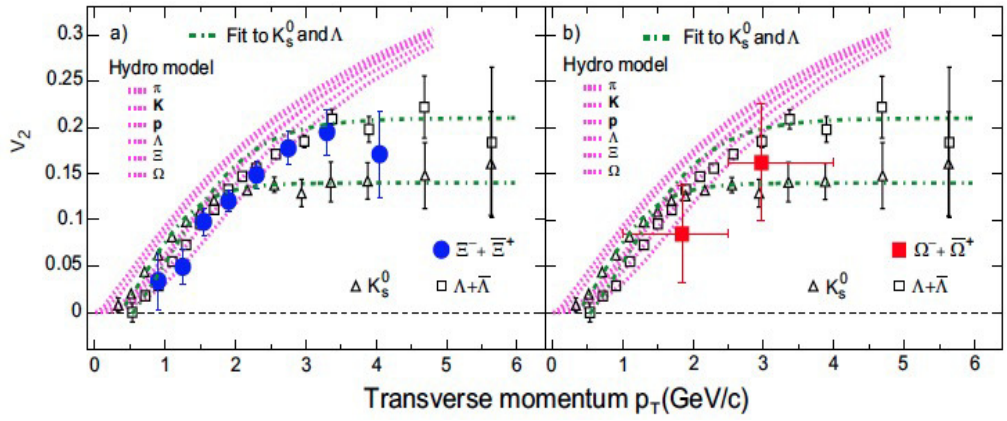

Figure 1.7: (Color online) Measurement of elliptic flow as function of p_T in $Au + Au$ collisions at 200 GeV for various hadrons produced in RHIC. The dotted lines represent the hydrodynamical fits to the data [31].

In Figure 1.7 the elliptic flow as a function of transverse momentum are shown for different hadrons measured in $Au + Au$ minimum bias events. It is observed that the v_2 of identified hadrons saturates in the higher p_T region. These saturation levels are different for particle species like mesons and baryons.

In Figure 1.8 the identified hadrons scaled elliptic flow measured in $Au + Au$ minimum bias collisions at 200 GeV are shown. Both the v_2 and p_T are scaled by their valance quark numbers (n_q). For $p_T/n_q > 1\ GeV/c$ the data shows very interesting features as its saturates. This can be interpreted as in the intermediate p_T region the data is saturating with the number of constituent quarks. These phenomenon indicates that the quark degrees of freedom was prevalent in the system produced in the heavy ion collisions.

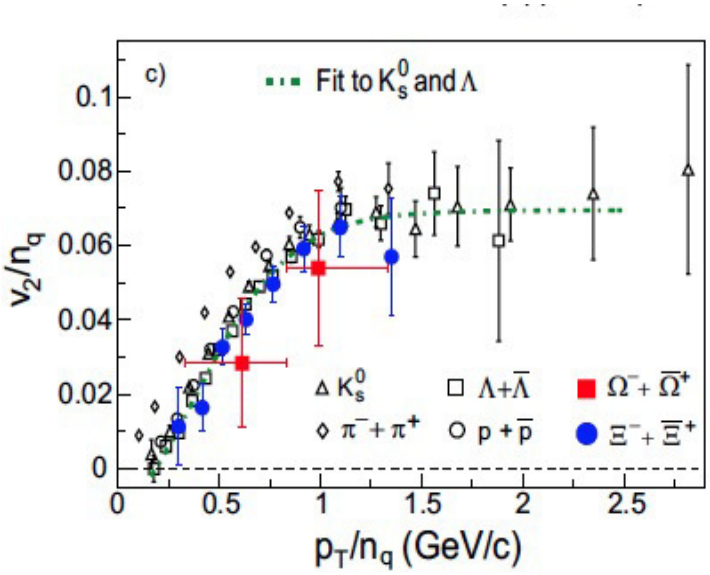

Figure 1.8: (Color online) Elliptic flow scaled by the constituent quarks number in the measured hadrons as a function of transverse momentum also scaled by corresponding quarks number [31].

Strangeness Enhancement

One of the key signatures of the quark gluon plasma formation in heavy ion collision is the strangeness enhancement [33]. It is expected that the strangeness will be equilibrated in QGP as compared to in the hadron gas due to the dynamical mass drop of strange quarks. Figure 1.9 shows the RHIC measurement of strangeness enhancement for strange particles as a function of average number of participants $< N_{part} >$ for $Au + Au$ and $Cu + Cu$ collision systems at 200 GeV. It is observed that along with the enhancement the central $Cu+Cu$ produce more strange hadrons than the mid-central $Au + Au$ collisions at RHIC top energy.

In the Figure 1.10 the upper panel shows the ratios of strange hadrons produced at RHIC for $Au + Au$ and $Cu + Cu$ at 200 GeV as a function of centrality normalized with the average number of participants and the corresponding yields from $p + p$ collisions. The lower panel shows the same of the ϕ mesons for both $Cu + Cu$ and $Au + Au$ collisions at 64.4 and 200 GeV. The enhancement of ϕ meson yield and other strange particle yields clearly indicates the formation of a dense medium. These two comprehensive study clearly indicates formation of

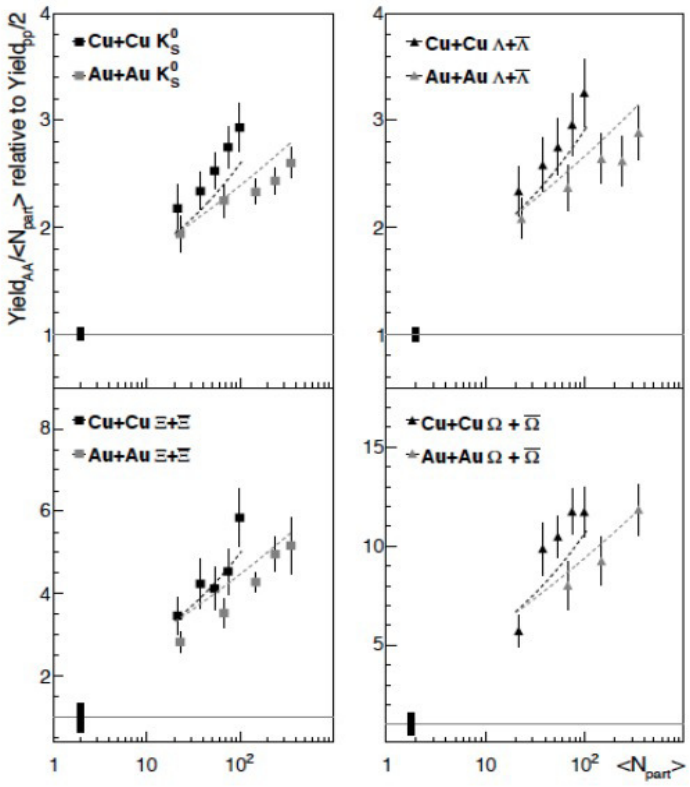

Figure 1.9: The strangeness enhancement factor as a function of centrality for various multi-strange particles measured in $Cu + Cu$ and $Au + Au$ collisions systems at 200 GeV [35].

dense medium produced in the heavy ion collisions.

There are several evidence of QGP formation in the heavy ion collisions both at RHIC and now at LHC. Many studies are undergoing in heavy ion collision experiments to understand the properties of QGP or QCD matter. The experiments at RHIC at Brookhaven national laboratory and now at LHC, CERN, Geneva have given valuable insight into the properties of QGP. The RHIC collider, at which this work was done is dedicated collider to understand the properties of QCD matter. This work pertains to mapping of the QCD phase diagram in the $T - \mu_B$ plain at various baryonic density by changing the center of mass energy of the nuclei-nuclei collisions.

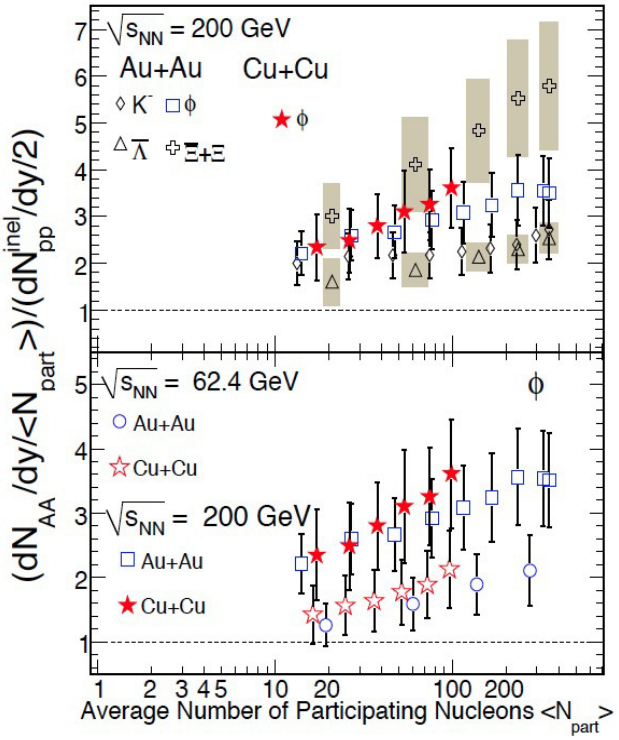

Figure 1.10: (Color online) Upper panel: Yield ratios of K^-, ϕ, $\Xi+\bar{\Xi}$ and $\bar{\Lambda}$ strange particles in $Cu+Cu$ and $Au+Au$ collisions at 200 GeV normalize with the corresponding yields from $p+p$ collisions as function of centrality. Lower panel: Same for the ϕ mesons at 62.4 and 200 GeV for $Cu+Cu$ and $Au+Au$ collision systems [36].

1.5 QCD Phase Diagram and Critical Point

Quantum Chromodynamics explains the QCD matter or the Quark matter and is a remarkable theory in the sense that for high momentum transfer the results agree with the experiment well. The theory of QCD describes a wide range of physical phenomena and their thermodynamic properties. The QCD theory can explain particle mass spectra as well as deep inelastic processes from the heavy ion collision experiments. Depending on the theoretical calculations both from Lattice QCD and simulation study along with some phenomenological inputs the QCD phase diagram was proposed to explain the thermodynamical properties of matter [38].

1.5.1 Phase Transition

The transformation of a state of matter into another is known as the **Phase transition**. The phase transition is characterized by the thermodynamic potential and its derivatives with respect to the thermodynamic quantity like temperature. The transition between two phases is described by the order parameter. These order parameters can changes very abruptly from one phase to another depending on the order of phase transition. For three states of water solid (ice), liquid (water) and gas (vapor) density play the role of an order parameter. If any of the first derivative of the thermodynamic potential is discontinuous then the transition is called **first order** phase transition. If one of the second order derivatives of the thermodynamic potential is divergent then the transition called the **second order** phase transition. For the **cross-over** there is no discontinuity in the derivatives of thermodynamical potential.

1.5.2 QCD Phase Diagram

The QCD phase diagram explains thermodynamic properties like temperature (T), pressure, baryon density (chemical potential (μ)) etc., as the fireball cools down and populates different phase of QCD matter. In this phase diagram each point characterized by these thermodynamic variables corresponds to a thermodynamic state.

The first phase diagram which explains different phases of matter as a function of baryon density and temperature was proposed by N. Cabibbo and G. Parisi in the year 1975 [39]. Hagedorn shows that for hadronic states the mass spectra increase exponentially [40, 41]. As conclusion to this fact it was predicted that, there may be a critical temperature (T_c) after which hadronic matters does not exist. Figure 1.11 shows the the first proposed phase diagram between baryon density (ρ_B) as a function of temperature (T). The diagram shows a boundary between the two phases of quark confinement and de-confinement.

To understand the QCD phase diagram the quark masses are the most im-

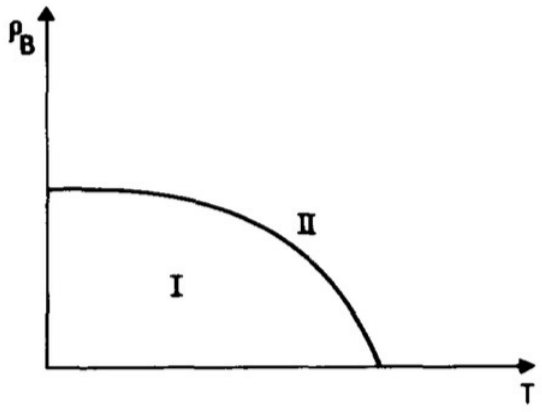

Figure 1.11: The first proposed phase diagram explaining the quark confinement (phase I) and de-confinement (phase II). The figure is taken from Ref.[39].

portant parameters which are also called as the symmetry breaking parameters as they break the Chiral symmetry. In conjunction with the Chiral symmetry argument, Pisarski-Wilczek [42] predicted that the transition between the confined and de-confined quarks is first (1^{st}) order at higher chemical potential (μ_B) region and at lower μ_B region its second (2^{nd}) order. The point in the first order transition line from where the second order begins is the tri-critical point. The second order criticality requires that the quark masses be set to zero. It also concludes that the nuclear matter is at lower temperature region where chiral symmetry is broken [38]. At the lower μ_B region the transition between lower temperature to a higher temperature QCD phase does not require to cross the singularity, where the quark masses (symmetry breaking parameters) are tuned to zero. Also the lattice calculation shows that at $\mu_B = 0$ the transition is a cross over [43]. Thus qualitatively there is an agreement, however, the location of the critical point can neither be calculated by Lattice QCD nor by first principles QCD and hence must be established experimentally.

Figure 1.12 shows a QCD phase diagram with temperature (T) as a function of baryon chemical potential (μ_B). In this figure the solid line is the first order transition line which separate the hadronic phase and the quark-gluon plasma phase. The end point of the first order transition line is the **Critical Point** (**CP**) of the sec-

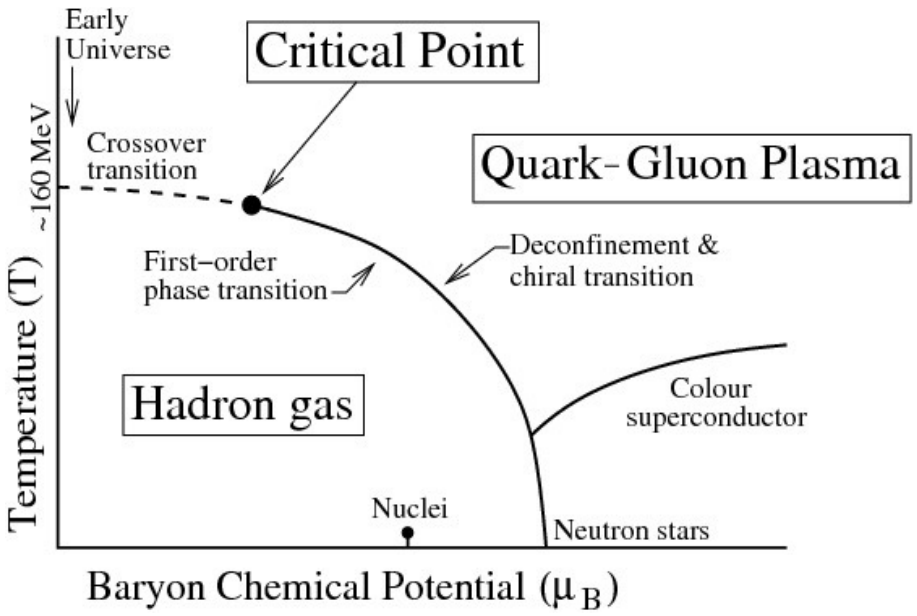

Figure 1.12: A contemporary sketch of QCD phase diagram in terms of temperature (T) as a function of baryon chemical potential (μ_B).

ond order. At negligible μ_B the transition (dotted line) between these two phase is a cross-over. With low temperature and very high baryon density the state of QGP matter is like Neutron stars which is a very high dense baryon plasma state. These plasma states are predicted to form the phase of color superconductor.

In Figure 1.12 different phase of QCD matters are shown. The lattice QCD is one of the strong aspect of the QCD. The energy density and the pressure normalized by 4^{th} power of the T as function of T calculated from lattice QCD are shown in the Figure 1.13 [47].

These plots shows the variation of normalized energy density and pressure for different flavours as a function of temperature normalized with the critical temperature and temperature respectively. From the left panel it is observed that the number of degrees of freedom rapidly increase at T approaches T_c and saturates for values $T > T_c$. This indicates that the degrees of freedom of the system at $T > T_c$ are that of quarks and gluons. Lattice QCD also predicts that the bulk thermodynamic properties of the system like pressure should reflect the degrees of freedom. The right panel of the Figure 1.13 shows that the pressure changes

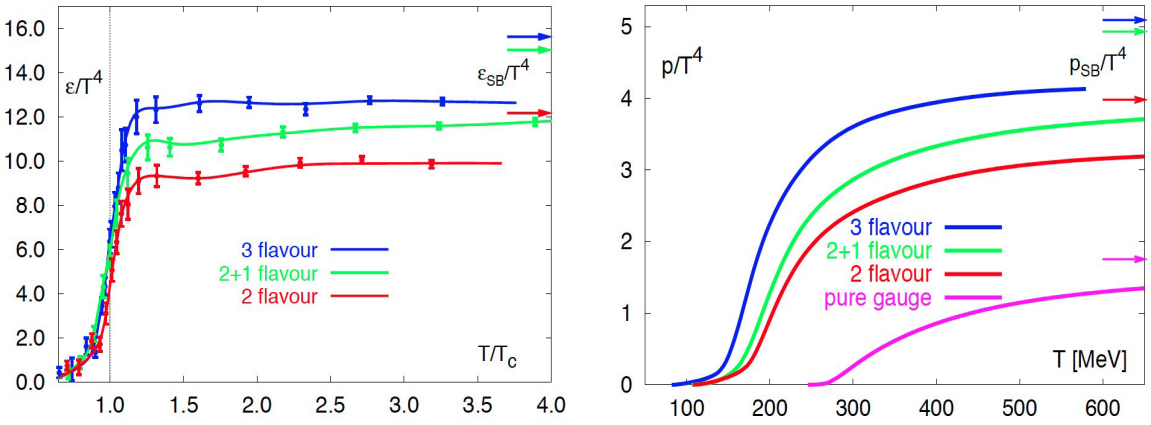

Figure 1.13: (Color online) (Left panel) Lattice calculation of energy density (ε) and (Right panel) pressure as a function of temperature for different degrees of freedom (flavours) [47].

strongly with the number of degrees of freedom which indicate that the number of degrees of freedom for quarks and gluons is much higher than that of light pions due to asymptotic freedom [47]. This sudden changes in the energy density or in the pressure at the critical temperature indicates the QCD phase transition or transition from the confined to the de-confined state.

1.5.3 QCD Critical Point and its Signatures

The most interesting and important point in the QCD phase diagram is the **Critical Point** (**CP**). If we go from higher to lower μ_B along the first order transition line the the transition stops beyond the critical point and the transition becomes a cross-over. From last few decades the main quest of the physicist in this field is about the QCD critical point and its existence.

Lattice calculation on finite size and vanishing chemical potential observe that the thermodynamic susceptibilities are very sensitive near the critical region [44, 45]. These thermodynamic susceptibilities are related with the higher moments of conserved quantities like net-baryon, net-strangeness and net-charges. The higher moments in turn vary as powers of the correlation length as discussed in

the Section 2.4 to Section 2.6. As mentioned earlier, for a system produced in heavy ion collision and populated near the critical point, the correlation length becomes large [46], it is expected that these higher moments and thermodynamic susceptibilities will show fluctuations near the critical region.

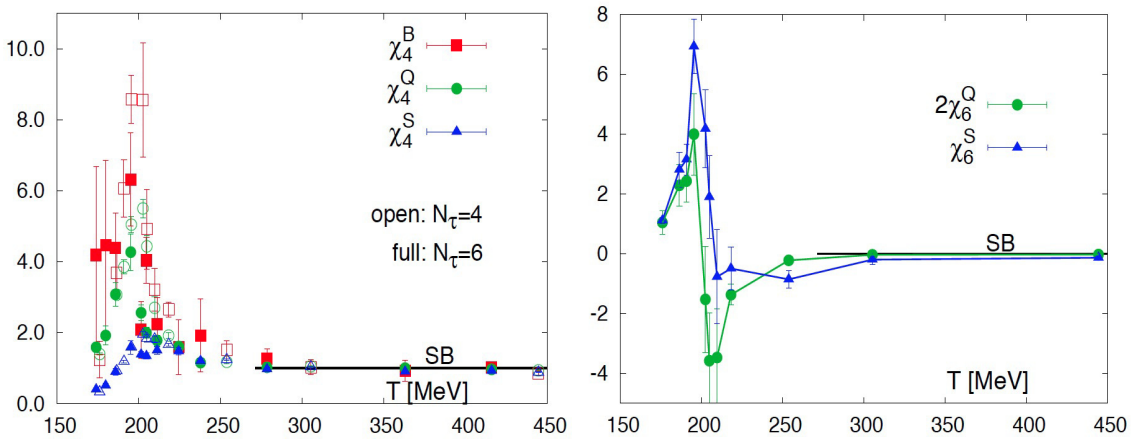

Figure 1.14: (Color online) The fourth order susceptibilities for net-baryon, net-strangeness and net-charges (left panel) and sixth order susceptibilities for net-charges and net-strangeness (right panel) [44].

In Figure 1.14 shows the fourth and sixth order susceptibilities calculated from lattice at vanishing chemical potential. The quadratic and quartic susceptibilities for net-baryon, net-strangeness and net-charges shows a rapid rise and a peak respectively at zero chemical potential in the transition region [44]. In the same study it is shown that the sixth order susceptibility of net-strangeness and net-charges changes sign near this transition region. It is also observed that after this transition region all susceptibilities match with the Stefan-Boltzmann limit of massless quarks. The ratio of the quartic and quadratic susceptibilities for net-strangeness are shown in the Figure 1.15 and compared with the HRG prediction. It is observed that the ratio have a peak at the transition temperature and falls down to the Stefan-Boltzmann limit after the transition temperature [44].

Various QCD based models try to predicts the QCD critical point from first principles by preserving the symmetries of QCD. A summary of QCD based model calculation for the search of critical point is shown in the Figure 1.16. The

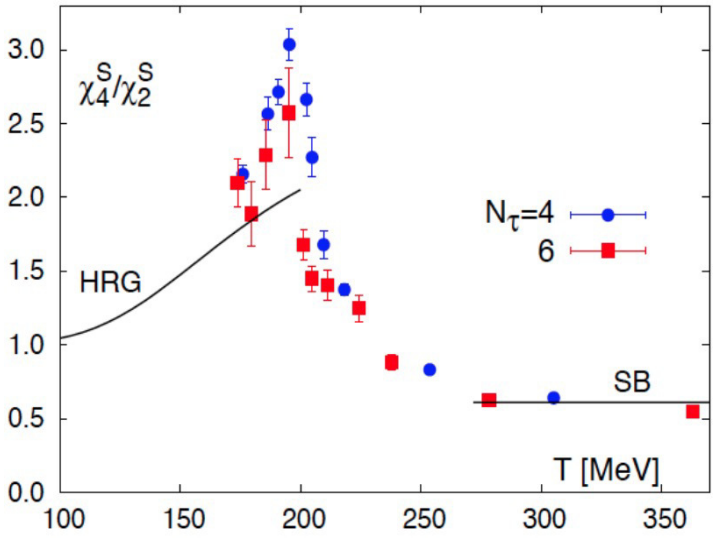

Figure 1.15: (Color online) The lattice QCD calculation of the ratio of fourth to second order susceptibilities in the T - μ_B plain compared with the HRG prediction [44].

dashed lines are the lattice predicted slopes of $dT/d\mu_B^2$ at $\mu_B = 0$ [48, 49]. The red open points are the freeze-out temperature (T_{fo}) for the corresponding center of mass energy marked on it from heavy ion collisions calculated from the measurement of particle yields from the ratio [64]. The prediction from the lattice calculation are the green points taken from LR01, LR04 [50], LTE03 [48] and LTE04 [45]. The black points are the predictions from the model calculation and taken from HB02 [51], CO94 [52, 53], INJL98 [54], RM98 [55], CJT02 [56], PNJL06 [57], NJL01, LSM01 [58], 3NJL05 [59] and NJL89a, NJL89b [60].

It is observed that these predictions have a wide range of possible critical point in the $T - \mu_B$ plain. The exact location of the critical point is still a mystery. Theoretical predictions suggest that by creating the state of QCD matter in heavy ion collision experiments, its may provide a probe to hunt the critical point.

In heavy ion collision experiments the most important question is whether during the freeze-out the system store the information of the thermal system or expansion period produce in the collision or not. If, yes the information will be reflected in the experimental measurements. Also if it has stored the memory of the phase space which pass through a critical point, the fluctuation will be reflected

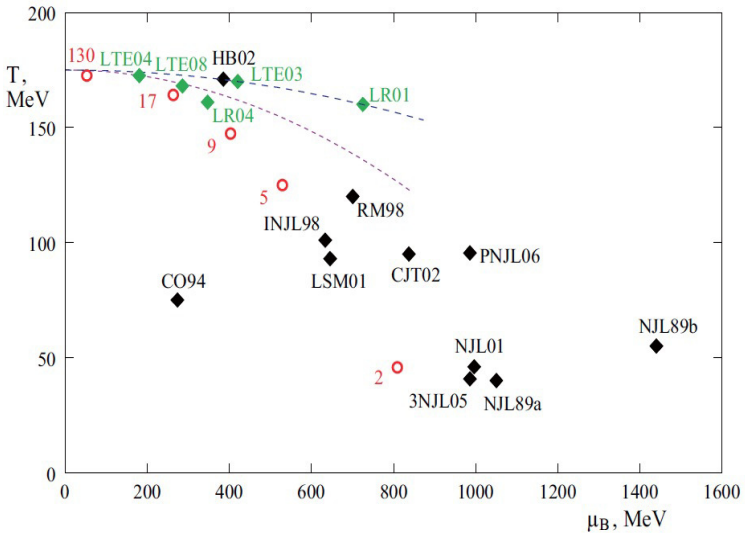

Figure 1.16: (Color online) A summary of critical points search in the T - μ_B plain predicted from different theoretical calculations [38]

during the freeze-out. Therefore, heavy ion collision experiments will provide a ideal probe to look for the signature of the phase transition and the critical point. The Relativistic Heavy-Ion Collisions at Brookhaven National Laboratory started its Beam Energy Scan program to find the critical point by scanning the QCD phase diagram.

1.6 Relativistic Heavy-Ion Collisions and its Beam Energy Scan Program

The Relativistic Heavy Ion Collider (RHIC) is the one of the most successful collider experiment in the world. Brookhaven National Laboratory in Upton, NY started the RHIC project in the year 2000 and accelerates heavy nuclei up to a energy of 100 GeV per nucleon, per beam [61, 62]. RHIC is capable of accelerating nucleus up to center of mass energy per nuclei for Au+Au collisions is $\sqrt{S_{NN}}$ = 200 GeV and that for proton is $\sqrt{S}$ = 500 GeV. The RHIC consists of several subsystems like Linear Accelerator (Linac), Tandem Van de Graaff (TVG), Tandem-to-Booster line (TTB), Booster Accelerator, Electron Beam Ion Source (EBIS), Al-

ternating Gradient Synchrotron (AGS), AGS-to-RHIC Line etc. [62, 63].

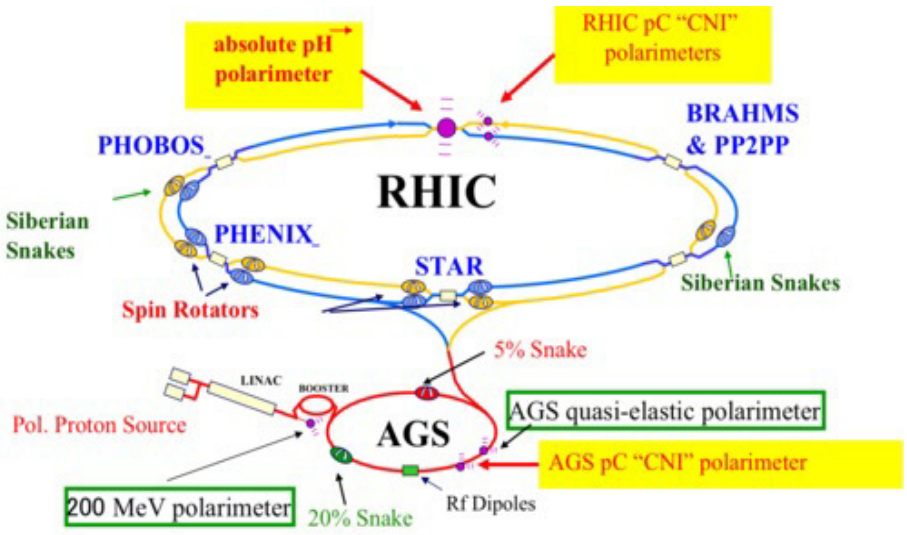

Figure 1.17: (Color online) A schematic diagram of the RHIC ring and its associated subsystems

The RHIC ring consists of two independent accelerator rings called "Blue" and "Yellow" rings. This independent ring carry heavy ions and proton circulating in opposite direction and allow a free choice of the interaction point. There are six interaction point in the ring where two opposite directed beam collide and give the ring a hexagonal shape. Among the six interaction points, RHIC had started initially with four detectors STAR, PHENIX, PHOBOS, BRAHMS one Supporting Building and one open access area in the ring [63]. PHOBOS and BRAHMS completed its operation in the year 2005 and 2006 respectively. STAR and PHENIX are ongoing experiment in the RHIC collider ring. The associated subsystems and the STAR detector system have been briefly discussed in Chapter 3.

The main aim of the RHIC Beam Energy Scan (BES) program is to study the phase diagram of QCD experimentally as a function of T and μ_B. As we measure the particles at the freeze-out, it is absolutely essential that we populate the system as near the critical point so that the time evolution to freeze-out is kept at the minimum. This can be done with the help of many QCD based statistical model which help in calculating the temperature and the baryon chemical potential at

the freeze-out.

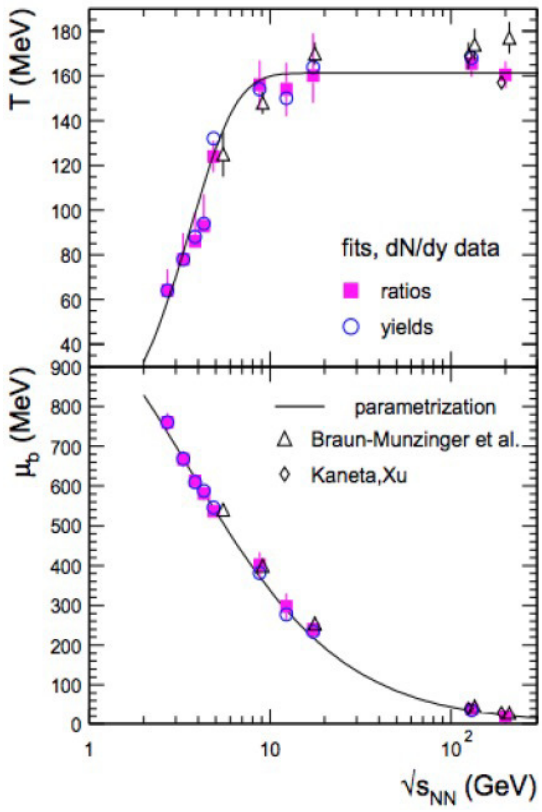

Figure 1.18: (Color online) Variation of the freeze-out temperature (T) and the baryon chemical potential (μ_B) corresponds to colliding energy [64].

Figure 1.18 shows the relation between the chemical potential and the temperature at the freeze-out in the QCD phase diagram with corresponding colliding energy [64]. As in the heavy ion collision experiments system evolves adiabatically the temperature get reduced with the expansion and the baryon chemical potential may also evolve. By changing the collision energy of the colliding nucleus it is possible to create systems with different initial condition in the T and μ_B plain. It is expected to have different trajectories in the T Vs. μ_B plain by creating a broad range of systems with different initial conditions. These trajectories are also expected to cross the phase boundary at different T and μ_B values which will allow access to many interesting features in the QCD phase diagram. The main physics goals of the BES program are:

(a) to find the evidence of the threshold energies for the signature of QGP and study the properties of the QGP with different chemical potential at freeze-out

(b) to search for the evidence of 1^{st} order phase transition in the QCD phase diagram and

(c) to locate the QCD Critical Point (CP) and find evidence of its existence.

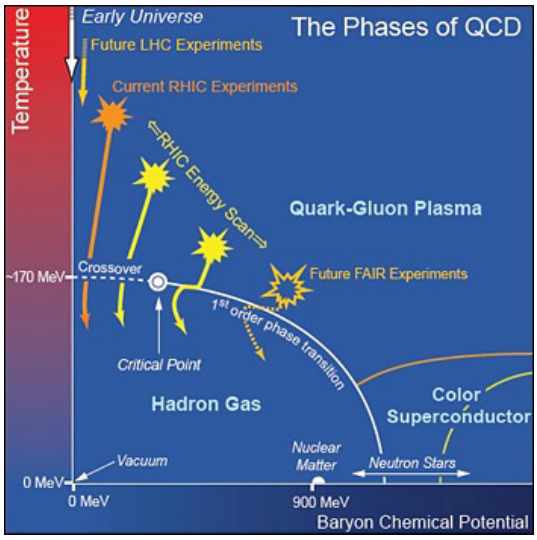

Figure 1.19: (Color online) A summary of the experiments to explore the phase diagram is shown along with the RHIC Beam Energy Scan program [24].

Figure 1.19 shows the summary of exploring the QCD phase diagram from different experiments. It is expected that the BES program of RHIC along with the two higher energies (62.4 and 200 GeV) will cover the region of interest where critical point lies, if there is any. The Large Hadron Collider (LHC) at CERN will cover the cross-over region at lower μ_B region and the future FAIR experiment will be performed at much higher μ_B region where the transition is of the **first order** type. RHIC has started its BES program in the year 2010 to fulfill its major goals. Table 1.1 briefly describe the details of BES-I program.

The phase-I of the Beam Energy Scan (BES-I) program carried out in the year 2010 (RUN 10) - 2014 (RUN 14). The BES-I program has been performed by colliding Au nucleus at the center of mass energy 7.7, 11.5, 14.6, 19.6, 27.0, 39.0, 62.4 and 200 GeV. By varying the centre of mass energy from 7.7 GeV to 200 GeV

Table 1.1: The year of production, centre of mass energy, number of events, calculated average baryon chemical potential ($\langle\mu_B\rangle$) and the duration of data production for BES-I program.

Year of production	Beam Energy (in GeV)	Event Statistics (in Million)	$\langle\mu_B\rangle$ (in MeV)	Beam Times (in Weeks)
2010	7.70	7	421	4.0
2010	11.5	16	316	2.0
2014	14.5	20	260	3.0
2011	19.6	27	206	1.5
2011	27.0	49	156	1.0
2010	39.0	240	112	2.0
2010	62.4	160	73	1.5
2010	200.0	360	24	11

BES-I allows one to cover the baryon chemical potential range from 421 MeV to 24 MeV in the QCD phase diagram.

By varying the baryon density the BES-I provide many new information and also conforms the evidence of formation of the QGP at the top RHIC energy. It is expected that the highest compression of baryonic matter corresponds to the lowest beam energy in the BES-I program. Several measurements from the BES-I program indicates that the hadronic interaction decreases with the increase of beam energy and partonic interaction increases with the beam energy. The most important feature of the QCD phase diagram is the critical point. Current QCD based lattice calculation suggest the critical point lie within the baryon chemical potential range of the BES program. The BES program at RHIC provides the access to the most interesting part of the QCD phase diagram in order to find the QCD critical point and to understand the properties of the QGP.

1.7 Scope and Organization of the thesis

The higher moments (Variance (σ^2), Skewness (S) and kurtosis (κ)) of conserved particle multiplicities such as net-baryon (ΔN_B, net-strangeness (ΔN_S) and net-charge (ΔN_Q) are related with the correlation lengths of the system produced in the heavy ion collisions and the thermodynamic susceptibilities [65]. It is expected that in the presence of the QCD **critical point** the correlation length becomes large and will show long range correlation and fluctuation at all length scales. Therefore the higher moments of conserved particle multiplicity are expected to show these fluctuation effects in its measurements. The kaons are dominated stable hadron in the strange sector and expected to interacts with the sigma fields more strongly than the pions. Therefore it is expected that the higher moments of net-kaon (ΔN_K) multiplicity distribution will reflect the critical phenomenon in the presence of the critical point.

The main aim of this work is to locate the QCD critical point by measuring the higher moments of net-kaon multiplicity distribution produced in the $Au + Au$ collision of the RHIC Beam Energy Scan program measured by the STAR experiment. By colliding $Au + Au$ nuclei freeze-out happens with different temperature (T) and baryon chemical potential (μ_B) which may pass through the QCD critical point. If the measured particles carry the information of freeze-out which may pass through the critical point it will reflect in the measured multiplicity. This study will explore the QCD phase diagram from a high T and small μ_B region to a region of very high μ_B. This study will also help to compare the experimental measurements with the results predicted by Lattice QCD.

The organization and a brief over view of this thesis is as follows:

Chapter 2

The higher moments and higher order cumulants and their relation along with their generating functions are discussed. Lattice QCD (LQCD) and thermody-

namic quantities from LQCD are briefly discussed. The relation between higher moments and cumulants of conserved quantities like net-baryon, net-strangeness, net-charge and their proxies like net-proton, net-kaon, net-pions with the susceptibilities and correlation lengths produced in heavy ion collisions are discussed. The probes to locate the critical point by measuring the higher moments of conserved quantities in heavy-ion collision are discussed.

Chapter 3

The experimental facilities at Relativistic Heavy Ion Collider (RHIC) and its associated subsystems are briefly described. The STAR experiment and its associated detectors are briefly described. The STAR Time projection Chamber (TPC) and Time of Flight (TOF) are described in more details since they are the main tracking detectors for the Particle Identification (PID) which have been used in the work described in this thesis.

Chapter 4

The analysis methodology has been presented in this chapter. The experimental trigger selection, data selection, bad run removal and details of the Quality Assurance (QA) plots of the data are also described. The kaon particle identification using TPC and TOF with different PID methods has been outlined. The collision centrality selection and its correction from ”Auto correlation”, ”Centrality resolution” and ”Bean Width” effects are presented. Finally we present the statistical and systematic error calculation along with the detector efficiency correction.

Chapter 5

Different models and baseline studied for the comparison with the experimental data are presented in this chapter. The prediction from Hadron Resonance Gas (HRG) model and Lattice QCD for the higher moments of net-strangeness

are presented. A comparison study of net-strangeness and net-kaon from Ultra-relativistic Quantum Molecular Dynamics (UrQMD) model are presented. The Central Limit Theorem (CLT) prediction to the data and its fits with the experimental observables are presented.

Chapter 6

In this chapter, the results from this analysis are presented for two different methods in performing the particle identification. Results are presented and compared with CLT expectation and predictions from various models and baseline studies followed by the physics discussions.

Chapter 7

This chapter contains the discussion based on the results obtained and the summary of this analysis. The outlook of this analysis for the future study is also discussed.

Chapter 2

Higher moments and Cumulants in Heavy Ion Collision

2.1 Higher Moments

2.1.1 Introduction

Statistically, moments are quantitative measure of the shape of a set of points. If the points represents the probability density the first moment gives the mean of the distribution. The "second moment" or more specifically the "second central moment", variance (σ^2) measures the "width" of the distribution. Other normalized central moments, Skewness (S), kurtosis (κ) describe other aspects like the tail and the peak of the distribution. A distribution can be characterized by its central and normalized central moments such as the mean(M), the variance(σ^2), the skewness(S), the kurtosis(κ), etc. [66, 67].

For a real continuous function $f(x)$ the n^{th} order moment around c is,

$$\mu_n = \int_{-\infty}^{\infty} (x-c)^n f(x) dx. \tag{2.1}$$

The moments about the mean is called the central moments. If the mean is μ, then

the n^{th} order central moment is,

$$\mu_n = E[(x-\mu)^n] = \int_{-\infty}^{\infty} (x-\mu)^n f(x) dx. \tag{2.2}$$

where $E[g(x)]$ is the expectation value of a function $g(x)$ with a probability density function $f(x)$ of a random variable x and define as,

$$E[g(x)] = \int_{-\infty}^{\infty} g(x) f(x) dx. \tag{2.3}$$

For the central moments the 1^{st} order central moment is zero, and other higher order central moments up to 4^{th} orders are,

$$\mu_2 = \int_{-\infty}^{\infty} (x-\mu)^2 f(x) dx. \tag{2.4}$$

$$\mu_3 = \int_{-\infty}^{\infty} (x-\mu)^3 f(x) dx. \tag{2.5}$$

$$\mu_4 = \int_{-\infty}^{\infty} (x-\mu)^4 f(x) dx. \tag{2.6}$$

The n^{th} order central moment divided by the n^{th} power of standard deviation is called normalized central moment or the standardized moment of n^{th} order and defined as,

$$M_n = \frac{E[(x-\mu)^n]}{\sigma^n} = \frac{E[(x-\mu)^n]}{(E[(x-\mu)^2])^{n/2}} \tag{2.7}$$

The 3^{rd} and 4^{th} order normalized central moments of the distribution are known as Skewness and kurtosis.

Skewness (S)

The normalized 3^{rd} central moment Skewness, represents the asymmetry of the probability distribution [68]. Skewness give the information about the tail of the probability distribution and defined as,

$$S = M_3 = \frac{E[(x-\mu)^3]}{(E[(x-\mu)^2])^{3/2}} = \frac{\mu_3}{\mu_2^{3/2}} \tag{2.8}$$

For a distribution with a longer tail in the left than that of the right one, will have a negative Skewness value and called negatively skewed. For a distribution with positive Skewness value have a longer tail in the right side and called positively skewed. For a symmetric or Gaussian distribution the Skewness value is zero. Figure 2.1 shows the example of two different distributions with two different

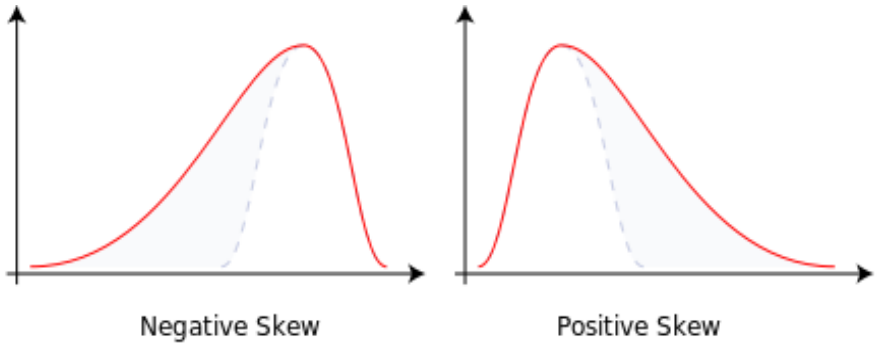

Figure 2.1: (Color online) Example of two different distributions with negative Skewness (left panel) and positive Skewness (right panel).

Skewness values. The right one with positive Skewness is right-skewed and the left one is left-skewed [68].

Kurtosis (κ)

The normalized 4^{th} central moment minus 3 is defined as the kurtosis (κ) of the probability distribution. Since the 4^{th} order central moment of a normalized or Gaussian probability distribution is $3\sigma^4$, to make the kurtosis equal to zero for the said distributions, minus 3 have been introduced [69]. The 4^{th} normalized moment is defined as,

$$M_4 = \frac{E[(x-\mu)^4]}{(E[(x-\mu)^2])^2} = \frac{\mu_4}{\mu_2^2} \tag{2.9}$$

Thus, kurtosis of the probability distribution is defined as,

$$\kappa = M_4 - 3 = \frac{E[(x-\mu)^4]}{(E[(x-\mu)^2])^2} - 3 = \frac{\mu_4}{\mu_2^2} - 3 \tag{2.10}$$

The kurtosis gives the information about the *"peakness"* of the probability distri-

bution. Figure 2.2 shows the kurtosis of seven well-known symmetric distribu-

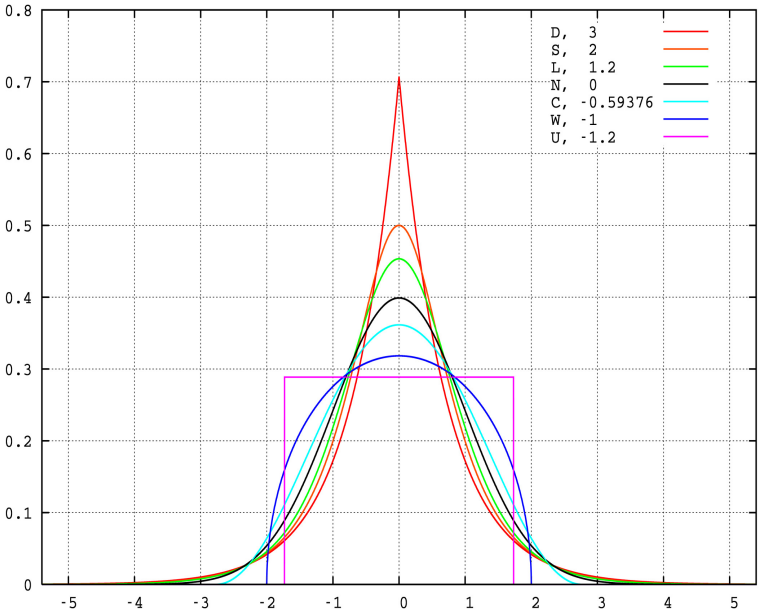

Figure 2.2: (Color online) Probability distribution for seven well known distribution with unity variance, zero mean and skewness. Each distribution shows different kurtosis(κ) values [69].

tions with unity variance, zero mean and skewness. The distributions are uniform distribution (U(magenta)), Wigner semicircle distribution (W(blue)), raised cosine distribution (C(cyan)), normal distribution (N(black)), logistic distribution (L(green)), hyperbolic secant distribution (S(orange)) and Laplace distribution (D(red)). The corresponding excess kurtosis are -1.2, -1, -0.593762, 0.0, 1.2, 2, 3 respectively. It is found that the distributions with a sharp peak have a larger kurtosis value than those distributions with broad tails. A distribution with higher kurtosis value has a sharper peak, longer and thick tails, while a distribution with a smaller kurtosis value has a less sharper peak, shorter and thin tails [69].

2.2 Cumulants

For a probability distribution cumulants are an alternative route for moments and are defined as [70],

$$c_n = \frac{\partial^n}{\partial t^n} g(t)|_{t=0} \tag{2.11}$$

where $g(t)$ is the cumulant generating function and the cumulants c_ns are the coefficients of Taylor expansion of $g(t)$, about the centre. For a random variable X defined as,

$$g(t) = logE[e^{tX}] = \sum_{n=1}^{\infty} c_n \frac{t^n}{n!} \tag{2.12}$$

here, $E[e^{tX}]$ is the moment generating function for random variable X,

$$M(t) = E[e^{tX}] = \int e^{tx} f(x) dx = E\Big[1 + tX + \frac{t^2X^2}{2!} + ... + \frac{t^nX^n}{n!} + ...\Big] \tag{2.13}$$

Hence,

$$M(t) = 1 + tm_1 + \frac{t^2m_2}{2!} + \frac{t^3m_3}{3!} + ... + \frac{t^nm_n}{n!} + ... \tag{2.14}$$

where, m_n is the n^{th} order moment of the probability distribution with random variable X and defined as,

$$m_n = \frac{d^nM(t)}{dt^n}|_{t=0} \tag{2.15}$$

For the cumulant-generating function we can derive the same as,

$$g(t) = tc_1 + \frac{t^2c_2}{2!} + \frac{t^3c_3}{3!} + ... + \frac{t^nc_n}{n!} + ... \tag{2.16}$$

2.2.1 Properties of Moments and Cumulants

In mathematical operations moments and cumulants follow same properties and they are almost similar. The properties of moments and cumulants are discussed below [70].

- **Homogeneity**

  For a probability distribution with random variable X, if m_n and c_n represent the n^{th} order moment and cumulant respectively, then for any constant k,

$$\begin{aligned} c_n(kX) &= k^n c_n(X) \\ m_n(kX) &= k^n m_n(X) \end{aligned} \tag{2.17}$$

- **Additivity**

  For two independent random variables, X and Y, if $c_n(X)$ and $c_n(Y)$ represent the n^{th} order cumulants and $m_n(X)$ and $m_n(Y)$ represent the n^{th} order moments, then,

$$\begin{aligned} c_n(X+Y) &= c_n(X) + c_n(Y) \\ m_n(X+Y) &= m_n(X) + m_n(Y), \quad \text{for } 1 \leq n \leq 3 \end{aligned} \tag{2.18}$$

- **Invariance and equivariance**

  For the random variable $X \to X + a$, the first cumulant and moment is,

$$\begin{aligned} c_1(X+a) &= c_1(X) + a \quad OR \quad c_1 \to c_1 + a \\ m_1(X+a) &= m_1(X) + a \quad OR \quad m_1 \to m_1 + a \end{aligned} \tag{2.19}$$

  which is shift-equivariant, but for the other cumulants for $n \geq 2$,

$$\begin{aligned} c_n(X+a) &= c_n(X) \\ m_n(X+a) &= m_n(X) \end{aligned} \tag{2.20}$$

  which is shift-invariant. Therefore we can say, by changing the random variable i.e. by adding a constant its shifts only the first moment/cumulant by the amount of the constant value and does not effects other moments/cumulants.

From the above section we argue that, under the mathematical operation moments and cumulants follow almost similar rules.

2.2.2 Relation between Moments with Cumulants

The moments and cumulants of a probability distribution are related. The lower order moments and cumulants are connected via simple mathematics while the higher orders follow complicated relations. Since the cumulant-generating func-

tion, $g(t) = lnM(t)$, from the Equation 2.14 and Equation 2.16 we can write,

$$exp(g(t)) = exp\left(\sum_{\infty}^{\infty} \frac{c_n t^n}{n!}\right) = 1 + \sum_{\infty}^{\infty} \frac{m'_n t^n}{n!} = M'(t) \tag{2.21}$$

The "prime" has been used to distinguished the moments m'_n from the central moments m_n. By taking derivatives on both side with respect to t, we can write,

$$\begin{aligned} &exp(g(t))\frac{dg(t)}{dt} = \frac{dM'(x)}{dt} \Rightarrow M'(t)\frac{dg(t)}{dt} = \frac{dM'(x)}{dt} \\ &\Rightarrow (1 + tm'_1 + \frac{t^2 m'_2}{2!} + ... + \frac{t^n m'_n}{n!} + ...) \times (c_1 + tc_2 + \frac{t^2 c_3}{2!} + ... + \frac{t^{n-1} c_n}{(n-1)!} + ...) \\ &\qquad = (m'_1 + tm'_2 + ... + \frac{t^{n-1} m'_n}{(n-1)!} + ...) \end{aligned} \tag{2.22}$$

We can relate the cumulants with the moments through the recursion formula as,

$$c_n = m'_n - \sum_{k=1}^{n-1} \binom{n-1}{k-1} c_k m'_{n-k} \tag{2.23}$$

By comparing coefficients of same powers of t from both sides of Equation 2.22, we can find,

$$\begin{aligned} m'_1 &= c_1 \\ m'_2 &= c_2 + c_1^2 \\ m'_3 &= c_3 + 3c_2 c_1 + c_1^3 \\ m'_4 &= c_4 + 4c_3 c_1 + 3c_2^2 + 6c_2 c_1^2 + c_1^4 \\ m'_5 &= c_5 + 5c_4 c_1 + 10c_3 c_2 + 10c_3 c_1^2 + 15c_2^2 c_1 + 10c_2 c_1^3 + c_1^5 \\ m'_6 &= c_6 + 6c_5 c_1 + 15c_4 c_2 + 10c_3^2 + 60c_3 c_2 c_1 + 20c_3 c_1^3 + 15c_2^3 + 45c_2^2 c_1^2 + 15c_2 c_1^4 + c_1^6 \end{aligned} \tag{2.24}$$

Since for the central moments the moments m_n are around the mean of the distribution which is the 1^{st} moment and therefore the 1^{st} order central moment is

zero, thus,

$$\begin{aligned} m_1 &= 0 \\ m_2 &= c_2 \\ m_3 &= c_3 \\ m_4 &= c_4 + 3c_2^2 \\ m_5 &= c_5 + 10c_3c_2 \\ m_6 &= c_6 + 15c_4c_2 + 10c_3^2 + 15c_2^3 \end{aligned} \tag{2.25}$$

We can express the n^{th} order cumulants for $n \geq 2$ as,

$$\begin{aligned} c_2 &= m_2 \\ c_3 &= m_3 \\ c_4 &= m_4 - 3m_2 \\ c_5 &= m_5 - 10m_3m_2 \\ c_6 &= m_6 - 15m_4m_2 - 10m_3^2 + 30m_2^3 \end{aligned} \tag{2.26}$$

For a probability distribution the first cumulant is the expectation value or the mean of the distribution. Also the second and third cumulants are the second and third central moments respectively. The higher cumulants are complicated polynomial function of moments and are not simple function of moments.

The four moments we will be constructing in this thesis is Mean (M), Sigma (σ), Skewness (S) and kurtosis (κ). The Mean is the first moment, σ is the positive square root of second central moment, S and κ is the third and fourth normalized central moments. These four moment define as,

$$\begin{aligned} M &= c_1 = m_1', \;\; \sigma = \sqrt{c_2} = \sqrt{m_2} \\ S &= \frac{c_3}{c_2^{3/2}} = \frac{m_3}{\sigma^3}, \;\; \kappa = \frac{c_4}{c_2^2} = \frac{m_4}{m_2^2} - 3.0 \end{aligned} \tag{2.27}$$

2.3 Lattice QCD approach

In 1974 K. Wilson proposed the Euclidean gauge theory on the Lattice to study non-perturbative QCD and its confinement [71, 72]. Monte Carlo integration by Feynman path integral technique of the Euclidean path has been used to formulate the Lattice QCD (LQCD). The discrete Euclidean space time grid formulates the QCD of the lattice where the quarks are at the lattice points and are connected by the gluons strings. The LQCD formulated in such a way that if QCD is the correct theory of strong interactions, all predictions from LQCD should match the experimental data [82].
The LQCD can be used:

- For the prediction of large momentum transfer phenomena.
- In the calculation of the hadronic spectrum in the domain of hadronic world by the use of non-perturbative tools. From the first principle, this tools also helps one to calculate the matrix elements of any operator within that hadronic state.
- In non-perturbative regularization method with discrete space-time lattice.
- To probe QCD by mapping it to a spacetime lattice.
- To understand chiral symmetry breaking and confinement mechanism. Furthermore, it serves as a basic tool to study of the role of topology and QCD equilibrium properties at finite temperatures.

The most useful property of LQCD is that the input parameters can be tuned for different physical processes. To study QCD one can predict the strong coupling constant or the running coupling constant (α_s) dependency and quark mass which helps one to construct various phenomenological models and theories like chiral perturbation theory, heavy quark effective theory.

2.4 Relation between Higher Moments and Thermodynamic Quantities from Lattice QCD

At equilibrium the intensive and extensive variables of any thermodynamic ensemble can be calculated with some inputs from the statistical model [74]. The intensive variables are independent of the system size and they are pressure (p), temperature (T), chemical potential (μ) etc.. The extensive variables are those that depend on the system size and scale linearly with the system, for example, the total energy (E), system volume (V), total particle number (N), magnetization (M) etc. [75].

In thermodynamics there are three kinds of ensembles for a system under equilibrium and they are micro canonical, canonical and grand canonical ensembles. For the thermodynamic micro canonical ensemble the system is isolated from the surroundings hence the particle number and energy is fixed. The canonical ensemble is the standard ensemble where the particle numbers are fixed but the energy is changeable. In grand canonical ensemble the system can change both the particle numbers and the energy.

If the partition function of a canonical system is $Z_N(V,T)$, then the grand canonical partition function is,

$$Z(z,V,T) = \sum_{N=0}^{\infty} z^N Z_N(V,T) \tag{2.28}$$

where $z = exp(\mu/kT)$ is the fugacity and μ is the chemical potential. Then the average number of particle within that ensemble is,

$$\begin{aligned} \langle N \rangle &= \frac{\sum N z^N Z_N}{\sum z^N Z_N} \\ &= z\frac{\partial}{\partial z} lnZ(z,V,T) \\ &= kT\frac{\partial}{\partial \mu} lnZ(z,V,T) \end{aligned} \tag{2.29}$$

In the similar way, we can calculate the higher moments of a thermodynamical

ensemble. For example, the mean-square of the ensemble will be,

$$\begin{aligned}\langle N^2\rangle - \langle N\rangle^2 &= \frac{\sum N^2 z^N Z_N}{\sum z^N Z_N} - \left[\frac{\sum N z^N Z_N}{\sum z^N Z_N}\right]^2 \\ &= z^2 \frac{\partial^2}{\partial z^2} lnZ(z,V,T) \\ &= (kT)^2 \frac{\partial^2}{\partial \mu^2} lnZ(z,V,T)\end{aligned} \tag{2.30}$$

In lattice QCD, it is possible to calculate the partition function by numerical or statistical methods. In the thermodynamic limit the thermodynamic quantities can be estimated from the derived partition function [76]. For example, the pressure, P, that describes a thermodynamics system can be expressed as,

$$P(T,\mu_B,\mu_Q,\mu_S) = \lim_{V\to\infty} \frac{T}{V} lnZ(T,\mu_B,\mu_Q,\mu_S,V) \tag{2.31}$$

and the dimensionless pressure is,

$$\frac{P(T,\mu_B,\mu_Q,\mu_S)}{T^4} = \lim_{V\to\infty} \frac{1}{VT^3} lnZ(T,\mu_B,\mu_Q,\mu_S,V) \tag{2.32}$$

where T, V represent the temperature and volume of the thermodynamic system. μ_B, μ_Q, μ_S are the baryonic, charge and strangeness chemical potential or the Lagrange multiplier [78]. In QCD the net-baryon number (ΔN_B), net-strangeness (ΔN_S) and net-electric charge (ΔN_Q) are the conserved quantities. Now, we can derive the n^{th} order susceptibility of conserved quantities by by taking derivatives to the dimension less pressure as,

$$\begin{aligned}\chi_q^n(T,\mu_B,\mu_Q,\mu_S) &= \frac{\partial^n (p/T^4)}{\partial(\mu_q/T)^n} \\ &= \frac{1}{VT^3} \frac{\partial^n lnZ}{\partial(\mu_q/T)^n}\end{aligned} \tag{2.33}$$

where, $q = B, Q, S$. The left hand side of this equation which represents the susceptibility of the system, can be measured experimentally while the quantity of right hand side can be obtained from lattice QCD calculations. Now, using

Equation 2.29 and Equation 2.30 we can write,

$$\begin{aligned} \langle N \rangle &= VT^3 \chi_q^{(1)} \\ \langle (\delta N)^2 \rangle &= \langle N^2 \rangle - \langle N \rangle^2 = VT^3 \chi_q^{(2)} \end{aligned} \tag{2.34}$$

The left side of the Equation 2.34 is the first and second order cumulant for the conserved quantities. Similarly, for the 3^{rd} and 4^{th} order we can show that,

$$\begin{aligned} \langle (\delta N)^3 \rangle &= VT^3 \chi_q^{(3)} \\ \langle (\delta N)^4 \rangle &= VT^3 \chi_q^{(4)} \end{aligned} \tag{2.35}$$

By calculating further we can show a generalized equation between the cumulants of conserved quantities and the susceptibility as,

$$c_n = VT^3 \chi_q^{(n)} \tag{2.36}$$

For any conserved distribution the mean, variance, Skewness and kurtosis can be expressed in terms of thermodynamic susceptibility as follows:

$$\begin{aligned} M_q &= \langle N \rangle = VT^3 \chi_q^{(1)} \\ \sigma_q^2 &= \langle (\delta N)^2 \rangle = VT^3 \chi_q^{(2)} \\ S_q &= \frac{\langle (\delta N)^3 \rangle}{\sigma_q^3} = \frac{VT^3 \chi_q^{(3)}}{\sigma_q^3} \\ \kappa_q &= \frac{\langle (\delta N)^4 \rangle}{\sigma_q^4} = \frac{VT^3 \chi_q^{(4)}}{\sigma_q^4} \end{aligned} \tag{2.37}$$

All these moments are volume dependent. In heavy ion collision experiments the measurement of system size or volume is very difficult. To cancel out these volume dependency different ratio of the cumulants hence the susceptibility have been taken to construct volume independent terms, and they are,

$$(S\sigma)_q = \frac{\chi_q^{(3)}}{\chi_q^{(2)}} \tag{2.38}$$

$$(\kappa\sigma^2)_q = \frac{\chi_q^{(4)}}{\chi_q^{(2)}} \tag{2.39}$$

$$(\frac{\sigma^2}{M})_q = \frac{\chi_q^{(2)}}{\chi_q^{(1)}} \tag{2.40}$$

From the Equation 2.38, 2.39 and 2.40 we can directly compare the experimental data with susceptibilities calculated from Lattice. The 4^{th} and 2^{nd} order susceptibilities calculated from lattice QCD [79] at zero baryon chemical potential ($\mu_B = 0$) for net-charge (ΔN_{ch}), net-baryon (ΔN_B), and net-strangeness (ΔN_S) are shown in the Figure 2.3. The results are obtained from temporal extent $N_\tau = 4$

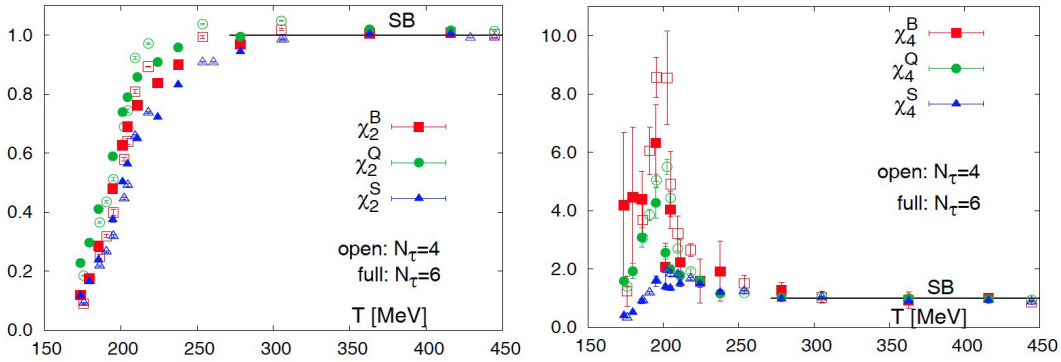

Figure 2.3: (Color online) The 2^{nd} and 4^{th} order susceptibilities calculated from LQCD for net-baryon number, net-strangeness and net-electric charge. The figure is taken from Ref.[79].

and coarser $N_\tau = 6$ on lattice QCD calculation. We can see the calculated 2^{nd} order susceptibilities rise rapidly near the transition region where the 4^{th} order susceptibilities show a peak [79].

2.5 Higher Moments in Heavy Ion Collision

In heavy ion experiments we measure the event by event multiplicity number. In the Figure 2.4 we have shown the net-kaon multiplicity distribution for $\sqrt{s_{NN}} = 62.4\ GeV$ at three different centrality, the black points are 0-5%, blue points are

30-40% and red points are 70-80%. For an event if we represent N as particle

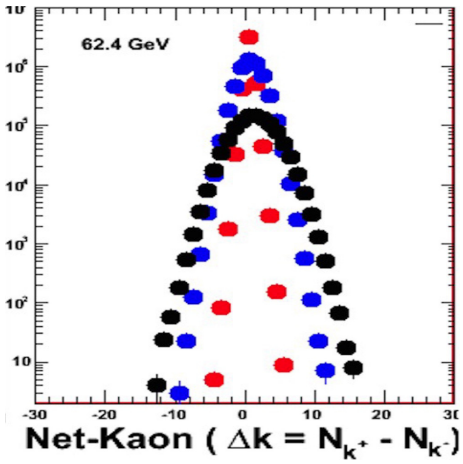

Figure 2.4: (Color online) Net-kaon distribution at $\sqrt{s_{NN}} = 62.4\ GeV$ for three different centrality black: 0-5%, blue: 30-40% and red: 70-80% measured at STAR in $Au + Au$ collisions.

multiplicity number then the deviation of N from the mean is,

$$\Delta N = N - \langle N \rangle \tag{2.41}$$

where $\langle N \rangle$ is the average number multiplicity of the multiplicity distribution. Then we can define the cumulants with different orders as:

$$C_1 = \langle N \rangle \tag{2.42}$$

$$C_2 = \langle (\Delta N)^2 \rangle \tag{2.43}$$

$$C_3 = \langle (\Delta N)^3 \rangle \tag{2.44}$$

$$C_4 = \langle (\Delta N)^4 \rangle - 3\langle (\Delta N)^2 \rangle^2 \tag{2.45}$$

We can also write the moments of the distribution as a function of these cumulants value,

$$M = C_1, \qquad \sigma^2 = C_2, \qquad S = \frac{C_3}{(C_2)^{3/2}}, \qquad \kappa = \frac{C_4}{(C_2)^2} \tag{2.46}$$

and moment products as,

$$\frac{M}{\sigma^2} = \frac{C_1}{C_2}, \qquad S\sigma = \frac{C_3}{C_2}, \qquad \kappa\sigma^2 = \frac{C_4}{C_2} \tag{2.47}$$

For a certain p_T and rapidity (or pseudo-rapidity) range we can measure the event-by-event particle number multiplicity. From the particle multiplicity distribution we can calculate the collision centrality using the MC Glauber model. With these above definition of various moments and their products we can measured event-by-event particle number fluctuations for each collision centrality.

2.6 Relation with Correlation Length in Heavy Ion Collision

The main aim of colliding heavy Ions in collider experiments at relativistic energies is to create a new form of matter with zero hadronic degrees of freedom, called QGP. Our major challenge is to experimentally probe this initial stage of QGP by detected particles coming out after the freeze-out. The basic idea in heavy ion collision experiments it to study the QCD phase diagram by creating a little **Big Bang** in the laboratory and measuring the fluctuations and correlations as a probe. The correlation of these particles, if the degrees of freedom were partonic, would give information about the de-confined matter [80]. In heavy-ion collisions the finite size, rapid expansion and time slowing down effects bring down the value of correlation length ξ, from infinity in the range of $2 - 3\ fm$ [83]. In experiments the event-by-event measured observable are believed to have sensitivity to the correlation length.

From the Hadron Resonance Gas (HRG) model [81] calculation and Lattice QCD calculation we see that the moments of conserved quantities are related to the thermodynamic susceptibilities. The QCD based models predict that the correlation length (ξ) of the system have sensitivity to the higher order moments of conserved quantities like net-charge (ΔN_{ch}), net-baryon (ΔN_B), and net-strangeness

(ΔN_S) number [81, 83]. It has been shown that the higher order non Gaussian moments of conserved quantities (ΔN_{ch}, ΔN_B and ΔN_S) are much more sensitive to correlation length as they depends on higher powers of ξ, than the 2^{nd} order moment. The 2^{nd} order moment or variances for any particle multiplicity is,

$$\sigma^2 = (\Delta N)^2 \tag{2.48}$$

where $\Delta N = N - M$. N represent the multiplicity within one event and M is the mean number of the multiplicity. The variance vary with the correlation length as [83],

$$\sigma \sim \xi^2 \tag{2.49}$$

The skewness($S = \langle(\Delta N)^3\rangle/\sigma^3$)) and kurtosis ($\kappa = [\langle(\Delta N)^4\rangle/\sigma^4] - 3$) are related to the correlation length as [83],

$$\begin{aligned} S &\sim \xi^{4.5} \\ \kappa &\sim \xi^7 \end{aligned} \tag{2.50}$$

As these higher moments are system volume dependent, to cancel out these volume dependency we have constructed moment products like $S\sigma$ and $\kappa\sigma^2$. These moment products can also be written as a ratio of the cumulants in the following manner,

$$S\sigma = \frac{C_3}{C_2} \tag{2.51}$$

$$\kappa\sigma^2 = \frac{C_4}{C_2} \tag{2.52}$$

These volume independent moment product having sensitivity to the correlation length (ξ) as S$\sigma \propto \xi^{2.5}$ and $\kappa\sigma^2 \propto \xi^5$ [84].

A change in the sign of Skewness value as a function of collision energy, may indicate a change of phase boundary [86]. Also the skewness and kurtosis are zero for a Gaussian distribution. Thus, these higher moments are promising probe for non-Gaussian fluctuation measurements.

In the vicinity of the critical point the correlation lengths are expected to diverges. The higher order moments of conserved quantities are strongly related

with the correlation length. In the presence of critical point the higher order moments are assume to be affected and expected to give some signature of the critical phenomena.

Chapter 3

The Experimental Set-up

3.1 Introduction

One of the main aim of Nuclear Physicists is to map the QCD phase diagram. It is believed that QCD matter undergoes two transitions, the chiral phase transition and the de-confinement transition in these ultra relativistic heavy ion collisions. The nature of theses transitions and the sequence that they follow is not known yet. As has been mentioned earlier, using the beam energy scan program of RHIC with the STAR detector, we would like to locate the second order critical point at which the first order phase transition of hadronic matter to QGP ends. Theoretically it is not possible to locate the critical point either by first principles or by Lattice QCD. The present thesis is part of the STAR collaboration effort to locate the critical point by studying certain experimental observables as a function of the centre of mass energy (the two Au beams were varied from 7.7 $AGeV$ to 200 $AGeV$). As pointed out earlier, higher moments of the distribution of conserved quantities such as net baryon, net strangeness and net charge could serve as valuable experimental observables in the search for the critical point. In this thesis we investigate the higher moments of the net-kaon distribution as a function of baryon chemical potential to locate the critical point. In this chapter we discuss the experimental set-up used for these studies. We first describe the essential components of the Relativistic Heavy Ion Collider and then the principal

detectors of STAR experiment.

3.2 The Relativistic Heavy-Ion Collider

The Relativistic Heavy Ion Collider is a world class particle accelerator located at Brookhaven National Laboratory, Upton, NY. The project to study matter created in relativistic heavy ion collisions was proposed to the US Department of Energy in the year 2000. It is capable of accelerating nuclei for Au+Au collisions upto centre of mass energy $\sqrt{S_{NN}}$ = 200 GeV and that for proton is $\sqrt{S}$ = 500 GeV. A diagram of RHIC area at Brookhaven National Laboratory along with a design diagram shown in the Figure 3.1[61, 62].

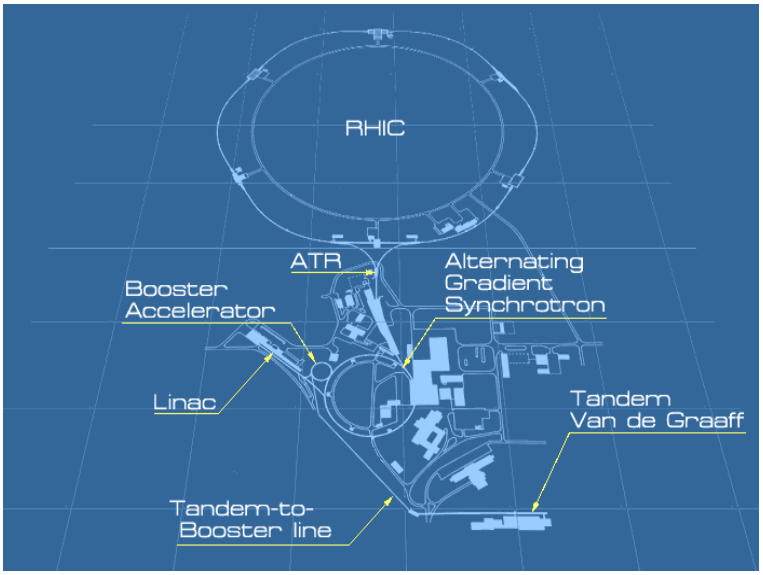

Figure 3.1: (Color online) RHIC at Brookhaven National Laboratory and its subsystems.

RHIC subsystems and supporting systems

RHIC consists of several subsystems. Ions goes through several stages before they enter the RHIC ring where the collisions take place after they attain the desired energy. The different subsystems are briefly described below [62].

- **Linear Accelerator (Linac):**

  In 1971 the Brookhaven Linear Accelerator (Linac) started to upgrade the Alternating Gradient Synchrotron (AGS). The Linac is the main source of polarized or a high intense proton beams for the RHIC and NASA Space Radiation Laboratory (NSRL). It is also used in the production of medical isotopes by accelerating protons at Brookhaven Linac Isotope Producer (BLIP) facility. The Linac can produce a negatively charged hydrogen beam up to 200 MeV energy and 135 μAmp of average current.

- **Tandem Van de Graaff:**

  Tandem Van de Graaff was the largest electrostatic facility for many years. It has the capability to provide a wide range of different types of ions. It can provide ions starting from hydrogen to uranium. It consists of two 24 meter long, 15 MeV accelerators placed at the ends.

- **Tandem-to-Booster line:**

  The TtB line is a beam transport system. TtB line is situated in a 700 meter long tunnel. For further acceleration the TtB deliver heavy ions from Tandem to the AGS. The presence of TtB make Tandem possible to supply the ions to the RHIC.

- **Booster Accelerator:**

  Booster is an important part of AGS with size less than a quarter of AGS operated by Collider-Accelerator Department. Booster receives heavy ions from Electron Beam Ion Source (EBIS) or proton from Linac. It then pre accelerates particles and injects it to the AGS ring. Booster also serves as an ion source for the NASA Space Radiation Laboratory.

- **Electron Beam Ion Source:**

  The EBIS is the ion source for RHIC and NSRL. It creates ion beams from the lightest to the heaviest elements. The EBIS consist with an inter-digital-H linac and a radio frequency quadrupole which lead to a electron beam

ionization source. EBIS injects ions after accelerating through Linac then Booster to the RHIC and NSRL.

- **Alternating Gradient Synchrotron:**
  The AGS is the final and most important part in the injector chain. It receives beam from Booster and accelerates it before releasing it to the two RHIC accelerator ring. It uses the concept of alternating gradient focusing. To focus both in horizontal and vertical direction, 240 magnets are alternated inward and outward. AGS is capable of accelerating 70 trillion ions in every pulse.

- **AGS-to-RHIC Line:**
  The AGS-to-RHIC (ATR) line is the last platform for the beam before entering the RHIC ring. The characterization of the beam extracted from AGS is done in this transfer line. At the end of this line a switching magnet gives direction to the ion bunches either in clockwise or in anti-clockwise direction. The opposite directed beam interact with each other at six different interaction point in the RHIC ring.

- **RHIC Ring:**
  The RHIC ring consists of two independent rings called ”Blue” and ”Yellow” rings, carry heavy ions and proton in opposite direction. There are six interaction point in the ring where the two opposite directed beam collide. Originally there were four detectors STAR, PHENIX, PHOBOS, BRAHMS one supporting building and one open access area in the ring[63].

PHOBOS (10 o’clock) and BRAHMS (2 o’clock) completed their operations in 2005 and 2006 respectively. STAR and PHENIX are presently the two ongoing experiment in the RICH collider ring.

3.3 The STAR Detector

STAR(**S**olenoidal **T**racker **A**t **R**HIC) is situated at the 6 o'clock position in the RHIC ring. The main goal of STAR is to explore the QCD phase diagram and study the characteristics of quark-gluon plasma formed in ultra relativistic heavy ion collisions. It is one of the most successful on going experiment in the world. The STAR is well equipped to identify charged particles and to measure their momentum. The setup of the experiment is shown in Figure 3.2[87].

The STAR detector has a large uniform acceptance with complete azimuthal

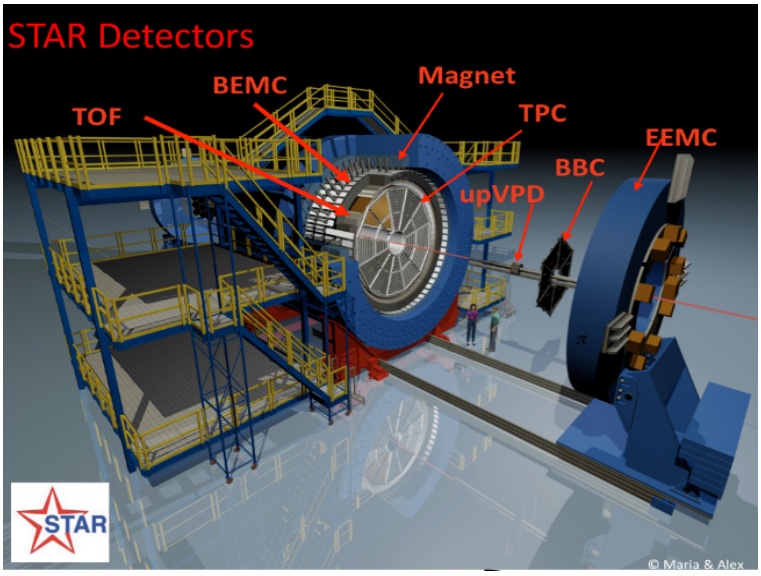

Figure 3.2: (Color online) A perspective view of the STAR detector system with a cutaway for viewing inner sub-systems.

coverage. Its solenoidal design helps one to measure many experimental observables simultaneously. The detector consists of several subsystems or detectors. The heart of the STAR detector is a large Time Projection Chamber (TPC) located in a uniform magnetic field of 0.5 Tesla[88]. The cross-section layout of the STAR detector system is shown in Figure 3.3. The main tracking detector systems are TPC, two Forward TPCs (FTPC) and the silicon vertex tracker (SVT). The event multiplicity is measured by the Central Trigger Barrel (CTB). The Time of Flight (ToF) and a ring-imaging Cherenkov detector extend the particle identification up to a very high p_T. The measurement of photons, electrons and transverse en-

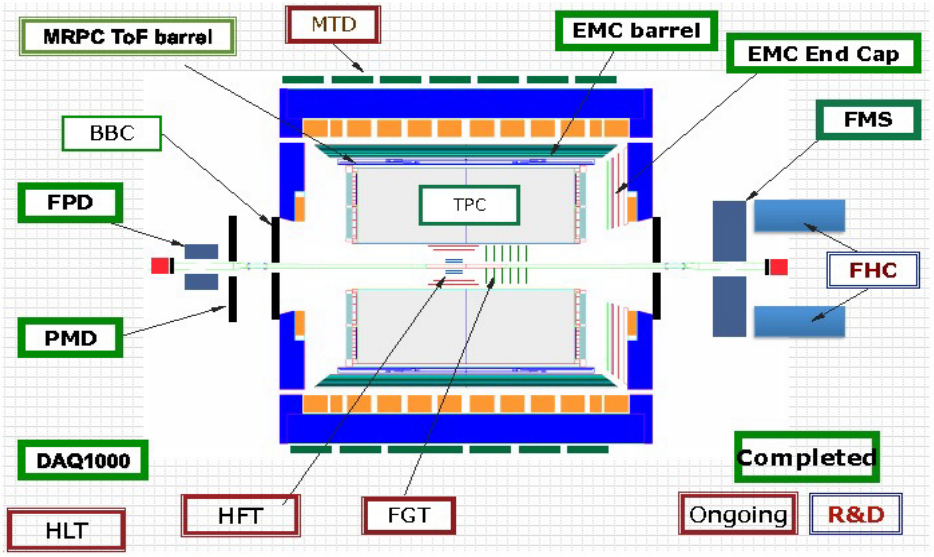

Figure 3.3: (Color online) A cross-sectional cutaway of the STAR detector in its configuration with other sub systems.

ergy of events use 10% of the barrel electromagnetic calorimeter. The detector subsystem also include two zero-degree calorimeters (ZDCs) at both of the ends which measure the daughter spectator neutrons.

The full azimuthal coverage and uniform acceptance of the STAR detector makes it ideal to study particle spectra, flavour composition, fluctuation, momentum distributions, source size (HBT), and source expansion (d and d'). Parton physics is accessible through studies of leading particles, as well as jet production when the TPC is used in conjunction with the EM calorimeter[89].

3.4 The STAR Time Projection Chamber

The **T**ime **P**rojection **C**hamber (TPC) is the primary detector of STAR and can track up to $\sim 4 \times 10^3$ particles per event. The TPC is mainly used for measurement of particle momenta from the tracks of the particle and also helps in particle

identification by measuring the energy loss as a function of distance traversed. It covers the pseudo-rapidity region $|\eta| < 1.8$ due to the collisions in its center. It can measure particle momentum within the approximate range $0.07 < p_T < 30$ $GeV/$c. The momentum resolution $\delta p/p$ depends on η and p_T of the tracks but for most tracks $\delta p/p \sim 0.02$. The associated detector subsystems mostly work in conjunction with the TPC to refine and improve itś measurements. Charged particles are detected, identified and their momenta measured with uniform acceptance for $|\eta| < 1.0$. It is 4.2 m long and 4 m in diameter and situated at the center of STAR detector.

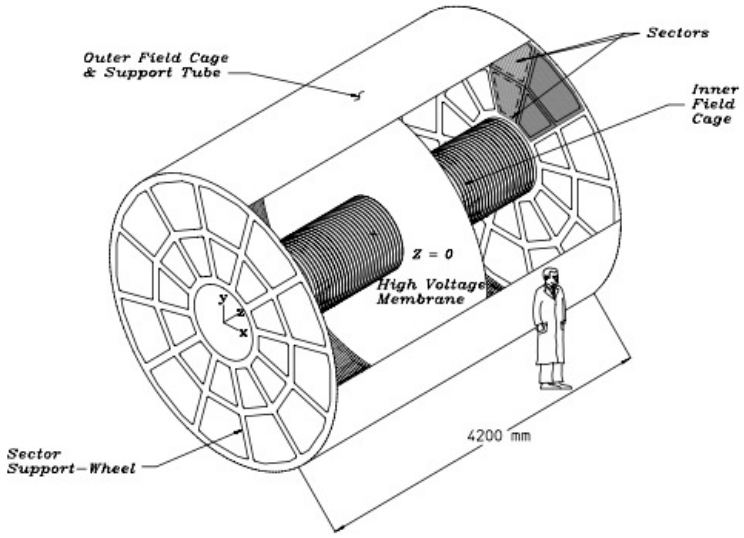

Figure 3.4: The schematic diagram of STAR Time Projection Chamber at RHIC.

CM Cathode

General Description

The CM cathode is a disk of 70 μm thickness made carbon-loaded Kapton film. CM has a surface resistance of 230 Ω/m^2. The Inner Field Cage (IFC) pass through the center of CM. Each side of CM attached with 36 aluminum stripes for the TPC laser calibration[89].

The field cage

The CM is connected with the anode with 182 equipotential cylindrical rings called the field cage. The outer rings of field cage also provide physical support to the CM. The field cages additionally serve as the container of the TPC gas. The rings are connected with a resistor chain to produce a uniform gradient between the CM an end cap. The mechanical design of field cage was done by using flex-

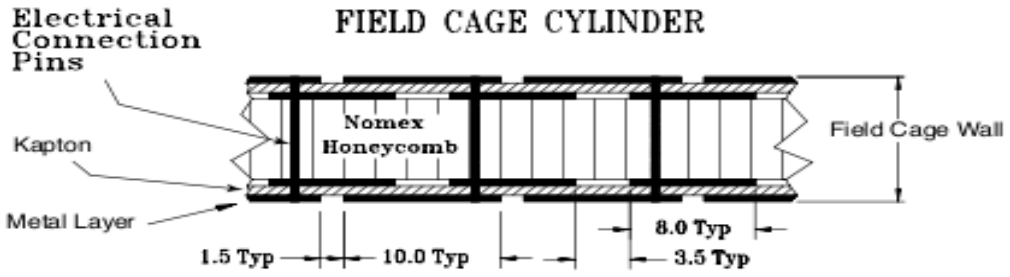

Figure 3.5: Field cage cylinder of TPC. The construction and composition are shown.

ible PCB material, Kapton. Both the sides of the flexible material have a metallic coating to provide Ohmic contact. This coating of metal helps to form 10 mm electrically 1.5 mm separated strips. The mechanical design has been optimized to reduce background from secondary particle and Coulomb scattering.

The end-caps and pad planes

The TPC end-caps readout planes consists of Multi Wire Proportional Chamber (MWPC) with pad readout. The end-caps are grounded and mounted on two aluminum support wheels at both the ends of the TPC. There are 12 readout modules or sector in each of the end-cap which looks like a circular clock. There is 3 mm space between two sectors and they are installed in side as the support wheels. The direction is chosen to determine the particles with highest transverse momentum (p_T), since the resolution is better along the direction of the anode wire and the high p_T tracks emerge almost straight and radial from the interaction point. Figure 3.6 shows a full sector of anode plane. The sectors are consist with

outer and inner sub-sectors. For dE/dx resolution optimization the outer radius

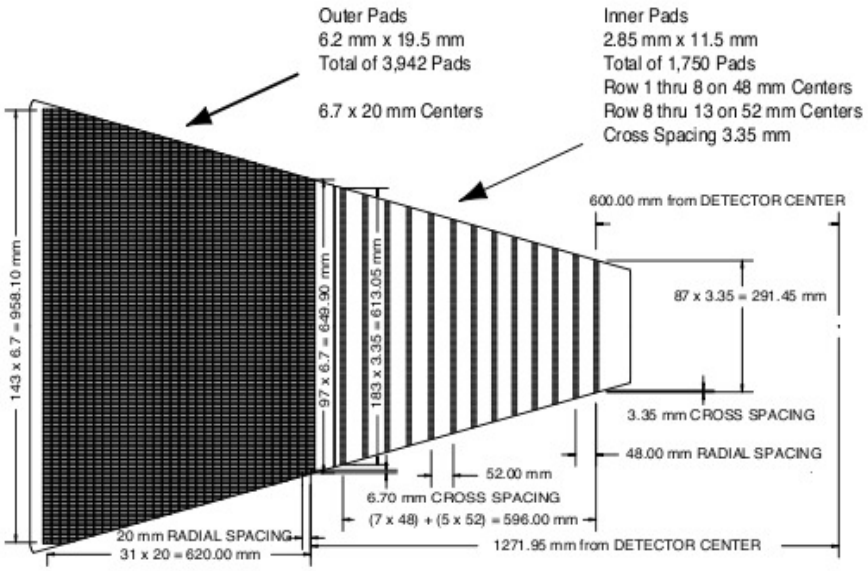

Figure 3.6: A diagram of one full sector of TPC anode pad plane. The inner sub-sector is shown on the right which has small pads and bigger spacing compared to the outer sub-sectors. The figure is taken from Ref.[89].

are arranged on a rectangular grid with no spacing between the pad rows. This also improve the tracking resolution and reduce dE/dx resolution with a small amount. A cross sectional view of an end cap's outer sub sector pad panel is

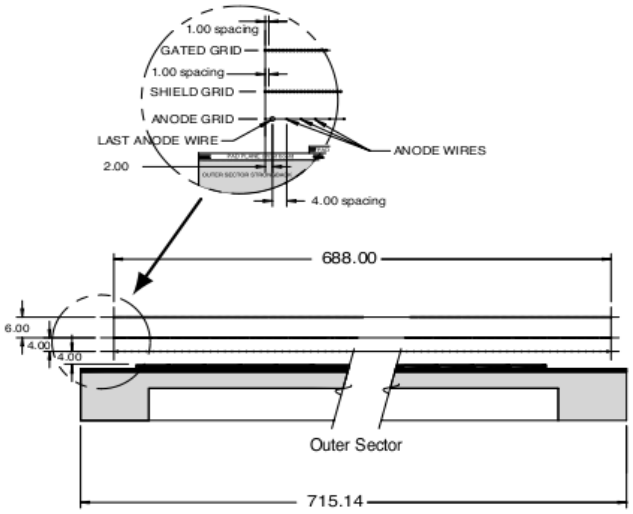

Figure 3.7: A cross sectional view of an outer sub sector pad plane. All dimension are in mm. The figure is taken from Ref.[89].

shown in the Figure 3.7. The inner sub sectors are optimized for two hit resolution by reducing the size as they are in the high track density region. For the improvement of two-track resolution the spacing between pad plane to anode wire is reduced to 2 mm. The inner sector mainly serve to the detection of low momentum particles and helps to improve the momentum resolution. There are total number of 45 pads in a sector so, the maximum number of sampling will be 45 if a track cross all pad rows[89].

Drift gas

TPC uses P10 (90% argon + 10% methane) as the working gas. The TPC gas has been chosen by considering the gas purity, drift velocity, cost and safety. To maintains purity, reducing electro-negative impurities which capture drifting electrons, the gas system always circulates the TPC gas and operates at atmospheric pressure. The longitudinal and transverse diffusion in P10 is about $\sigma_T = 3.3\ mm$ and $\sigma_T = 5.2\ mm$ after drifting 210 cm at 0.5 T magnetic field. For Pl0 gas system shaping time is 180 ns and TPC operate with 12.3 MHz sampling rate.

TPC performance

Since the momentum of the particles is finite, track may not cross all 45 rows. The number of hits in the pad rows depends on the radius of curvature, pseudo-rapidity and other parameters of particle's trajectory. Even the signals arriving at the end-cap from the secondary electrons the over all efficiency is not 100% due to several factors like the track merging, fiducial cuts, dead channels, bad pads etc..

Reconstruction of the position

Assuming the incident charge distribution on the pads are Gaussian distribution

the the x(y) coordinate given by,

$$x(y) = \frac{\sigma^2}{2w} ln(\frac{h_3}{h_1}) \tag{3.1}$$

where h_1, h_2 and h_3 represent the amplitudes on three adjacent pads and with pad h_2 centered at y(x) = 0. The width of the signal is σ and given by,

$$\sigma^2 = \frac{w^2}{ln(h_2^2/h_1 h_3)} \tag{3.2}$$

where, w is the pad width. The z coordinate within the TPC volume determined by measuring the drift time from the origin to the anodes of secondary clusters.

Particle identification

When a charged particle passes through the TPC gas volume, its ionizes the gas medium and loses energy. For the particle identification the information of dE/dX energy loss in the TPC gas medium is a valuable tool. The total charge collected on pad rows from each hit of a track are proportional to the ionization energy loss of the particle. The energy loss information works very well for the low momentum particles for particle identification. For the particles with higher momentum the energy loss depends very weakly on the mass and after $v > 0.7c$ its hard to separate particle species. For a particle passing through the gas medium the dE/dX energy loss given by the Bethe-Bloch formula:

$$\langle \frac{dE}{dX} \rangle = 2\pi N_0 r_e^2 m_e c^2 \rho \frac{Z z^2}{A\beta^2} [ln \frac{2m_e \gamma^2 v^2 E_M}{I^2} - 2\beta^2] \tag{3.3}$$

where z is the particle charge with velocity $v = \beta/c$ passing through a medium of density ρ, N_0 is Avogadro's number, m_e is the mass of electron, r_e is the classical electron radius, Z and A are the atomic number and atomic weight of the absorbing material, I is the average excitation energy, $\gamma = 1/\sqrt{1-\beta^2}$ and $E_M = 2m_e c^2 \beta^2 \gamma^2$ is the maximum energy transfer in a single collision[92]. From this equation it is very clear that for different charged particle species with the same momentum, the energy loss is different within the same medium.

The energy loss (dE/dX) as a function of particle momentum (p) is shown in the

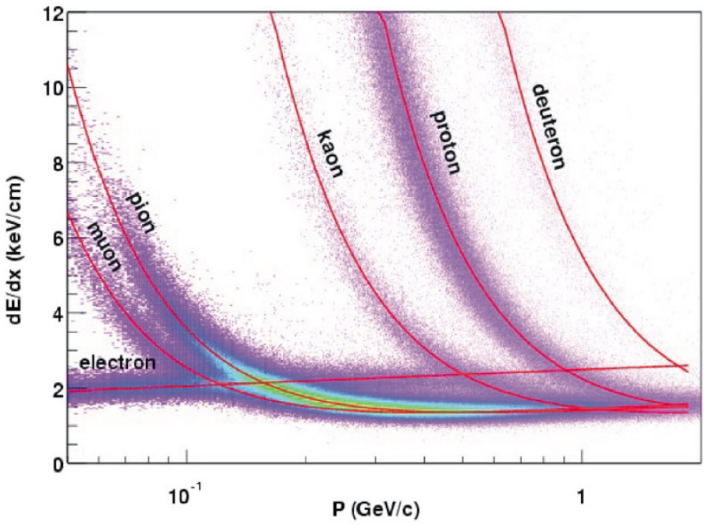

Figure 3.8: (Color online) The energy loss (dE/dX) distribution for different particles in the TPC as a function momentum of the particles in a magnetic field of 0.25 T.

Figure 3.8. From the figure one can see that particles with different charge have different ionization energy loss. The energy loss when plotted as a function of momentum clearly identifies the particles such as e, μ, π, k, p and deuteron [93].

3.5 The STAR's Time of Flight

Introduction

One of the major upgrade in STAR is the Time of Flight (ToF) detector which increase the discovery potential of STAR by increasing the capability of particle identification [94, 95]. This has enhanced the data quality being presented in this thesis. The increased particle identification helps to understand the large scale correlation and multi particle correlations produce in $Au + Au$ collisions. From the Figure 3.5 we can see along with the TPC the upgrade of TOF extend the momentum range of particle identification is STAR with a substantial amount.

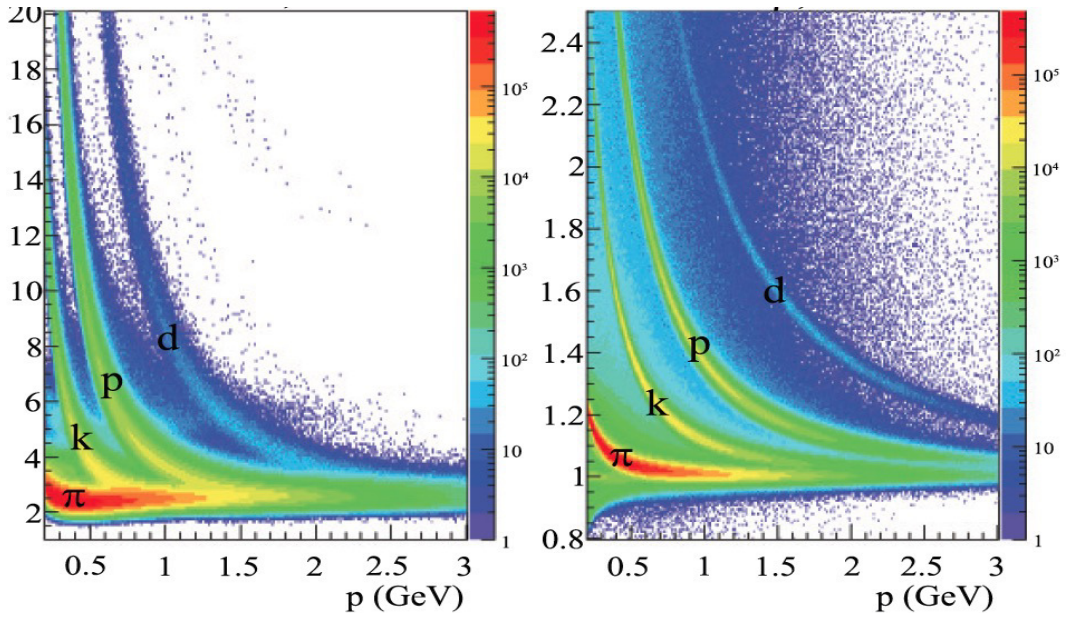

Figure 3.9: (Color online) The dE/dX energy loss and $1/\beta$ as a function of the momentum (p) of the primary particle in a magnetic field for TPC and TOF respectively.

TOF Upgrade and Physics Overview

The upgrade of the TOF detector has significantly extended STAR's physics reach capabilities. The extended range of particle identification in transverse momentum p_T, increases the measurement efficiency of particle correlations and fluctuations. As the heavy quarks are created at the beginning of the fireball formation, it is important to measure the yields and p_T spectra of D mesons and Ω baryons. The increased PID efficiency has helped to constrain the initial parton flux and the magnitude of the elliptic flow and transverse radial flow of heavy quarks. The extended PID capabilities of the full TOF would certainly help in the search for exotic di-Ω particles, one of the most stable di-baryon according to chiral SU(3) phenomenological calculations. The extended p_T of PID increase the accuracy in measurement of mass and width of the resonance particles. There are many other aspects of the TOF detector in the measurement of fluctuations and correlations, collective flow observable, D meson production, hadronic dynamics etc [95, 96].

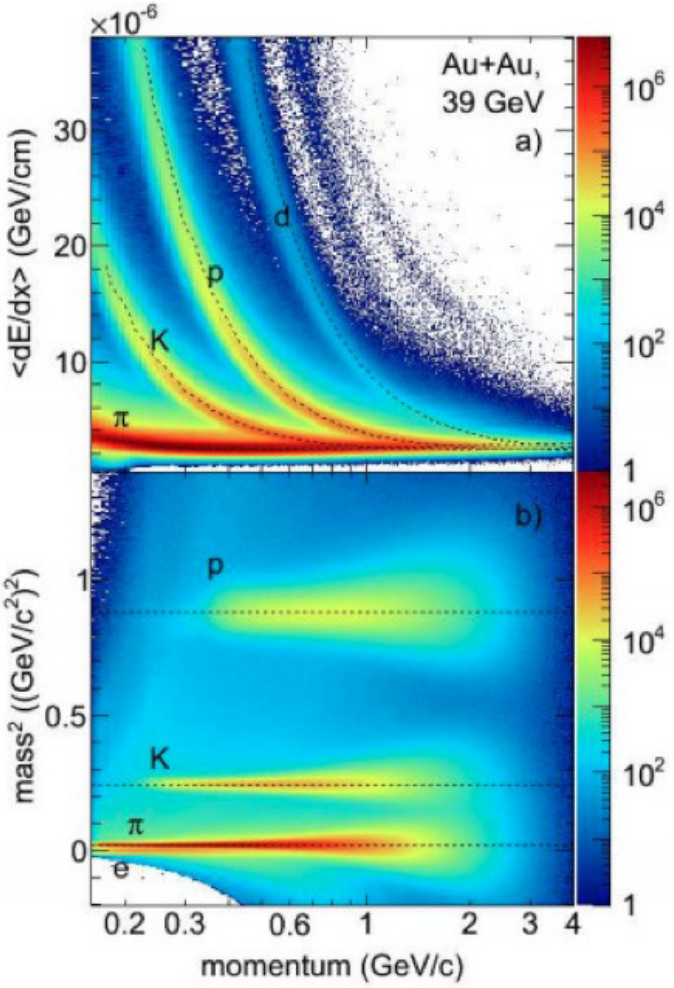

Figure 3.10: (Color online) The Particle identification using dE/dx of TPC (top panel) and using square of mass from TOF detector (bottom panel) vs momentum of the particles measured in STAR.

Technical Design

The basic principle of TOF is to measure the time intervals of particle traveling within the TPC volume by using TPC information. The integrated TOF system consists of MRPC detectors, the gas system, the mechanical components and the electronics.

Approach to Time Of Flight

TOF measures the time interval of TPC tracks with the help of an ”event start” and a charged particle ”stop detector”. For each TPC reconstructed track with

momentum, p, TOF measures the time interval Δt and inverse velocity $(1/\beta)$ by using,

$$\frac{1}{\beta} = \frac{c\Delta t}{s} \tag{3.4}$$

where, c is the speed of light and s total path length measure by TPC. The particle mass, M calculated by the associated momentum and inverse velocity via,

$$M = p\sqrt{(\frac{1}{\beta})^2 - 1} \tag{3.5}$$

TOF has 100 ps of time interval resolution. The combination of TPC and TOF made STAR a powerful particle identifier. The PID capability of STAR using TOF is shown in the Figure 3.11 [96]. The momentum and path length resolution along

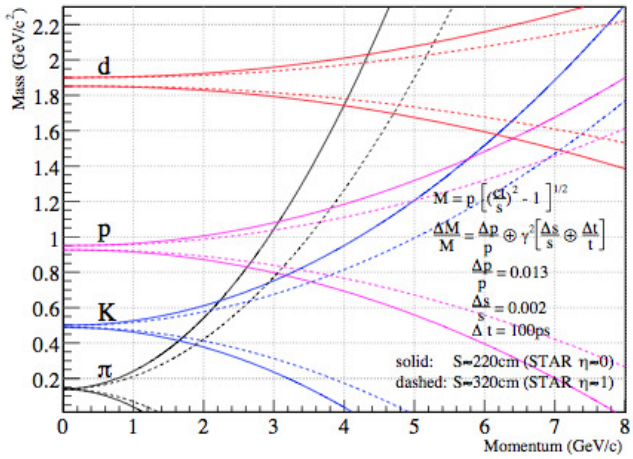

Figure 3.11: (Color online) The particle mass resolution for a 100 ps total resolution of TOF as a function of momentum. Particles can be identified up to the regions where the lines are overlapping. The figure is taken from Ref.[95].

with the measured hadron masses using TOF are also shown in the Figure 3.11. The upper (lower) pair shows the $M + \Delta M$ $(M - \Delta M)$ dependence with the momentum. The solid and dashed pair lines represent the tracks near the center $(\eta \sim 0)$ and near the end of TPC $(\eta \sim 1)$. Using TOF, "2σ" of PID is possible with a time interval resolution of 100 ps up to the interaction point of lower and upper lines of two particle species.

Design

The design of TOF used the multi-gap resistive plate chamber (MRPC) which developed by the CERN ALICE group. The design of MRPC provides the necessary time resolution. The MRPC module used in STAR is shown in the Figure 3.12 [96]. The upper view in this Figure 3.12 shows the long edge and the lower view in this

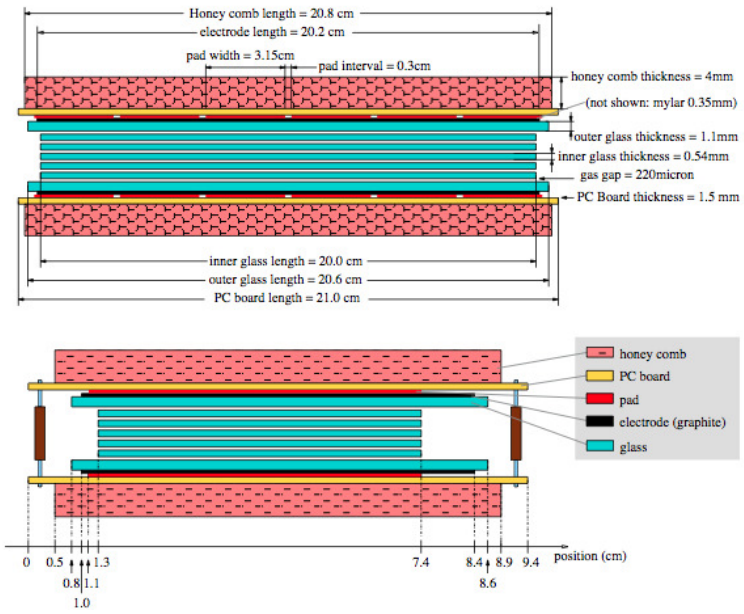

Figure 3.12: (Color online) A design of MRPC module with two side view. The upper and lower view shows the long and short edges respectively. The figure is taken from Ref.[96].

figure shows the short edge of a module. MRPCs are consist of parallel resistive plate chambers with uniform spacing of gas. By applying a high voltage in the external electrodes at the outer surface of the outer plates a strong electric field is generated in the gas spaces. A charge particle generates avalanches when it passes through the chamber. The resistive glass plates are electrically floating and transparent to charge induction from avalanches in the gaps. The sum of the avalanches from all gas gaps is the induced signal on the pads.

The electrodes are also transparent to charge, made of graphite strips. Finally, to read out the signals from the pads copper pickup pads are used. A schematic diagram of these pads for the MRPCs is shown in Figure 3.13. The electrodes

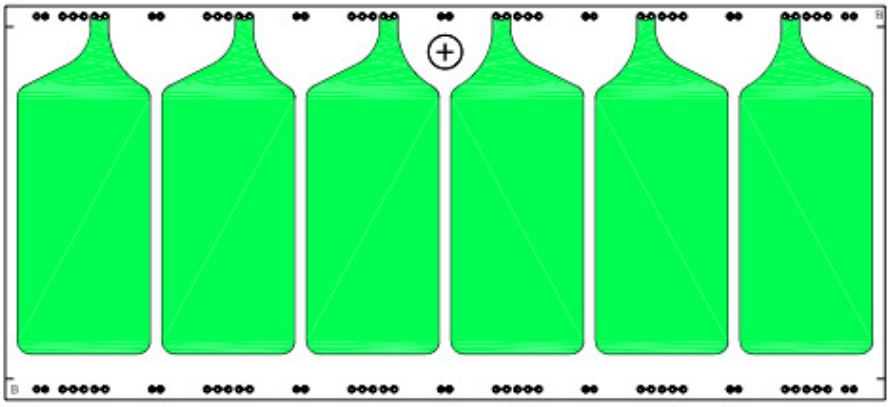

Figure 3.13: (Color online) A schematic diagram of the circuit with the copper pickup pads for the MRPC detectors.

cover the entire active area with a surface resistivity of 10^5 Ω. The glass plates has a thickness of 0.54 mm and are kept parallel with 0.22 mm spacing. The array of copper read-out pads are separated by 0.33 mm Mylar from the outer electrodes.

3.6 The STAR Silicon Vertex Tracker

The main objective of the Silicon Vertex Tracker (SVT) is to enhance the capability of the Time Projection Chamber (TPC). Along with improving the primary vertex position it helps to reconstruct very short lived particles like D-mesons, primary strange and multi-strange baryons. The kinematic acceptance of very low momentum particle is also enhanced by the SVT. This is especially true for the charged particle unable to reach the TPC active volume due to the magnetic field. The high resolution energy loss measurements from SVT add unique physics capabilities to STAR by improving its particle identification capabilities. By the charge particle energy loss in each layer of SVT, its provide an information of the charge particle energy[97].

The SVT placed around the interaction region is based on silicon drift detector (SDD) technology. The silicon drift technology was chosen due to high charged multiplicity per events and to minimize the readout channel numbers. The SDD

is capable to provide two dimensional hit position with a resolution of 20 μm for each coordinate. SDD is like a solid Time Projection Chamber with homogeneous Neutron Transmutation Doped (NTD). The STAR SDD is 63 $\times$ 63 mm^2 with a drift region and a focusing region. The detector consists of two halves and electrons drift from one to the other half[97].

3.7 Silicon Strip Detector

The STAR Silicon Strip Detector (SSD) located inside TPC completes the three layer tracking system by connecting Silicon Vertex Tracker to the TPC [97, 98]. This additional layer improves the measurement of TPC tracks through SVT by providing additional energy loss information in it and two dimensional hit position. SSD also improves detection efficiency for long-lived meta-stable particles[100]. SSD is a half million channel detector with $\sim 1\ m^2$ sensitive surface which make it the longest one-layer system. SSD is at 230 mm away from the beam axis which cover $|\eta|< 1.2$ of pseudo rapidity. SSD is double sided containing 10 carbon fiber ladder which support 16 wafer. There are 768 strips in each side of the SSD and they are connected to the front end electronics. The design of SSD was inspired by its use in ALICE experiment[100].

3.8 Photon Multiplicity Detector

The Photon Multiplicity Detector (PMD) is a pre shower gas ionization detector. PMD located at 550 cm from the centre of the STAR detector and its out side the magnet system. PMD cover the pseudo rapidity range 2.3 to 3.5 in full azimuth. The STAR PMD measures the photon multiplicity in the forward region [101]. A layout of STAR PMD is shown in the Figure 3.14. The honeycomb structure provides the spatial distribution of photons. By comparing the measured multiplicity with the produced charged particle multiplicity it also gives information about the photon enrichment in an event or set of events. This recent measure-

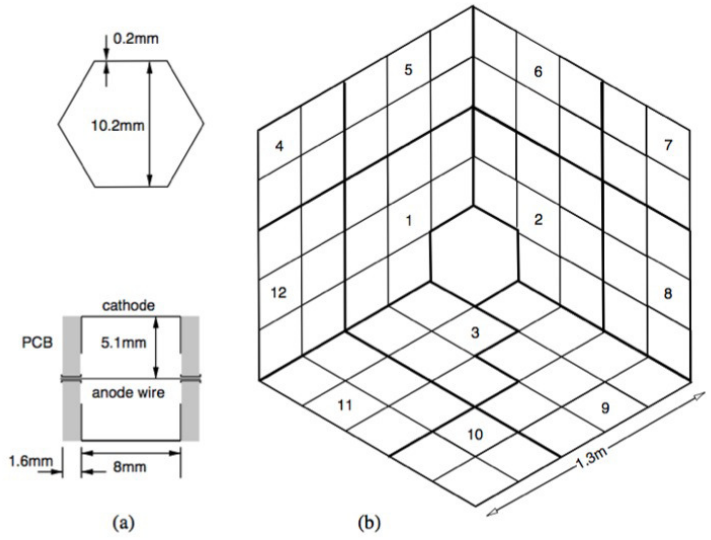

Figure 3.14: (a) Schematic diagram of Unit cell cross-section of STAR PMD and it's cathode extension, (b) STAR PMD layout. There are 12 super-modules (the thick lines are the boundaries) divided by several unit modules (thin lines are the boundaries).

ment has helped us to examine the restoration of chiral symmetry, although the efficiency and purity of the photon sample is not good enough to make conclusive statements [102]. A better efficiency and purity of the photon sample would have helped us to understand the vacuum structure of strong interaction and nature of chiral phase transition. The study of event-by-event photon multiplicity fluctuation as well as neutral to charge fluctuation was one of the main aims of PMD. The collective flow of photon multiplicity is possible to study using PMD.

The STAR PMD consists of 15 mm lead converter sandwiched between two planes of charged particle detector of high granularity. One front detector plane rejects the charged hadrons where the back detector plane behind the lead detects photons through the electromagnetic shower produced in the lead. Each cell detector are designed with the principle of proportional counter with a copper cathode and tungsten wire anode. They contain a mixture of Ar (70%) and CO_2 (30%) gas. The cell are honeycomb structure with 1 cm^2 facing read and 8 mm of depth. A unit module consists of 24 $\times$ 24 honeycomb cells and 4 to 9 unit modules make a super-module. 12 super modules make a plane. The detector has

a hexagonal shape and consists of vertically attached two planes which contains 83,000 total number of cells [101].

3.9 Barrel Electromagnetic Calorimeter

Events with highest density and temperature are most interesting and can lead us to the information of de-confinement. These events are expected to show high multiplicity at mid-rapidity and high transverse energy deposition (E_T). It is very hard to find E_T events for the dilution of E_T due to the experimental resolution. With the Barrel Electromagnetic Calorimeter (BEMC) the resolution of measuring E_T increases several folds. BEMC plays a significant role for high-p_T physics. For both $p + p$ and $Au + Au$ collision, BEMC provide large acceptance for electrons, photons, π^0 and η mesons. BEMC also helps for general event characterization for ultra peripheral collisions [103]. The BEMC is located inside the aluminum

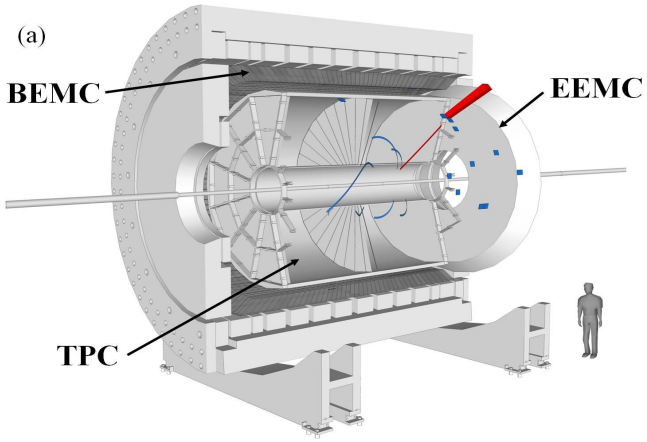

Figure 3.15: (Color online) BEMC and EEMC of STAR detector.

magnet coil of the STAR solenoid. Its covers $-1.0 < |\eta| < 1.0$ and full 2π in azimuth and thus covers full TPC tracking acceptance. The radius of the front face of the calorimeter is 220 cm. The BEMC contains total number of 120 calorimeter modules each of them is roughly 26 cm wide 293 cm long and with 23.5 cm depth.

3.10 Endcap Electromagnetic Calorimeter

To enhance the capabilities of STAR and to determine the preference of helicity for the gluons and its contribution to the spin, the forward Endcap Electromagnetic Calorimeter (EEMC) was proposed[107, 108]. EEMC provides crucial coverage to measure the photon and away side jets in the forward side of the collider. EEMC also plays an important role in the detection of the photon, electromagnetic decaying mesons like, π^0 and η in the lower RHIC energy range. The EEMC pro-

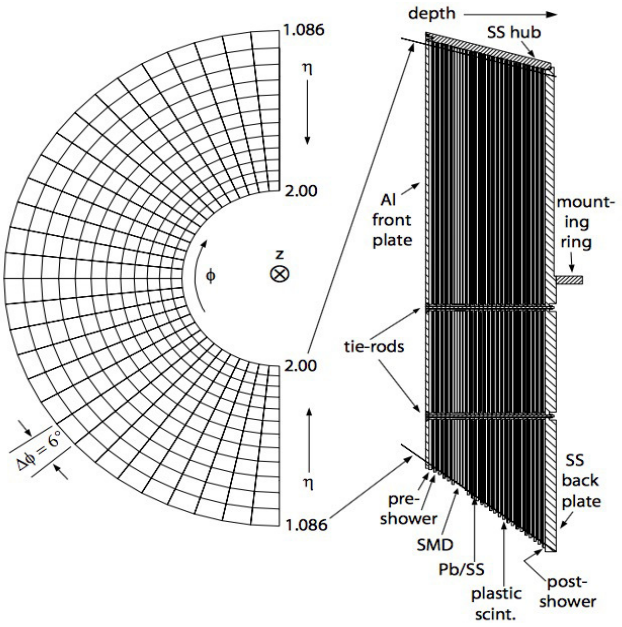

Figure 3.16: EEMC of STAR detector. The figure is taken from Ref.[107].

vides coverage of $1.086 \leq |\eta| \leq 2.0$ pseudo rapidity values, over the full azimuthal range. EEMC supplements the BEMC in the forward region. The EEMC is build with total 720 towers and each of them are 2.7 m long along the z-axis. The EEMC also helps the STAR triggering system for jets and in discriminating pre-shower and post-shower layers intended to discriminate charge hadrons from electrons.

3.11 The STAR Trigger

The STAR trigger system is a 10 MHz pipeline system which controls tracking detectors for the event selection and digitizes the signal. The slower detector can be

operated at the rate of 100 Hz. The only interaction sent to the storage which pass all selection criteria in the successive trigger level. Based on the tracking in slow detectors the final trigger is decided in the Level3 trigger [111]. A schematic diagram of the STAR DAQ interface is shown in the Figure 3.17. The Data Storage

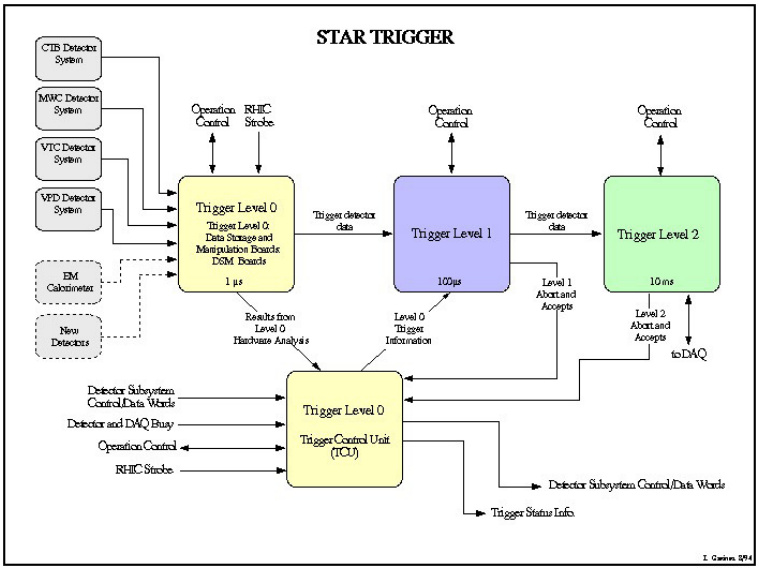

Figure 3.17: (Color online) Schematic diagram of the STAR Trigger.

and Manipulation (DSM) board analyzes and combines the digital signal from detector channel with the other signal in a multilayer pipeline which forms a fast decision tree. The output of DSM tree goes to the Trigger Control Unit (TCU) to be combined with detector status and acts as an 18 bit address in the lookup table (LUT). There is a trigger word assigned by LUT for each bit combination. The Action Word LUT decides the detector involvement and action from the trigger word information. The Level-0 trigger fed by DSM, takes decision within 1.5 μs about the STAR detectors contributing to the event. The information about the fast detectors is gathered and examined by VME processor at Level-1. If the Level-1 information has not aborted then its continues with the data acquisition while the raw trigger data set evaluates the Level-2 trigger. The central Data Acquisition System (DAQ) is notified by the Level-2 system if there is any interaction. This total process from an interaction take place with in 5 ms. All raw

detector data from Level-1 and Level-2 to DAQ, associate with a token. This token help STAR to organize the data collection [111, 112].

In the STAR experiment the primary trigger detectors are the Zero Degree Calorimeters (ZDCs), , the Electromagnetic Calorimeter (EMC), the Beam-Beam Counter (BBC), the Central Trigger Barrel (CTB) and a Multi Wire proportional Counter (MWPC). The BBC is used for normalizing the event rate in $p + p$ by covering the high η region.

3.12 The STAR DAQ

The DAQ of STAR is the main part of the computing facility where all raw data are stored from Level-1 and Level-2 with a token. DAQ combines custom parallel architecture interconnected VME-based receiver electronics. The maximum event size of 200 MB, when all detectors are readout and at input rates up to 100 Hz. By using customized ASICs the events can be reduced up to 10 MB and using Level-3 trigger which is physics based it can be reduced up to 30 MB. The main task of the DAQ system is to read 20,000 MB data from STAR detectors per second and store it to HPSS or in NFS in the RHIC RCF facility via Gigabit Ethernet [113]. A schematic diagram of the STAR DAQ interface is shown in the Figure 3.18. In addition, the Buffer Box in the DAQ system also writes the summary data for event, run and data file to the tag database containing information. The run control handles the distribution of run control commands for Run Control GUI. The DAQMAN and Solaris node, is used for running the Run Control and booting the VxWorks nodes. This node also contains monitor login for all other nods.

3.13 STAR Trigger-DAQ Interface

The interface between DAQ and Trigger is shown in Figure 3.19. The DAQ front-end boards receives all the raw data from the corresponding detectors. The DAQ

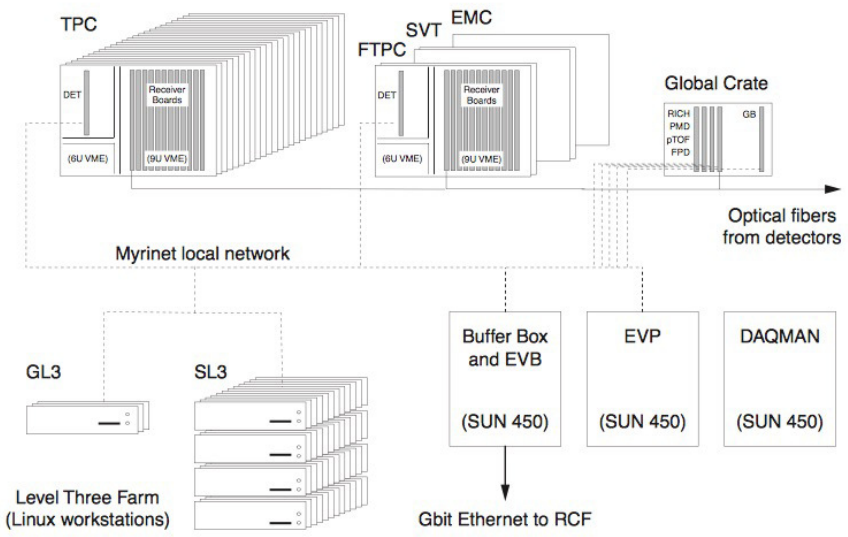

Figure 3.18: Schematic diagram of the STAR DAQ. The figure is taken from Ref.[113].

readouts are in the counting house and all raw data received through high speed unidirectional optical fiber links from the detector. The DAQ front-end gets electrical signals through these fiber links for the trigger actions [111, 113]. There are

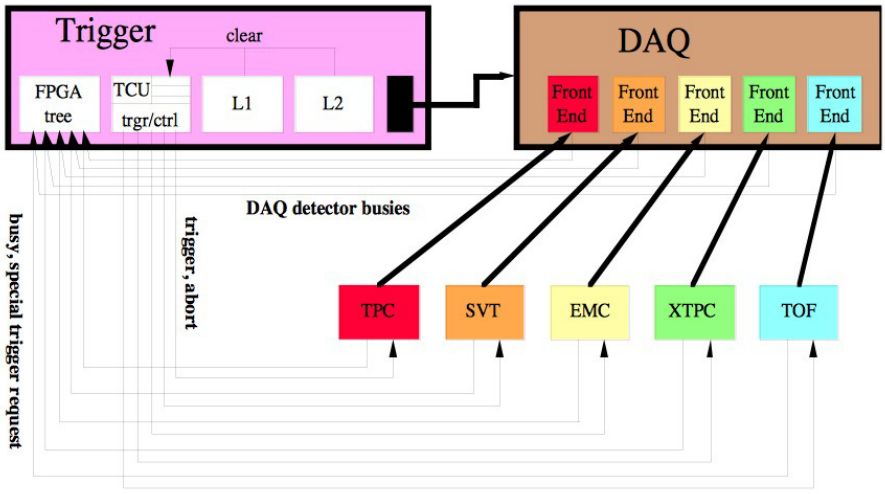

Figure 3.19: (Color online) An over all view of the STAR detector, Trigger and DAQ systems. The figure is taken from Ref.[111].

Slow Control and Experiment control along with the trigger and DAQ that inter-

face between them. They have been removed from this Figure 3.19 for simplicity. The Trigger and DAQ interface mainly consists of DAQ-detector signals and a shared memory.

3.14 STAR Computing Facilities

During an experimental run period data collected by different experiment at RHIC, directly stored the data to the RHIC computing facility (RCF). RCF is centralized facility for all users for all experiments at RHIC. The data stored at RCF is used for further process of reconstruction and to write the reconstructed output in an user friendly format for further analysis. Since the data size is huge (in TB range), RHIC needs enough computing facility to do the reconstruction and to write the reconstructed output. STAR has one more computing facility, the National Energy Research Scientific Computing Center (NERSC) for data reconstruction at Lawrence Berkeley National Laboratory (LBNL).

Chapter 4

Analysis Methods

The main aim of the Beam Energy Scan (BES) program is to map the QCD phase diagram [114, 115]. One normally plots the temperature as a function of Baryon Chemical potential. At their highest energies both RHIC and LHC populate the system (the fire ball) at low baryon chemical potential and high temperature. What makes RHIC unique is its ability to vary the energy of the colliding beams which in turn varies the baryon chemical potential as the number density of the baryons increases with the decrease in the centre of mass energy of the collisions. One of the most distinctive feature of this phase diagram is the critical point. RHIC has carried out the BES program in the year 2010, 2011 and 2014 to understand the hot and dense nuclear systems created in heavy-ion collisions [116] and to locate the critical point. At the critical point, if we assume infinite system with infinite life time the correlation length would diverge. For a finite system, populated for a finite time the correlation length would remain finite. The distribution of conserved quantities at the critical point would fluctuate. The higher moments of these distributions then become a sensitive probe in the search for the critical point as they vary as higher power of the correlation length. This higher moment analysis is based on the statistics of identified particles and depends crucially on purity of the identified particles. With this method it is possible to calculate the higher moments irrespective of signal to noise ratio.

As mentioned before we have constructed the net-kaon ($\Delta N_K = N_{K^+} - N_{K^-}$)

multiplicity distribution and from that we have derived the higher moments and volume independent products of the moment for the BES energies. In this chapter, we describe the selection criteria of the data, run number, event number and particle tracks. We discuss several factor which affect the determination of the higher moments like centrality bin width effect, auto-correlation and centrality resolution effect. We will also present methods to overcome these said effects so that the extracted moments deliver a non biasing physical conclusions.

4.1 Data Selection

4.1.1 Trigger for Data

For this analysis we have used STAR experiment's Run10 and Run11 data from the Beam Energy Scan program with center of mass energy ($\sqrt{s_{NN}}$ = 7.7, 11.5, 19.6, 27, 39, 62.4, 200 GeV) [114, 115]. In the STAR experiment, the number of useful events for our analysis has been more than 50% of the total data recorded. For this analysis we have used the Minimum Bias (MB) data. The only requirement from these events, therefore is that they occurred in the center of the STAR detector. In $Au + Au$ collisions, the minimum bias trigger was defined using Zero Degree Calorimeters (ZDC). The ZDC located in the beam direction at $\theta \leq 2$ $mrad$ and measured the spectator neutrons. For a MB trigger the two ZDCs need to coincide. Table 4.1 lists the trigger criteria for the useful data from Run10 and Run11.

4.1.2 Run Selection

There are several bad runs associated with the data, depending on several conditions during the recording. It happens many times that the detector is not fully functional and that introduces a numbers of bad runs. Sometimes there are electronic problem during the run that may introduce bad runs. In RHIC the filling of the beam last between 15 minutes and 8 hours. The background noise is different

Table 4.1: Basic information of the Trigger for the RHIC data set in $Au+Au$ system from BES phase - I.

Energy (GeV)	Minimum-bias Production	Trigger Name	Trigger Id
7.70	AuAu7_Production	P10ih	290001, 290004
11.5	AuAu11_Production	P10ih	310004, 310014
19.6	AuAu19_Production	P11ik	340001, 340011, 340021
27.0	AuAu27_Production_2011	P11id	36001
39.0	AuAu39_Production	P10ik	28001
62.4	AuAu62_Production	P10id	270001, 270011, 270021
200.	AuAu200_Production	P10ij, P10ik	26001, 260011, 260021, 260031

for each fill and also depends on the beam energy. As the beam energy increase the beam spreads less in its lateral side so the background is reduced which in turn increases the relative number of good events.

The run quality assurance has been done depending on some event and track variables. The event variables used are average number of global tracks per event, average number of primary tracks per event, average value of reference multiplicity (Refmult2), $\langle V_z \rangle$, $\langle V_r \rangle$, average number of TOF matching and average number of TOF multiplicity per events. For this run number selection we have used the track variables also and they are $\langle DCA \rangle$, $\langle p_T \rangle$, $\langle \eta \rangle$, $\langle \phi \rangle$ per run number. For all beam energies we have studied these variable for all the recorded data and rejected bad runs by 3σ cut for a given observable. In the Figure 4.1 we show the average V_r over the run period as a function of run number at $\sqrt{s_{NN}} = 7.7\ GeV$.

4.1.3 Event Selection

In this analysis, we select only minimum bias trigger events for all Beam Energy Scan data. Along with the sensitivity in the critical fluctuations, higher moments are also very sensitive to the experimental effects. These experimental effects includes background noise, drift in the TPC volume, noise due to the electrical signals etc.. Sizable number of events that did not satisfy these criterion have

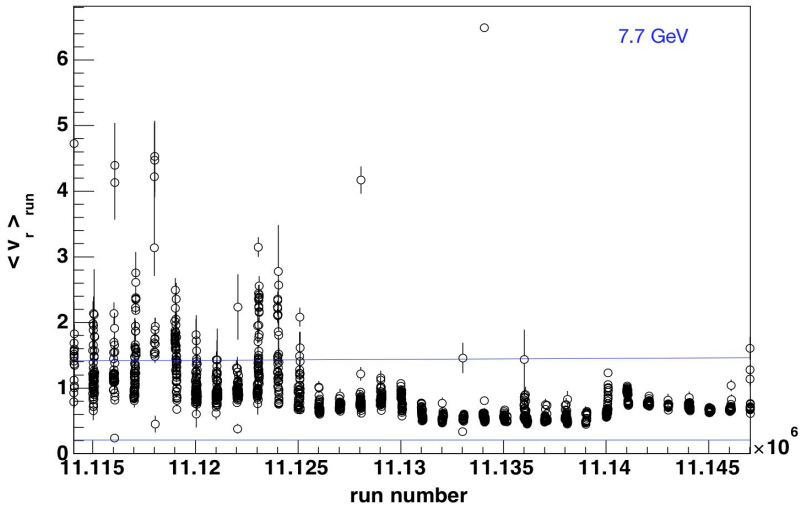

Figure 4.1: (Color online) Average V_r over the run period plotted as a function of run number at $\sqrt{s_{NN}} = 7.7\ GeV$ in $Au + Au$ collision. 3σ cut has been used to reject the bad runs.

been discarded to remove trigger biases. To remove these experimental effects from the data a good Quality Assurance (QA) is very important.

Z_{vertex} (V_Z) and r_{vertex} (V_r) Selection

Events for which no primary vertex were found have been rejected as bad events. Events with z-vertex less than $\pm 30\ cm$ from the TPC center have been selected for analysis. The criterion to select the range of vertex was to achieve uniform acceptance in the pseudo-rapidity range in which the distributions have been calculated. In addition, $V_r \leq 2.0\ cm$ have been used in the transverse plane of the beam where,

$$V_r = \sqrt{V_x + V_y} \tag{4.1}$$

For centre of mass energy $\sqrt{s_{NN}} = 7.7$ and $11.5\ GeV$ the statistics is very low. Hence for these energies the selection criterion on the z-vertex was relaxed to ± 50 cm from the TPC center. In additional a $|VpdV_z$ - $V_z| \leq 4\ cm$ is used for 200, 62.4,

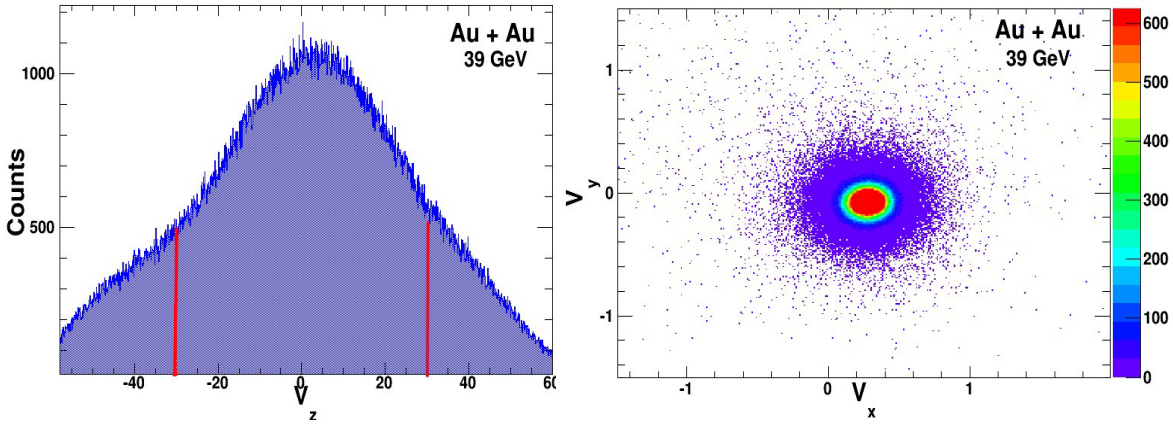

Figure 4.2: (Color online) (Left Panel) V_Z distribution and (Right panel) V_x Vs. V_y distribution for $Au + Au$ collision at 39 GeV.

and 39 GeV $Au + Au$ collisions. The left panel of Figure 4.2 shows Vz distribution

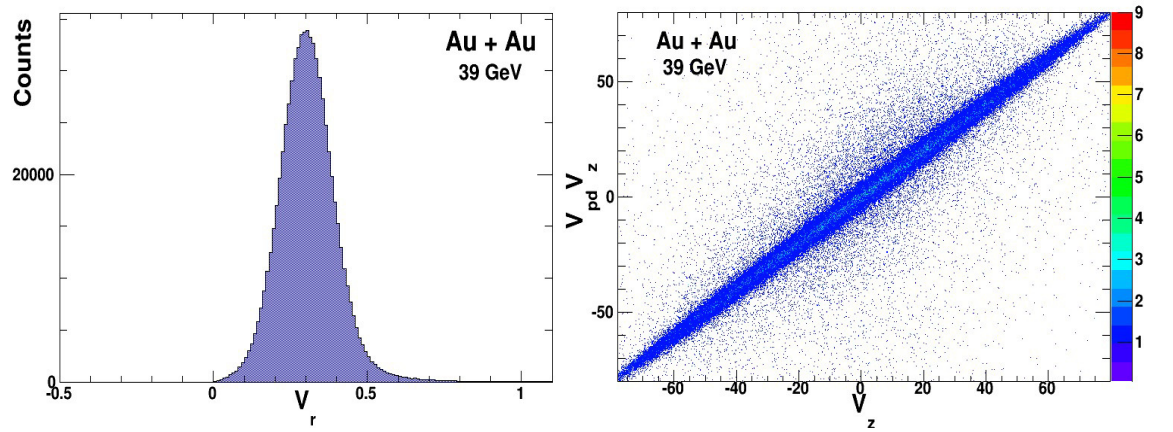

Figure 4.3: (Color online) (Left Panel) V_r distribution and (Right panel) $V_{pd}V_Z$ Vs. V_Z distribution for $Au + Au$ collision at 39 GeV.

for $Au + Au$ 39 GeV and the cuts (red lines) applied on the distribution. The right panel of Figure 4.2 shows V_y as a function of V_x for $Au + Au$ 39 GeV. The V_r distribution for $Au + Au$ 39 GeV is shown in the left panel of Figure 4.3 and the right panel shows the $V_{pd}V_Z$ as a function of V_Z. By applying this tight z-vertex cut on the level zero trigger, one can see that its biases the sample. To remove the biasing these events need more careful QA analysis. The events outside this

applied cuts are not included in this analysis.

Tof Match Correction

To remove the pile-up events we study the TOF matching tracks and TOF multiplicity. In the Figure 4.4 the number to TOF matching tracks plotted as a function of reference multiplicity (Refmult2). From this Figure 4.4 pile-up can be seen. To remove this pile-up one dimensional histograms were plotted for each Refmult2 and 3.5σ cut on both the sides of the distribution was applied. After the 3.5σ

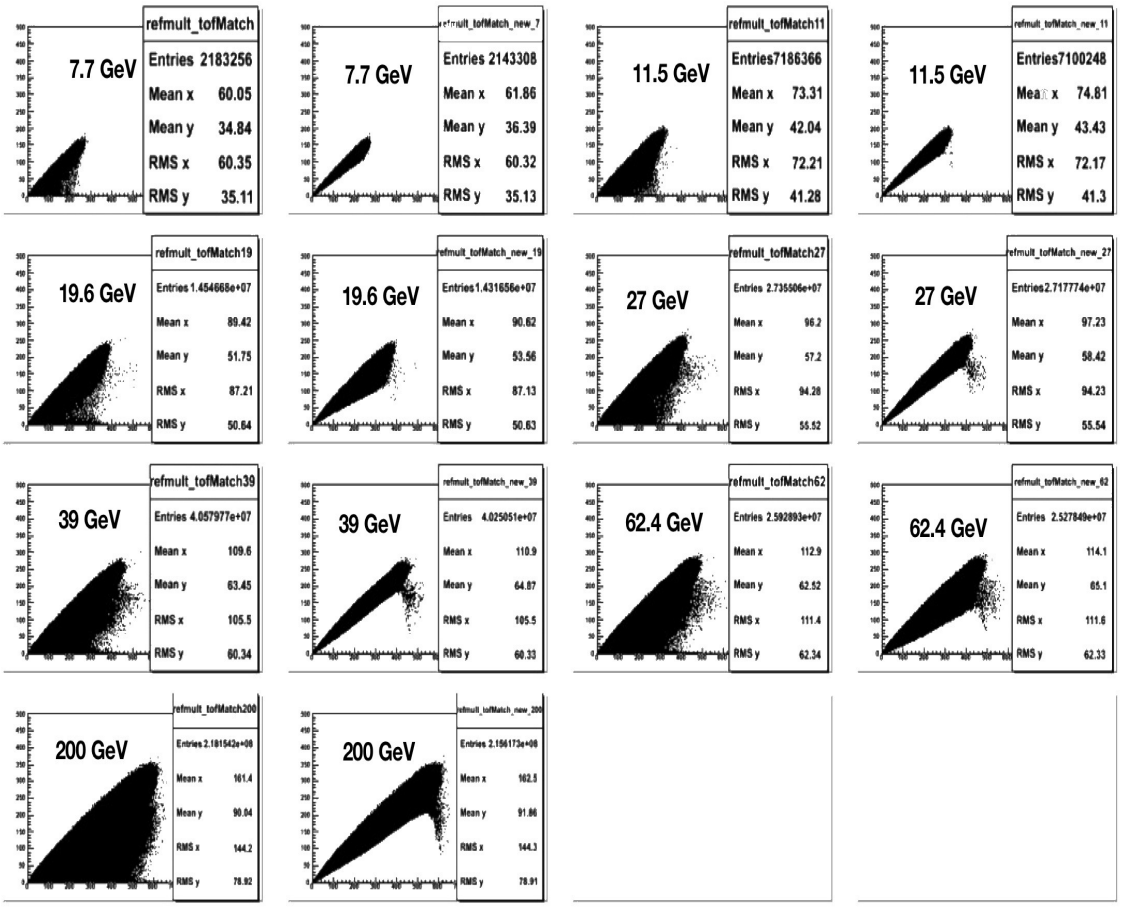

Figure 4.4: TOF match as a function of Refmult2 before and after 3.5σ selection on TOF match for $\sqrt{s_{NN}}$ = 7.7 - 200 GeV.

cut on Tofmatch, we apply a linear cut to remove further contamination of bad events towards the central collision shown in Figure 4.5. To remove the pile-up events in TOF multiplicity we followed the same procedure for all RHIC energies.

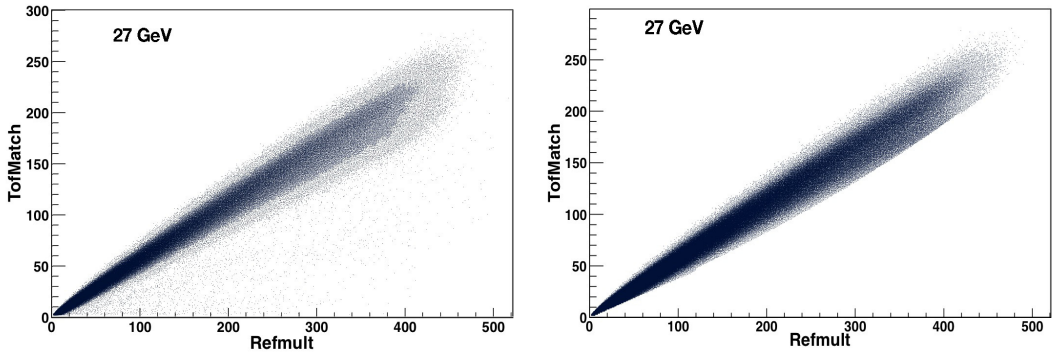

Figure 4.5: (Color online) TofMatch Selection for the removal of bad events.

The number of $Au + Au$ events used in this analysis listed for different colliding beam energies are shown in the Table 4.2. The first column represent the year of data production the second column represent the centre of mass energy the third, fourth and fifth column show the event cuts, Vertex-z, Vertex-r and $V_{pd}V_z$ used for different data sets respectively, the sixth and seventh column shows the recorded and used statistics for this analysis.

Table 4.2: The number of $Au + Au$ events used in our analysis listed for different colliding beam energies. The event cuts, Vertex-z, Vertex-r and $V_{pd}V_z$ used for different data sets also shown.

Production year	$\sqrt{s_{NN}}$ (GeV)	$\|V_z\|$ (cm)	$\|V_z\|$ (cm)	$\|V_{pd}V_z$ - $V_z\|$ (cm)	Minimum-bias Recorded	Data Used
2010	7.70	50	2	Nan	7 M	3.2 M
2010	11.5	50	2	Nan	16.6 M	9.2 M
2011	19.6	30	2	Nan	27.5 M	16.2 M
2011	27.0	30	2	Nan	48.8 M	33.0 M
2010	39.0	30	2	4	240 M	108 M
2010	62.4	30	2	4	160 M	47.0 M
2010	200.	30	2	4	360 M	220 M

4.1.4 Track Quality Assurance (QA)

One of the most important part of this analysis is the track quality. In heavy ion collision like RHIC, there are thousand of tracks coming from the collision center. All tracks that we detect in the detectors are not coming from the fireball and hence they are not 100% pure event tracks. The main impurity comes from the secondary particles, not produced in the collision and comes from the secondary reactions. These secondary particle or tracks comes from the reaction with the detector material and scattering effects etc. this making it imperative to check the track quality. The particle distance of closest approach (DCA) and the momentum

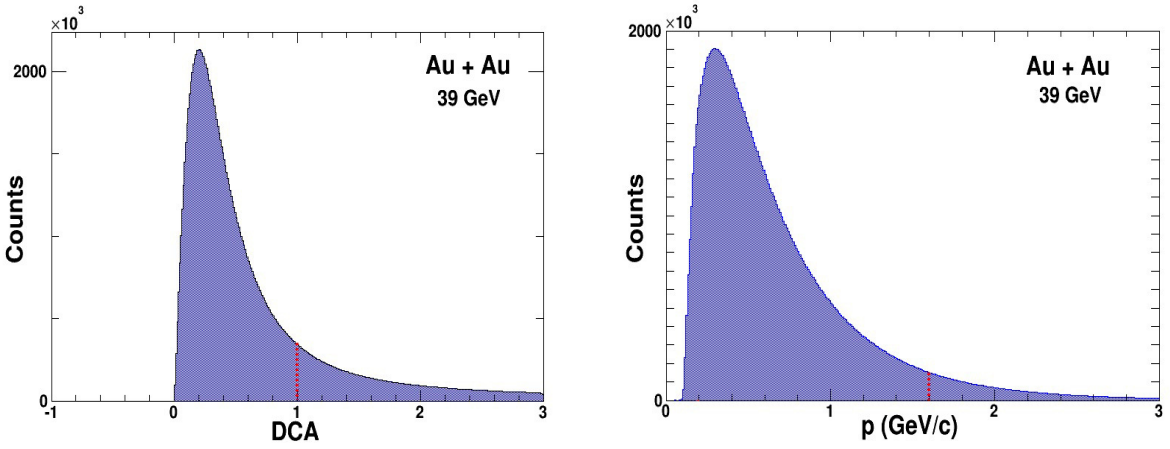

Figure 4.6: (Color online) (Right panel) Particle DCA and (Left panel) momentum distribution at $\sqrt{s_{NN}} = 39\ GeV$.

distribution at $\sqrt{s_{NN}} = 39\ GeV$ are shown in the Figure 4.6. For good quality of the tracks we use DCA to the primary vertex less than 1 cm. To suppress the contamination from secondary protons, we required each $K^{\pm}$ track to have a minimum p_T of 0.2 GeV/c. To separate $K^{\pm}$ tracks from $\pi^{0,\pm}$ and $p^{\pm}$ we use maximum momentum range up to 1.6 GeV/c. The pseudo rapidity and number of TPC hit fitted points are shown in the Figure 4.7. Tracks in the TPC with 15 or more fit points, more than 10 dE/dx hits were included. For this analysis tracks within pseudo rapidity range $|\eta| \leq 0.5$ were included. Therefore for the centrality selection we use the pseudo rapidity range within $[-1.0, -0.5]$ and $[0.5, 1.0]$ to

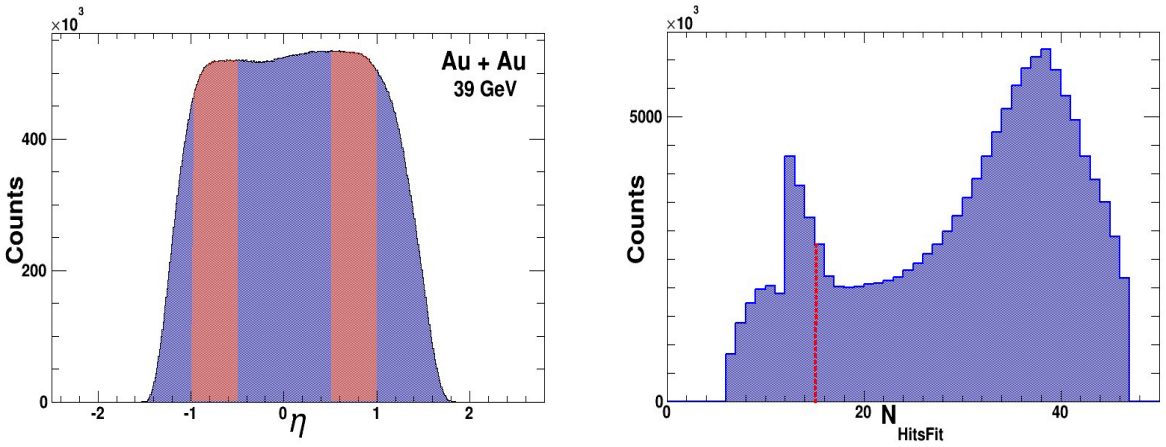

Figure 4.7: (Color online) Pseudo rapidity (η) and number of fitted hit points distribution at $\sqrt{s_{NN}} = 39\ GeV$.

remove the auto-correlation effects. Table 4.3 list the selection criteria for primary tracks used in this analysis for all Bean Energy Scan data.

Table 4.3: Selection criteria for good quality tracks used in this analysis.

Track set	Global	Primary	Used
DCA to primary vertex (cm)	na	≤ 3	≤ 1
Number of hits	≥ 15	≥ 15	≥ 20
Number of Fit	≥ 15	≥ 15	≥ 15
Number of hits/possible hits	na	≥ 0.52	≥ 0.52
$\|\eta\|$ for analysis	na	≤ 1.5	$\|\eta\| \leq 0.5$
$\|\eta\|$ for centrality	na	≤ 1.5	$1.0 \leq \|\eta\| \leq 0.5$
Momentum (GeV/c)	$p \geq 0.01$	$0.1 \leq p \leq 24$	$0.2 \leq p \leq 1.6$

4.2 Particle Identification

The large size, uniform acceptance and the capability of identifying particles over a wide momentum range produced in the heavy Ion collision along with the capability of RHIC to collide ions at wide energy range makes STAR, a unique experiment for the study outlined in this thesis. STAR is capable of measuring and

identifying a large fraction of produced particles. The techniques to identify π^+, π^-, K^+, K^-, P^+, P^-, e^+, e^- etc. candidates with the STAR detector are well established [93]. Along with particle identification, STAR is also capable of measuring the transverse momentum (p_T) and rapidity (y) of the identified particles. The ionization energy loss (dE/dx) in the TPC gas system provides information for the particle identification[93]. From the Figure 4.8 we can see that, the ionization

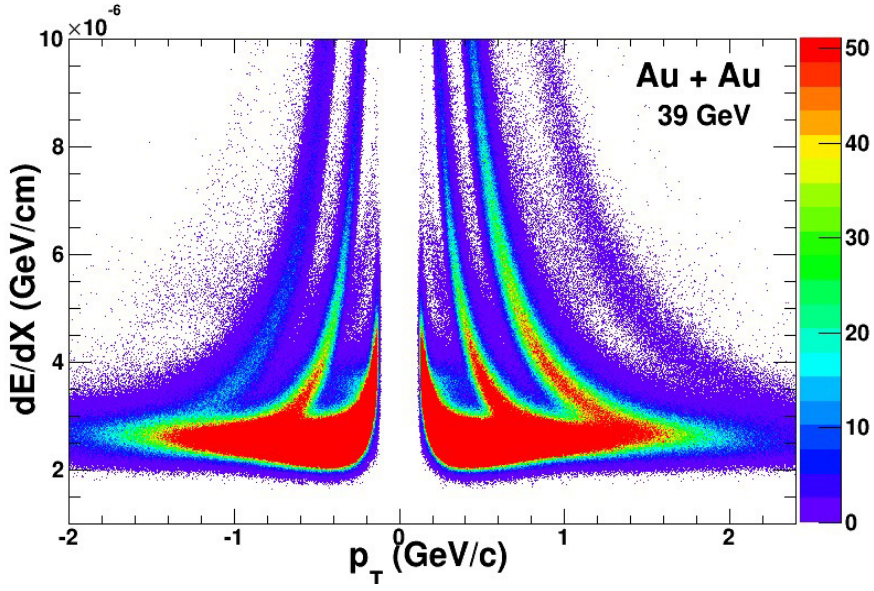

Figure 4.8: (Color online) The particle ionization energy loss (dE/dx) as a function of particle transverse momentum (p_T).

energy loss (dE/dx) provides the particle identification up to $p_T \leq 0.6\ GeV/c$ for kaon ($K^{\pm}$) and pion ($\pi^{\pm}$) and $p_T \leq 0.8\ GeV/c$ for proton ($P^{\pm}$) respectively. The Bethe-Bloch function provides the normalized dE/dx ($n\sigma_{particle}$) used for the associated Bichsel function for PID . From the $n\sigma_{\pi^+,\pi^-,K^+,K^-,P^+,P^-,e^+,e^-}$ distribution we select the particle to identify, where $n\sigma$ is the normalized dE/dx of the particle. The normalized dE/dx is defined by,

$$n\sigma_{\frac{Y}{X}} = \frac{log\left[\left(\frac{dE}{dx}\right)_Y / B_X\right]}{\sigma_X} \tag{4.2}$$

where X,Y can be $\pi^+, \pi^-, K^+, K^-, P^+, P^-, e^+, e^-$ any of these particle species. B_X is the average dE/dx of a particle X and σ_X represents the dE/dx resolution of

TPC. In general with an ideal calibration the $n\sigma$ distribution is a normal or Gaussian distribution. In our analysis we are looking for higher moments of net-kaon multiplicity distribution. The selection criteria of $n\sigma$ is $|n\sigma_k| \leq 2.0$ has been used for the identification of charged kaons. However, the indispensable condition to study the strong early-stage interaction in the hot and dense medium created in relativistic heavy ion collisions is to identify the particle in the intermediate and high p_T and this was done with the help of TOF. The STAR particle identification

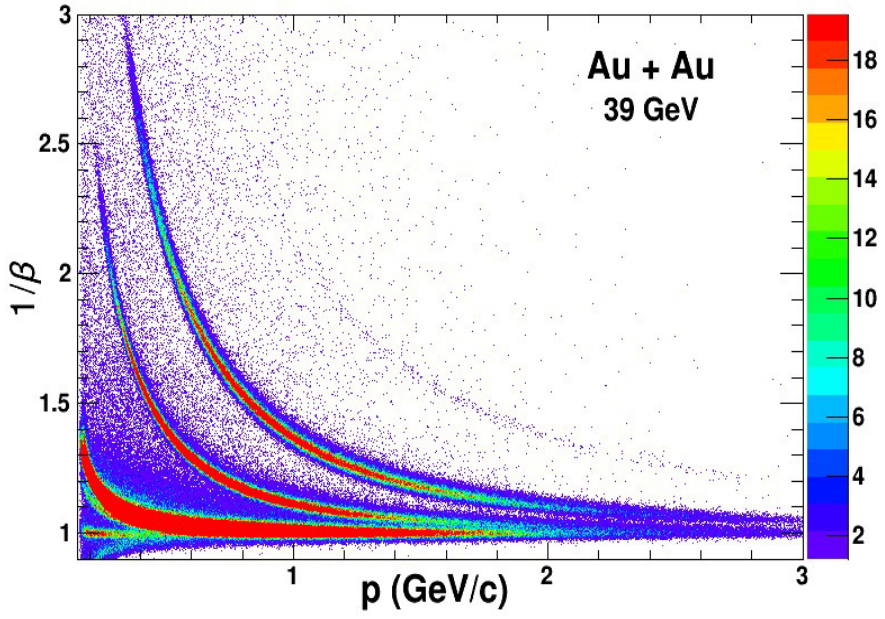

Figure 4.9: (Color online) The $1/\beta$ as a function of particle momentum (p) at $\sqrt{s_{NN}} = 39\ GeV$.

capability is further enhanced by the Time of Flight (TOF) detector with its time resolution up to $\leq 100\ ps$. With the help of TOF, STAR is capable to identify $K^{\pm}$, $\pi^{\pm}$ up to $p \leq 1.6\ GeV/c$, and $P^{\pm}$ up to $p \leq 2.0\ GeV/c$ respectively. In the Figure 4.9 we show the $1/\beta$ as a function of the particle momentum where we can see the particle bands are separated up to a larger momentum value than that given by the TPC dE/dx information. Also in the Figure 4.10, the m^2 as a function of particle momentum are shown. From this Figure 4.10 we observed that the particle species like $K^{\pm}$, $\pi^{\pm}$ and $P^{\pm}$ can be identified up to a momentum which is much

higher than what is possible by using the signal from TPC alone. To identify the

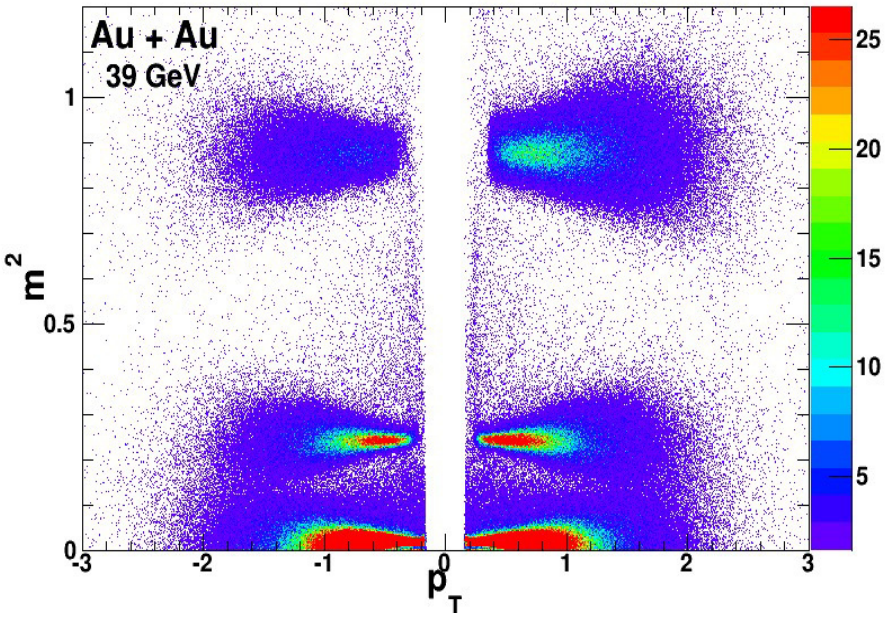

Figure 4.10: (Color online) Identified particle m^2 as a function of p_T and m^2 distribution of identified particles at $\sqrt{s_{NN}} = 39\ GeV$.

particles, the mass square (m^2) information has been used, calculated form the $1/\beta$ information of the particle species.

$$m^2 = p^2 \left(\frac{1}{\beta^2} - 1 \right) \tag{4.3}$$

The mass square (m^2) distribution for $\sqrt{s_{NN}} = 39\ GeV$ are shown in the Figure 4.11. In this Figure 4.11 we see clear m^2 peak for different particle species. To remove the contamination with other particles and to use higher momentum value we use TOF, where we can distinguish the kaons from other particle up to p = 1.6 GeV/C. To suppress the contamination from secondary protons, we required each $K^+(K^-)$ track to have a minimum p_T of 0.2 GeV/c.

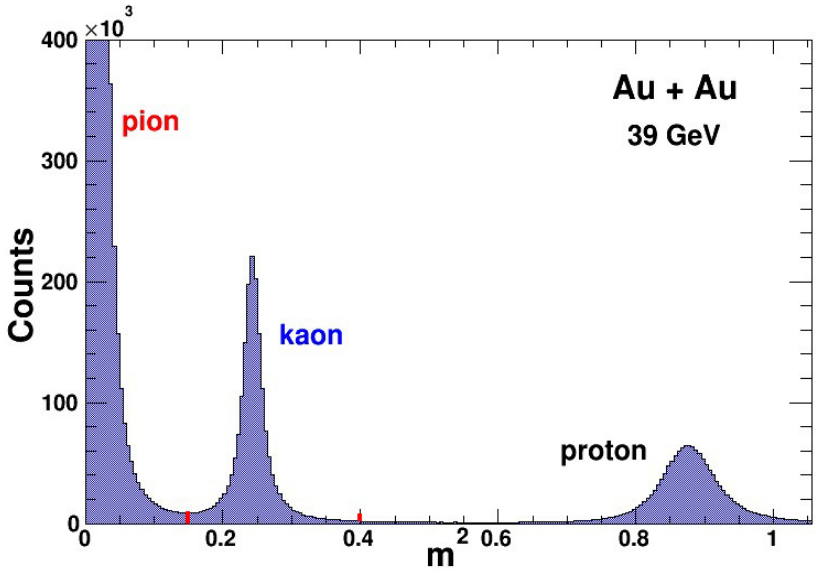

Figure 4.11: (Color online) Identified particle m^2 at $\sqrt{s_{NN}} = 39\ GeV$.

Different PID Selection Using TPC and TOF

Using dE/dx information from TPC and m^2 information from TOF, it is possible to select high purity of identified tracks up to a certain momentum range [93]. In our analysis kaon and anti-kaon tracks have been identified using $n\sigma_K \leq 2.0$ from TPC and $0.15 \leq m^2 \leq 0.4$ from TOF with in $|\eta| \leq 0.5$, $p_T \geq 0.2$ and $p \leq 1.6$. Since in the lower momentum region the dE/dx is more useful and in the higher momentum range the m^2, we have chosen the lower and upper momentum cut from p_T and p respectively. For this analysis we select the kaon PID using TPC and TOF cut simultaneously. An example of selected kaon tracks shown in Figure 4.12. Comparing Figure 4.9 and Figure 4.12 we can say that the selection of the kaon particle band is well done with this PID selection. However, since the total detector efficiency is the multiplication of individual efficiencies, the efficiency value gets reduced if one uses both the detectors. We observe that, in the lower momentum range the TOF is not very effective due to the reason that, many tracked particles because of their low momentum do not reach the TOF detector. As a result, many tracks do not have TOF information in the lower momentum range. For this reason another PID have been defined by not using TOF in the

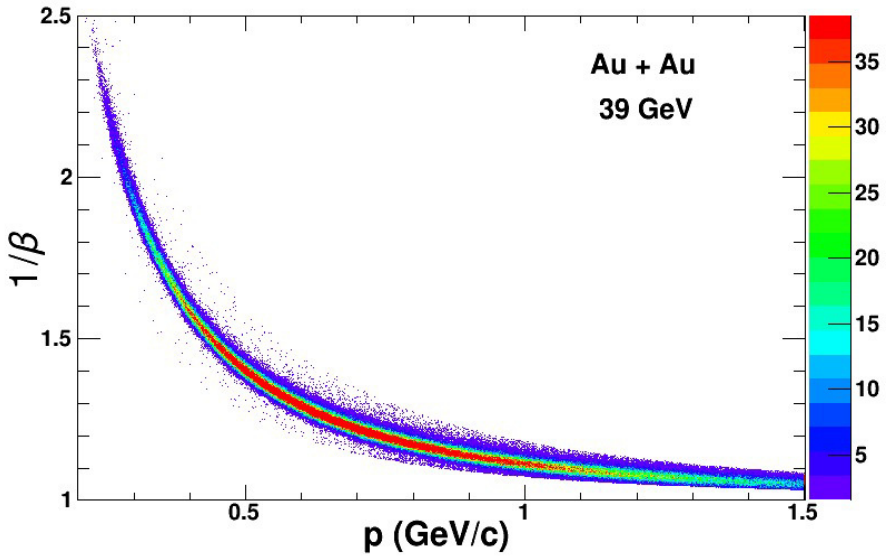

Figure 4.12: (Color online) $1/\beta$ as a function of particle momentum at at $\sqrt{s_{NN}} = 39\ GeV$. Identified kaon particles band.

lower momentum range. For this new PID, we have included those tracks that

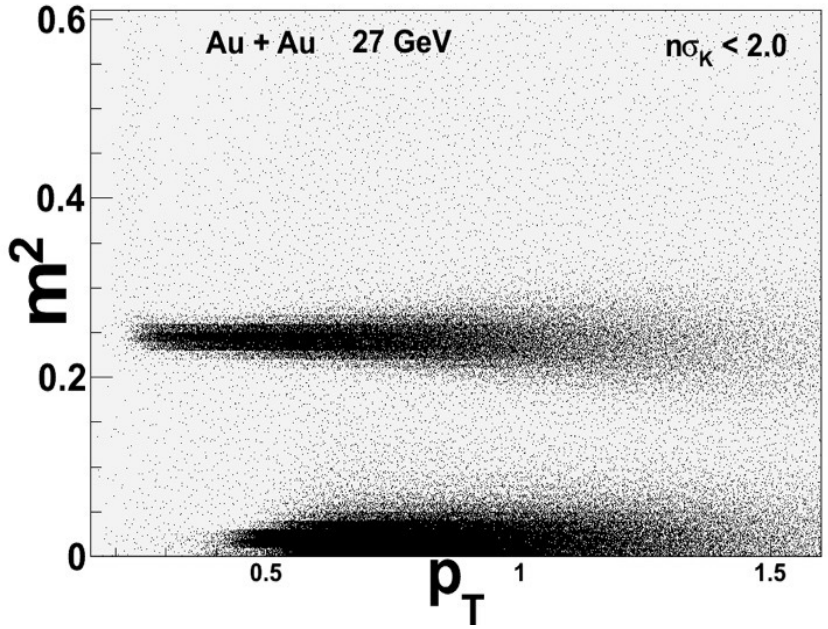

Figure 4.13: TPC Identified kaon's m^2 as a function of transverse momentum at $\sqrt{s_{NN}} = 27\ GeV$.

do not have the TOF information but $n\sigma_K \leq 2.0$ and with in $0.2 \leq p_T \leq 0.4$. The

upper limit of the momentum have been applied to avoid contamination from other particles. From the Figure 4.13 it is very clear that, after $p_T \geq 0.4$ there are other particles contaminating when we use only $n\sigma_K < 2.0$. A illustration of these two PID selection criteria has been demonstrated in the Figure 4.14.

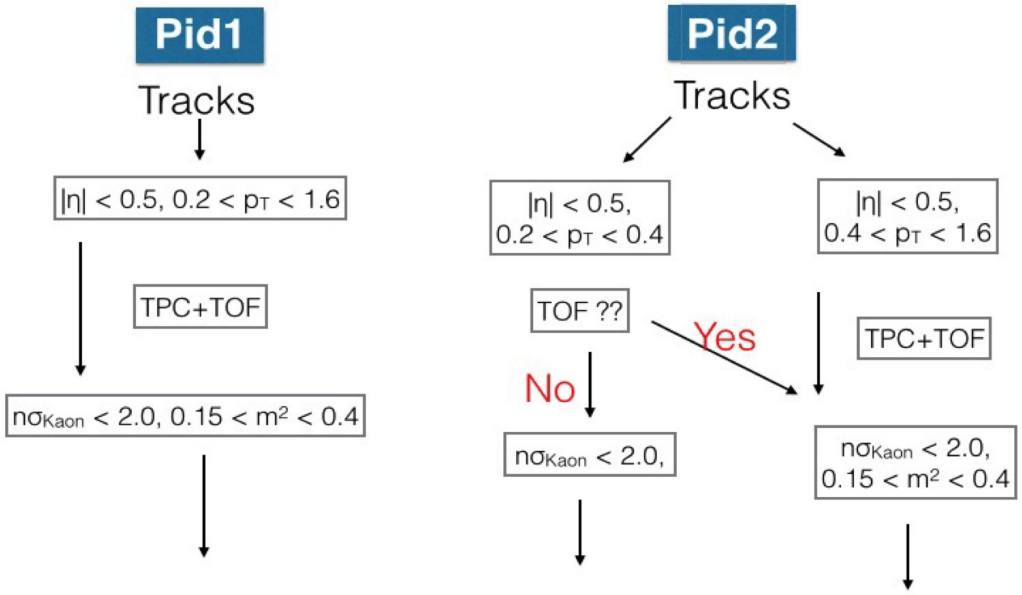

Figure 4.14: (Color online) Different PID selection using TPC and TOF.

4.3 Centrality Selection

In heavy ion collisions, the medium formed is dependent on whether the collision is head-on or peripheral. The characteristics of these collisions depend on the percentage of nuclei overlapping or on the impact factor of the colliding nuclei and we define it as the centrality. Also, centrality is used as a basic characteristic of the events with different multiplicities. This has implications in the analysis mentioned in the thesis because for lower centrality values or for more central collisions the size of the system would be larger and hence it will take longer time to reach the freeze-out (what our detectors measure) than a smaller system resulting from higher values of centrality. Figure 4.15 shows a heavy ion collision

geometry which defines the impact parameter. To define centrality in heavy ion

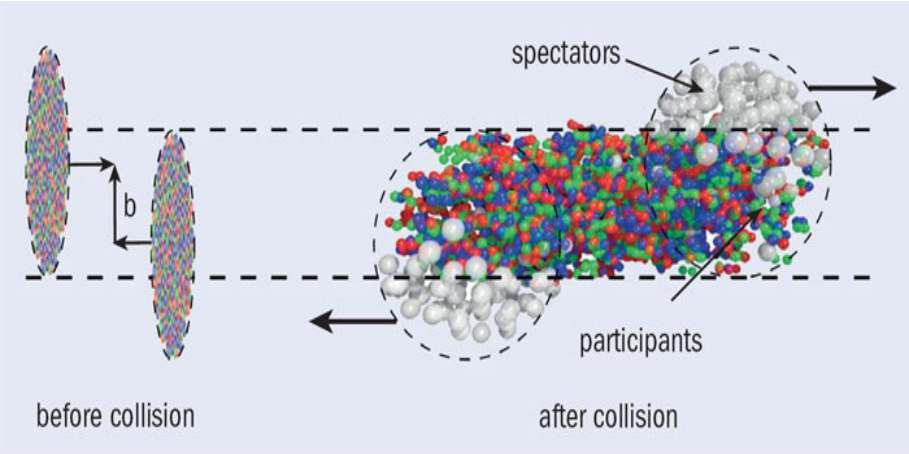

Figure 4.15: (Color online) A schematic diagram of the nucleus-nucleus collision. Here impact parameter (b) and number of participants are shown.

collision we use the number of participating nuclei N_{part} or the number of binary collisions N_{coll}. Where N_{coll} is the total number of inelastic nucleon-nucleon collision and N_{part} is the nucleon which participates at least one inelastic collision. The particle production scale with these two parameters, soft particle production with N_{part} and hard process with N_{coll}. The particle production can be calculated using formulation put forward by Glauber [26]. The average values of N_{coll} and N_{part} are also related to the collisions geometry of the colliding system [117] and from there we derive the impact parameter. Figure 4.16 shows number of participating nucleons and binary collisions as a function of impact parameter calculated from Glauber model. It is very difficult to measure N_{part}, b or N_{coll} in heavy ion collision experiment. However, it is possible to map the said variables by charged particles multiplicity N_{ch}, since its describe the collision system geometry for a given acceptance. Figure 4.17 show how we can map the number of participant (N_{part}) and impact parameter (b) of the $Au + Au$ collisions from the Glauber calculation. Figure 4.17 also illustrates the extraction of the centrality from the collision geometry.

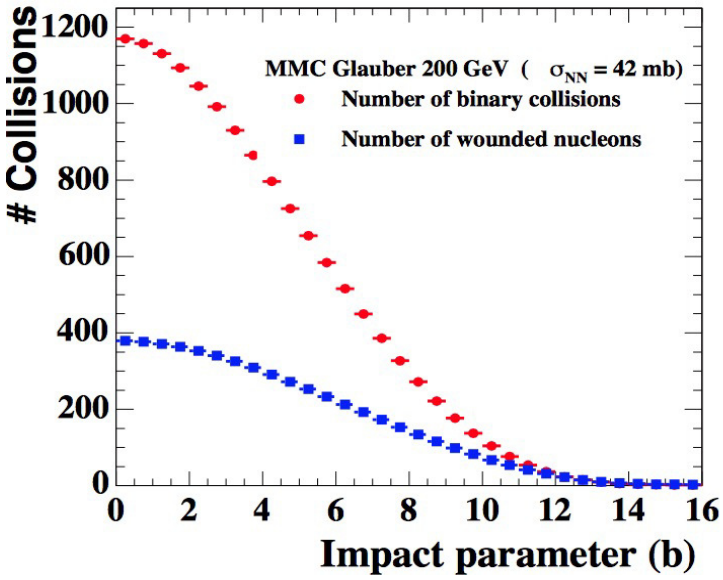

Figure 4.16: (Color online) Number of participating nucleons and binary collisions versus impact parameter. The figure is taken from Ref.[117].

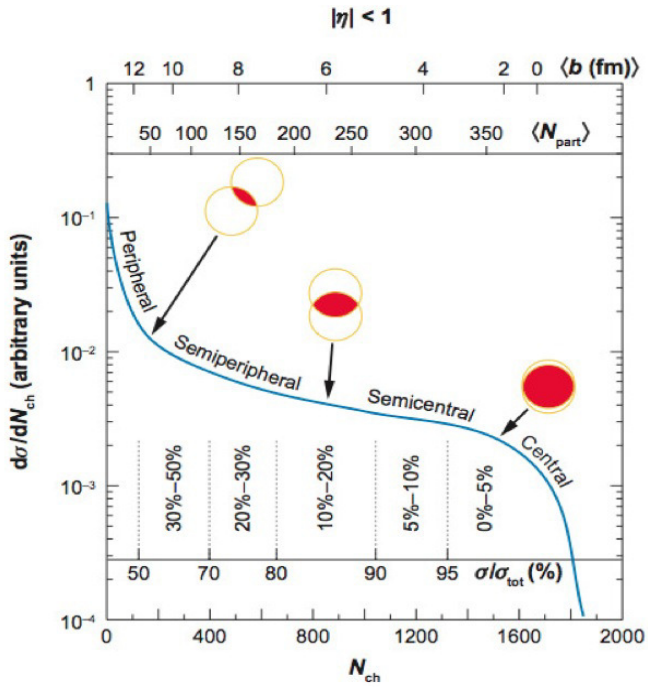

Figure 4.17: (Color online) An Example of mapping the average number of participant ($\langle N_{part} \rangle$) and impact parameter (b) using the charge particle multiplicity for the $Au + Au$ collisions from the Glauber calculation [26].

4.3.1 Autocorrelation Effects and Refmult2

We have used the charged particle multiplicity within the $0.5 \leq |\eta| \leq 1.0$ to define the centrality which is different from traditional centrality selection in the STAR

experiment using $|\eta| < 0.5$. The reason is to avoid the self-correlation or auto-correlation effect which comes into play when the same particles are used for analysis as well as to define the centrality. In this analysis positively charged kaons and negatively charged kaons were identified with eta window, $|\eta| < 0.5$ and the centrality was determined using charged particles in the eta window $0.5 \leq |\eta| \leq 1.0$ thus avoiding auto correlation effects.

Figure 4.18 shows different reference multiplicity distribution associated with

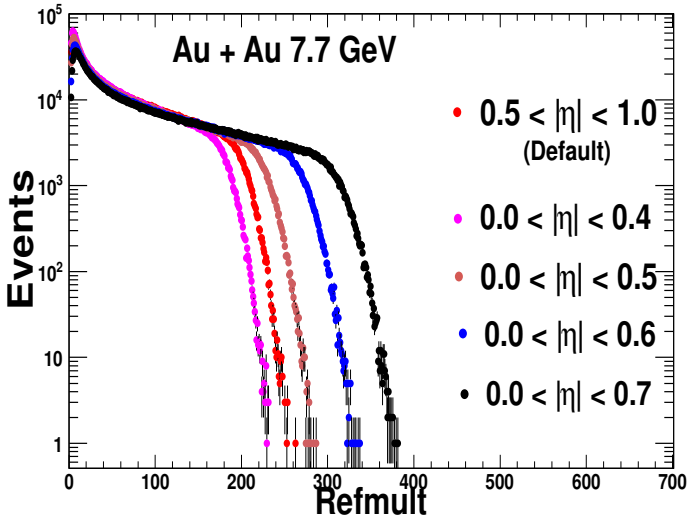

Figure 4.18: (Color online) Reference multiplicity distribution for different η window at $Au + Au$ 7.7 GeV.

different η window. In the same figure, the red distribution represent the default distribution using for this analysis within $0.5 \leq |\eta| \leq 1.0$. In Figure 4.19 we show the calculated moments for the different reference multiplicity distribution shown in Figure 4.18. It is very clear that the moments are not same from default (Refmult2) and traditional (Refmult) centrality definition. This effect arise due to the auto-correlation effect and can be seen in the volume independent moment products also shown in Figure 4.20. From this study, it is obvious that if one uses the same η window for the higher moments (or fluctuation) analysis and centrality definition, it results in auto-correlation. To reduce the auto-correlation effect, "Refmult2" has been introduce for the centrality definition within $0.5 \leq$

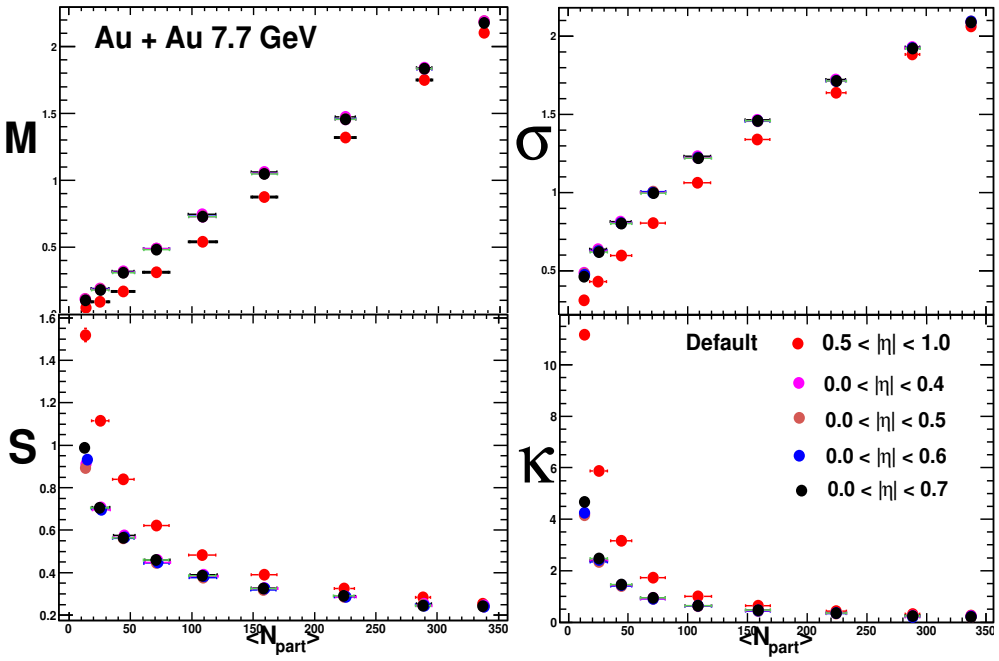

Figure 4.19: (Color online) Moments of ΔN_K multiplicity distribution calculated from different centrality definition for different reference multiplicity distribution at $Au + Au$ 7.7 GeV.

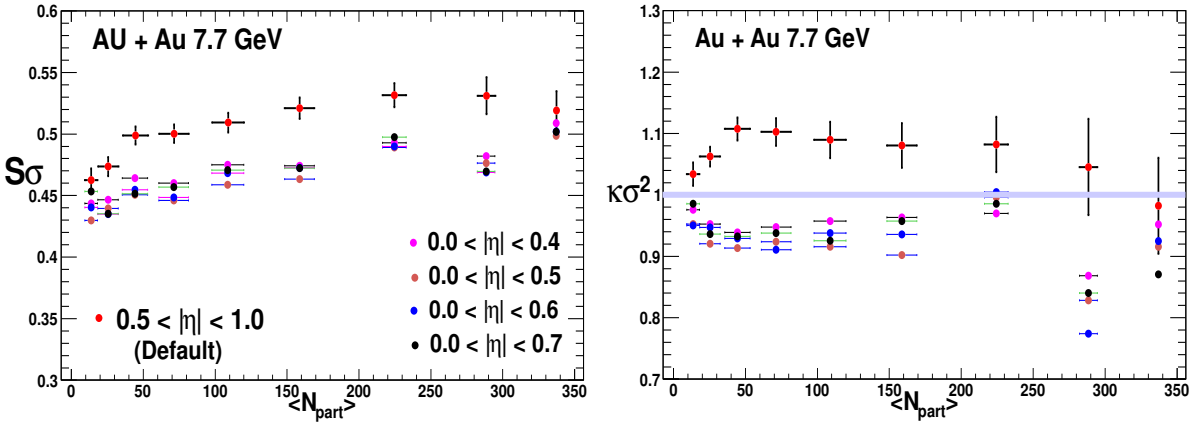

Figure 4.20: (Color online) $S\sigma$ and $\kappa\sigma^2$ of ΔN_K multiplicity distribution defined from different centrality definition from this five different multiplicity distribution for AuAu 7.7 GeV.

$|\eta| \leq 1.0$.

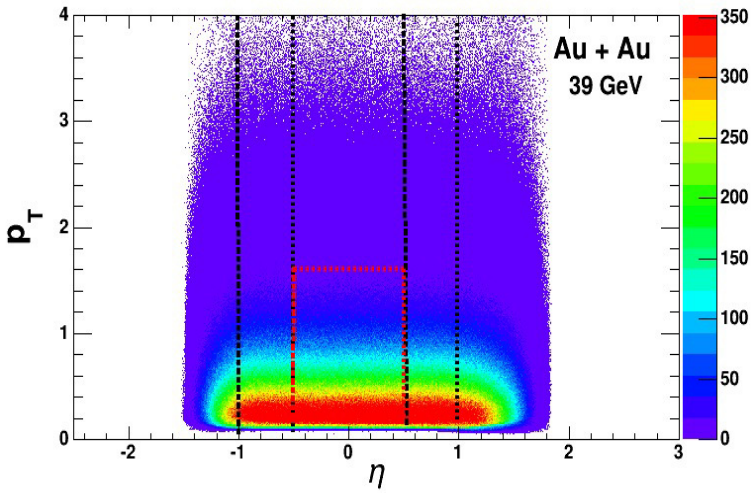

Figure 4.21: (Color online) The transverse momentum (p_T) as a function of η at $\sqrt{s_{NN}} = 7.7\ GeV$.

4.3.2 Centrality Selection from MC Glauber Model

The centrality selection for our higher moment analysis is done by the uncorrected charged particle multiplicity as mentioned above in a different eta window. For each centrality, the average numbers of participants ($< N_{\rm part} >$) are obtained by Glauber model calculations [26]. In heavy ion collision experiments it is not possible to reconstruct the vertex at high precision with low multiplicity. In the peripheral events the multiplicity is very low hence the vertex reconstruction efficiency is also low. To correct for this inefficiency dN^{MC}_{event}/dN_{ch} mapping with true experimentally measured dN_{event}/dN_{ch} was done by convolution of N_{part} from MC Glauber simulation. For this convolution we use a Negative Binomial Distribution (NBD) along with the Glauber simulation.

$$NBD(n;\mu,k) = \frac{\Gamma(n+k)}{\Gamma(n+1)\Gamma(k)}\frac{(\mu/k)^n}{(n/k+1)^{n+k}} \tag{4.4}$$

To calculate the centrality, MC Glauber simulation was done for all energies from the Beam Energy Scan program. The simulated N_{coll} and N_{part} from the Glauber simulation at $\sqrt{s_{NN}}$ = 7.7 and 200 GeV for $Au + Au$ collisions are shown in the Figure 4.22 and Figure 4.23. By repeated use of NBD parameters it is possible

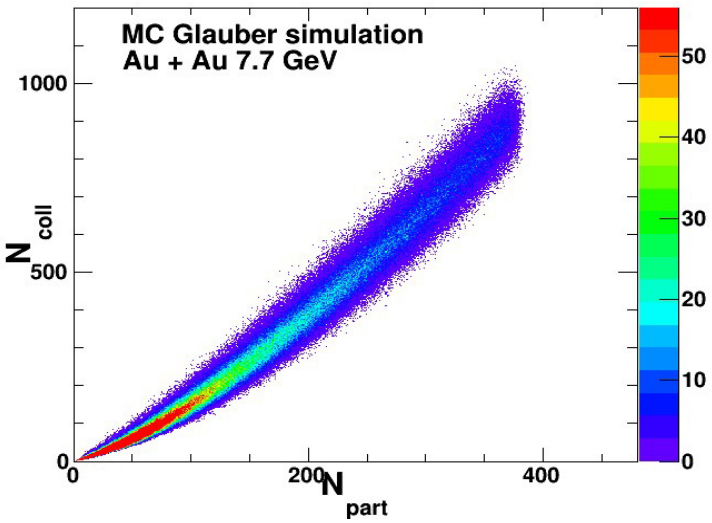

Figure 4.22: (Color online) The estimated N_{coll} as a function of N_{part} are plotted for $Au + Au$ collisions at $\sqrt{s_{NN}} = 7.7\ GeV$ from MC Glauber simulation.

to reproduce the Glauber MC multiplicity. We will discuss the centrality selection procedure in details after the next discussion. To validate this new centrality

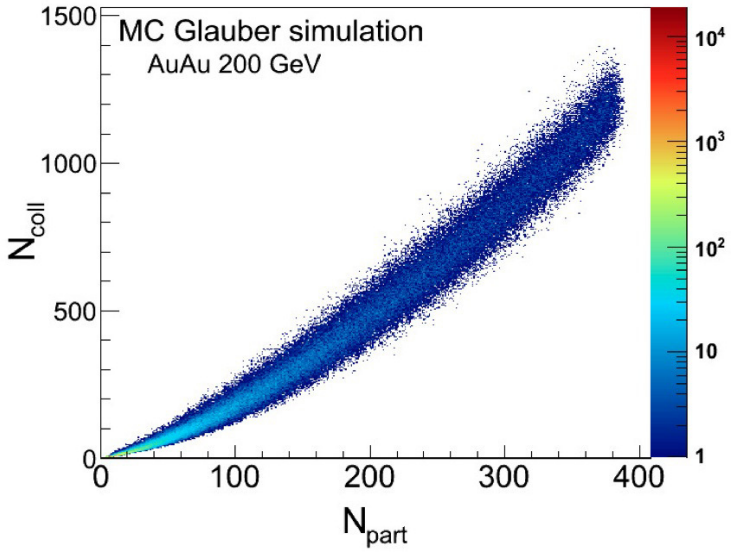

Figure 4.23: (Color online) The estimated N_{coll} as a function of N_{part} are shown for $Au + Au$ collisions at $\sqrt{s_{NN}} = 200\ GeV$ from MC Glauber simulation.

definition, MC Glauber simulation has been performed for all energies. The produced multiplicity distribution from the MC Glauber simulation has been compared with the data. In the Figure 4.24, the MC simulated as well as measured

multiplicity distributions are shown. The ratio of the measured multiplicity with

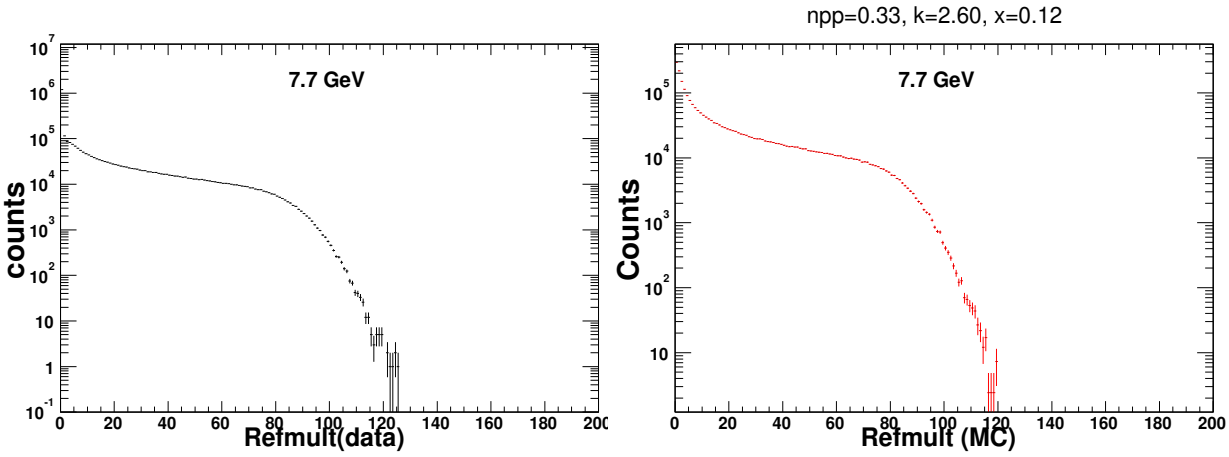

Figure 4.24: (Color online) The Refmult2 distribution of data and MC at $\sqrt{s_{NN}} = 7.7\ GeV$.

the MC Glauber simulated multiplicity is shown in Figure 4.25. We observe that,

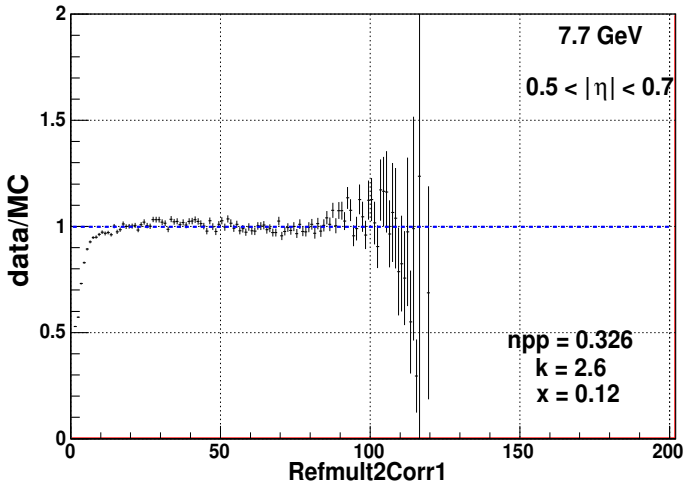

Figure 4.25: (Color online) The Refmult2 ratio of data to MC at $\sqrt{s_{NN}} = 7.7\ GeV$.

at peripheral collisions, the ratio of data to MC is less than unity. This effect arises due to the vertex reconstruction in-efficiency for low multiplicity events in the peripheral collisions. Based on this MC Glauber simulated multiplicity, centrality definition has beed performed.

To calculate the centrality the procedure is same as the standard procedure. The difference is only in selecting the charge particle multiplicity from a different η window, Refmult2. From the simulated MC multiplicity distribution we calculate the centrality by the fraction of total integrated multiplicity. This can be formulated in mathematics as,

$$\frac{\int_{\infty}^{n_{m1-m2}} \frac{dN_{event}^{MC}}{dN_{ch}} dN_{ch}}{\int_{\infty}^{0} \frac{dN_{event}^{MC}}{dN_{ch}} dN_{ch}} = \frac{N_{bin}}{N_{Total}} \tag{4.5}$$

Here n_{m1-m2} represents the bin number at which number the percentage of total integral occurred. $m1$ and $m2$ represents lower and upper cut of multiplicity of that particular centrality bin. So, n_{0-10} is considered to be the top 0-10% central events. N_{bin} and N_{Total} represents the multiplicity in that particular bin and the total multiplicity of the distribution.

By using this method we have performed the centrality selection for our analysis. An example of the centrality selection is illustrated in the Figure 4.26. For

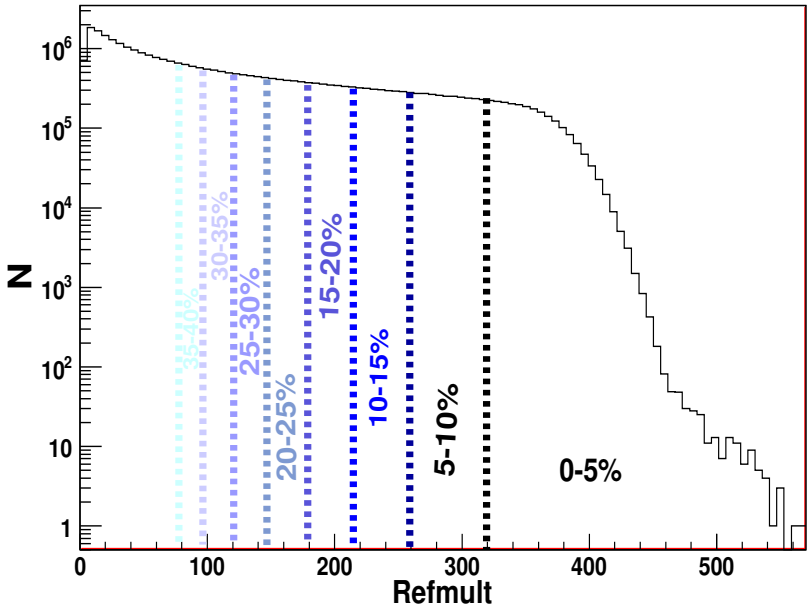

Figure 4.26: (Color online) An example of centrality definition for $Au + Au$ 39 GeV.

the Refmult2 centrality determination all charged particle multiplicity selected within $|V_z| < 30\ cm$ of vertex position from the center of TPC. In STAR run-by-run V_z correction has been done for the Refmult2 for all beam energy data. The corrected Refmult2 has been taken from the "StRefmult2Corr" class of the analysis package for STAR data. Details about this class can be found at Ref.[118].

Table 4.4: Estimated centrality using MC Glauber model for all BES energies at RHIC in $Au + Au$ collisions.

Energy (GeV)	70-80% (R2)	60-70% (R2)	50-60% (R2)	40-50% (R2)	40-30% (R2)	20-30% (R2)	10-20% (R2)	5-10% (R2)	0-5% (R2)
7.7	3	7	14	25	41	64	95	137	165
11.5	4	9	19	32	52	80	118	172	206
19.6	5	12	22	40	65	100	149	215	258
27	6	13	25	43	71	111	164	237	284
39	7	14	27	47	78	121	179	257	307
62.4	7	15	29	51	84	131	194	279	334
200	9	20	40	71	117	181	268	383	453

The estimated centrality using MC Glauber model for all BES energies at $Au + Au$ collisions are shown in the Table 4.4. The R2 represent the Refmult2 and for each centrality the Refmult2 value is higher than or equal to the mentioned value and lower than the value mentioned for the next lower centrality. The corresponding $< N_{part} >$ to the Refmult2 is shown in the Table 4.5.

4.3.3 Centrality Resolution Effects

In heavy ion collision the collision geometry and centrality are represented by the impact parameter b, number of participant nucleons (N_{part}) and number of binary collisions (N_{coll}). These parameters are strongly correlated with each others. The collision centrality is obtained by mapping the experimentally measured charged particle multiplicity with that obtained by the MC Glauber simulation. Along with the relation on physics process and initial geometry there are fluctuation associated with the charge particle multiplicity. This associated fluctuation can

Table 4.5: Average number of participants for all calculated centrality using MC Glauber model for all BES RHIC energies at $Au + Au$ collisions.

Energy (GeV)	0-5% $\langle N_{part}\rangle$	5-10% $\langle N_{part}\rangle$	10-20% $\langle N_{part}\rangle$	20-30% $\langle N_{part}\rangle$	30-40% $\langle N_{part}\rangle$	40-50% $\langle N_{part}\rangle$	50-60% $\langle N_{part}\rangle$	60-70% $\langle N_{part}\rangle$	70-80% $\langle N_{part}\rangle$
7.7	337.36	288.71	224.64	158.94	109.02	71.36	44.56	25.62	13.85
11.5	338.42	288.74	224.29	158.38	109.30	71.92	44.32	25.59	14.04
19.6	340.67	293.93	232.41	167.02	117.86	79.93	51.21	31.43	17.96
27	340.96	291.78	227.42	167.17	110.87	72.93	45.43	26.06	13.43
39	341.76	291.95	227.72	160.87	110.54	72.86	45.25	26.23	14.07
62.4	344.40	296.71	232.00	164.59	113.49	75.08	46.26	26.56	13.78
200	349.81	300.86	235.60	167.66	115.87	76.37	47.68	27.46	14.43

be different even for same initial geometry. Therefore there could be different geometry resolution of the initial collisions for different centrality definition. The choice of centrality definition for the higher moments, calculated from event-by-event charged particle multiplicity distributions, therefore plays a vital role.

Our aim is to calculate the centrality using Refmult2 centrality definition and to include maximum number of charge particle multiplicity. It is very natural and expected that if we include more particles for the centrality definition the resolution gets better. Using Refmult2 centrality definition, we check the centrality resolution effect by varying η windows in the net-kaon higher moments. Different η windows have been studied like, $0.5 < |\eta| < 0.8$, $0.5 < |\eta| < 0.9$, $0.5 < |\eta| < 1.0$ (Default), $0.5 < |\eta| < 1.1$ and $0.5 < |\eta| < 1.2$. The Refmult2 distributions for different η windows are shown in the Figure 4.27 for $Au + Au$ 7.7 and 200 GeV. Figure 4.27 show that as we increase the size of the η window the particle multiplicity increases. The higher moments of net-kaon distribution for $|\eta| \leq 0.5$ have been studied for all of the different multiplicity distribution. In the Figure 4.28 the volume independent $S\sigma$ as a function of N_{part} for $Au + Au$ 7.7 and 200 GeV are shown for different Refmult2 centrality definition. For both of these energies, the $S\sigma$ value gets saturated after η window $0.5 \leq |\eta| \leq 1.0$ which is the default reference multiplicity value i.e Refmult2. In the Figure 4.29 the volume independent $\kappa\sigma^2$ as a function of N_{part} for $Au + Au$ 7.7 and 200 GeV are shown

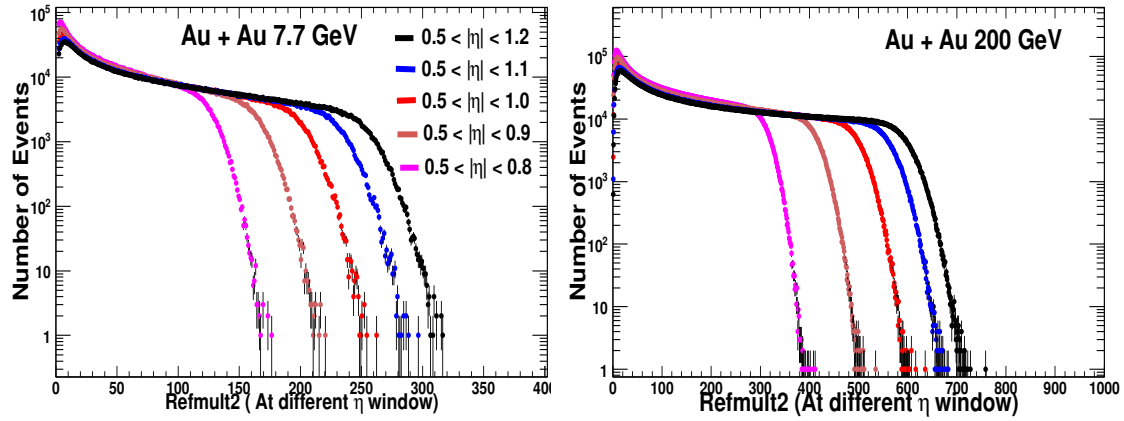

Figure 4.27: (Color online) Refmult2 distribution for various η window for $Au + Au$ 7.7 GeV and 200 GeV.

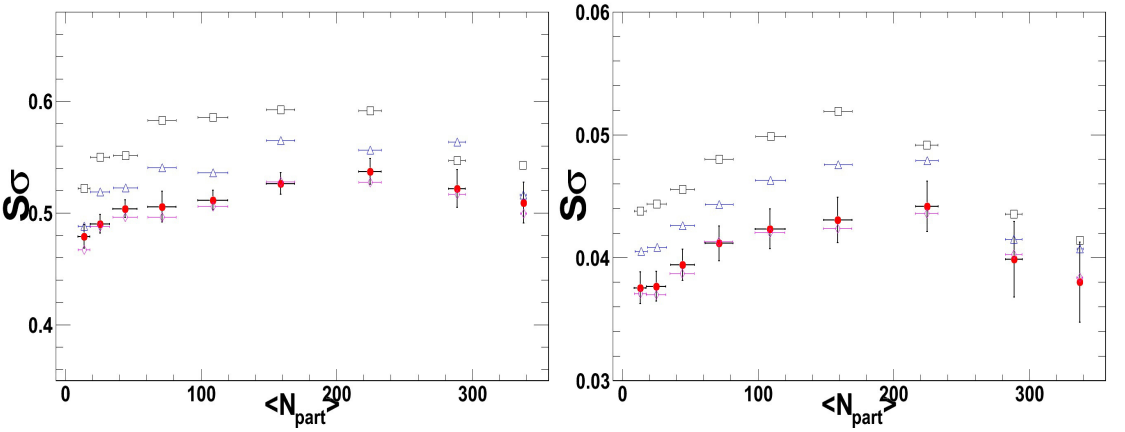

Figure 4.28: (Color online) $S\sigma$ as a function N_{part} for various η window for Au+Au 7.7 GeV and 200 GeV.

for different Refmult2 centrality definition. From Figure 4.29 we see the same tendency of the moment product $\kappa\sigma^2$ as a function of N_{part} as we see in the $S\sigma$ as a function of centrality. We observe significant differences for moment products ($S\sigma$, $\kappa\sigma^2$) in higher moment analysis for the different $|\eta|$ range of the centrality definition. When we increase the η upper range ($|\eta|< 0.8, 0.9, 1.1, 1.2$), the values of $S\sigma$ and $\kappa\sigma^2$ decreases. Both of the the $\kappa\sigma^2$ and $S\sigma$ shows negligible effect for higher η-windows than the smaller η-window comparing with its default values. Therefore it is safe to use the Refmult2 ($0.5 < |\eta|< 1.0$) for the centrality selection in higher moment of net-kaon analysis.

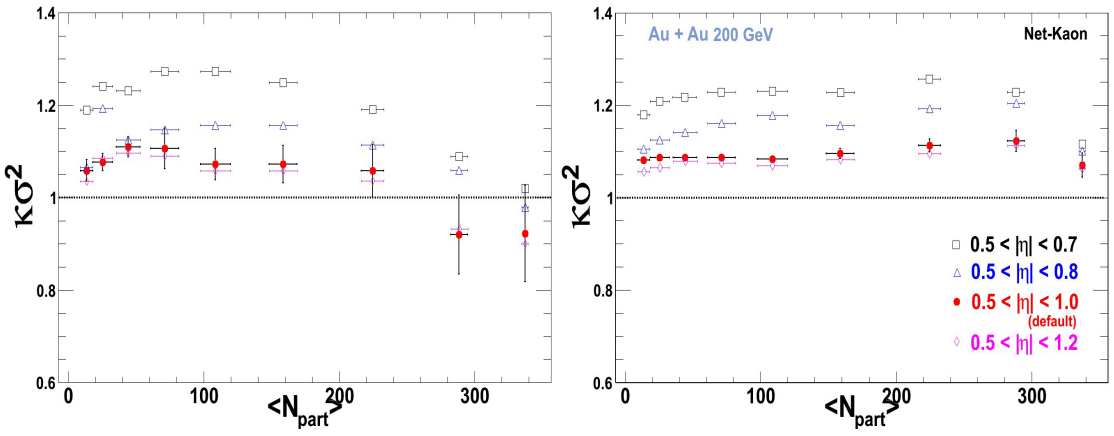

Figure 4.29: (Color online) $\kappa\sigma^2$ as a function N_{part} for various η window for AuAu 7.7 GeV and 200 GeV.

4.3.4 Centrality Bin Width Effects and it's Corrections

The centrality selection as defined earlier uses the Refmult2 ($0.5 < |\eta| < 1.0$) for this analysis. In heavy ion collision experiments it is customary to express the centrality by quoting the percentage of the collision cross-section. In our analysis we define nine centrality bins like, 0-5%, 5-10%, 10-20%, 20-30% up to 70-80%. In the higher moment analysis there are associated fluctuation due to the size of the centrality bin. Therefore it is very important to reduce this so called Centrality Bin Width Effect (CBWE) before going to any further physics analysis.

The Bin Width Effects

Centrality as defined in the heavy ion collision experiments depends on a particular range of impact parameter or the average number of participating nuclei hence on the charge particle multiplicity. Thus for each centrality we have different number of produced particles which lead us to additional fluctuations in the physics analysis. The bin-width effect arises due to the size of the centrality chosen for the analysis, defined by the charged particle multiplicity. To study the effects of the CBW we have defined three sets of centrality class which have the bin width size of 5%, 10% and 20%. In Figure 4.30 and Figure 4.31 we show

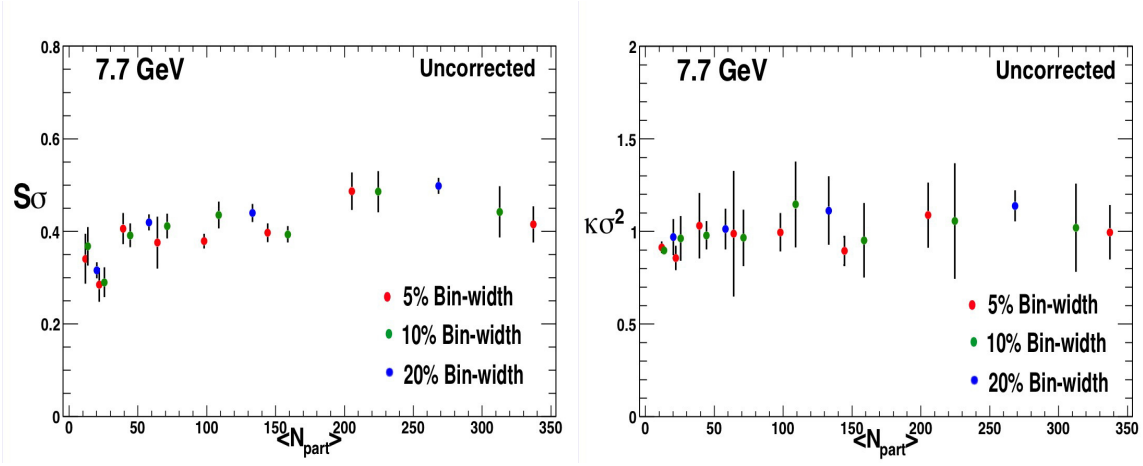

Figure 4.30: (Color online) Bin-Width effect in volume independent moment product $S\sigma$ and $\kappa\sigma^2$ at $\sqrt{s_{NN}} = 7.7\ GeV$.

centrality bin width effects with the three defined centrality for volume independent moment product $S\sigma$ and $\kappa\sigma^2$ at $\sqrt{s_{NN}} = 7.7$ and 200 GeV respectively. From

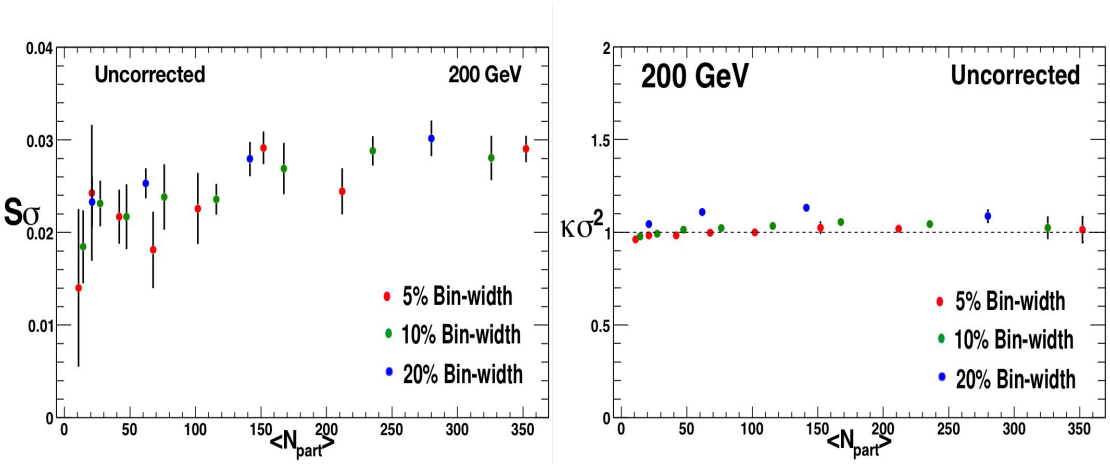

Figure 4.31: (Color online) Bin-Width effect in the moment products $S\sigma$ and $\kappa\sigma^2$ at $\sqrt{s_{NN}} = 200\ GeV$.

the Figure Figure 4.30 and Figure 4.31 it is observed that the volume independent moment product are not smoothly changing with the different bin width size. This bin width effects is also seen at other centre of mass energies. For each

centrality bin the net-kaon (ΔN_K) distribution is a superposition of many impact parameters. These bin width effects can be reduced using several techniques.

Methods to Reduce Bin Width Effects

There are three known methods which can reduce the effect due to the finite centrality bin. The three methods are:

- **Method I: Direct Weighted**
  For each defined centrality, various moments are calculated for each reference multiplicity and weighted by the number of events of that reference multiplicity.

- **Method II: Central Direct Weighted**
  For each defined centrality, central moments are calculated for for each reference multiplicity and weighted by the number of events of that reference multiplicity.

- **Method III: Cumulant Weighted**
  For each defined centrality, cumulants are calculated for each reference multiplicity and weighted by the number of events of that reference multiplicity.

In general we can write the mathematical expression for all of these three methods as:

$$x = \frac{\sum_i n_i x_i}{\sum_i n_i}, \tag{4.6}$$

where x can be moments, central moments or cumulants, depending on the three different methods, i is the dummy index represent each centrality within a defined bin width, n_i is the number of events in each fine centrality bin and $\sum_i n_i$ is the total number of events within the defined bin width.
Applying these correction on the data we see that, except the larger kurtosis value

from method II than from method I and III, all three methods are in good agreement. We see that the bin width correction for method I and III are in very good agreement. More so, they converge to the uncorrected smaller centrality bin results. We report only the 1^{st} method's results in this thesis.

CBW Corrected Results

Based on the direct weighted method (Method I) we show the CBW corrected results for $\sqrt{s_{NN}}$ = 7.7 and 200 GeV. In the Figure 4.32 we can see the bin width effect gets reduced after this correction for volume independent moment product $S\sigma$ and $\kappa\sigma^2$ at $\sqrt{s_{NN}} = 7.7\ GeV$. The bin width corrected results for volume

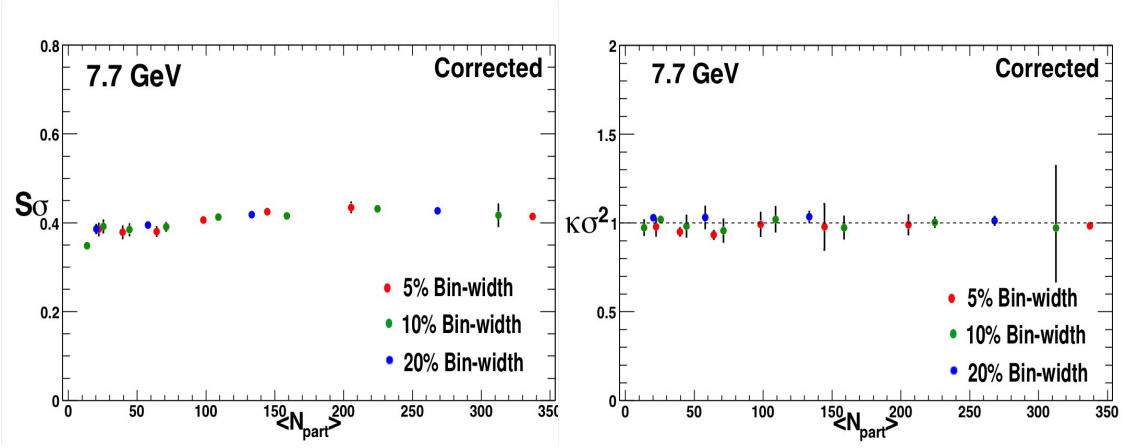

Figure 4.32: (Color online) Bin-Width effects and it's correction in volume independent moment product $S\sigma$ and $\kappa\sigma^2$ at $\sqrt{s_{NN}} = 7.7\ GeV$.

independent moment product $S\sigma$ and $\kappa\sigma^2$ at $\sqrt{s_{NN}} = 200\ GeV$ are shown in the Figure 4.33 and Figure 4.34. These results are compared with the uncorrected results.

It is observed that, after this correction the finite centrality bin size effect get reduced. Therefore we can use this method to reduce centrality bin width effect.

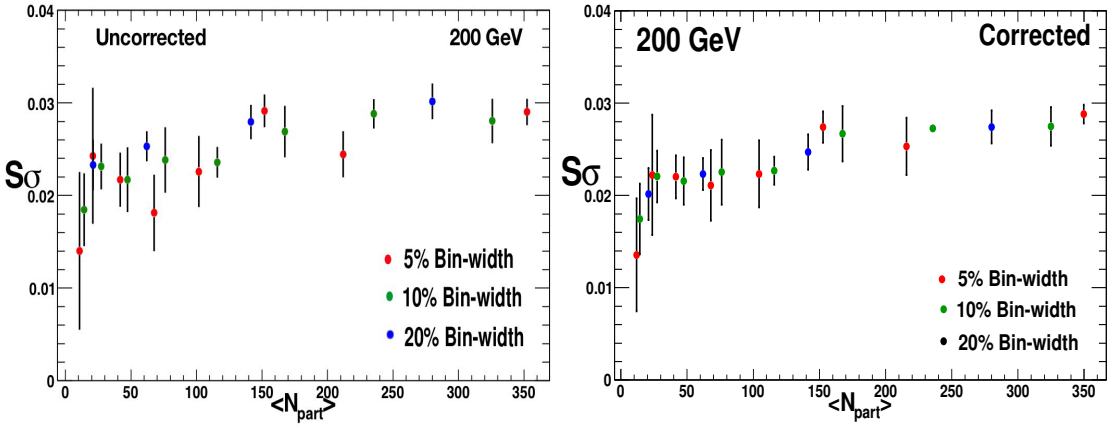

Figure 4.33: (Color online) Bin-Width effects and it's correction in volume independent moment product $S\sigma$ at $\sqrt{s_{NN}} = 200\ GeV$.

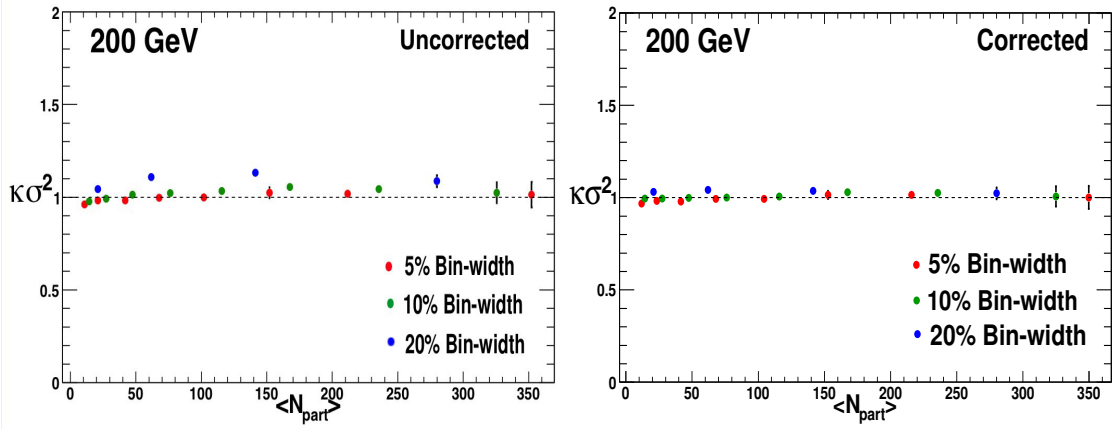

Figure 4.34: (Color online) Bin-Width effects and it's correction in volume independent moment product $\kappa\sigma^2$ at $\sqrt{s_{NN}} = 200\ GeV$.

4.4 Error Estimation

The error calculation is one of the most important aspect of any experimental measurement. For this analysis the error estimation has been divided into two part, the statistical and the systematic error estimation. The statistical error for an observable is the amount by which it differs from its expected value of a statistically measured observable [119]. In the following section we discuss several methods to calculate the statistical errors. The systematic errors are due to ex-

perimental acceptance. The systematic errors have been studied for this analysis by varying the experimentally accepted windows used to select the data sample. In addition, the inefficiencies of various detectors also contribute to the systematic error. The final results presented in this thesis are therefore corrected for the inefficiency of detectors involved in this analysis, namely TPC and TOF.

4.4.1 Statistical Error Estimation

Initially the sub-group method was used in calculation of the statistical error. Since higher moments are the fluctuations in a distribution we can think that, while we are calculating errors, we are calculating error of an error. Therefore, the statistical error analysis will not be as simple as we estimated before by using five-sub-group method. Also this higher moment analysis demands large statistics. So, it is very crucial to use the proper method to calculate the statistical errors with limited statistics. For this analysis we have used Sub-Group method, Delta theorem and Bootstrap method to calculate the statistical errors. Details about these method can be found in Appendix **A**.

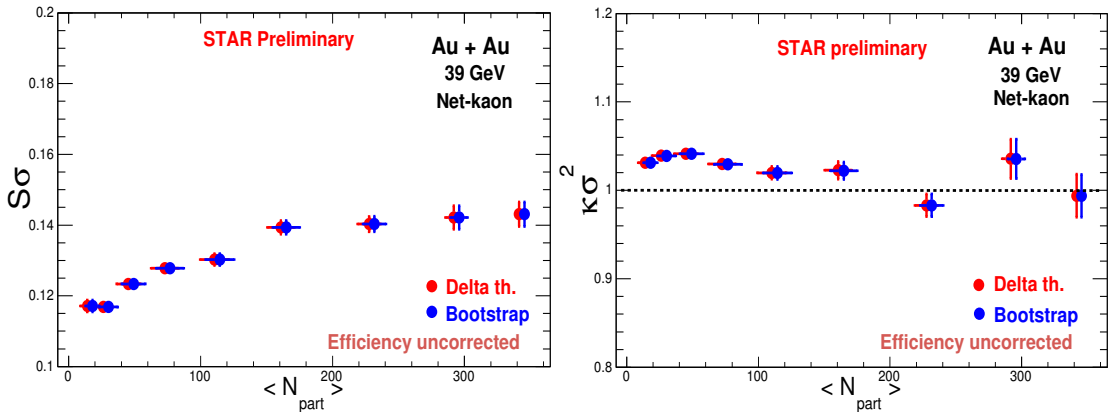

Figure 4.35: (Color online) A comparison of errors calculated from Delta Theorem and Bootstrap Method for the volume independent moment product $S\sigma$ and $\kappa\sigma^2$ at $\sqrt{s_{NN}} = 39\ GeV$.

A comparison of errors calculated for the volume independent moment products $S\sigma$ and $\kappa\sigma^2$ at $\sqrt{s_{NN}} = 39\ GeV$, from Delta Theorem and Bootstrap Method

are shown in the Figure 4.35. It is observed that the Bootstrap and Delta theorem method are consistent with each other. For this analysis Delta theorem method have been used for statistical error calculation in some analysis methods. For the detector efficiency calculation we used the Bootstrap Method and also for the final results after the efficiency calculation the Bootstrap Method was used.

4.4.2 Systematic Error Estimation

To evaluate the systematic uncertainties in this analysis we have studied four basic track quality parameters. The parameters used for the systematic study are the distance of closest approach (DCA) to the primary vertex, number of fit points used to fit the trajectory of each tracks (nFitPoints), number of dE/dx hit points (nhitsdedx), η and the $n\sigma_K$ used for the kaon PID. The systematic uncertainties have been estimated using the following track quality cuts;

- nFitpoints : 9, 12, 15 (Default), 18, 21
- DCA : 0.8, 0.9, 1.0 (Default), 1.1, 1.2
- nhitsdedx : 8, 9, 10 (Default), 11, 12
- η : 0.3, 0.4, 0.5 (Default), 0.6, 0.7
- $n\sigma_K$: 1.0, 1.5, 2.0 (Default), 2.5, 3.0

Since, we have used the η for the centrality definition as well, we have not included the η systematic contribution to the final systematic errors calculation. Mean square root of relative deviation for the systematic errors for each of the mentioned parameters have been estimated as follows,

$$RMS = \sqrt{\frac{1}{n}\sum_{i}\frac{Y_i - Y_{St.Cut}}{Y_{St.Cut}}} \tag{4.7}$$

where, Y_i is the observable in our case moments and moments products from different systematic cuts and $Y_{St.Cut}$ is the moments and moment products from

Standard (default) cut. The systematic errors calculated as,

$$Sys.Err = Y_{St.Cut}\sqrt{\sum RMS^2} \tag{4.8}$$

where, the summation is over the number of the variables. The systematic study has been done both before and after efficiency calculation. The efficiency uncorrected moments and moment product at different DCA cut and its RMS values for $Au+Au$ collisions at $\sqrt{s_{NN}} = 39\ GeV$ are shown in the Figure 4.36 and Figure 4.37. It is observed that by changing the DCA values moments and the moment prod-

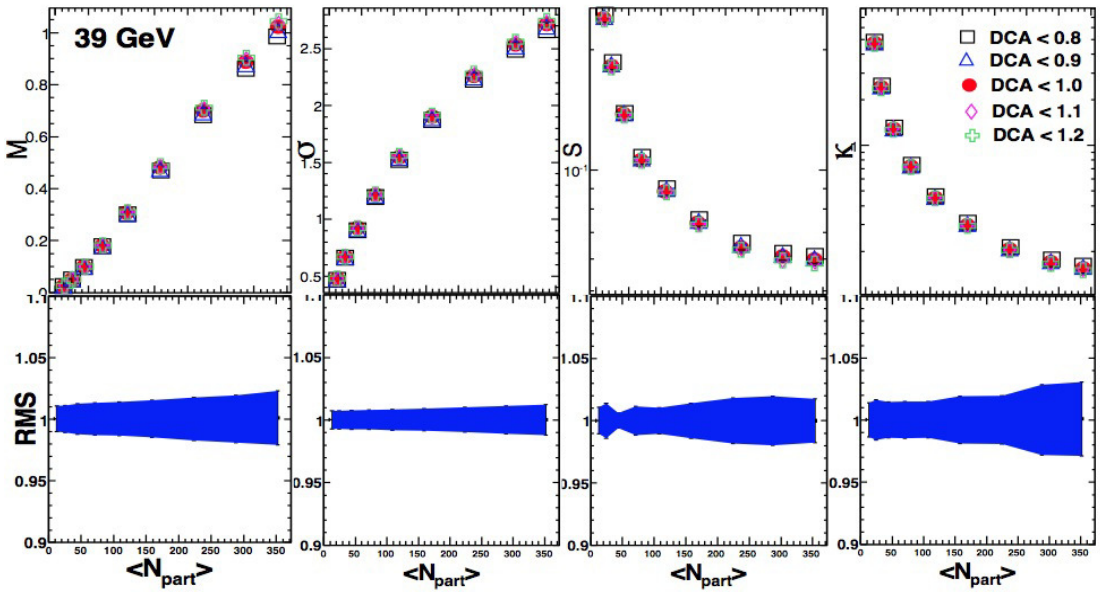

Figure 4.36: (Color online) Centrality dependence of moments of ΔN_K distributions for $Au+Au$ collisions at $\sqrt{s_{NN}} = 39\ GeV$ for PID1 with different DCA value.

ucts have very negligible effects which is nearly 2% and 1% respectively about its mean value for $Au + Au$ collisions at $\sqrt{s_{NN}} = 39\ GeV$ The efficiency uncorrected moments and moment product at different $n\sigma_K$ cut and its RMS values at $Au+Au$ 39 GeV are shown in the Figure 4.38 and Figure 4.39.

It is observed that for $Au + Au$ collisions at $\sqrt{s_{NN}} = 39\ GeV$ by changing the $n\sigma_K$ value, the moments change by nearly 10-15% and the moment products change by nearly 2% respectively about their mean value. The same systematic studies have been done for all the tracking parameters outlined above and for

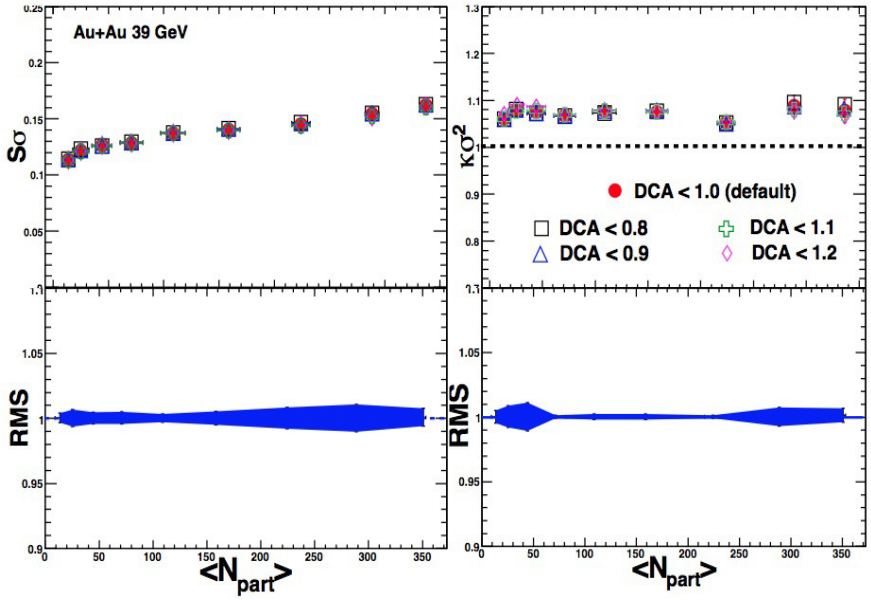

Figure 4.37: (Color online) Centrality dependence of efficiency uncorrected moment products $S\sigma$ and $\kappa\sigma^2$ for $Au + Au$ collisions at $\sqrt{s_{NN}} = 39\ GeV$ for PID1 with different DCA value.

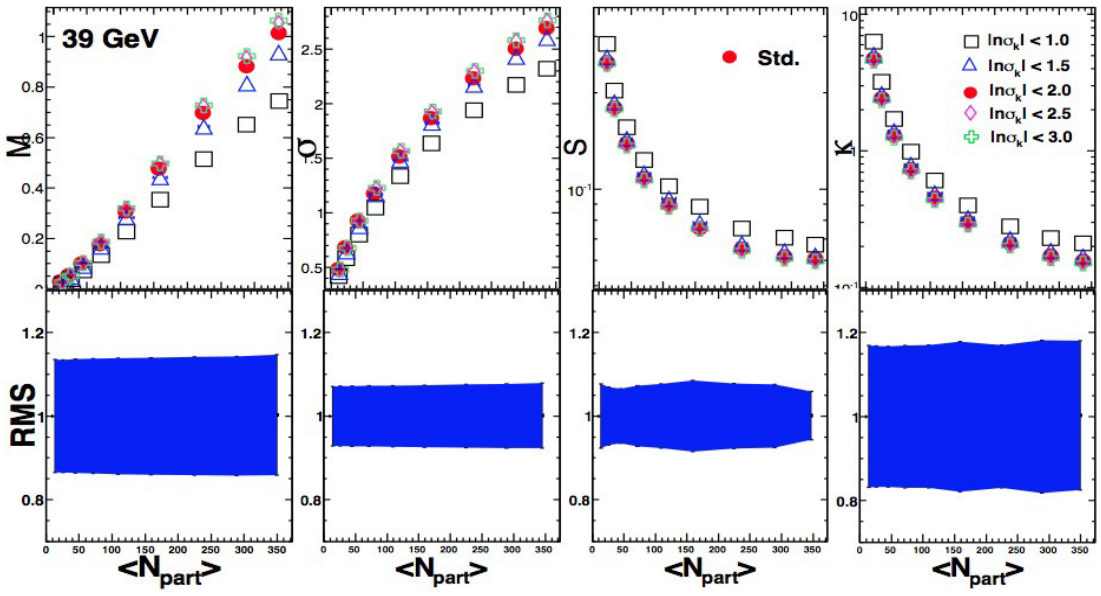

Figure 4.38: (Color online) Centrality dependence of moments of ΔN_K distributions for $Au + Au$ collisions at $\sqrt{s_{NN}} = 39\ GeV$ for PID1 with different $n\sigma_K$ value.

all BES energies. Systematic studies have also been done for efficiency corrected moments and moment products as well. We show some of them in the Figure 4.40 - Figure 4.43.

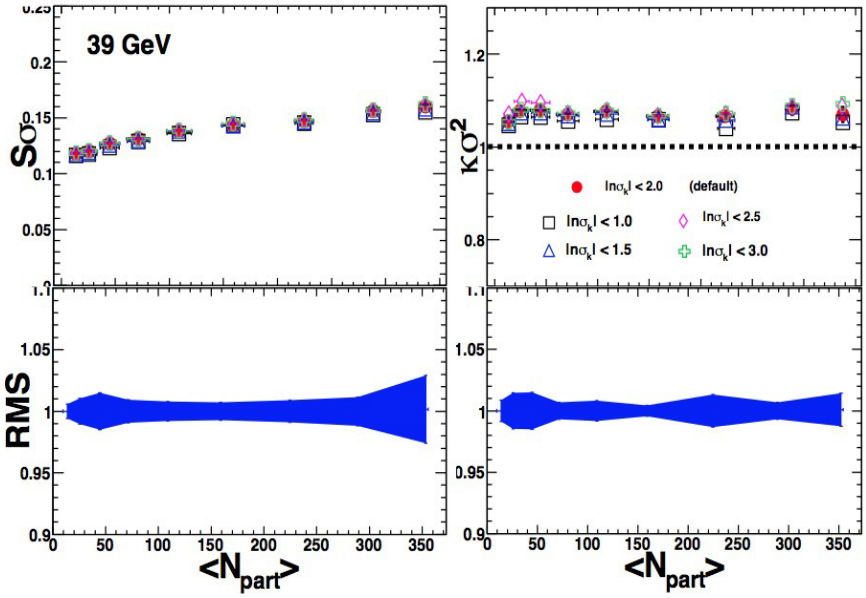

Figure 4.39: (Color online) Centrality dependence of efficiency uncorrected moment products $S\sigma$ and $\kappa\sigma^2$ for $Au + Au$ collisions at $\sqrt{s_{NN}} = 39\ GeV$ for PID1 with different $n\sigma_K$ value.

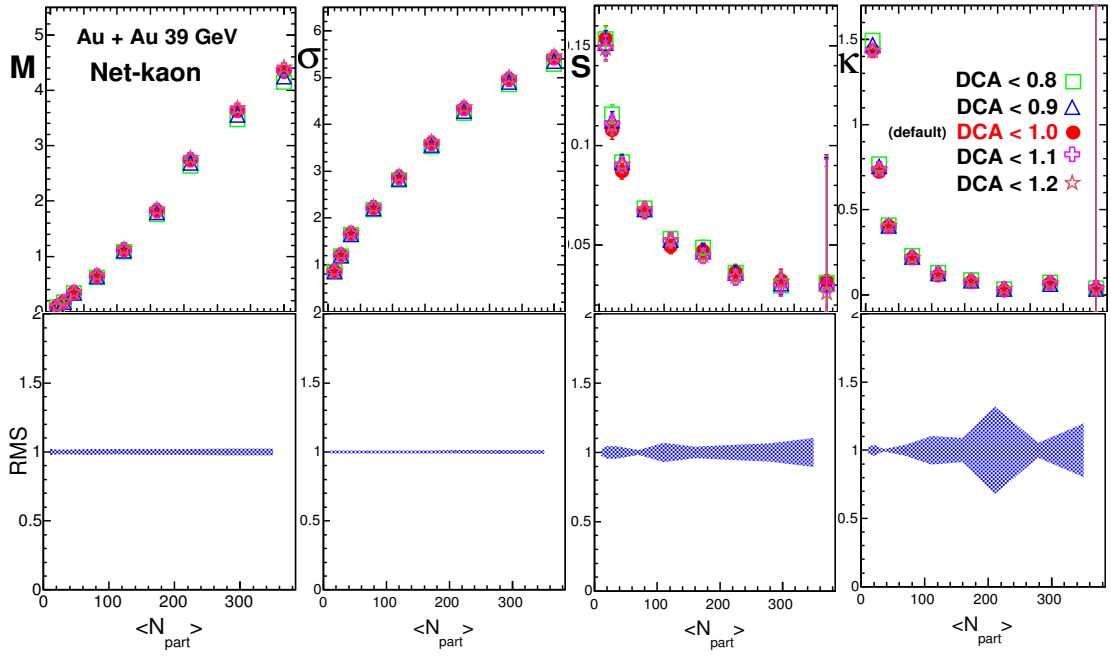

Figure 4.40: (Color online) Centrality dependence of efficiency corrected moments of ΔN_K distributions for $Au + Au$ collisions at $\sqrt{s_{NN}} = 39\ GeV$ for PID2 with different $n\sigma_K$ value.

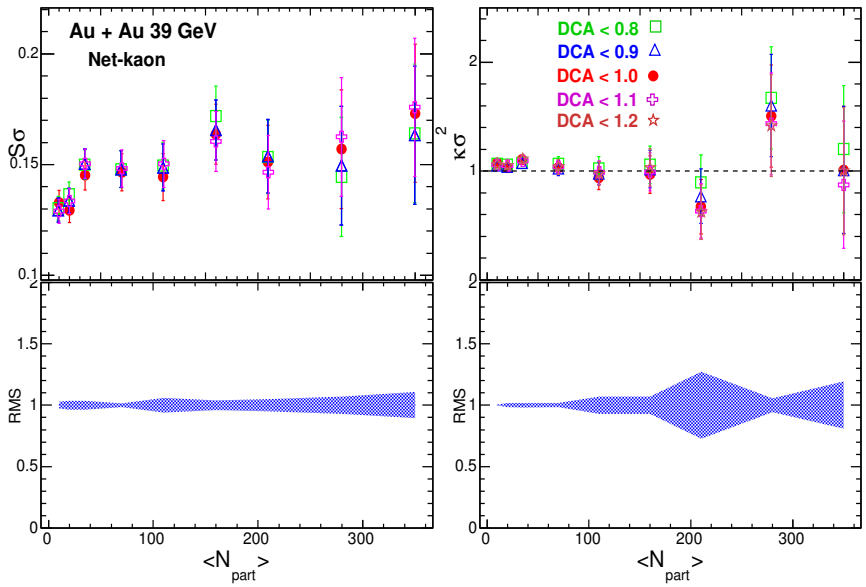

Figure 4.41: (Color online) Centrality dependence of efficiency corrected moment products $S\sigma$ and $\kappa\sigma^2$ for $Au + Au$ collisions at $\sqrt{s_{NN}} = 39\ GeV$ for PID2 with different $n\sigma_K$ value.

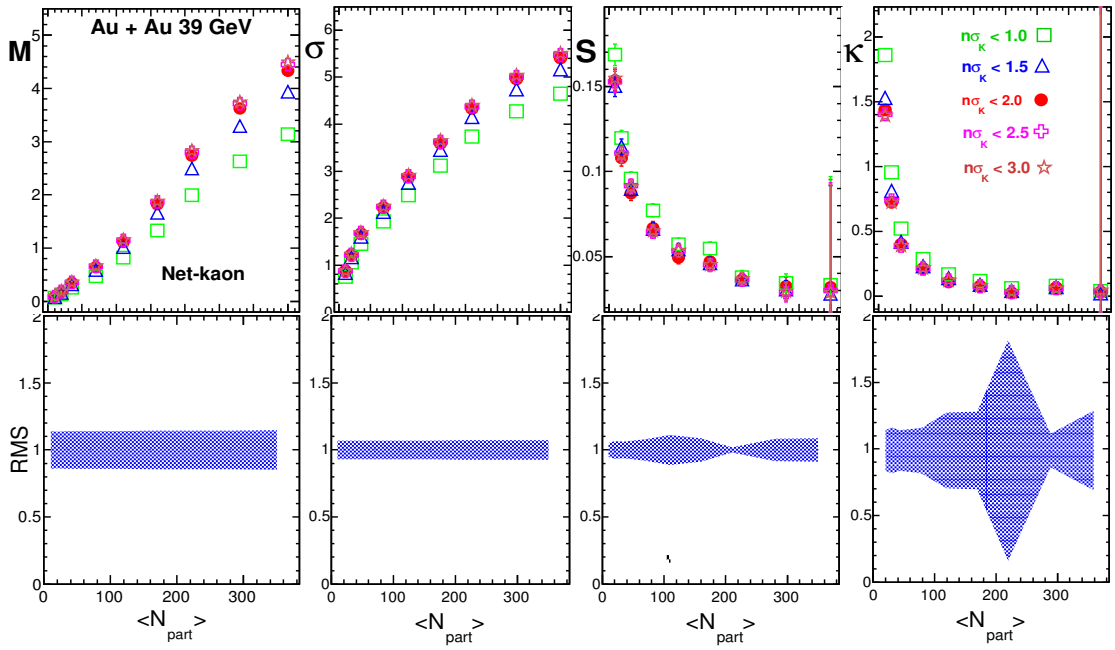

Figure 4.42: (Color online) Centrality dependence of efficiency corrected moments of ΔN_K distributions for $Au + Au$ collisions at $\sqrt{s_{NN}} = 39\ GeV$ for PID2 with different $n\sigma_K$ value.

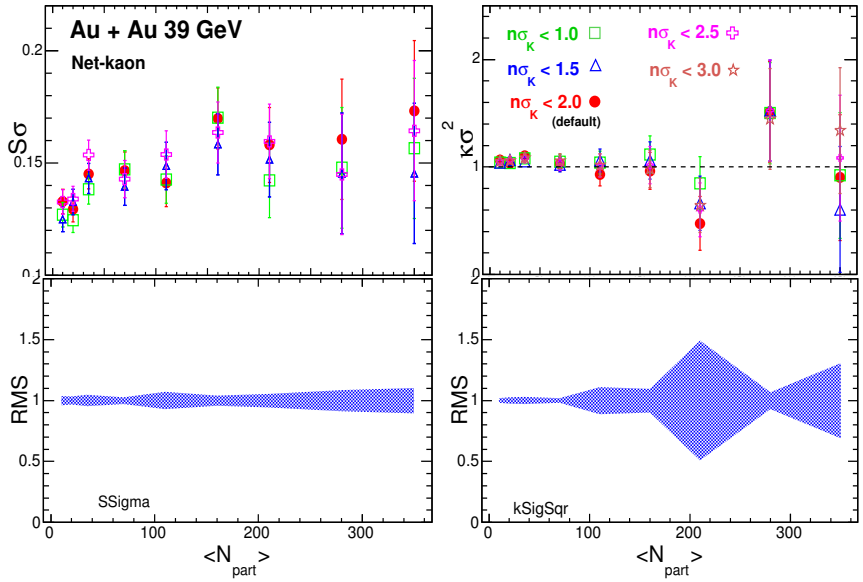

Figure 4.43: (Color online) Centrality dependence of efficiency corrected moment products $S\sigma$ and $\kappa\sigma^2$ for $Au + Au$ collisions at $\sqrt{s_{NN}} = 39\ GeV$ for PID2 with different $n\sigma_K$ value.

From Figure 4.40 and Figure 4.42 we observe that the efficiency corrected moments for different DCA values for $Au + Au$ collisions at $\sqrt{s_{NN}} = 39\ GeV$ show approximately 2%, 1%, 4% and 15% deviation from the mean value for mean, standard deviation, skewness and kurtosis respectively, where the same for different $n\sigma_K$ values are 12%, 6%, 8% and 25% respectively. Systematics in volume independent moment products for different DCA values show nearly 5% and 10% for $S\sigma$ and $\kappa\sigma^2$ respectively, the systematic for $S\sigma$ and $\kappa\sigma^2$ for different $n\sigma_K$ values are approximately 10% and 20% respectively.

4.5 Detector Efficiency and it's Correction

4.5.1 Introduction

Like all other detectors, STAR detectors also have finite efficiency. The detector consist of several subsystems and each system has a finite efficiency. In the procedure from the triggering to the PID all used subsystem bound by their finite efficiency. The finite efficiency of the system determines the data taken which

in turn influences the analysis. Therefore for an experimental measurement it is very important to correct the results for finite efficiency. The higher moment analysis carried out in this work is also effected by the finite efficiency and we need to correct for it.

There are several factors which contribute to the finite efficiency, for example, uncertainties in tracking, uncertainties due to acceptance, uncertainties in measuring momentum, uncertainties in vertex reconstruction etc.. It is very difficult to measure these uncertainties event by event or separately for different subsystems due to the reason that these efficiencies are not additive. The higher order cumulants hence the higher order moments are very sensitive to these efficiencies. Hence we need to estimate the detector efficiency and correct the observable for its effect to the best extent possible.

4.5.2 Detector Efficiency Correction for Cumulants

The particle identification efficiency of a detector can be expressed as a Binomial function with a certain efficiency parameter. For an ideal detector with efficiency 100%, let us consider the net-kaon probability distribution, P(K^+, K^-), of positively charged kaons (K^+) and Negatively charged kaons (K^-). The measured net-kaon probability distribution with positively and negatively charged kaon efficiency ϵ_+ and ϵ_- is,

$$p(k^+, k^-) = \sum_{K^+=k^+} \sum_{K^-=k^-} B(k^+|K^+, \epsilon_+) B(k^-|K^-, \epsilon_-) P(K^+, K^-) \tag{4.9}$$

Here we assuming the detector efficiency is a binomial probability distribution function. Then the moment generating function is,

$$m(z) = \sum_{K^+=k^+} \sum_{K^-=k^-} p(K^+, K^-)[1-(1-z)\epsilon_+]^{K^+}[1-(1-z^1)\epsilon_-]^{K^-} \tag{4.10}$$

And then we can define the cumulant generating function as,

$$g(t) = ln[l(e^t)] = \sum_{n=1}^{\infty} \frac{t^n}{n!} \tag{4.11}$$

From this cumulant generating function we can construct different cumulants for both the true and measured as,

$$c_n = \frac{d^n g(t)}{dt^n}|_{t=0}, \qquad C_n = \frac{d^n G(t)}{dt^n}|_{t=0} \tag{4.12}$$

where, c_n represents the n_{th} order measured cumulants and C_n represents the n_{th} order true cumulants calculated from corresponding cumulant generating function $G(t)$ at $\epsilon_- = \epsilon_+ = 1$. In this net-kaon analysis for simplicity we assumed $\epsilon_- = \epsilon_+ = \epsilon$. Using above expressions, the true values of the cumulants can be derived from the measured values as,

$$\begin{aligned}
C_1 =& c_1/\epsilon, \\
C_2 =& (c_2 - n(1-\epsilon))/\epsilon^2, \\
C_3 =& (c_3 - c_1(1-\epsilon^2) - 3(1-\epsilon)(f_{02} - f_{02} - nc_1))/\epsilon^3, \\
C_4 =& (c_4 - n\epsilon^2(1-\epsilon)3n^2(1-\epsilon)^2 - 6\epsilon(1-\epsilon)(f_{20} + f_{02}) + 12c_1(1-\epsilon)(f_{20} - f_{02}) \\
& - (1-\epsilon^2)(c_2 - 3c_1^2) - 6n(1-\epsilon)(c_1^2 - c_2) - 6(1-\epsilon)(f_{03} - f_{12} + f_{02} + f_{20} - \\
& f_{21} + f_{30}))/\epsilon^4
\end{aligned}$$

where n is the total measured average kaon particles, f_{ij} represents the measured factorial moment of the net-kaon distribution [121]. From the measured probability distribution function it can be shown that the true factorial moments F_{ij} is related to the measured factorial moment f_{ij} of the net-kaon distribution as,

$$f_{ij} = \epsilon_+^i + \epsilon_-^j F_{ij} \tag{4.13}$$

In the next section we discuss the procedure to calculate the detector efficiency for identified kaons and anti-kaons which can be used to estimate the efficiency for any charged particle detected in the STAR experiment.

4.5.3 Efficiency Calculation

In this analysis we have selected two sets of PID. For both the PIDs we have used TPC as the main tracking detector. We have also used the TOF detector with different kinematic range for different PIDs. In the next two sections we discuss the procedure to calculate the tracking efficiency and TOF matching efficiency.

4.5.3.1 Tracking Efficiency

For the tracking efficiency calculation we have used the Monte Carlo (MC) simulation along with the real data. In STAR, the tracking efficiency estimation uses the method of embedding Monte Carlo (MC) simulated tracks into the real events from the data. From Monte Carlo (MC) simulation identified charged particle tracks like p^+, p^-, π^+ ,π^- , K^+ and K^- are used in the embedding procedure to the real data. The MC reconstructed tracks and events are selected based on the net-kaon analysis track and vertex cuts. The embedding efficiency is calculated by taking the ratio of number of embedded MC tracks and reconstructed tracks (matched pair) from the real events. These embedding efficiency is p_T dependent efficiency as shown in the Figure. 4.45. Finally, we calculate the tracking efficiency from this p_T dependent efficiency as,

$$\epsilon_x = \frac{\int \epsilon_x^{'}(p_T) f(p_T) p_T dp_T}{\int f(p_T) p_T dp_T} \tag{4.14}$$

where $\epsilon_x^{'}$ is the embedding efficiency for each p_T bin, $f(p_T)$ is the transverse momentum spectra fitted function for all BES energies and centrality, p_T is the average value of each p_T bin and dp_T is the width of the p_T bin. The calculated tracking efficiency for all BES energies and centrality is shown in the Table 4.6.

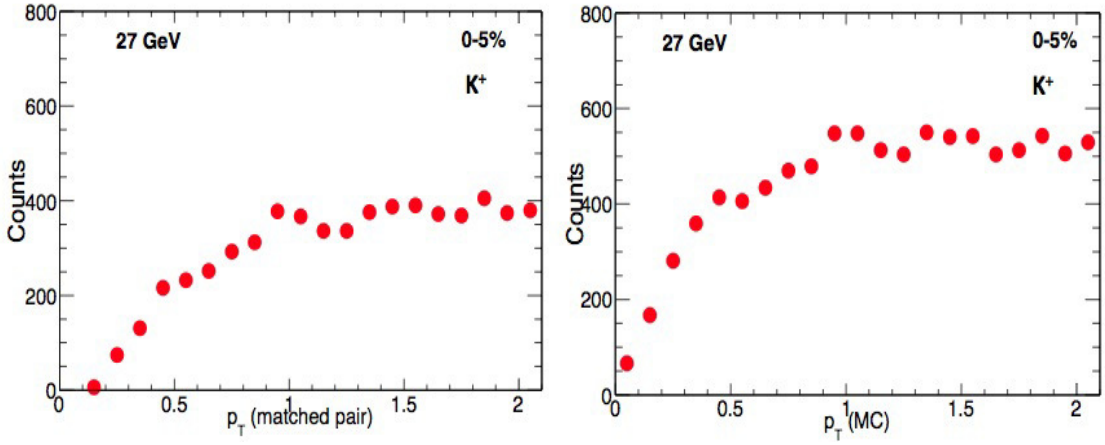

Figure 4.44: (Color online) Number of matched pairs and MC tracks for $\sqrt{s_{NN}} = 27\ GeV$ at 0-5% central collision.

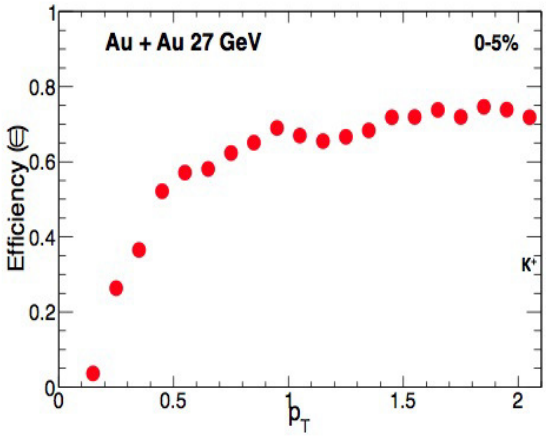

Figure 4.45: (Color online) p_T dependent tracking efficiency for $\sqrt{s_{NN}} = 27\ GeV$ at 0-5% central collision.

4.5.3.2 TOF Matching Efficiency

The TOF matching efficiency is the TOF efficiency to identify TPC tracks. In the STAR experiment, the TOF matching efficiencies are estimated by taking the ratio of number of tracks from TPC after applying the m^2 window with the number of tracks from TPC for identified particle species. For example, lets assume we pass N number of tracks through the TPC and we get N_1 number of tracks, those N_1 number of tracks passed through TOF and we get N_2 number of tracks as shown

Table 4.6: Estimated tracking efficiency from embedding for all BES $Au + Au$ collisions.

Energy (GeV)	70-80%	60-70%	50-60%	40-50%	40-30%	20-30%	10-20%	5-10%	0-5%
7.7	0.593	0.580	0.583	0.583	0.575	0.571	0.565	0.558	0.549
11.5	0.607	0.605	0.592	0.585	0.588	0.573	0.565	0.559	0.546
19.6	0.680	0.623	0.644	0.641	0.638	0.630	0.624	0.609	0.601
27.0	0.643	0.617	0.620	0.637	0.645	0.624	0.606	0.595	0.587
39.0	0.606	0.581	0.590	0.577	0.576	0.556	0.539	0.518	0.511
62.4	0.620	0.618	0.605	0.598	0.599	0.586	0.576	0.570	0.558
62.4	0.620	0.618	0.605	0.598	0.599	0.586	0.576	0.570	0.558

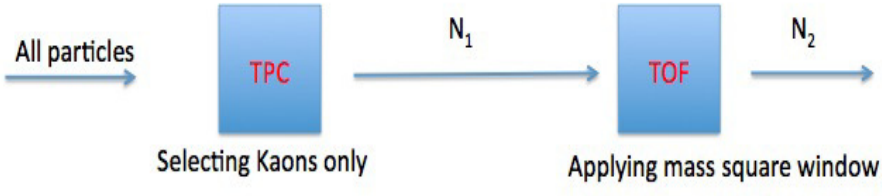

Figure 4.46: (Color online) An example of particle tracks selection for the TOF matching efficiency calculation.

in the Figure 4.46. Then to get the p_T dependent TOF matching efficiency we take the ratio of N_2 with N_1 as,

$$\epsilon_{TOF}(p_T) = N_2/N_1 \tag{4.15}$$

The p_T dependent matching efficiencies for all centrality are shown in the Figure. 4.47.

The matching efficiencies for each centrality are estimated by integrating over p_T.

4.5.4 Final Efficiency Calculation

For the final efficiency calculation we multiply both the efficiency and with the corresponding fitted function, fitted to the corrected p_T spectra and then integrate

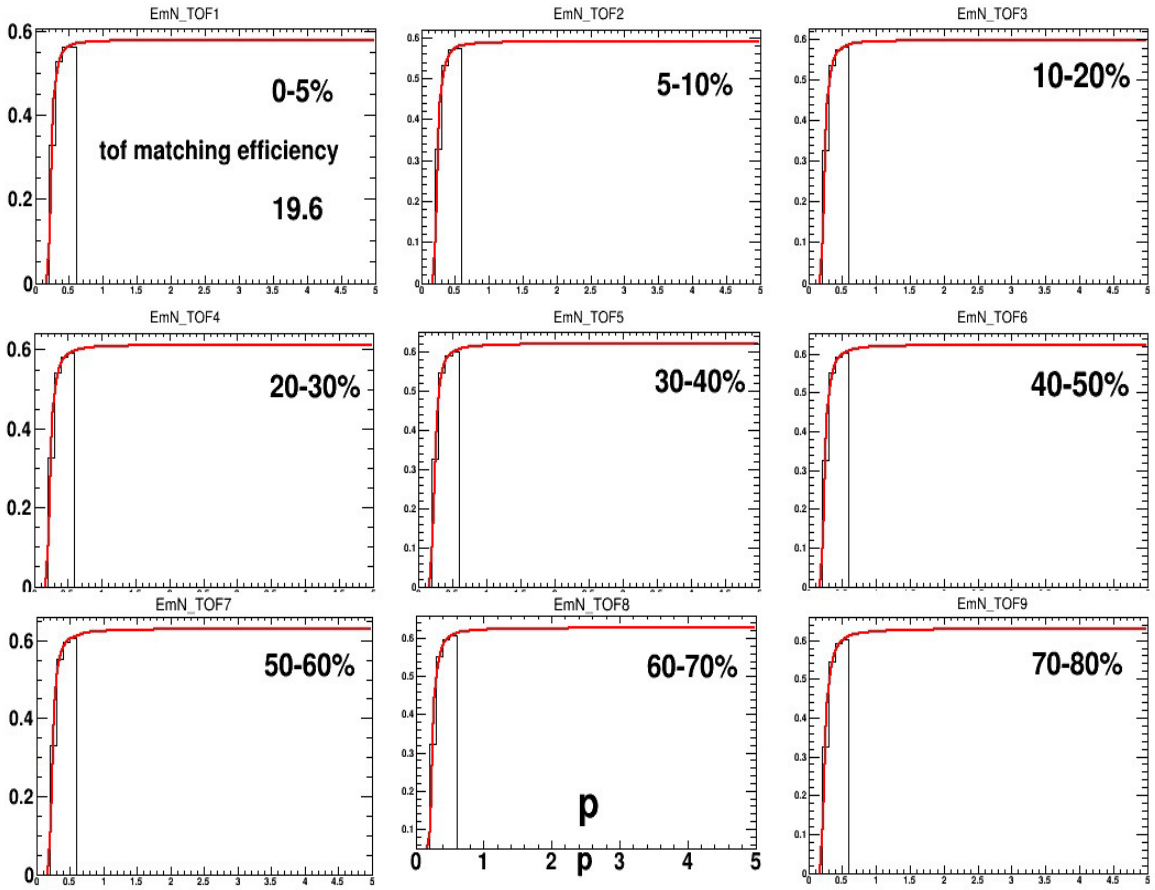

Figure 4.47: (Color online) p_T dependent ToF matching efficiency for $\sqrt{s_{NN}} = 19.6$ GeV for all centrality.

it over the accepted momentum range as,

$$\epsilon_{Final} = \frac{\int_{p_T^{min}}^{p_T^{max}} \epsilon_{TPC}\epsilon_{ToF}(p_T)f(p_T)p_T dp_T}{\int_{p_T^{min}}^{p_T^{max}} f(p_T)p_T dp_T} \tag{4.16}$$

In this net-kaon analysis we have selected two types of PIDs. For each PID the efficiency have been calculated separately. For PID1 we have used the TPC and TOF simultaneously for the whole accepted momentum range, hence the final efficiency is,

$$\epsilon_{Final} = \frac{\int_{p_T^{min}=0.2}^{p_T^{max}=1.6} \epsilon_{TPC}\epsilon_{ToF}(p_T)f(p_T)p_T dp_T}{\int_{p_T^{min}=0.2}^{p_T^{max}=1.6} f(p_T)p_T dp_T} \tag{4.17}$$

The final efficiency estimated from embedding and TOF matching efficiency for PID1 is tabulated below.

Table 4.7: Final efficiency estimated for PID1 from embedding and TOF matching efficiency for $Au + Au$ collisions.

Energy (GeV)	70-80%	60-70%	50-60%	40-50%	40-30%	20-30%	10-20%	5-10%	0-5%
7.7	0.391	0.390	0.381	0.376	0.372	0.373	0.370	0.364	0.349
11.5	0.402	0.41	0.405	0.398	0.392	0.372	0.365	0.358	0.350
19.6	0.428	0.410	0.395	0.388	0.382	0.373	0.365	0.362	0.359
27.0	0.408	0.40	0.395	0.388	0.382	0.373	0.365	0.364	0.359
39.0	0.374	0.365	0.36	0.35	0.342	0.334	0.326	0.318	0.312
62.4	0.3844	0.38	0.374	0.368	0.360	0.352	0.346	0.342	0.336
200	0.3844	0.38	0.374	0.368	0.360	0.352	0.346	0.342	0.336

For the PID2 selection we have not used the TPC and TOF simultaneously for the whole range of momentum, thus the efficiency is not same as before. In this PID selection we have used only the TPC for the momentum range $0.2 \leq p_T \leq 0.4$ and TPC+TOF for momentum range $0.4 \leq p_T \leq 1.6$. Since we have not used TOF in the lower momentum range for $0.2 \leq p_T \leq 0.4$, the final efficiency can be written as,

$$\epsilon_{Final} = \frac{\int_{p_T^{min}=0.2}^{p_T^{max}=0.4} \epsilon_{TPC} f(p_T) p_T dp_T}{\int_{p_T^{min}=0.2}^{p_T^{max}=1.6} f(p_T) p_T dp_T} + \frac{\int_{p_T^{min}=0.4}^{p_T^{max}=1.6} \epsilon_{TPC} \epsilon_{ToF}(p_T) f(p_T) p_T dp_T}{\int_{p_T^{min}=0.2}^{p_T^{max}=1.6} f(p_T) p_T dp_T} \quad (4.18)$$

The final efficiency estimated from embedding and TOF matching efficiency for PID1 is tabulated below.

Since there is no spectra available now for 200 GeV Run10 data, we use 62.4 GeV efficiency value for the correction of 200 GeV results. It is observed that efficiency is very much dependent on multiplicity of the event. As we see in Table 4.7 and Table 4.8 the efficiency increases with the decrease in centrality. This is due to the fact that the tracking is inefficient for higher multiplicity events. However, using the 62.4 GeV efficiency to correct for 200 GeV data would not affect the physics interpretation of the results as the thesis aims to look for the

Table 4.8: Final efficiency estimated for PID2 from embedding and TOF matching efficiency for $Au + Au$ collisions.

Energy (GeV)	70-80%	60-70%	50-60%	40-50%	40-30%	20-30%	10-20%	5-10%	0-5%
7.7	0.426	0.414	0.407	0.409	0.390	0.388	0.382	0.374	0.367
11.5	0.428	0.428	0.410	0.403	0.399	0.386	0.377	0.373	0.362
19.6	0.485	0.447	0.433	0.435	0.426	0.419	0.419	0.405	0.407
27	0.442	0.422	0.419	0.426	0.432	0.416	0.402	0.392	0.395
39	0.414	0.400	0.396	0.389	0.382	0.367	0.362	0.354	0.348
62	0.423	0.423	0.406	0.400	0.396	0.384	0.376	0.372	0.370
62	0.423	0.423	0.406	0.400	0.396	0.384	0.376	0.372	0.370

QCD critical point which cannot be at Baryon chemical potential associated with 200 GeV energy.

The statistical uncertainties for efficiency corrected moments contain higher order moments like 5^{th}, 6^{th} and 8^{th} order which are very difficult to calculate from Delta Theorem since they contain huge number of terms for these higher order calculation. For the statistical error estimation of efficiency corrected moments and their products we used Bootstrap method to avoid the mathematical complexity.

By comparing the efficiencies from Table 4.7 and Table 4.8 one can conclude that the PID2 is more efficient than PID1. We have corrected the results from both of these PIDs with corresponding efficiency values.

Chapter 5

Models and Baseline study

5.1 Introduction

A collision between two heavy ions is governed by many different physical processes. There are processes that govern the initial approach, then the region of overlap and finally the evolution of the system. In our detectors we measure the stable particles and from their energy momentum four vectors and vertex we construct other secondary particles. The topic of this work is to measure the higher moments of the net-kaon multiplicity distribution, which in the proximity of the critical point would interact with the critical mode giving rise to increase in fluctuations. However, there are other physical processes, such as scattering, jet-production, jet-quenching, hadronic interaction, baryon stopping resonance production and decay, thermal equilibrium etc. which can also introduce addiction fluctuation in this higher moment analysis. To understand the QCD critical phenomenon one needs to understand non-critical phenomena from the processes that lead to "background fluctuation". One therefore needs to perform extensive simulations. In this work we have used UrQMD model to understand the fluctuations arising in the absence of critical point. Furthermore, to search for a critical point, it is very important to compare the data with some models which do not include the critical phenomena. The Hadron Resonance Gas (HRG) model which does not contain any critical phenomenon is one of the very promising event

generator in the field of heavy ion collision experiments. The results have been compared with the HRG model predictions.Thus the studied models provides a suitable baseline for this analysis and in the presence of critical point experimental results are expected to show difference from these models.

As mentioned earlier, this study relies on the fact that the net-kaon multiplicity distribution represents net-strangeness to a reasonable approximation. It is thus very important to compare the higher moments of net-kaon with the higher moments of net-strangeness. A study from UrQMD model was performed to see how net-kaon gives proxy for net-strangeness in higher moment analysis.

To understand and study the critical phenomenon it is very important to have a suitable non-critical baseline. It is observed that many background fluctuation results as a Poisson or Negative Binomial (NBD) distribution depending on the collision system and centre of mass energy. For the non-critical baseline the kaon and anti-kaon multiplicity distribution have been studied assuming both Poisson and Negative Binomial Distribution.

5.2 Hadron Resonance Gas Model

The Hadron Resonance Gas (HRG), as mentioned earlier, has been very successful in describing the produced particle multiplicity [125]. In HRG model it is assumed that the system is a mixture of hadrons and resonance gas and they interact at equilibrium. Also near the transition temperature HRG model is useful to estimate the QCD transport coefficients [126] and the chemical equilibrium rates [127]. By tuning the mass of hadrons appropriately to the large quark masses the HRG model agrees well with the lattice QCD calculation of thermodynamic quantities [128, 129].

The produced large particle multiplicity of the baryons, both strange and non-strange in heavy ion collisions can be described by the freeze-out temperature and the baryon chemical potential in terms of the collision energies. In the $T\ Vs.\ \mu_B$ plane the freeze-out curve can be parametrized by fitting the experi-

mental data as [130],

$$T(\mu_B) = a - b\mu_B^2 - c\mu_B^4 \tag{5.1}$$

and,

$$\mu_B(\sqrt{s_{NN}}) = \frac{d}{1 + e\sqrt{s_{NN}}} \tag{5.2}$$

where, a = (0.166 $\pm$ 0.002) GeV, b = (0.139 $\pm$ 0.016) GeV^{-1} and c = (0.053 $\pm$ 0.021) GeV^{-3}. The values of d and e are given in the table 5.1 by parametrization of μ_B, μ_S and μ_Q along the freeze-out curve from the assumption in Equation 5.2 [129].

Table 5.1: The values of d and e from the parametrization of μ_B, μ_S and μ_Q along the freeze-out curve from the assumption in Equation 5.2 [129].

X	d [GeV]	e [GeV^{-1}]
B	1.308(28)	0.273(8)
S	0.214	0.161
Q	0.0211	0.106

The charge and strangeness chemical potential can be parametrized in the same way as is done for baryon chemical potential by including isospin asymmetry and strangeness neutrality in the initial state of $Au + Au$ collisions. The strangeness density vanishes in the initial state, as the ratio of the baryon chemical potential (μ_B) to the strangeness chemical (μ_S) shows very weak dependence on the freeze-out curve as given by the following expression [129],

$$\frac{\mu_S}{\mu_B} \approx 0.164 + 0.018\sqrt{s_{NN}} \tag{5.3}$$

Using Equation 5.1, Equation 5.2 and Equation 5.3 we can calculate the chemical potentials corresponding to the RHIC beam energies. Table 5.2 show the summary of the chemical potential calculated for the RHIC BES data. The first column shows the year of production the second column shows the center of mass energy of the collisions third column shows the data used for this analysis fourth and fifth column show the average baryon chemical potential and average

Table 5.2: The year of production, centre of mass energy, number of events, calculated average baryon chemical potential ($\langle\mu_B\rangle$) and average strangeness chemical potential ($\langle\mu_S\rangle$), for the data sets present in this thesis.

Production year	$\sqrt{s_{NN}}$ (GeV)	Data used $(Million)$	$\langle\mu_B\rangle$ (MeV)	$\langle\mu_S\rangle$ (MeV)
2010	7.70	3.2	421	127
2010	11.5	9.2	316	117
2011	19.6	16.2	206	106
2011	27.0	33.0	156	101
2010	39.0	108	112	97
2010	62.4	47.0	73	94
2010	200.	220	24	90

strangeness chemical potential estimated from the HRG prediction [129].

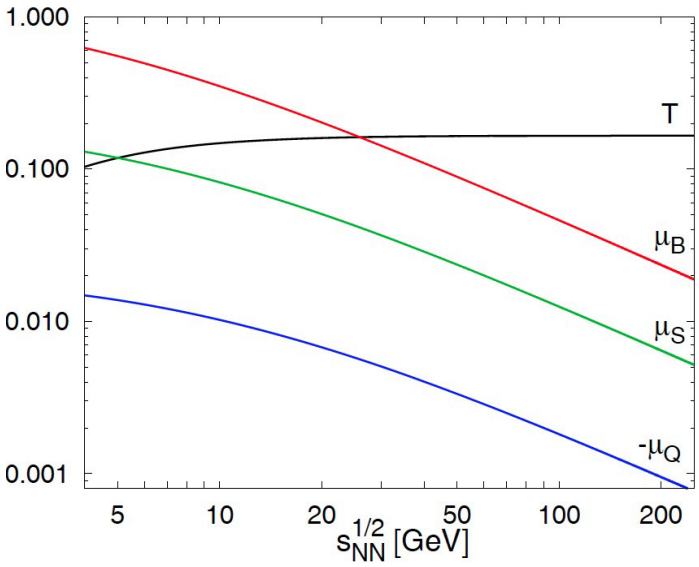

Figure 5.1: (Color online) The baryon chemical potential (μ_B), strangeness chemical potential (μ_S) and charge chemical potential ((μ_Q)) at the chemical freeze-out as a function of centre of mass energy.

Figure 5.1 shows the center of mass energy dependence of the baryon chemical potential (μ_B), strangeness chemical potential (μ_S) and charge chemical potential

(μ_Q) at the chemical freeze-out. The partition function, In the HRG model can be written as,

$$lnZ(T,\mu_B,\mu_S,\mu_Q) = \sum_{i\in mesons} lnZ_i^+(T,\mu_S,\mu_Q) + \sum_{i\in baryons} lnZ_i^-(T,\mu_B,\mu_S,\mu_Q) \quad (5.4)$$

For each particle species with baryon number B_i, strangeness S_i, charge Q_i the partition function is expected as,

$$lnZ^{\pm}(T,V,\bar{\mu}) = \frac{VT}{2\pi^2} g_i m_i^i \sum_{k=1}^{\infty} \frac{(\pm 1)^{k+1}}{k^2} F_2(km_i/T) exp(k\bar{c_i}\bar{\mu}/T) \quad (5.5)$$

where m_i is the mass of the particle species with spin degeneracy g_i, $\bar{c_i} = (B_i, S_i, Q_i)$, $\bar{\mu} = (\mu_B, \mu_S, \mu_Q)$ and F_2 is the modified Bessel function. Then the dimension less pressure which describes thermodynamics of the system can be obtained as,

$$\frac{p}{T^4} = \frac{1}{\pi^2} \sum_i g_i (m_i/T)^2 F_2(m_i/T) \times cosh[(B_i\mu_B + S_i\mu_S + Q_i\mu_Q)/T] \quad (5.6)$$

where the index i stands for all stable hadrons and all resonance particles. Then from this above Equation 5.6 the generalized susceptibilities can be derived as,

$$\chi_q^{(n)} = \frac{\partial^n [p(T,\mu)/T^4]}{\partial(\mu_q/T)^n} \quad (5.7)$$

Therefore as we seen before for any conserved multiplicity distribution the mean, variance, Skewness and kurtosis can be expressed in terms of thermodynamic susceptivity as follow,

$$\begin{aligned} M_q &= \langle N \rangle = VT^3\chi_q^{(1)} \\ \sigma_q^2 &= \langle (\delta N)^2 \rangle = VT^3\chi_q^{(2)} \\ S_q &= \frac{\langle (\delta N)^3 \rangle}{\sigma_q^3} = \frac{VT^3\chi_q^{(3)}}{\sigma_q^3} \\ \kappa_q &= \frac{\langle (\delta N)^4 \rangle}{\sigma_q^4} - 3 = \frac{VT^3\chi_q^{(4)}}{\sigma_q^4} - 3 \end{aligned} \quad (5.8)$$

The higher moments calculation of net-strangeness multiplicity distribution from the HRG model calculation in Ref. [129] is shown in Figure 5.2. In this

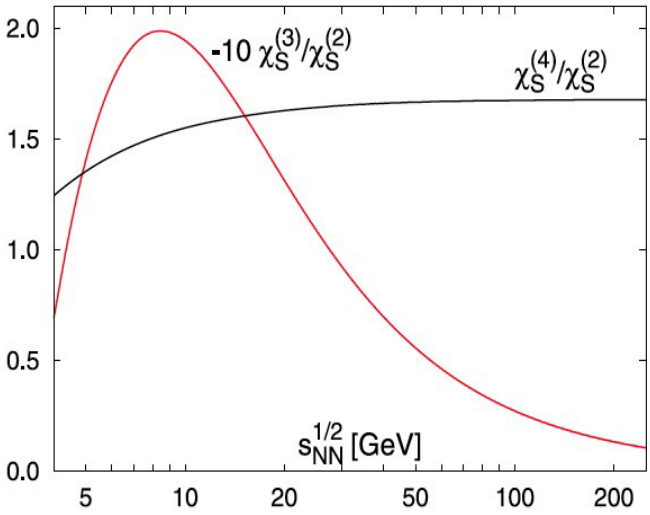

Figure 5.2: (Color online) The ratio of moments, $\chi_S^{(3)}/\chi_S^{(2)}$ and $\chi_S^{(4)}/\chi_S^{(2)}$ of strangeness fluctuations on the freeze-out curve [130].

Figure 5.2 the ratio of susceptibilities $\chi_S^{(3)}/\chi_S^{(2)}$ and $\chi_S^{(4)}/\chi_S^{(2)}$ corresponds to the moment products in the higher moment analysis, $S\sigma$ and $\kappa\sigma^2$ are plotted as a function of the center of mass energy [130].

The variation of $\chi_S^{(3)}/\chi_S^{(2)}$ and $\chi_S^{(4)}/\chi_S^{(2)}$ for different strangeness group from the Ref. [131] as a function of energy are shown in Figure 5.3. The ratio of these susceptibilities are shown for strange particle species containing strangeness $|S|\geq 1$, $|S|= 1$ and $|S|> 1$. The ratio for net-strangeness are also shown by introducing flow in it. For this study the effect of flow is very low and it is 2-4% [131].

The ratio of susceptibilities $\chi_K^{(3)}/\chi_K^{(2)}$ and $\chi_K^{(4)}/\chi_K^{(2)}$ for the net-kaon corresponds to the volume independent moment products in the net-kaon higher moment analysis, $S\sigma$ and $\kappa\sigma^2$ as a function of the center of mass energy are shown in Figure 5.4. The HRG predictions are compared with the Poisson expectation from the PID2 selection.

It is observed that the HRG calculation predict the susceptibility ratio $\chi_K^{(3)}/\chi_K^{(2)}$ higher than the Poison expectation of $S\sigma$, below center of mass energy 62.4 GeV.

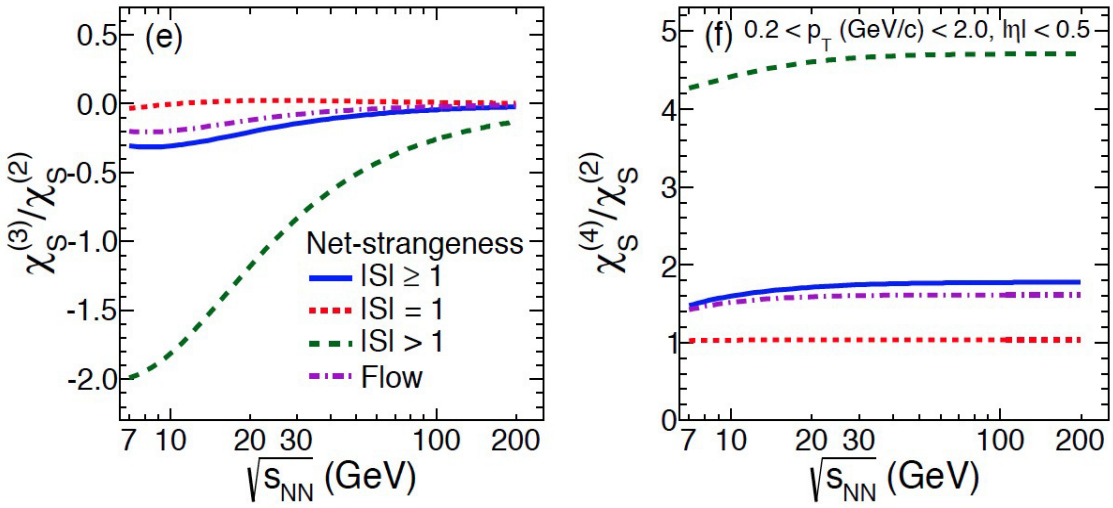

Figure 5.3: (Color online) The ratio of susceptibilities, $\chi_S^{(3)}/\chi_S^{(2)}$ and $\chi_S^{(4)}/\chi_S^{(2)}$ of strangeness fluctuations for different particles contains different number of strangeness in it as a function of center of mass energies [131].

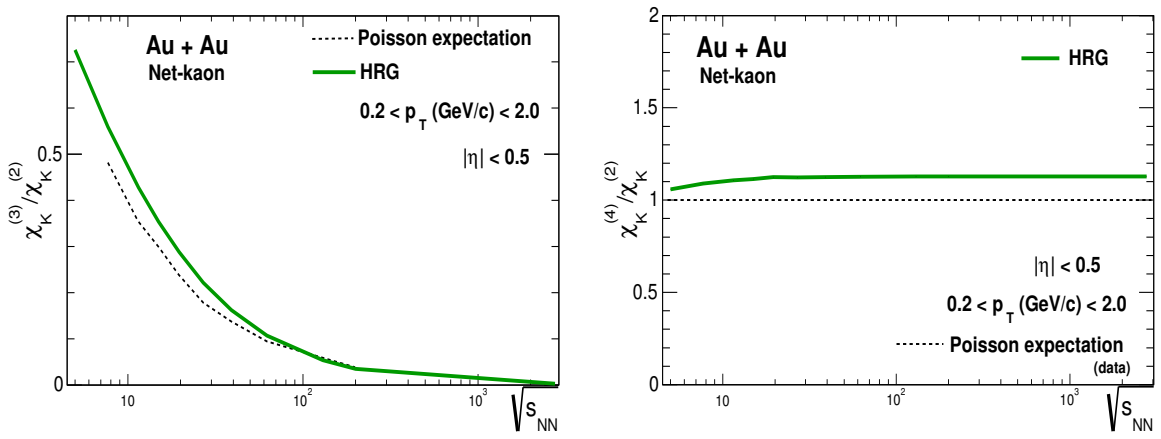

Figure 5.4: (Color online) The ratio of susceptibilities, $\chi_K^{(3)}/\chi_K^{(2)}$ (left panel) and $\chi_K^{(4)}/\chi_K^{(2)}$ (right panel) of net-kaon fluctuation as a function of center of mass energies are shown. The data points taken from Ref.[131].

For the $\chi_K^{(4)}/\chi_K^{(2)}$ susceptibility ratio HRG predicts higher value than the Poison expectation of $\kappa\sigma^2$ in net-kaon analysis for all the center of mass energies.

5.3 UrQMD

The Ultra-relativistic Quantum Molecular Dynamics (UrQMD) model is an integrated Monte Carlo simulation tool for ultra-relativistic heavy ion collisions for $p + p$, $p + A$ and $A + A$ systems [132, 133]. The UrQMD model is a microscopic model which has been now used to simulate in the energy range from Bevalac [134] to RHIC [61] top energies to LHC energies. This model is part of the GEANT4 [135] simulation. The main goals of this model are to understand the following phenomena [133];

- Formation of hot and dense hadronic matter.
- Properties of nucleons, Delta and resonance particles.
- Mesonic particles and anti particles production.
- Hadronic transport phenomena and its creation.
- Strange particle production.
- Electromagnetic probe emissions.

In various hybrid transport phenomena, UrQMD model has also been used as a basic component [136]. Details about this model can be found in the Ref. [137, 138].

Net-Kaon as a Proxy of Net-Strangeness in Higher Moments Analysis

In heavy ion collision experiment it is very difficult to measure on an event-by-event basis all the produced particles which have their origin in the various conserved quantum numbers (baryons(B), strangeness(S) and charge(Q)). Its also could be self defeating in our objective to look for the increase in fluctuation around the critical point as a heterogeneous distribution constructed with different particles would have very large systematic errors. This would make any inference from such a study very difficult. A distribution with only one parti-

cle type (and its anti-particle) is a much better construct for the type of studies carried out in this work. In this work, event-by-event net-kaon multiplicity ($\Delta N_K = N_{K^+} - N_{K^-}$) distribution is measurable for proxy of the net-strangeness. At the critical point, theoretical calculations predicts that ΔN_K fluctuations reflect the singularity of the charge and strangeness number susceptibility.

For the proxy of event by event net-strangeness in higher moments analysis the event by event net-kaon multiplicity number have been calculated. UrQMD model studies have been performed to investigate the validity of the assumption that net-kaons can serve as a proxy for the net-strangeness in the higher moments analysis. We compare the higher moments of net-strangeness with higher moments of all strange particles produced in the events.

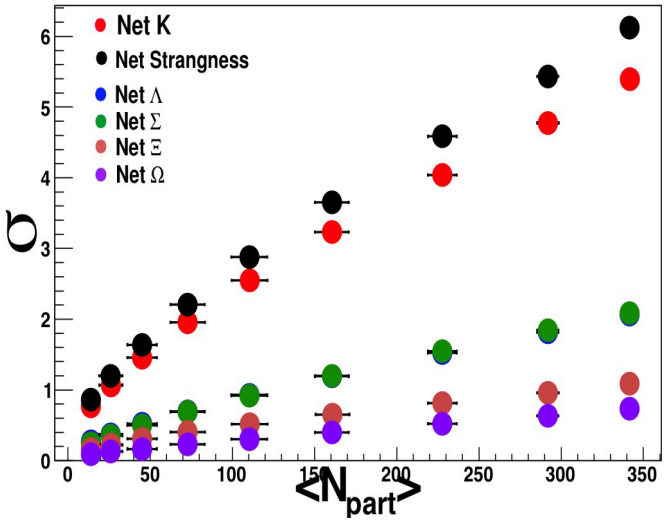

Figure 5.5: (Color online) The 2^{nd} order moment σ, for all strange particle from UrQMD study at $\sqrt{s_{NN}}$ = 39 GeV.

In Figure 5.5 the 2^{nd} order moment σ for all strange particles (red (net-kaon), blue (net-Λ), green (net-Σ), brown (net-Ξ) and purple (net-Ω)) along with the net-strangeness (black) are plotted as a function of average number of participants (or centrality) from UrQMD model for $Au + Au$ collisions at 39 GeV. It is observed that the σ for net-kaon have a similar centrality dependency as in net-

strangeness with almost similar value. The σ of the net-kaon follow the same of net-strangeness better than other strange particles.

The 3^{rd} and 4^{th} order moments of net-strangeness along with all other net strange particles, at $Au + Au$ 39 GeV centre of mass energy in UrQMD model as a function of the centrality are shown in Figure 5.6. The Skewness of net-strangeness has lower value but almost similar centrality dependency compared to that of net-kaon. The net-kaon kurtosis almost overlap to the net-strangeness kurtosis. The Figure 5.6 shows similar effects as in Figure 5.5 as S and κ of net-kaon follow the net-strangeness better than other strange particles. From these higher moments study it is very clear that the higher moments of net-kaon multiplicity distribution give a very good proxy for the net-strangeness moments with respect to other strange particles.

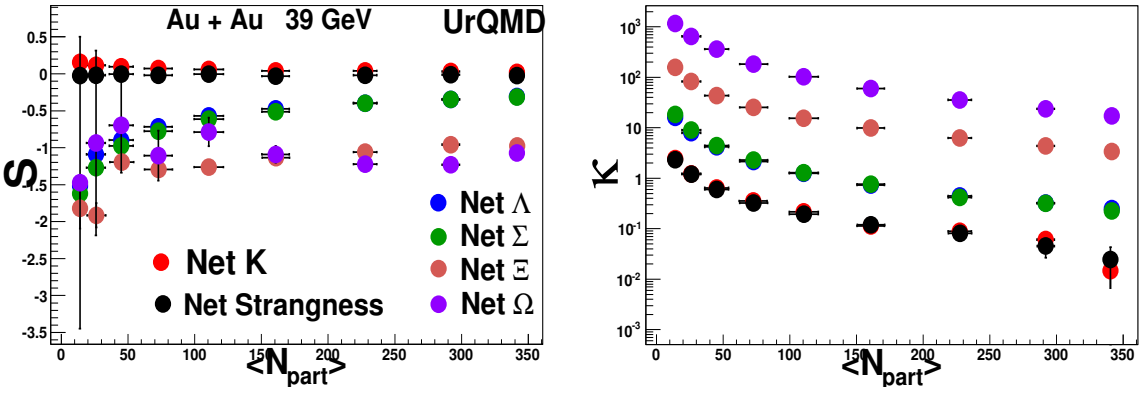

Figure 5.6: (Color online) 3^{rd} and 4^{th} order central moments, S and κ for all strange particle from UrQMD study at $\sqrt{s_{NN}}$ = 39 GeV.

The volume independent moment products $S\sigma$ and $\kappa\sigma^2$ of net-strangeness along with all other strange particles moment as a function of centrality, at $Au + Au$ 39 GeV centre of mass energy from UrQMD model are shown in Figure 5.7. The left panel of Figure 5.7 shows $S\sigma$ as a function of the centrality. The right panel shows that the volume independent moment product $\kappa\sigma^2$ as a function of

centrality.

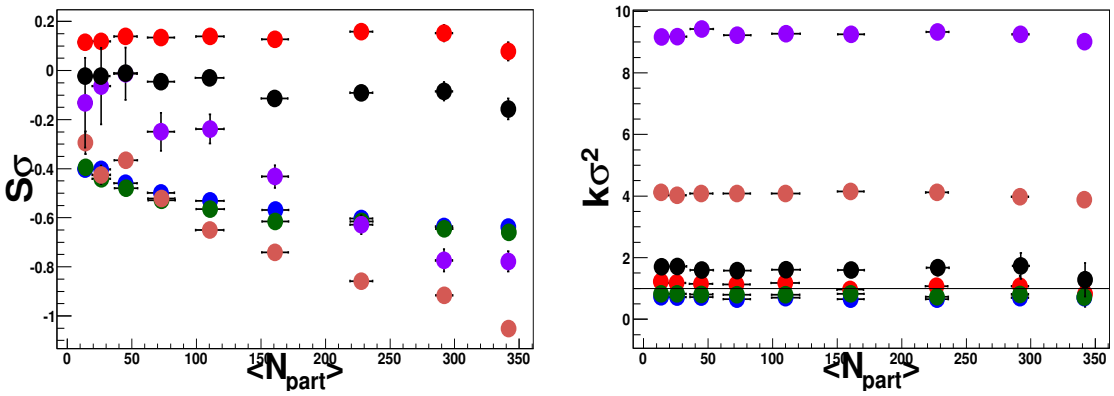

Figure 5.7: (Color online) Volume independent moment products $S\sigma$ and $\kappa\sigma^2$, for all strange particle from UrQMD study at $\sqrt{s_{NN}}$ = 39 GeV.

It is observed that the $S\sigma$ value of net-kaon higher than that of net-strangeness but have similar centrality dependency. This is due to the low Skewness value in the net-strangeness as seen in Figure 5.6. The $\kappa\sigma^2$ of net-strangeness has higher value than that of net-kaon with similar centrality dependency. The difference between these two values are arises due to the wider width of net-strangeness distribution than the net-kaon distribution as it reflected in Figure 5.5.

It is expected that at lower center of mass energies baryon will be dominated. So, to check whether net-kaon gives good proxy for net-strangeness or not in the baryon dominated lower energies, the same study at $\sqrt{s_{NN}}$ = 7.7 GeV was performed. In Figure 5.8, the volume independent moment product $\kappa\sigma^2$ plotted as a function of average number of participants for $Au + Au$ collisions at 7.7 GeV from UrQMD model.

The Figure 5.8 shows the volume independent moment product $\kappa\sigma^2$ of net-kaon has the same centrality dependency as in net-strangeness and numerically also they are very close as well. Therefore, it can be concluded that the net-kaon gives a good proxy for net-strangeness in lower RHIC energies as well.

From this study it can also be concluded that the net-kaon higher moments is a

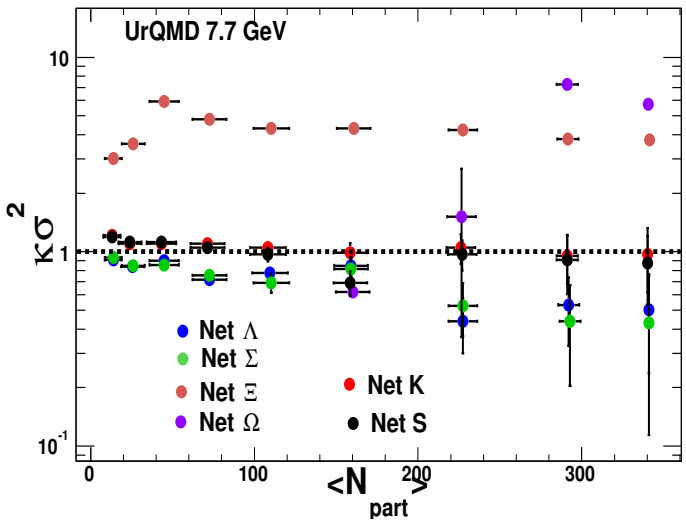

Figure 5.8: (Color online) Volume independent moment product $\kappa\sigma^2$ as a function of centrality, for all strange particles from UrQMD study at $\sqrt{s_{NN}}$ = 7.7 GeV.

very good approximation for the net-strangeness higher moments corresponding at least at the available RHIC energies which this work pertains to. It is therefore expected that the net-kaon will reflect the fluctuation in the net-strangeness due to the critical phenomena in the presence of a CP.

5.4 Baseline Study

In this higher moments analysis, it is assumed that in the presence of a CP the measured moments and their volume independent products will show fluctuation or local change with respect to the center of mass energy. In order to look for the localized change in the measured observable, it is very important to compare them with appropriate baseline [139]. In this net-kaon analysis the kaon and anti-kaon distribution as individual Poisson and Negative Binomial Distribution (NBD) are studied as a baseline.

5.4.1 Poisson Baseline Study

For a large number of statistic many statistical fluctuations or background obey the Poisson statistics. If the signature or the signal for the presence QCD critical point are independent of those backgrounds or statistical fluctuations then the Poisson exception of the measured observable can be studied as the non-critical baseline. Poisson distribution is a Binomial distribution with probability of success $p \to 0$ [140]. Poisson distribution provides discrete probability for certain number of events occurring in a particular time period [141]. Mathematically, the Poisson probability distribution with parameter $\lambda > 0$, can be expressed as:

$$P(k) = \frac{e^{-\lambda}\lambda^k}{k!} \tag{5.9}$$

where k is any random variable of the Poisson distribution [140]. The various moments and the moment products of a single Poisson distribution are:

$$M = \sigma^2 = \lambda \tag{5.10}$$

$$S = \frac{1}{\sqrt{\lambda}} \tag{5.11}$$

$$\kappa = \frac{1}{\lambda} \tag{5.12}$$

$$\kappa\sigma^2 = S\sigma = 1 \tag{5.13}$$

These expressions can be used to calculate the moments and moment products for a particle multiplicity distribution assuming the distribution is a Poisson. The net-kaon analysis is associated with two particle multiplicity distributions, kaon and anti-kaon distribution. Each of these multiplicity distribution are assumed to be Poisson to study the Poisson expectation value. To get the net-kaon multiplicity distribution anti-kaon multiplicity distribution is subtracted from the kaon multiplicity distribution. The difference of two Poisson distribution is called "Skellam" distribution [142]. For a Skellam distribution the probability density function for mean value of two Poisson distributions μ_1 and μ_2, can be expressed

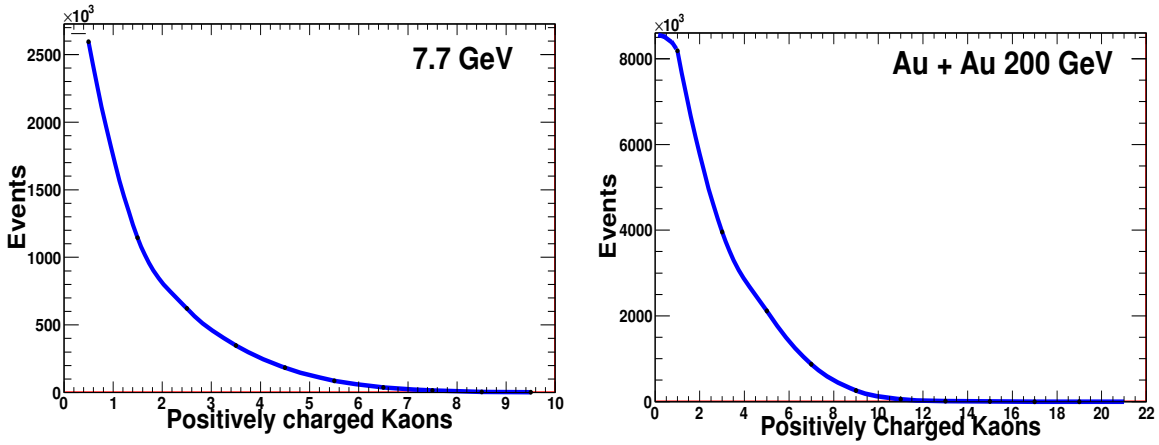

Figure 5.9: (Color online) Positively charged kaon distribution for $\sqrt{s_{NN}}$ = 7.7 and 200 GeV.

as,

$$P(N) = e^{-(\mu_1+\mu_2)} \left(\frac{\mu_1}{\mu_2}\right)^{k/2} I_{|k|}(2\sqrt{\mu_1\mu 2}) \tag{5.14}$$

where, N is the count difference between the two Poisson distribution and $I_k(z)$ is the modified Bessel function for the first kind.

For this analysis the Poisson expectation have been studied as a non-critical base line assuming both of the kaon and anti-kaon multiplicity distribution for a certain centrality bin, is a Poisson distribution.

Hence, the net-kaon distribution is taken as a Skellam distribution, which serve as one of the non-critical baseline for this analysis. For the Skellam distribution the moments are,

$$M = \mu_1 - \mu_2 \tag{5.15}$$

$$\sigma = \sqrt{\mu_1 + \mu_2} \tag{5.16}$$

$$S = \frac{\mu_1 - \mu_2}{(\mu_1 + \mu_2)^{3/2}} \tag{5.17}$$

$$\kappa = \frac{1}{\mu_1 + \mu_2} \tag{5.18}$$

Hence the volume independent moment products will be.

$$S\sigma = \frac{\mu_1 - \mu_2}{\mu_1 + \mu_2} \tag{5.19}$$

$$\kappa\sigma^2 = 1 \tag{5.20}$$

For both Poisson and Skellam distributions $\kappa\sigma^2 = 1$, while volume independent moments product $S\sigma$ changed from unity to the value which describe asymmetry between μ_1 and μ_2 of the Poisson distributions to the Skellam distribution. Assuming the net-kaon distribution as a Skellam distribution the four moments (Mean (M), Sigma (σ), Skewness (S), kurtosis (κ)) and volume independent moment products ($S\sigma$ and $\kappa\sigma^2$) have been studied. The four moments are shown in Figure 5.10. This moment are calculated from the PID2 selection. It is observed

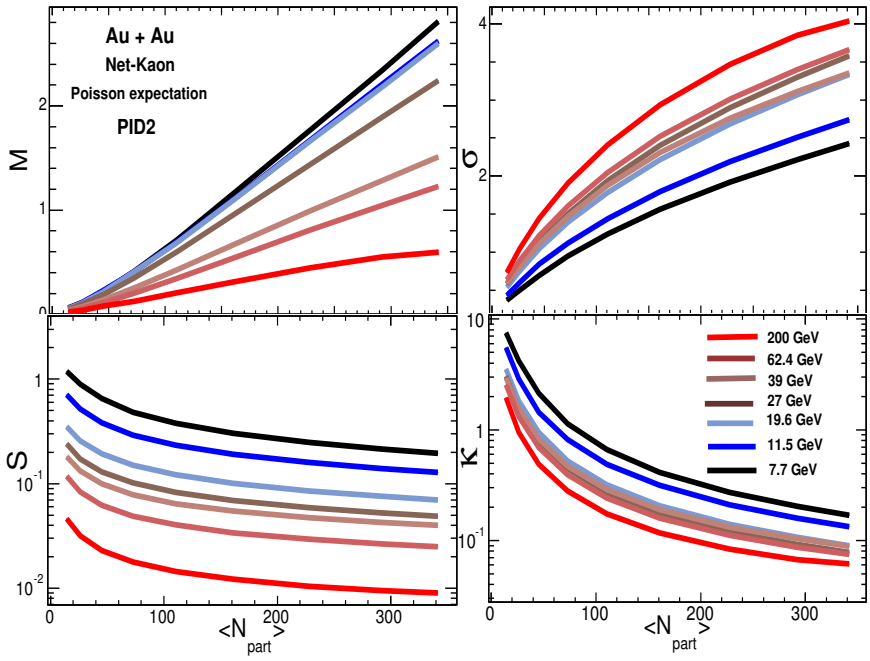

Figure 5.10: (Color online) Skellam expected moments from net-kaon (ΔN_K) multiplicity distribution calculated at $\sqrt{s_{NN}}$ = 7.7 - 200 GeV.

that the volume independent moment product $\kappa\sigma^2 = 1$, for the Skellam distribu-

tion. The volume independent moments product $S\sigma$ as function of centrality for the Skellam expectation shown in Figure 5.11 for all BES energies. It shows that

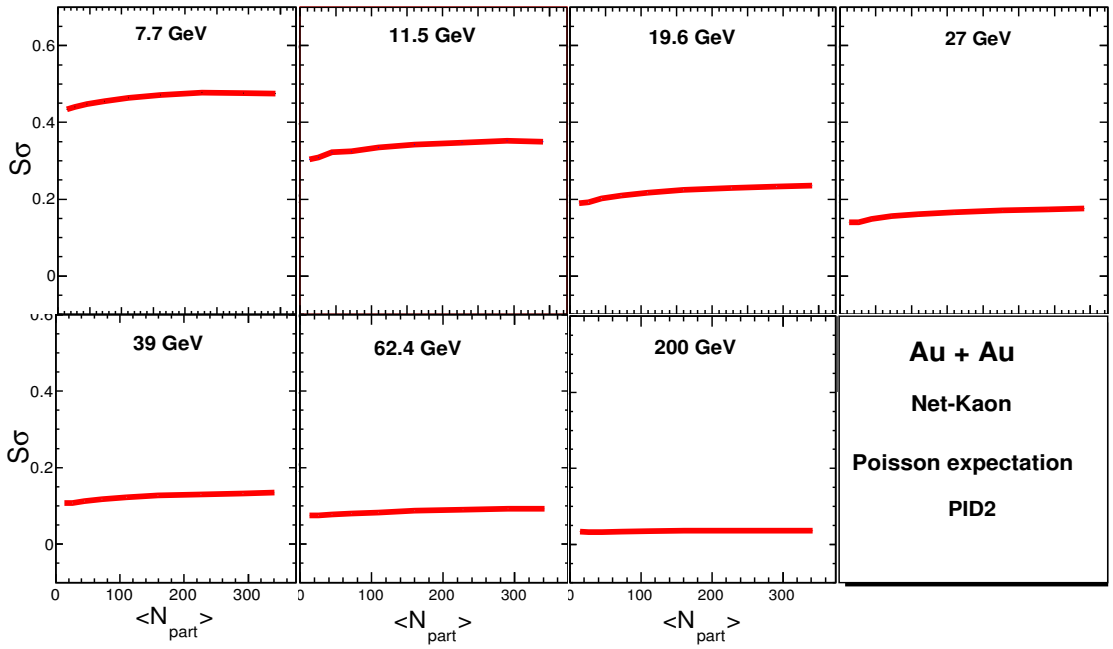

Figure 5.11: (Color online) Skellam expected $S\sigma$ from net-kaon (ΔN_K) multiplicity distribution calculated at $\sqrt{s_{NN}}$ = 7.7 - 200 GeV.

volume independent moments product $S\sigma$ have a very low increasing centrality dependency from peripheral to central collisions. $S\sigma$ decreases with increasing center of mass energy. The experimental results have been compared in the next chapter with these Poison expectation. It is expected that for any deviation in the experimental measurement with respect to these expectation may indicates the dynamical fluctuation within the produced system in heavy ion collisions.

5.4.2 Negative Binomial Distribution Study

It has been observed that many statistical fluctuations follow Negative Binomial Distribution (NBD) [143]. The NBD is same as Binomial distribution with variance greater than the mean. The Poisson distribution is a limiting case of the NBD where the variance becomes equal to the square root of mean. Its a discrete probability distribution and the probability p of success and r as the probability

to fail, the distribution can be expressed as,

$$f_{NBD}(k;r,p) = \binom{k+r-1}{k} p^r (1-p)^k \tag{5.21}$$

where, k represents the failure before r^{th} success.

In the net-kaon distribution the mean and the variance are not equal but similar. If the variance is less (greater) than the mean then the baseline is Binomial (Negative Binomial). If the variance becomes equal to the mean, then the baseline is Poisson type. In other words we can say, NBD is a alternative for Poisson distribution for $r \to \infty$. The parameter r also controls deviation from Poisson. Thus NBD is a very good alternative to the Poisson distribution. For a NBD distribution with mean μ, the probability defined as $p = \frac{\mu}{\sigma^2}$. Then the cumulants of the NBD distribution can be expressed as,

$$c_1 \sim \mu = \frac{r(1-p)}{p} \tag{5.22}$$

$$c_2 \sim \sigma^2 = \frac{r(1-p)}{p^2} \tag{5.23}$$

$$c_3 = \frac{r(p-1)(p-2)}{p^3} \tag{5.24}$$

$$c_4 = \frac{r(1-p)(6-6p+p^2)}{p^4} \tag{5.25}$$

To study the NBD expectation it is assumed that for a certain centrality bin the kaon and anti-kaon multiplicity distribution are individually NBD. If the n^{th} order cumulants from kaon multiplicity distribution and anti-kaon multiplicity distribution are C_n^+ and C_n^-, then the n^{th} order cumulant for net-kaon distribution is,

$$C_n = C_n^+ + (-1)^n C_n^- \tag{5.26}$$

In Figure 5.12 and Figure 5.13 the NBD expectation of volume independent moment products $S\sigma$ and $\kappa\sigma^2$ are shown as a function of collision centrality for all BES energies. These moment products calculated assuming the kaon and anti-

kaon distribution for a given centrality follow the NBD. It is observed that $S\sigma$

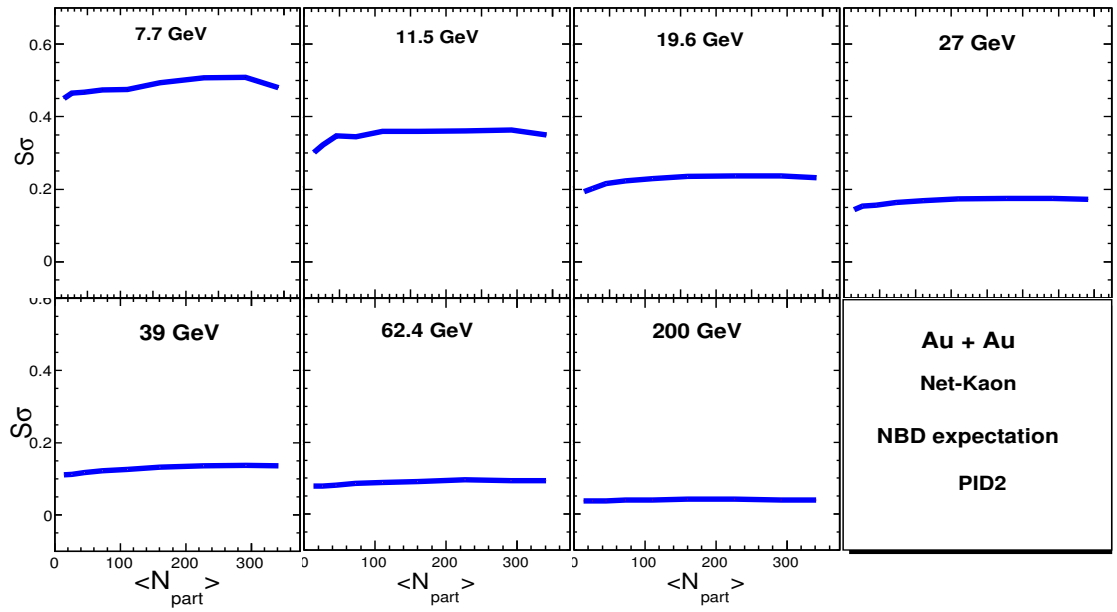

Figure 5.12: (Color online) NBD expected $S\sigma$ from net-kaon (ΔN_K) multiplicity distribution calculated at $\sqrt{s_{NN}}$ = 7.7 - 200 GeV.

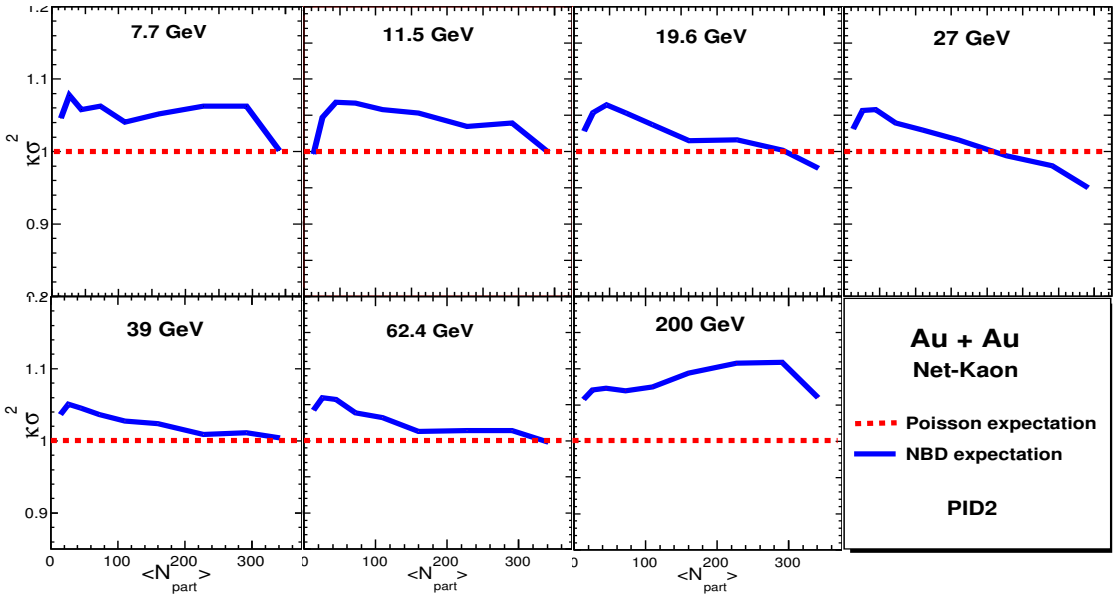

Figure 5.13: (Color online) Skellam and NBD expected $\kappa\sigma^2$ from net-kaon (ΔN_K) multiplicity distribution calculated at $\sqrt{s_{NN}}$ = 7.7 - 200 GeV.

have a very low increasing centrality dependency from peripheral to central col-

lisions. $S\sigma$ decreases with increasing center of mass energy. The volume independent moment product $\kappa\sigma^2$ has a very small centrality dependency which is within 10%. These expectation compared with the experimental data along with the Poison expectation in the next chapter.

5.5 Central Limit Theorem Study

In the theory of probability the Central Limit Theorem (CLT) is a fundamental theorem [144]. The CLT states that, for a large number of independent random and identically distributed variables with well defined mean and variance the sum will be approximately normal/Gaussian, despite of the underlying distributions [144, 145]. The Poisson and Binomial (both BN and NBD) distribution approach a Gaussian distribution under certain conditions or limits.

For a probability distribution, $f_i(x_i)$ of a random variable $x_i, i = 1, 2, 3, ..., n$, with mean M_i and variance σ^2, the average of the random variable, $\bar{x} = \frac{\sum_i x_i}{n}$, for each $f_i(x_i)$ distribution tends to Gaussian in the limit $n \to \infty$ [146]. The Gaussian distribution has mean and variance as,

$$\begin{aligned} M(\bar{x}) &= \frac{\sum_i M_i}{n} \\ \sigma^2(\bar{x}) &= \frac{\sum_i \sigma_i^2}{n} \end{aligned} \tag{5.27}$$

Therefore, assuming the mean and the variance is same for all random variable x_i, one can write,

$$\begin{aligned} M_i &= nM(\bar{x}) \\ \sigma_i^2 &= n\sigma^2(\bar{x}). \end{aligned} \tag{5.28}$$

Similarly, we can show for the higher order moments as,

$$\begin{aligned} S_i &= \frac{1}{\sqrt{n}} S(\bar{x}) \\ \kappa_i &= \frac{1}{n}\kappa(\bar{x}) \end{aligned} \tag{5.29}$$

In heavy ion collision experiments, the particle multiplicity distributions are independent, random and identically distributed. The CLT can therefore be applied in this analysis to the net-kaon multiplicity distribution and can be used to understand the evolution of the centrality. The CLT helps one in understanding the dependence of the higher moments on the number of participating nuclei. In this net-kaon analysis, centrality is defined by the average number of participating nuclei, $< N_{part} >$ and can be considered as the volume of the system or the number of sample size. By considering $< N_{part} >$ as independent emission source of particle production irrespective of parent distribution the moments can be written as follows,

$$\begin{aligned} M &\propto < N_{part} > \\ \sigma &\propto \sqrt{< N_{part} >} \\ S &\propto \frac{1}{\sqrt{< N_{part} >}} \\ \kappa &\propto \frac{1}{< N_{part} >} \end{aligned} \tag{5.30}$$

The CLT fitting of these higher moments give information of the multiplicity distribution and the geometry produced in the collision. As the system size increases with decreasing centrality and increasing centre of mass energy the multiplicity distribution as expected tend towards the Gaussian distribution as the particles are coming from large independent emission sources.

In Figure 5.14-5.17 the efficiency uncorrected moments are fitted with the CLT expected dependance. These moments are calculated from the PID1 selection. The efficiency corrected moments from PID1 and PID2 selection fitted with CLT are discussed in the next chapter.

In the most central collision, the number of participating nuclei (N_{part}) increases and the system size as well. For the peripheral collision the number of participating nuclei decreases, hence the system size. From Equation 5.30 and Figure 5.14-5.17 it is observed that these higher moments are system size/volume dependent. To cancel out these volume dependency different volume independent moment products can be constructed as $S\sigma$, M/σ^2, $\kappa\sigma^2$, $\kappa\sigma/S$, etc..

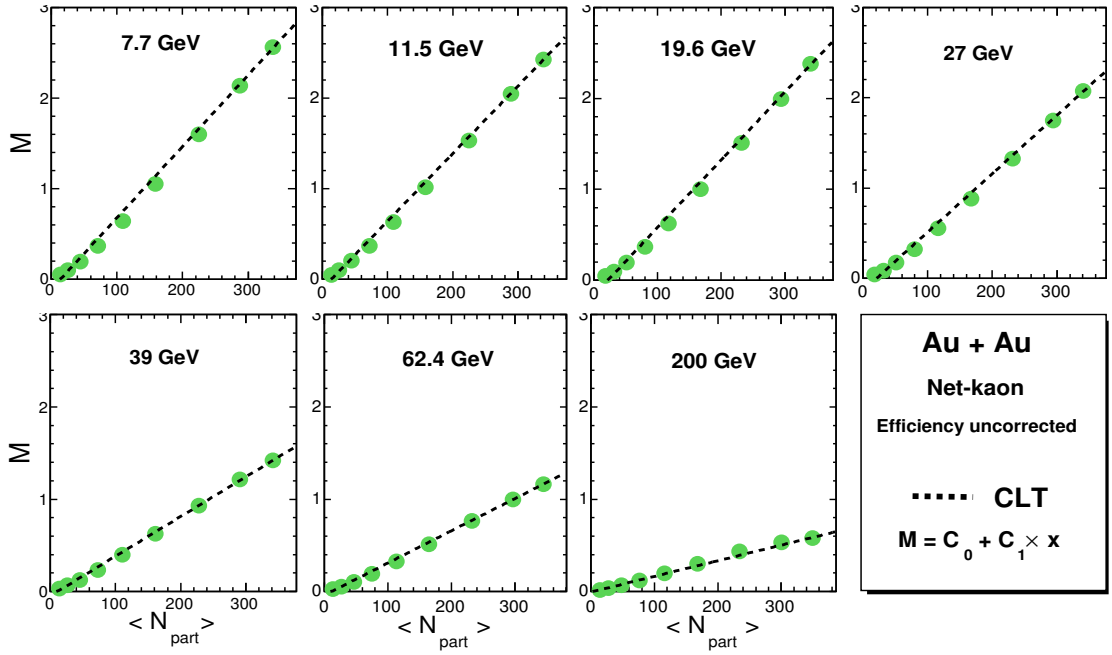

Figure 5.14: (Color online) Efficiency uncorrected mean (M) as a function of average number of participating nuclei fitted with the CLT expectation (Black dotted lines) for $\sqrt{s_{NN}}$ = 7.7 - 200 GeV. The results are from PID1 selection.

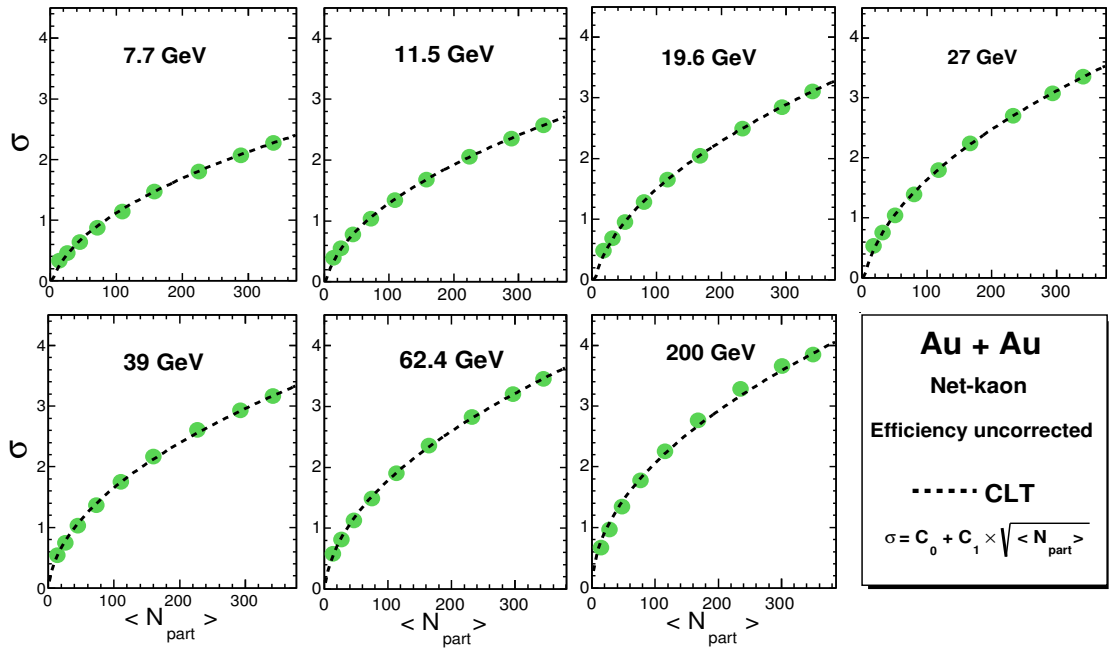

Figure 5.15: (Color online) Efficiency uncorrected sigma (σ) as a function of average number of participating nuclei fitted with the CLT expectation (Black dotted lines) for $\sqrt{s_{NN}}$ = 7.7 - 200 GeV. The results are from PID1 selection.

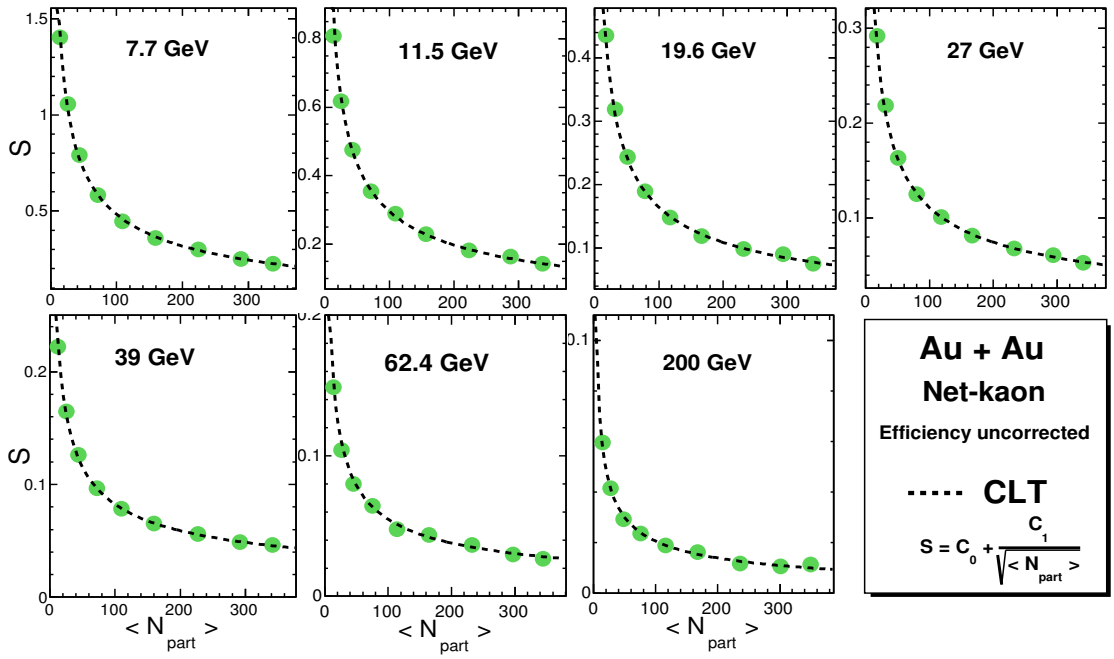

Figure 5.16: (Color online) Efficiency uncorrected Skewness (S) as a function of average number of participating nuclei fitted with the CLT expectation (Black dotted lines) for $\sqrt{s_{NN}}$ = 7.7 - 200 GeV. The results are from PID1 selection.

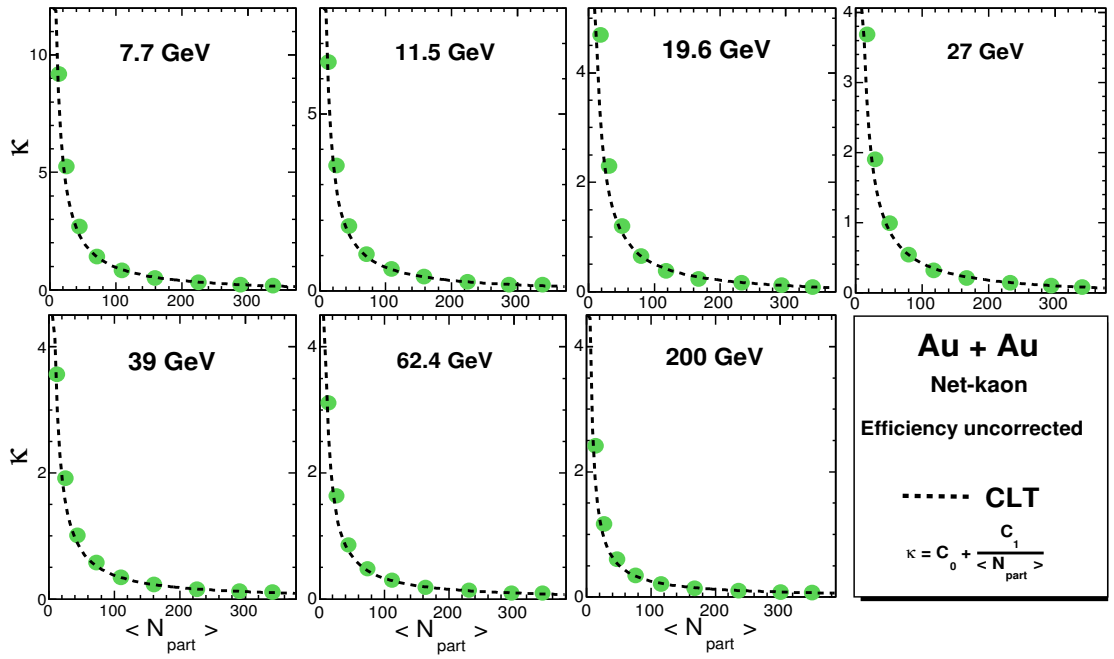

Figure 5.17: (Color online) Efficiency uncorrected kurtosis (κ) as a function of average number of participating nuclei fitted with the CLT expectation (Black dotted lines) for $\sqrt{s_{NN}}$ = 7.7 - 200 GeV. The results are from PID1 selection.

Chapter 6

Results and Discussion

In heavy ion collision experiments, the path to obtaining physics results from the data collected in these collisions is long and arduous. As discussed in Chapter 4, it involves many corrections and also certain assumptions. For instance, experimentally measuring conserved quantum numbers such as baryons (B), strangeness (S) and charge (Q) may not be possible in any experiment. One therefore on the basis of simulations, could establish that measuring the number of protons and anti-proton could serve a proxy for baryon number, similarly to obtain the strangeness quantum number one could use the number of kaons and anti-kaons. Likewise for total charge one could use the sum total of pions, kaons, protons and their anti-particles. The higher moments analysis for these identified particles one requires a pure data sample. As in the $Au + Au$ collision systems the initial state is baryon (or proton) dominated the higher moment results from experimental measurements could be biased for net-proton and net-charge analysis. However, the event by event measured kaons are purely from the system created by $Au + Au$ collisions and are thus not from the initial states. We have also established using simulations, that in our analysis net-kaon gives a good proxy for net-strangeness (a conserved quantum number). It is expected that if the freeze-out of the system created by colliding Au nucleus, pass through the critical region of phase space the conserved quantities and hence their measured proxies will also reflect associated fluctuations.

In this chapter the results from net-kaon higher moments analysis are presented. The results presented in this chapter are obtained from the data measured by the STAR experiment of RHIC at the Brookhaven National Laboratory. For this analysis STAR Run10 and Run11 data have been used from the $Au + Au$ collision system with center of mass energy $\sqrt{s_{NN}}$ = 7.7, 11.5, 19.6, 27, 39, 62.4 and 200 GeV. The data were taken by the STAR experiment in 2010 and 2011 as a part of the Beam Energy Scan (BES) program at RHIC. In this chapter, we first discuss the event by event kaon and anti-kaon distribution, followed by the net-kaon distribution. Then we discuss the various moments and moment products as a function of centrality. The volume independent moment products as a function of center of mass energy for the top 0-5% central $Au + Au$ collisions are presented in the following sections.

As discussed in Chapter 4, various methods have been used to calculate the statistical errors for this analysis. However, in this chapter all statistical errors presented have been calculated from the Bootstrap method. The systematics have been studied for this analysis by varying the experimentally accepted basic track quality parameters used to select the data sample. The systematic errors arise due to finite experimental acceptance and have been corrected in the final results. The detector efficiency correction method have been developed and implemented in the results obtained from this analysis.

6.1 Kaon and Anti-Kaon Distribution

The most important part of this analysis is to identify the charged kaons as the analysis is totally dependent on the number of measured kaons and anti-kaons. The analysis presented in this thesis was carried out with the event-by-event identified positively charged kaons(K^+) and negatively charged kaons(K^-) in full azimuthal coverage. The kaons are selected from the collisions occurring within $50\ cm$ of the TPC center along the beam line for center of mass energy 7.7 and 11.5 GeV and within 30 cm for rest of the energies. The kaons and anti-

kaons are identified at mid-rapidity ($|\eta|< 0.5$) and within the momentum range $0.2 < p_T < 1.6\ GeV/c$ by using the ionization energy loss (dE/dx) information of charged particles measured by the TPC along with the mass information from TOF. In Figure 6.1 the K^+ (blue markers) and K^- (black markers) multiplicity

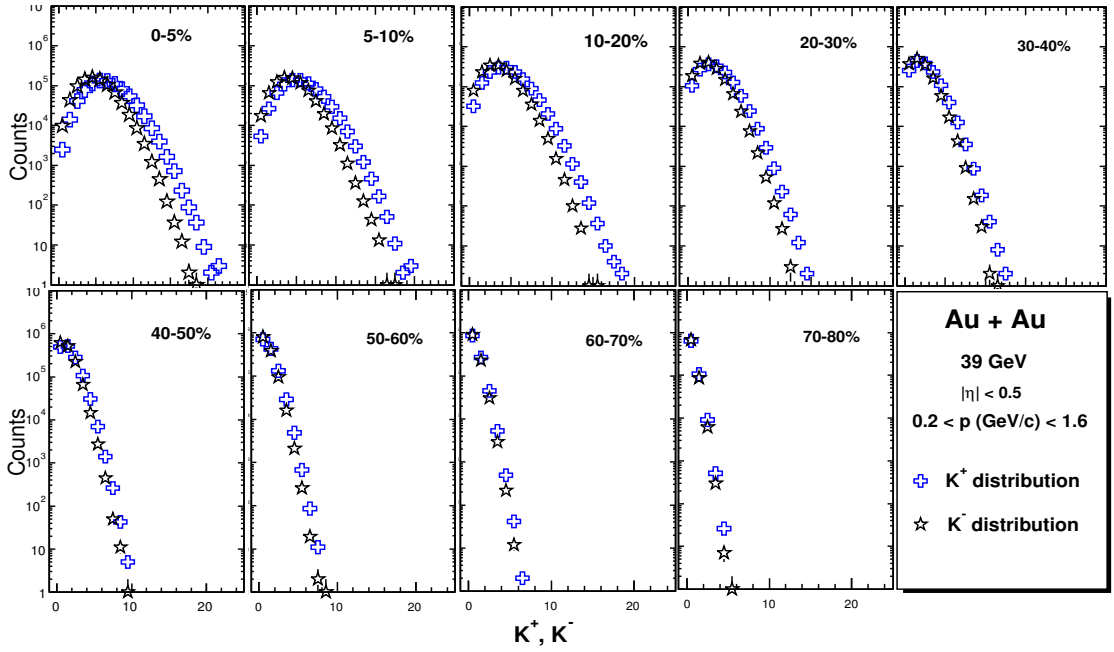

Figure 6.1: (Color online) K^+ and K^- multiplicity distribution in $Au + Au$ collisions at $\sqrt{s_{NN}} = 39\ GeV$ for various collision centralities at mid-rapidity ($|\eta|< 0.5$).

distribution in $Au + Au$ collisions at $\sqrt{s_{NN}} = 39\ GeV$ are shown. The K^+ and K^- multiplicity distribution are shown for nine different collisions centralities defined using MC Glauber model. Both of the K^+ and K^- distributions have larger width in the central collisions as compared to the peripheral collisions. These distributions are raw distributions and not corrected for the detector efficiency and centrality bin width effects. The difference between K^+ and K^- distributions for each centrality increases from peripheral to central collisions.

6.2 Event by Event Net-Kaon Distribution

The event-by-event raw net-kaon multiplicity distribution is obtained by taking difference between the number of kaons and anti-kaons measured in each event. If K^+ and K^- are the number of kaons and anti-kaons respectively then the net-kaon is defined as,

$$\Delta N_K = K^+ - K^- \tag{6.1}$$

These distributions are tagged as "raw" distributions since they are not corrected for the detector efficiency and centrality bin width effects. In Figure 6.2 the raw ΔN_K multiplicity distribution in $Au+Au$ collisions at $\sqrt{s_{NN}} = 39\ GeV$ for various collision centralities are shown. The centrality dependency of these net-kaon distribution shows wider distribution in central collisions as compared to peripheral collisions.

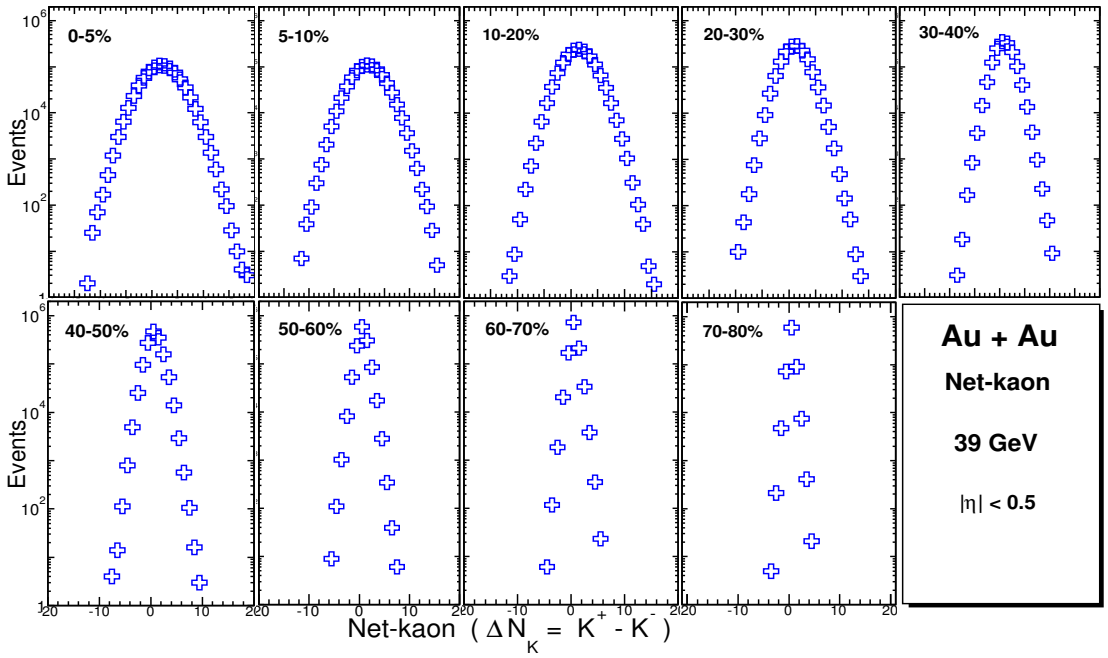

Figure 6.2: (Color online) ΔN_K multiplicity distribution in $Au + Au$ collisions at $\sqrt{s_{NN}} = 39\ GeV$ for various collision centralities at mid-rapidity ($|\eta| < 0.5$). The statistical errors are shown.

Typical ΔN_K distributions from 70% to 80% (black markers), 30% to 40% (blue markers) and 0% to 5% (red markers) centralities in $Au + Au$ collision at $\sqrt{s_{NN}} =$

7.7 - 200 GeV are shown in Figure 6.3.

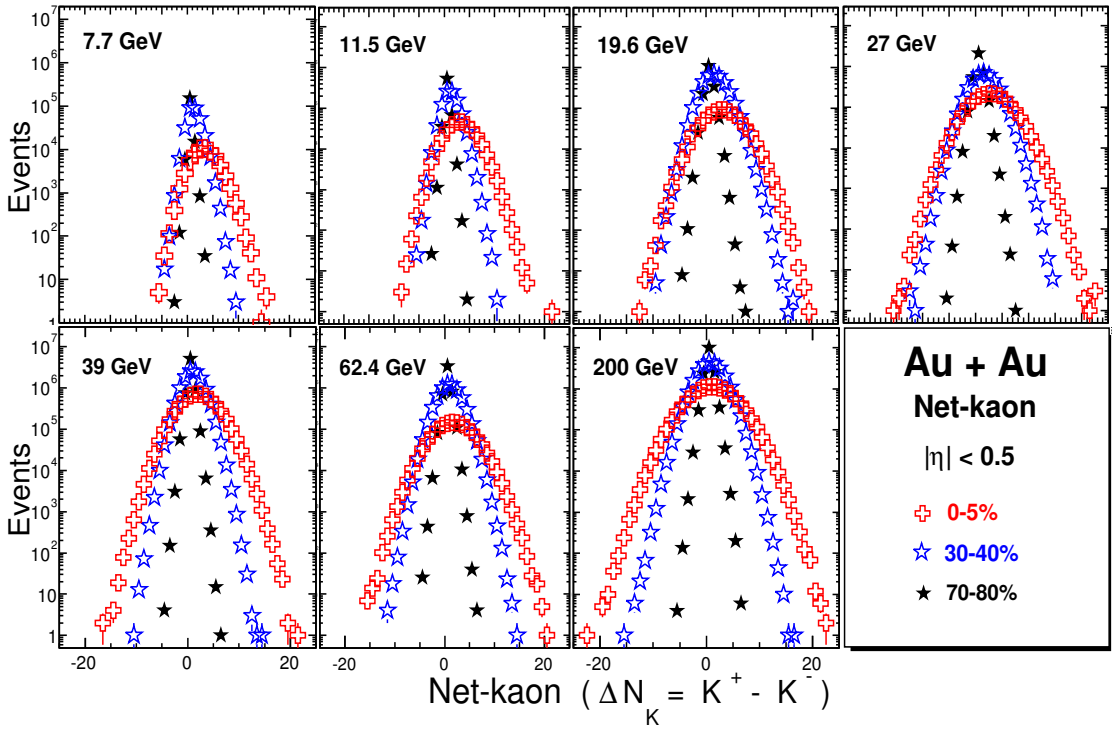

Figure 6.3: (Color online) ΔN_K multiplicity distribution in $Au + Au$ collisions at $\sqrt{s_{NN}} = 7.7$ to 200 GeV for various collision centralities at mid-rapidity ($|\eta| < 0.5$). The statistical errors are shown.

It is observed that the central collision has much wider distribution than the peripheral collisions for all the BES energies. As the center of mass energy increases, the width of the distribution increases for all centralities. With increase in center of mass energy the distribution becomes more symmetric and looks like a normal distribution. This is an indication of bigger system size with higher center of mass energies as expected from Central Limit Theorem (CLT). It is also observed that the mean of the distribution shifted towards zero as the center of mass energy increases towards the higher BES energies. This indicates that the number of produced kaons and anti-kaons becomes similar in the higher energies. The moments calculated from these ΔN_K distributions need to take proper care for the detector efficiency and centrality bin width effects as these distributions are not corrected for those effects.

6.3 Centrality Dependency of the Moments

The shape of ΔN_K distributions can be characterized by its various moments. The four moments Mean (M), Sigma (σ), Skewness (S), and kurtosis (κ) of the ΔN_K distributions at various collision energies in $Au + Au$ collision systems has been extracted after taking care of the bin width effects. In Figure 6.4 and Figure 6.5 the efficiency uncorrected moments as a function of average number of participants ($\langle N_{part} \rangle$) are shown. They have been extracted from PID1 and PID2 selection in $Au + Au$ collisions at $\sqrt{s_{NN}} = 7.7$, 11.5, 19:6, 27, 39, 62.4, and 200 GeV. The efficiency corrected moments form PID1 and PID2 selection as a function of $\langle N_{part} \rangle$ are shown in the Figure 6.6 and 6.7 respectively. These $\langle N_{part} \rangle$ are calculated from MC Glauber model and provides information about the evolution of the produced system volume and centrality. The statistical errors on M, σ, S, and κ are shown as bars and the systematic errors are shown as cross bars for all centralities in $Au + Au$ collisions and at all center of mass energies.

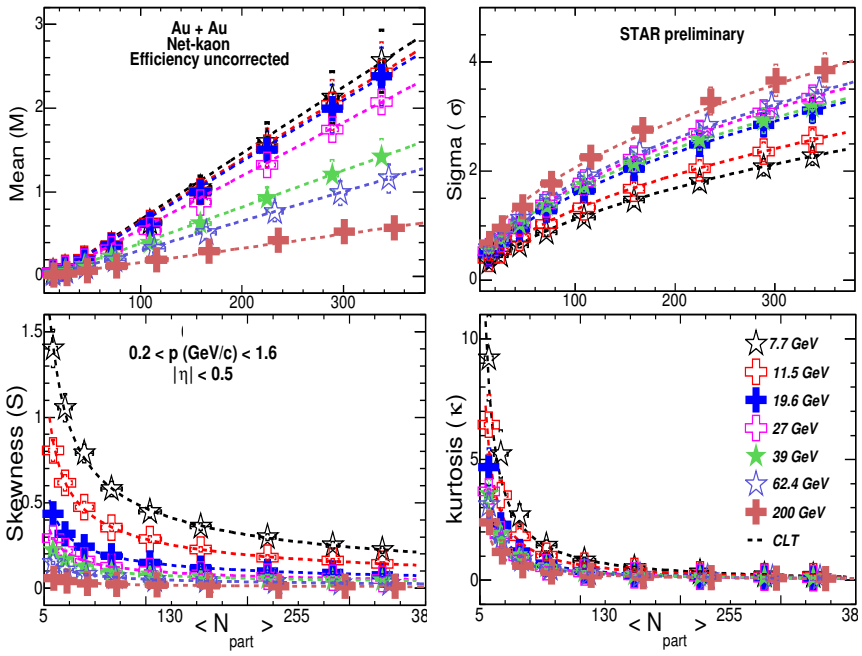

Figure 6.4: (Color online) Efficiency uncorrected moments of ΔN_K distributions as a function of $\langle N_{part} \rangle$ for $Au + Au$ collisions at $\sqrt{s_{NN}} = 7.7$, 11.5, 19.6, 27, 39, 62.4, and 200 GeV. These moments are calculated from the PID1 selection. The dashed lines are the expected values from the central limit theorem.

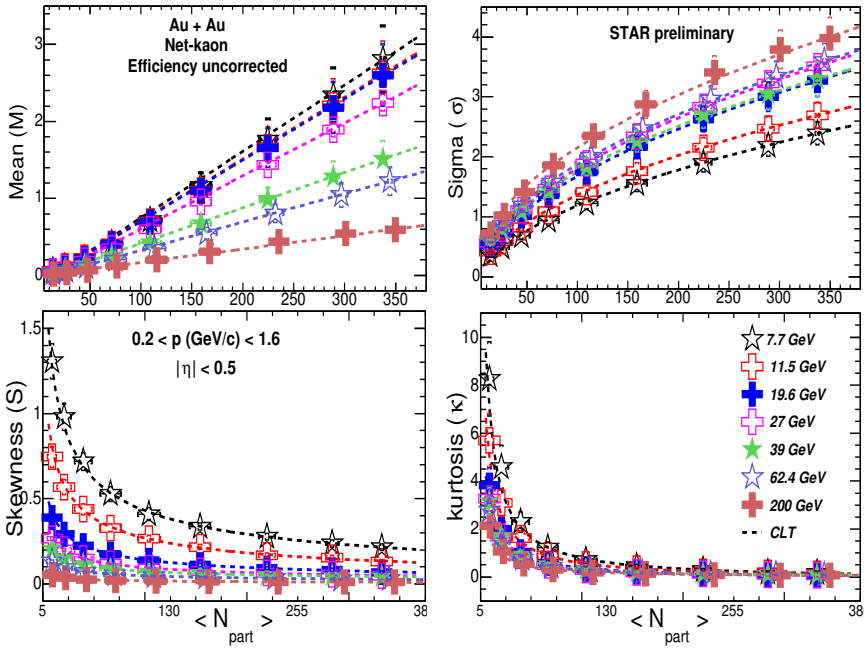

Figure 6.5: (Color online) Efficiency uncorrected moments of ΔN_K distributions as a function of $\langle N_{part} \rangle$ for $Au + Au$ collisions at $\sqrt{s_{NN}}$ = 7.7, 11.5, 19.6, 27, 39, 62.4, and 200 GeV. These moments are calculated from the PID2 selection. The dashed lines are the expected values from CLT.

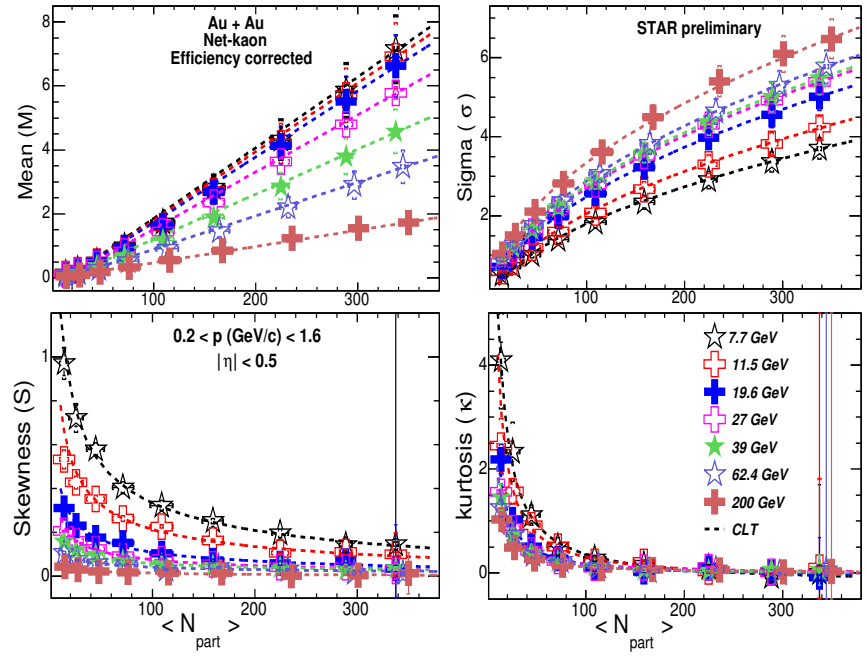

Figure 6.6: (Color online) Efficiency corrected moments of ΔN_K distributions as a function of $\langle N_{part} \rangle$ for $Au + Au$ collisions at $\sqrt{s_{NN}}$ = 7.7, 11.5, 19.6, 27, 39, 62.4, and 200 GeV. These moments are calculated from the PID1 selection. The dashed lines are the expected values from the CLT.

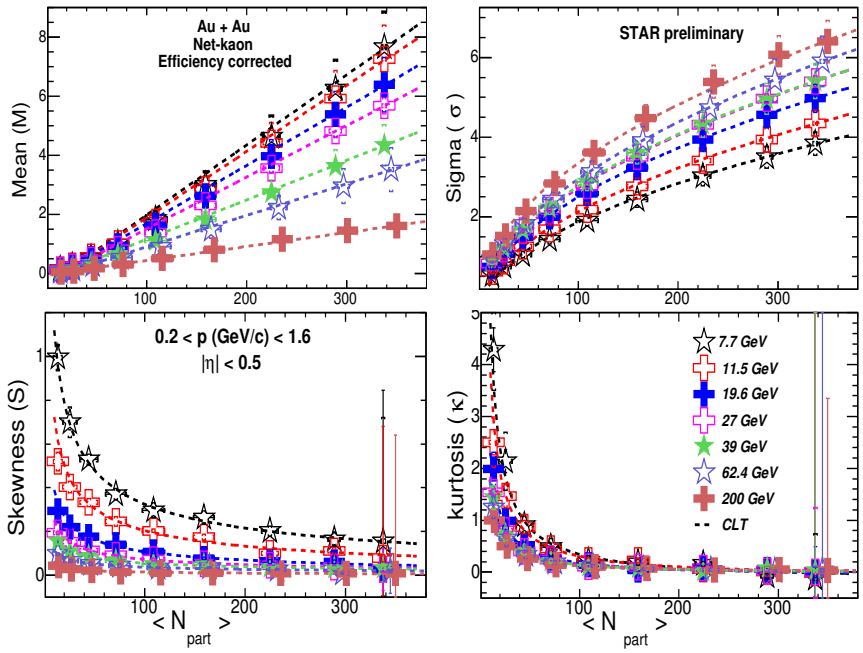

Figure 6.7: (Color online) Efficiency corrected moments of ΔN_K distributions as a function of $\langle N_{part} \rangle$ for $Au + Au$ collisions at $\sqrt{s_{NN}}$ = 7.7, 11.5, 19.6, 27, 39, 62.4, and 200 GeV. These moments are calculated from the PID2 selection. The dashed lines are the expected values from the CLT.

Both in the efficiency corrected and uncorrected results, M shows a linear variation with increasing $\langle N_{part} \rangle$ and increases as $\sqrt{s_{NN}}$ decreases, in accordance with energy and centrality dependence of baryon transport. The σ increases with $\langle N_{part} \rangle$ and decreases as a function of collision energies. Skewness decreases as a function of $\langle N_{part} \rangle$ and increases with collision energies. Kurtosis decreases as a function of $\langle N_{part} \rangle$ and collision energies. The variation in σ is less compared to the M and κ as compared to S as a function of $\sqrt{s_{NN}}$. The energy dependency in S is more compared to that of κ. The vanishing S and κ indicates that the distributions become symmetric towards the central collisions and for higher beam energies. It is observed that the systematic errors are much larger than the statistical errors for M and σ, while they are comparable for S and κ. As can be seen from the figures, after the efficiency correction the values of M and σ increased significantly. The value of S decreases after efficiency correction but is comparable with the uncorrected value while after the efficiency correction κ decreases

significantly.

The centrality evolution within the systems can be understood from the Central Limit Theorem (CLT) expectation of these higher moments. The CLT predicts that the particle emission sources for a colliding system are finite, independent and identical. In accordance with CLT the average number of participants for a given centrality could serve as a proxy of the system volume. CLT predicts that for a system with volume v the higher moments M, σ, S and κ vary as v, $\sqrt{v}$, $1/\sqrt{v}$ and $1/v$ respectively. The data points are fitted with the CLT expected dependency and shown as the dashed lines in Figure 6.4-6.7. From these plots it is observed that the extracted moments of the ΔN_K distributions follow the CLT very well which indicates that the particles are from independent emission sources. The centrality dependency of these moments for all center of mass energies shows system volume dependency. To cancel out these system volume dependency different combination of moment products have been constructed.

6.4 Centrality Dependence of the Moment Products

The volume independent moment products give a microscopic view of the system produced in the heavy ion collisions. The volume independent moment products have been constructed as per CLT scenario as seen from the $\langle N_{part} \rangle$ dependency. As discussed in the above section the moments M, σ, S and κ of the ΔN_K distributions has a volume dependency as v, $\sqrt{v}$, $1/\sqrt{v}$ and $1/v$ respectively for a system with volume v. To remove these volume dependency, moment products $S\sigma$ and $\kappa\sigma^2$ have been constructed. The bin width effects and detector effects have been taken into account to construct these moment products. Close to the critical point, models predicts that the distribution of net conserved quantities will be non-Gaussian and susceptibilities corresponding to these conserved quantities would diverge. As these volume independent moment products are related to the ratio of susceptibilities as $S\sigma = (\chi^{(3)}/T)(\chi^{(2)}/T^2)$ and $\kappa\sigma^2 = \chi^{(4)}/(\chi^{(2)}/T^2)$, they too will deviate from a constant value. It is expected that the proxy of

the conserved quantities reflect the fluctuation and singularities near the critical point. Therefore in presence of critical point the volume independent moment products $S\sigma$ and $\kappa\sigma^2$ of the ΔN_K distribution are expected to deviate from being a constant.

For the baseline of these moment products Poisson and NBD expectation have been studied by considering the kaon and anti-kaon distributions as Poisson and NBD for a given centrality. The Poisson expectation have been calculated from the mean of the both kaon and anti-kaon distributions assuming the difference of these distributions are Skellam distribution. The NBD expectation is calculated from the mean and variance of the kaon and the anti-kaon distributions.

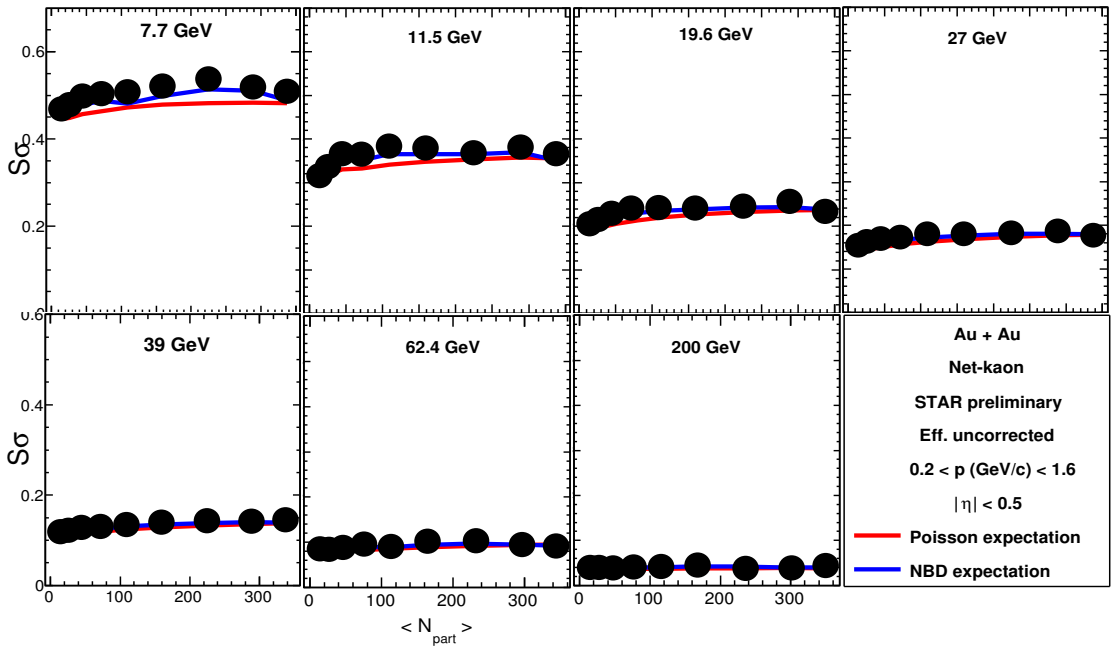

Figure 6.8: (Color online) Efficiency uncorrected v moment product $S\sigma$ of the ΔN_K distribution from PID1 as a function of centrality in $Au + Au$ collisions from the RHIC BES program measured by STAR compared with the Poisson (red line) and NBD (blue line) expectation.

Figure 6.8 and Figure 6.9 shows the efficiency uncorrected volume independent moments product $S\sigma$ of the ΔN_K distribution as a function of average number of participants. The experimental values shown in these figures are weighted average values for the selected centrality range studied. The $S\sigma$ in Figure 6.8 and

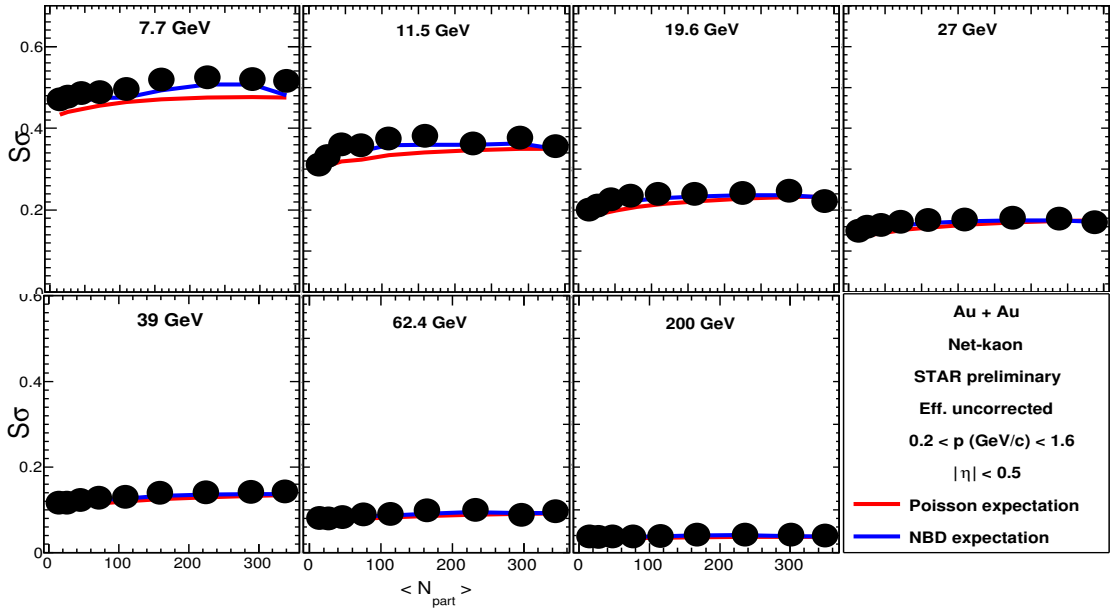

Figure 6.9: (Color online) Efficiency uncorrected moment product $S\sigma$ of the ΔN_K distribution from PID2 as a function of centrality in $Au + Au$ collisions from the RHIC BES program measured by STAR compared with the Poisson (red line) and NBD (blue line) expectation.

Figure 6.9 are obtained from the PID1 and PID2 selection respectively for center of mass energy $\sqrt{s_{NN}} = 7.7$, 11.5, 19.6, 27, 39, 62.4, and 200 GeV in $Au + Au$ collisions systems. In Figure 6.10 and Figure 6.11 efficiency corrected $S\sigma$ of the ΔN_K distribution as a function of $\langle N_{part} \rangle$ are shown for all BES energies obtained from PID1 and PID2 selection. The solid bars on the data points represents the statistical error and the shade bars represents the associated systematic errors. The data points have been compared with the Poisson (red lines) and NBD (blue lines) expectations. It is observed that for a given center of mass energy there is a very small centrality dependency in $S\sigma$ value. It increases marginally with centrality, however, the effect is nearly within 15%. The NBD expectation is higher than the Poisson expectation. $S\sigma$ value is above Poisson and NBD baseline but closer to NBD baseline for beam energy below 200 GeV. $S\sigma$ increases with decreasing collision energies. After the efficiency corrections both the statistical and systematic errors increase significantly. The systematic errors are comparable with the statistical errors for all cases.

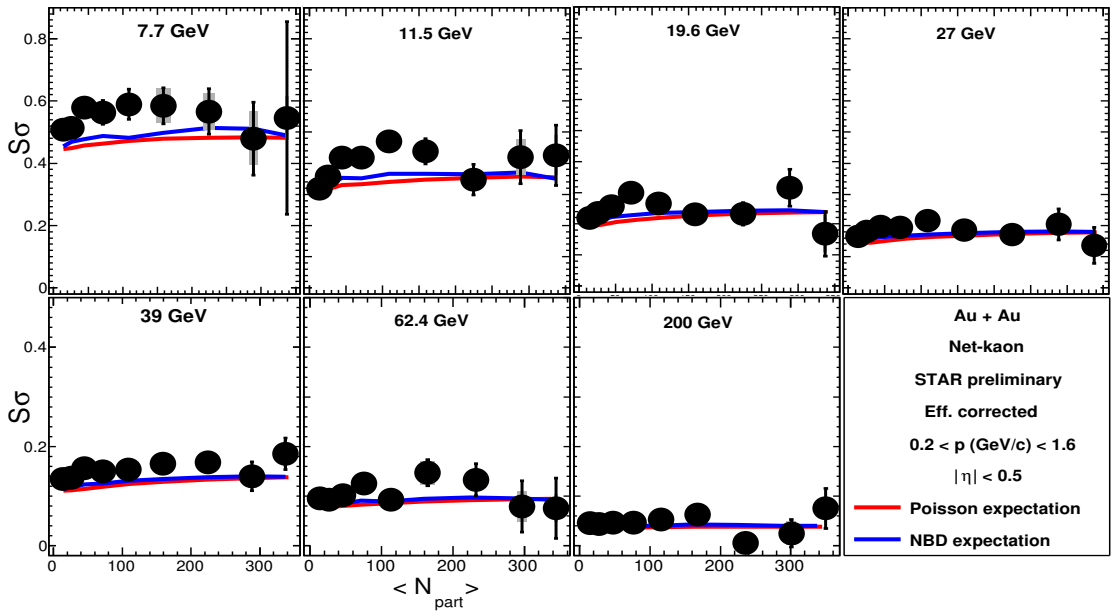

Figure 6.10: (Color online) Efficiency corrected moment product $S\sigma$ of the ΔN_K distribution from PID1 as a function of centrality in $Au + Au$ collisions from the RHIC BES program measured by STAR compared with the Poisson (red line) and NBD (blue line) expectation.

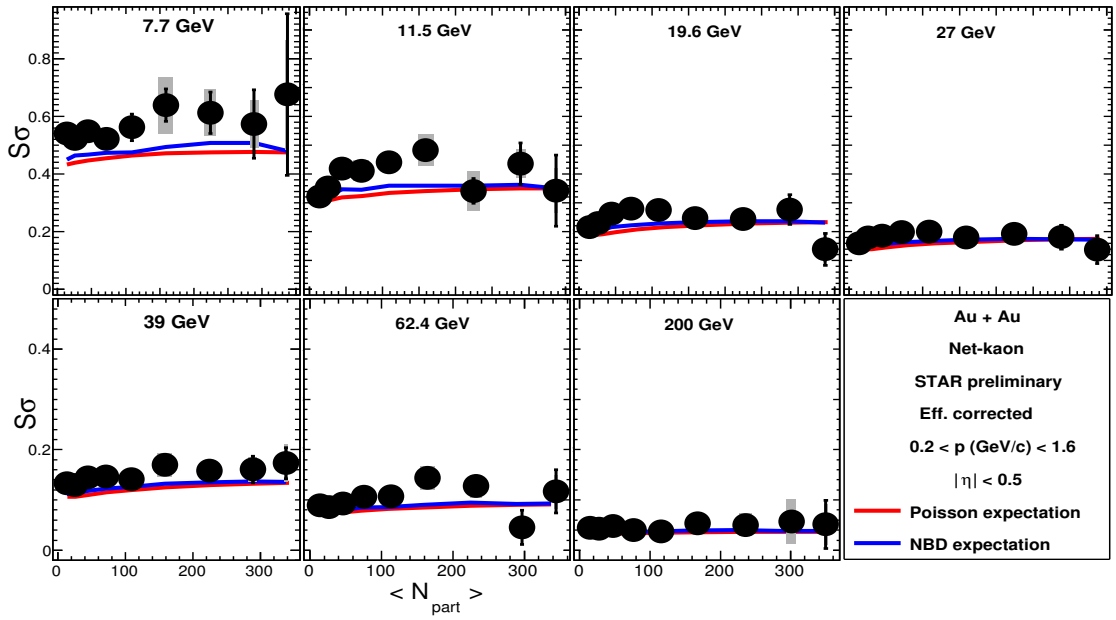

Figure 6.11: (Color online) Efficiency corrected moment product $S\sigma$ of the ΔN_K distribution from PID2 as a function of centrality in $Au + Au$ collisions from the RHIC BES program measured by STAR compared with the Poisson (red line) and NBD (blue line) expectation.

Figure 6.12 and Figure 6.13 shows the efficiency uncorrected volume independent moments product $\kappa\sigma^2$ of the ΔN_K distribution as a function of $\langle N_{part} \rangle$. The $\kappa\sigma^2$ in Figure 6.12 and Figure 6.13 are obtained from the PID1 and PID2 selection respectively for center of mass energy $\sqrt{s_{NN}}$ = 7.7, 11.5, 19.6, 27, 39, 62.4, and 200 GeV in $Au + Au$ collision systems. The efficiency corrected $\kappa\sigma^2$ of the ΔN_K distribution as a function of $\langle N_{part} \rangle$ for all BES energies are shown in Figure 6.14 and Figure 6.15. The centrality dependency of $\kappa\sigma^2$ in Figure 6.14 and Figure 6.15 are obtained from PID1 and PID2 selection respectively.

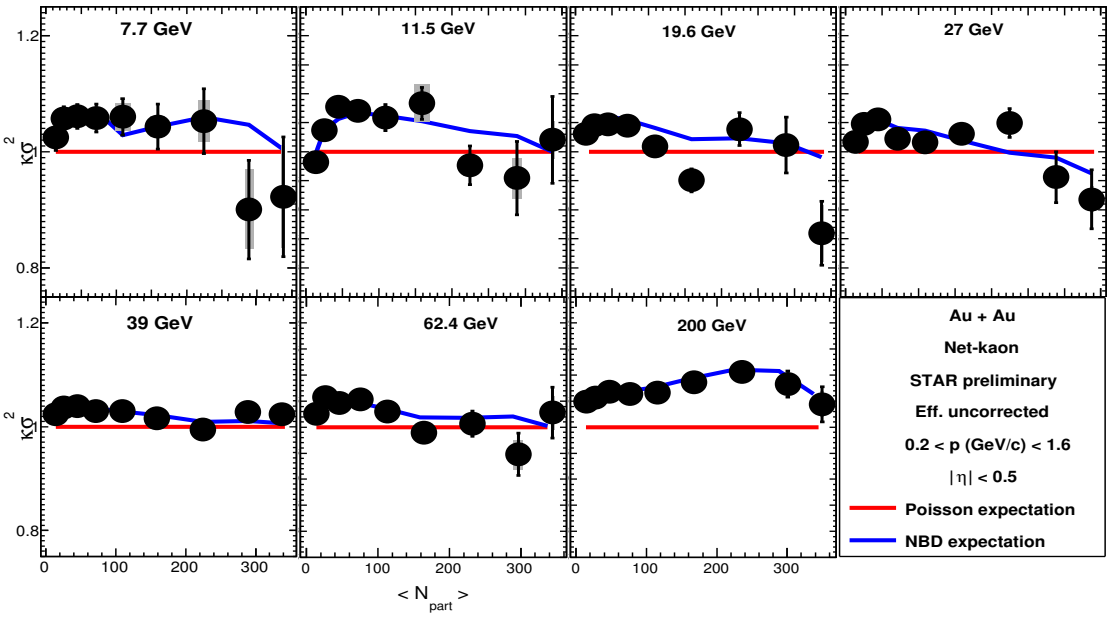

Figure 6.12: (Color online) Efficiency uncorrected moment product $\kappa\sigma^2$ of the ΔN_K distribution from PID1 as a function of centrality in $Au + Au$ collisions from the RHIC BES program measured by STAR compared with the Poisson (red line) and NBD (blue line) expectation.

The solid bars on the data points represents the statistical error and the shaded bars represents the associated systematic errors. The data points have been compared with the Poisson (red lines) and NBD (blue lines) expectations. It is observed that the NBD expectation is above Poisson expectation except top central collisions at 19.6 and 27 GeV. Within the statistical uncertainty the efficiency uncorrected volume independent product $\kappa\sigma^2$ is independent of centrality within 10% except central collisions below 39 GeV for both the PIDs. It is observed that

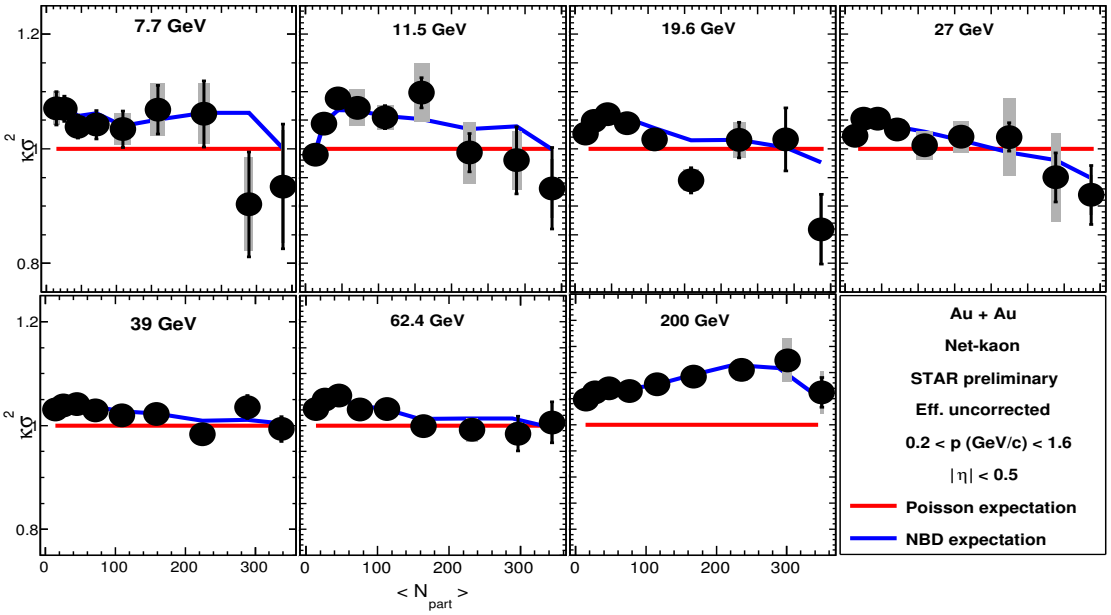

Figure 6.13: (Color online) Efficiency uncorrected moment product $\kappa\sigma^2$ of the ΔN_K distribution from PID2 as a function of centrality in $Au + Au$ collisions from the RHIC BES program measured by STAR compared with the Poisson (red line) and NBD (blue line) expectation.

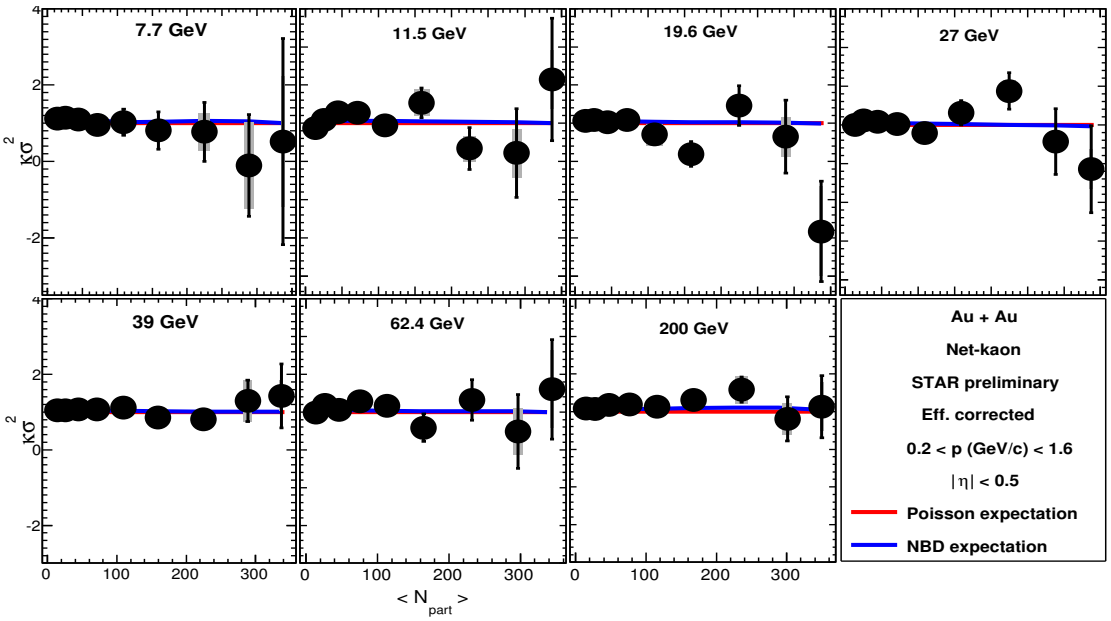

Figure 6.14: (Color online) Efficiency corrected moment product $\kappa\sigma^2$ of the ΔN_K distribution from PID1 as a function of centrality in $Au + Au$ collisions from the RHIC BES program measured by STAR compared with the Poisson (red line) and NBD (blue line) expectation.

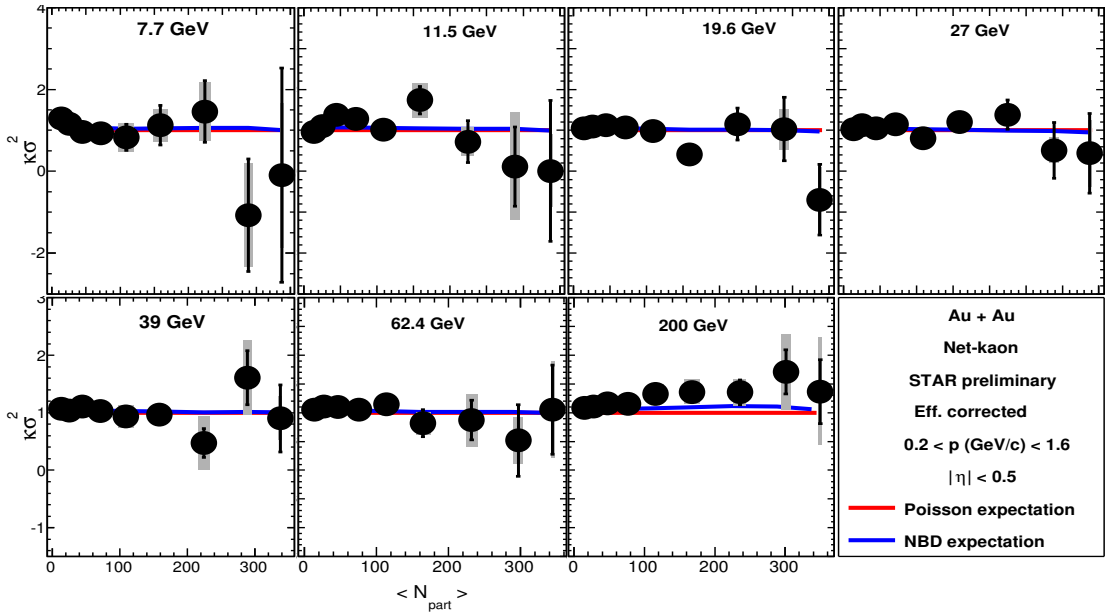

Figure 6.15: (Color online) Efficiency corrected moment product $\kappa\sigma^2$ of the ΔN_K distribution from PID2 as a function of centrality in $Au + Au$ collisions from the RHIC BES program measured by STAR compared with the Poisson (red line) and NBD (blue line) expectation.

efficiency uncorrected $\kappa\sigma^2$ is much closer to the NBD expectation than the Poisson expectation. Efficiency corrected $\kappa\sigma^2$ show centrality dependency towards the central collisions below 39 GeV for both the PIDs. The systematic and statistical errors are comparable for the efficiency corrected as well as the uncorrected results for both the PIDs .

6.5 Energy Dependence of Volume Independent Moment Product

The main aim of the BES program is to scan the QCD phase diagram by regulating the center of mass energy of the colliding system. It was shown that by varying the center of mass energy it is possible to vary μ_B in the QCD phase diagram. In conjunction with the theoretical calculation RHIC results showed that BES program cover a μ_B range of 24 to 410 MeV by varying the center of mass energy from 200 to 7.7 GeV. The extracted μ_Bs are obtained from the measurement

of the top 0-5% central collisions. The top central collisions are the most important part of the heavy ion collision experiment measurements and indispensable to see the macroscopic view of the colliding systems.

In Figure 6.16 the efficiency uncorrected volume independent moments product $S\sigma$ of the ΔN_K multiplicity distributions as a function of center of mass energy are shown for top 0-5% central collisions for all BES energies. The left panel shows the $S\sigma$ of the ΔN_K distribution for PID1 selection and the right panel shows the same from the PID2 selection. The solid bars on data points show the statistical uncertainties and the cross bars show the systematic uncertainties. The red line is the Poisson expectation and the blue line is the NBD expectation for top 0-5% central collisions. The efficiency corrected $S\sigma$ of the ΔN_K multiplicity distribu-

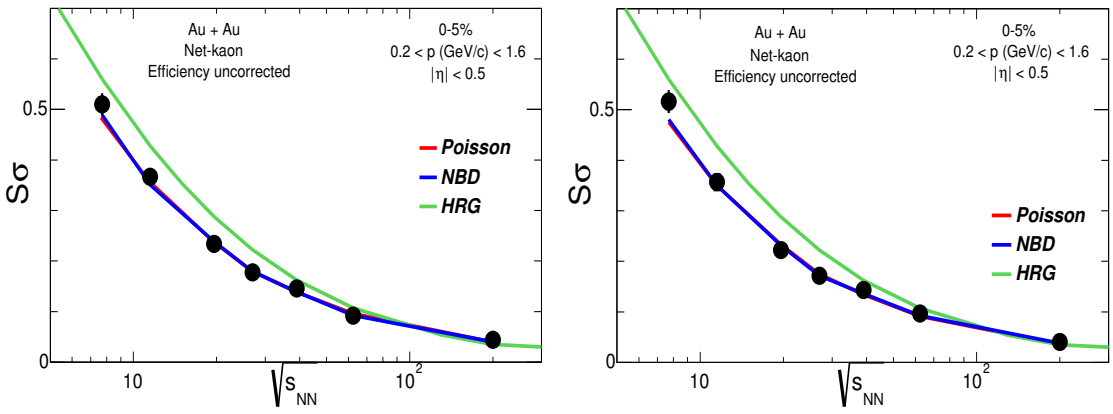

Figure 6.16: (Color online) Energy dependency of efficiency uncorrected $S\sigma$ for $Au + Au$ collisions at $\sqrt{s_{NN}}$ = 7.7-200 GeV at top central 0-5% collision from PID1 (left panel) and PID2 (right panel). Data compared with the Poisson (red line) and NBD (blue line) expectation. The green line is the prediction from HRG model calculation from Ref.[131].

tions for all BES energies are shown in the Figure 6.17 for PID1 (left panel) and PID2 (right panel). The red, blue and green lines are from Poisson, NBD and HRG predictions.

It is observed that for top 0-5% central collisions the $S\sigma$ of the ΔN_K multiplicity distributions decreases with increasing center of mass energy. For the most

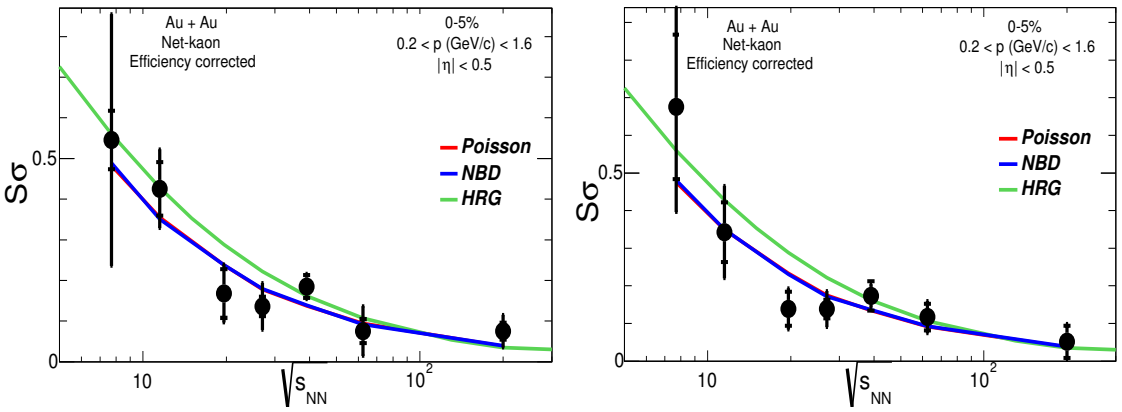

Figure 6.17: (Color online) Energy dependency of efficiency corrected $S\sigma$ for $Au+Au$ collisions at $\sqrt{s_{NN}} = 7.7\text{-}200\ GeV$ at top central 0-5% collision from PID1 (left panel) and PID2 (right panel). Data compared with the Poisson (red line) and NBD (blue line) expectation. The green line is the prediction from HRG model calculation from Ref.[131].

central collisions the $S\sigma$ value for 200 GeV center of mass energy is nearly zero. The efficiency uncorrected $S\sigma$ for top 0-5% central collisions is below HRG expectation for center of mass energy below 200 GeV and matches with Poisson and NBD expectation. HRG expectation is above Poisson and NBD expectation. The efficiency corrected $S\sigma$ matches with Poisson and NBD expectation except at 19.6 GeV center of mass energy. Within statistical uncertainties $S\sigma$ deviates from HRG expectation at 19.6 and 27 GeV for top 0-5% central collisions. As $S\sigma$ is energy dependent, a scaling with respect to the baseline gives a better understanding. It is expected that these ratio will have a value equal to unity if the ΔN_K distribution follows the corresponding baselines.

The energy dependency of efficiency uncorrected and corrected $S\sigma$ scaled with the Poisson, NBD and HRG expectations are shown in the Figure 6.18 and Figure 6.19 respectively. The red, blue and green points are the $S\sigma$ scaled with $S\sigma$ of Poisson, NBD and HRG exception respectively. The bars represents the statistical errors and the cross bars are the systematic errors estimated from error propagation method from errors on $S\sigma$. The left panel shows the results from

PID1 and the right panel shows that of PID2.

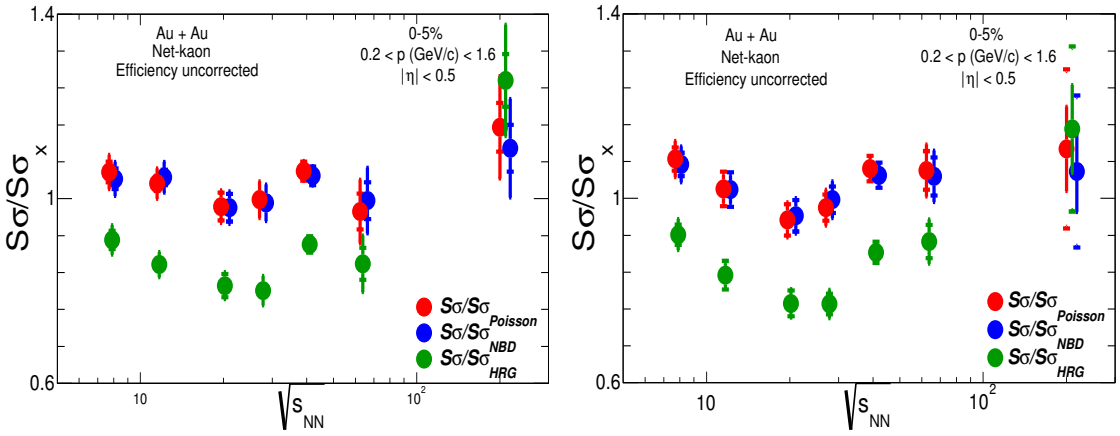

Figure 6.18: (Color online) Energy dependency of ratios of efficiency uncorrected $S\sigma$ with $S\sigma_{Poisson}$, $S\sigma_{NBD}$ and $S\sigma_{HRG}$ for $Au + Au$ collisions at $\sqrt{s_{NN}}$ = 7.7-200 GeV at top central 0-5% collision from PID1 (left panel) and PID2 (right panel). The estimated statistical and systematic errors are shown. The HRG prediction (green line) from the Ref. [131] compared with the data.

It is observed that all of these ratio of $S\sigma$ with different baseline expectations for 0-5% top central collisions have a dip kind of structure near 19.6 GeV. The ratio of $S\sigma$ with Poisson and NBD expectation are consistent with each other for efficiency uncorrected results. The ratio of efficiency uncorrected $S\sigma$ with respect to the HRG prediction shows larger deviation from unity near 19.6 GeV center of mass energy. The efficiency corrected ratio of $S\sigma$ with these three different baseline for 0-5% central collisions are consistent with each other. Within the uncertainties the efficiency corrected ratios are close to unity except near 19.6 GeV center of mass energy.

The efficiency uncorrected moment product $\kappa\sigma^2$ for top 0-5% central $Au + Au$ collisions as a function of center of mass energy for PID1 and PID2 are shown in the Figure 6.20 and Figure 6.21 respectively. The data has been compared with the Poisson, NBD expectations along with HRG prediction. The results from non-CP HRG models as a function of $\sqrt{s_{NN}}$ have values between 1 and 2. The Poisson

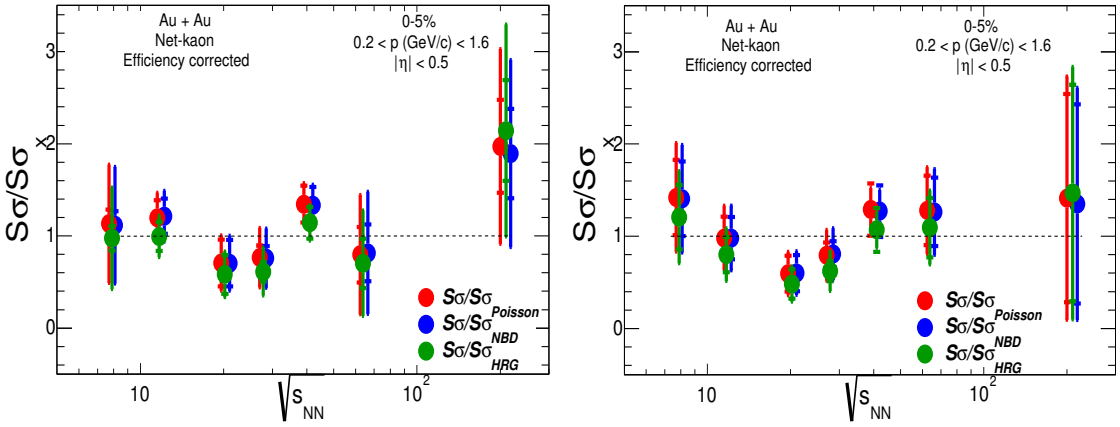

Figure 6.19: (Color online) Energy dependency of ratios of efficiency corrected $S\sigma$ with $S\sigma_{Poisson}$, $S\sigma_{NBD}$ and $S\sigma_{HRG}$ for $Au + Au$ collisions at $\sqrt{s_{NN}}$ = 7.7-200 GeV at top central 0-5% collision from PID1 (left panel) and PID2 (right panel). The statistical and systematic errors are shown. The HRG prediction (green line) from the Ref. [131] compared with the data.

expectation for $\kappa\sigma^2$ is equal to unity and that for NBD expectation is very close to unity. For both the PIDs the Poisson and NBD expectation are very close to each other and below the HRG prediction for all BES energies.

The efficiency uncorrected $\kappa\sigma^2$ of the ΔN_K multiplicity distributions for top 0-5% central collision shows a dip kind of structure below 39 GeV center of mass energy. With respect to Poisson expectation the $\kappa\sigma^2$ deviates at 19.6 and 27 GeV and the maximum deviation is found at 19.6 GeV. With respect to NBD expectation the $\kappa\sigma^2$ deviates at 19.6 GeV center of mass energy. The $\kappa\sigma^2$ are below HRG prediction and the deviation is maximum at 19.6 GeV center of mass energy.

In Figure 6.22 and Figure 6.23 the efficiency corrected moment product $\kappa\sigma^2$ for top 0-5% central $Au + Au$ collisions as a function of center of mass energy for PID1 and PID2 are shown respectively. In both the figures, data has been compared with the Poisson and NBD expectation. The prediction from HRG model calculation have been compared with data.

Within the statistical uncertainties the efficiency corrected $\kappa\sigma^2$ for 0-5% central

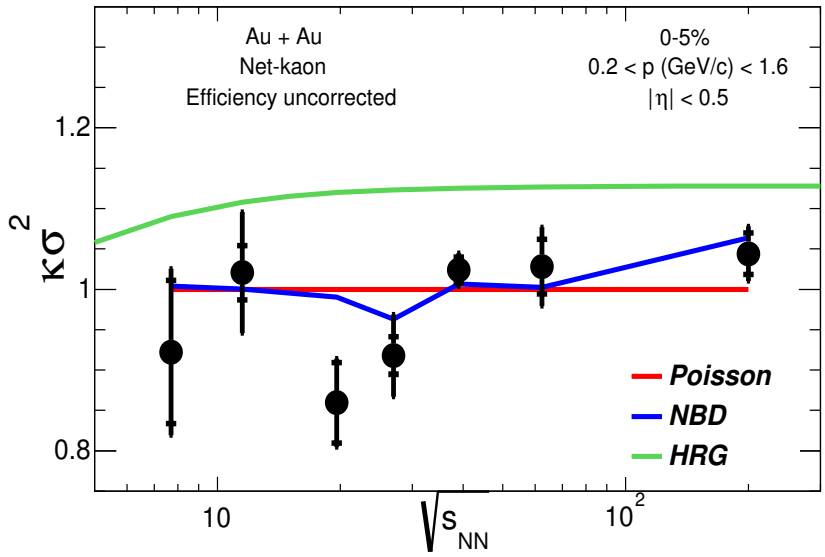

Figure 6.20: (Color online) Efficiency uncorrected volume independent moment product $\kappa\sigma^2$ from PID1 as a function of center of mass energy for top 0-5% central $Au + Au$ collisions from the RHIC BES program measured by STAR compared with the Poisson (red line) and NBD (blue line) expectation. The HRG prediction (green line) from the Ref. [131] compared with the data.

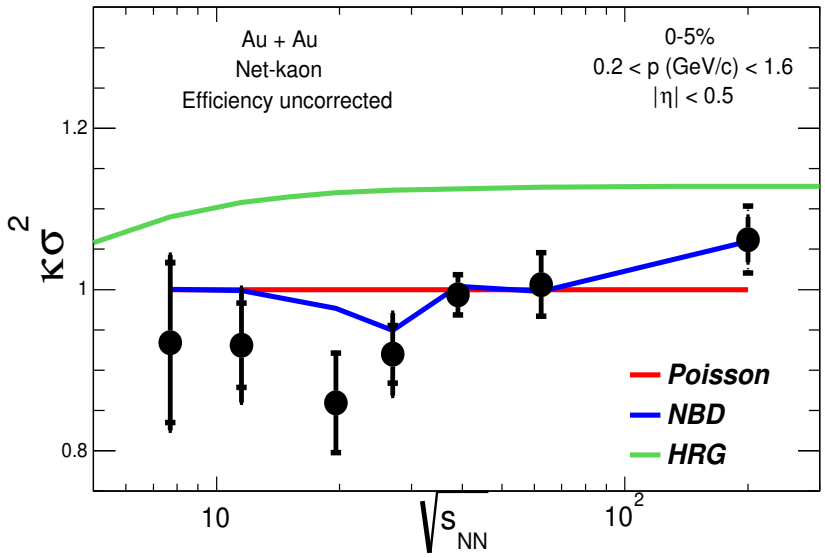

Figure 6.21: (Color online) Efficiency uncorrected volume independent moment product $\kappa\sigma^2$ from PID2 as a function of center of mass energy for top 0-5% central $Au + Au$ collisions from the RHIC BES program measured by STAR compared with the Poisson (red line) and NBD (blue line) expectation. The HRG prediction (green line) from the Ref. [131] compared with the data.

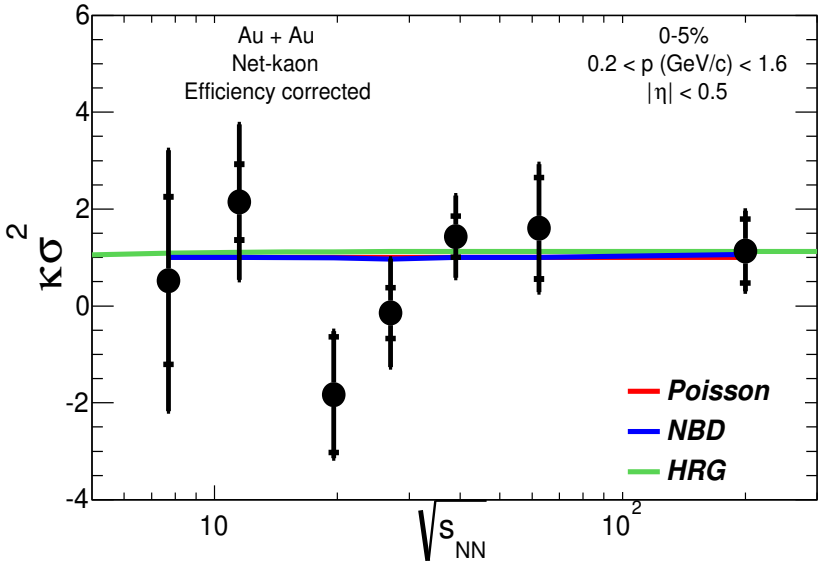

Figure 6.22: (Color online) Efficiency corrected volume independent moment product $\kappa\sigma^2$ from PID1 as a function of center of mass energy for top 0-5% central $Au + Au$ collisions from the RHIC BES program measured by STAR compared with the Poisson (red line) and NBD (blue line) expectation. The HRG prediction (green line) from the Ref. [131] compared with the data.

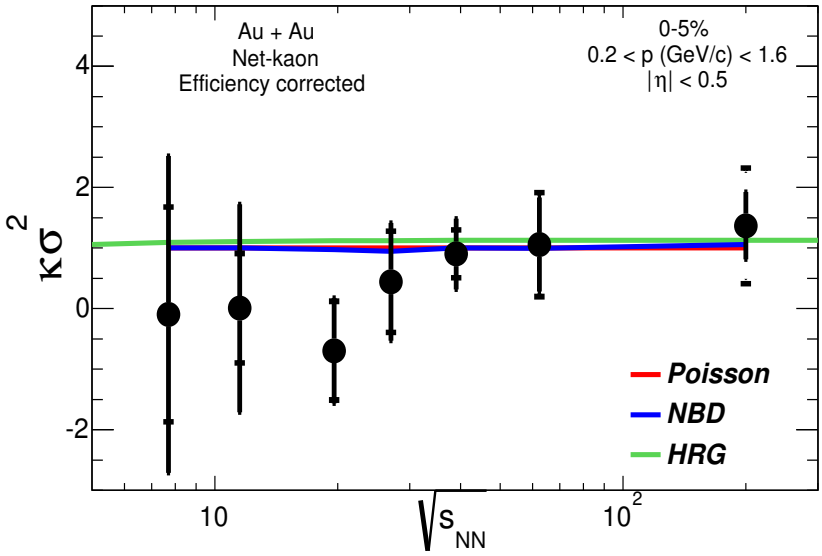

Figure 6.23: (Color online) Efficiency corrected volume independent moment product $\kappa\sigma^2$ from PID2 as a function of center of mass energy for top 0-5% central $Au + Au$ collisions from the RHIC BES program measured by STAR compared with the Poisson (red line) and NBD (blue line) expectation. The HRG prediction (green line) from the Ref. [131] compared with the data.

$Au + Au$ collisions matches with Poisson and NBD expectation except at 19.6 GeV for both of the PIDs measured. With respect to HRG model prediction $\kappa\sigma^2$ deviates at 19.6 GeV for both of the PIDs. It is observed that the deviation at 19.6 GeV with respect to Poisson and NBD expectation is more in PID1 with respect to PID2 but have larger error bar. With respect to errors on both of the data points at 19.6 GeV the significant deviation is similar for both of the PIDs and nearly equal to 2σ.

The volume independent moment products are found to be consistent within statistical uncertainty for the peripheral collisions for all BES energies and towards central collisions for energy above 27 GeV. We observe collision centrality dependence of these moment products for energy below 39 GeV. From the comparisons with Poisson and NBD baseline studied in net-kaon higher moments analysis a deviation of volume independent moment products $S\sigma$ and kσ^2 observed for top central $Au + Au$ collisions at 19.6 GeV. The deviation from the HRG model prediction and baseline expectation could be linked with the critical point of the QCD phase and the chiral phase transition. Recent calculation of σ-model predict that near the critical point the fourth order cumulant of the conserved quantities will be negative as we approach from the cross over region. The ratio of the fourth to second order cumulants is equal to $\kappa\sigma^2$. Hence the $\kappa\sigma^2$ is expected to be negative as well. The lattice QCD calculation already showed a negative value of the $\kappa\sigma^2$ for the net-baryon at 19.6 GeV. Therefore based on the theoretical predictions and experimental measurements described in this thesis it can be inferred that there is a possible indication that the QCD critical point lies in a region at μ_B corresponding to $Au + Au$ collisions at 19.6 GeV.

Chapter 7

Summary and Outlook

7.1 Summary

The Relativistic Heavy-Ion Collider at the Brookhaven National Laboratory was constructed to study QCD. In the last decade and half, it has provided deep insight into the way the strongly interacting matter behaves. The strong elliptic flow, jet quenching, chiral magnetic effect, etc. have provided valuable information of the primordial matter created during the fist few microseconds after the big bang. The possibility of colliding polarized proton beam has further enhanced the richness of the results obtained from RHIC and has thrown light on the proton spin problem. It is the largest energy polarized proton machine. Lattice calculations at zero baryon chemical potential predict a cross over while models at finite baryon chemical potential predict a first order phase transition. The two facts coupled together lead to the existence of a critical point in the QCD phase diagram. In near future, the possibility of theoretically locating the critical point is very small. One of the crowning glories of experimental results from RHIC would be the location of the critical point. In the last five years, tremendous effort has been spent on experimentally locating the critical point. The RHIC started the BES program in the year 2010 to achieve its goal by varying the chemical potential from 410 to 24 MeV at the freeze-out by varying the center of mass energy of the $Au + Au$ nucleus from 7.7 to 200 GeV. The STAR experiment, with its ex-

cellent particle identification capabilities has collected data from BES program in $Au + Au$ collisions at 7.7, 11.5. 19.6, 27, 39, 62.4 and 200 GeV.

In this work, as mentioned earlier, we have looked at the higher moments of net-kaon multiplicity distribution in an effort to locate the critical point. In an infinite thermodynamic system with infinite lifetime at the critical point the correlation lengths (ξ) of the system and the magnitude of the fluctuations at all length scales diverge. For a finite system at RHIC energies it has been estimated to be 2-3 fms. Theoretical calculations show that the correlation lengths of the system are related with the higher moments of conserved quantities such as net-baryons (ΔB), net-strangeness (ΔS) and net-charge (ΔQ). Lattice QCD calculations predict that these these higher order moments are related to the corresponding susceptibilities. QCD based calculations predict that the higher non Gaussian moments of conserved quantities are much more sensitive to the correlation length as they depend on higher powers of ξ. QCD based models predict that close to the critical point ΔB, ΔS and ΔQ distributions will be non-Gaussian causing $S\sigma$ and $\kappa\sigma^2$ to deviate from being constants. Therefore, in the presence of critical point the higher order moments and their products should be sensitive probes for the signature of the critical phenomenon. In this work we have therefore undertaken the task of measuring the higher moments of the net-kaon multiplicity distribution (as a proxy for net-strangeness) to locate the critical point.

For the net-kaon higher moments analysis the experimental run numbers and events numbers have been selected through extensive cleanup processes. The kaons were selected from the collisions occurring within $50\ cm$ of the TPC center along the beam line for center of mass energy 7.7 and 11.5 GeV and within 30 cm for rest of the BES energies. The ΔN_K multiplicity measurements have been measured within the pseudo-rapidity $|\eta| \leq 0.5$ in the momentum range of $0.2 < p < 1.6\ GeV/c$. To reduce the contamination from secondary kaons, each $K^+(K^-)$ track was required to have a minimum p_T of 0.2 GeV/c and a distance of closest approach (DCA) to the primary vertex of less than 1 cm. To select the charged kaons and to suppress the contamination from other particles, it was required

their dE/dx to be within 2σ of the value from the Bethe Bloch formulation. The whole analysis has been performed by selecting two types of PIDs by using TPC alone and TPC and TOF simultaneously in the selected momentum range. For centrality determination the uncorrected charged particle multiplicity from TPC within $0.5 \leq |\eta| \leq 1.0$ have been used. The centrality selection was performed out side of the analysis pseudo rapidity range to avoid autocorrelation effects. For each centrality at all center of mass energies, the average number of participants ($\langle N_{part} \rangle$) were calculated by using the Glauber model.

For the centrality determination, all results have been corrected for the finite bin width effects. Various methods have been used to calculate the statistical errors for this analysis. The systematics have been studied for this analysis by varying the experimental acceptance and the systematic errors due to the same have been calculated and corrected in the final results. The detector efficiency correction method have been developed by Binomial efficiency using the STAR embedding data and implemented in the results obtained from this analysis. In each centrality bin, considering each of the kaon and anti-kaon distribution to be a Poisson distribution, the Skellam distribution is obtained from their difference. The Poisson baseline have been estimated from these Skellam distribution. In the same way the Negative Binomial Distribution (NBD) have been estimated and compared with the data by considering each of the kaon and anti-kaon distribution to be a NBD in each centrality bin and for all the center of mass energies. The volume independent moment products have been compared with the estimated Poisson and NBD expectation from the N_{K^+} and N_{K^-} distribution. The prediction of HRG Monte Carlo model which does not include the critical point have been compared with the data for non-critical baseline. To understand the centrality evolution in the collision system the moments are fitted with the expectation from Central Limit Theorem, which gives information of the multiplicity distribution and the geometry produced in the collision.

Both the K^+ and K^- multiplicity distributions have larger width in the central collisions than the peripheral collisions. The difference between K^+ and K^-

distribution for each centrality increases from peripheral to central collisions. It is observed that the central collisions of the ΔN_K multiplicity has much wider distributions than the peripheral collisions for all BES energies. As the center of mass energy increases, the width of the distributions increases for all centralities. With increase in center of mass energy the distribution becomes more symmetric and looks like a normal distribution. The M of the ΔN_K multiplicity distribution shows a linear variation with increasing $\langle N_{part} \rangle$ and increases as $\sqrt{s_{NN}}$ decreases. The σ increases with $\langle N_{part} \rangle$ and as a function of collision energies. The Skewness and kurtosis decrease as a function of $\langle N_{part} \rangle$ and with collision energies. The kurtosis decreases much faster in higher energies than in the lower energies and has similar value towards the central collision for all BES energies. The vanishing S and κ in the top central collisions indicate that the distributions become symmetric towards the central collisions and for higher beam energies. These higher moments follow the dependency from the Central Limit Theorem, which helps one to understand the centrality evolution of the system produced in the $Au + Au$ collisions. As these higher moments are system size dependent different combination of moment product such as $S\sigma$ and $\kappa\sigma^2$ have been calculated (to cancel out the dependence on the volume) as a function of collision centrality and energy. QCD based calculations expect a non-monotonic dependence of these moment products near the critical point.

It is observed that $S\sigma$ has a very small increasing centrality dependency going from most peripheral to central collision. The $S\sigma$ values are greater than Poisson and NBD baseline for beam energy below 200 GeV. The $S\sigma$ increases with decreasing center of mass energies and is closer to the NBD baseline than the Poisson baseline for beam energy below 200 GeV. The volume independent moment product $\kappa\sigma^2$ is independent of centrality in the peripheral collisions but shows centrality dependency in top central collisions below 39 GeV. With respect to the Poisson and NBD expectations $\kappa\sigma^2$ shows no centrality dependency in peripheral collisions for all center of mass energies. However, $\kappa\sigma^2$ shows some centrality dependency in the central collisions with respect to the Poisson and

NBD expectations below 39 GeV.

The moment product $S\sigma$ shows a decreasing energy dependency both in peripheral and central collisions with increasing center of mass energy. In the peripheral collisions, $S\sigma$ shows no deviation with respect to the Poisson and NBD expectation. However, for the top central 0-5% collisions $S\sigma$ does show a deviation with respect to the Poisson and NBD expectation near 19.6 GeV. Similarly, $\kappa\sigma^2$ is independent of collision energy for peripheral collisions. Again for the most central 0-5% collision $\kappa\sigma^2$ shows a nearly two sigma deviation from the both Poisson and NBD expectation near 19.6 GeV. Thus nearly two sigma deviation is observed with respect to the HRG prediction at 19.6 GeV in both the volume independent moment products. The deviation from the theoretical expectation could be an indication of the presence of the critical point around that energy. The deviation of the volume independent moment products from the baseline and non CP models are expected as the freeze-out passes through both the critical region and the critical point. As the order of magnitude of the deviations at the critical point and in the critical region is unknown it is difficult to say whether the freeze-out passes through the critical point or the critical region. Although this work has observed a possible signature of QCD critical point, a definite value of the critical point on the T - μ_B diagram, cannot be concluded from this work due to limited statistics and for its exact location a finer binning in center of mass energies is required.

7.2 Future Prospective

The higher moments analysis is very much statistically hungry and affected by the statistical uncertainties. To reduce the statistical uncertainties, the BES data at lower energies with much larger statistics than the present data is required. The BES phase-II program has been proposed in RHIC, which aims to take much higher statistics of the data than the present data in the lower energies. For a better dE/dx resolution, it has been proposed to upgrade the Time Projection

Chamber for the BES-II program. The new upgraded TPC (iTPC) will provide $|\eta| \leq 1.7$ unit of pseudo rapidity and better momentum resolution. Therefore, it is expected that with the higher momentum resolution and larger statistics BES-II data will provide much clear scenario for the search of critical point in the QCD phase diagram. This study has already narrowed the region for the critical point search in BES-II.

As it is expected that the deviation will be maximum at the critical point, BES needs intermediate data in the lower energies with much higher statistics for a definite location of the QCD critical point. In addition to these data presented in this thesis, BES-I also collected data at $\sqrt{s_{NN}}$ = 14.6 GeV in the year 2014 which is under process and will be available very soon. As it is expected that the behaviour of these sensitive observables will be different in the either side of the critical point in the QCD phase diagram, this new data at 14.6 GeV may help to determine the location of the critical point. Some intermediate energies below 19.6 GeV in the BES-II program will also allow more sensitive search of the QCD critical point. The upgrades leading to higher momentum resolution will further improve our sensitivity in locating the critical point. With the higher statistics these intermediate energies might also help to find the exact location of the critical point in the QCD phase diagram.

The Compressed Baryonic Matter (CBM) experiment at Facility for Antiproton and Ion Research (FAIR) aims to cover the baryon chemical potential range in the QCD phase diagram near the theoretical prediction of critical point by varying the center of mass energies. The NA61/SHINE experiment at CERN is running with the same aim to find the evidence of the QCD critical point of strongly interacting matter by changing the μ_B and system size by varying the collision energy and colliding nuclei. This analysis can be carried out with the data from the above mentioned experiments. Along with these experimental results RHIC result will give a complete picture of the QCD phase diagram and probably a definite position of the critical point. There are many interesting aspects to study the QCD phase diagram at RHIC energies. Many interesting study are presently go-

ing on at RHIC and which will be continued in BES-II which will provide further information about the QCD phase diagram and the critical point.

Theoretical calculations predicts that the cross-over at low μ_B in the QCD phase diagram is sensitive to the 6^{th} order moment of the conserved quantities. For the signature of the cross-over the 6^{th} moments of the net-proton, net-charge (π, p, k), and net-kaon can be study for the proxy of net-baryon (ΔN_B), net-charge (ΔN_Q) and net-strangeness (ΔN_S) in the higher center of mass energies from RHIC. As the 6^{th} order moment is much more sensitive to the correlation lengths of the systems than the 4^{th} order moments, it will require much more statistics ($\sim 10^9$ events) than we have from BES-I program. The proposed BES-II program in RHIC, also aims to take much larger data set in the higher center of mass energies. The ALICE experiment at the Large Hadron Collider at CERN has much higher acceptance and better momentum resolution which taking data in $Pb+Pb$ collisions at much higher center of mass energies. With a large set of $Pb+Pb$ data at LHC a study can be carried out for the signature of the cross over.

Lattice QCD based simulation predicts that the extraction of freeze-out parameter (T_x, μ_x (where, $x = B, Q, S$)) is possible from the experimentally measured higher moments of these conserved quantities. The extraction of the freeze-out parameter assumed that all particle species freeze-out at the same time which is also one of the biggest quest in this field. Hence, the extraction of the strangeness freeze-out parameter will be one of the biggest goal and for that some theoretical inputs are indispensable. Furthermore, many theoretical calculation indicates that the flavour dependent higher moments are useful to draw the freeze-out line near the crossover region.

In a nutshell, this study has provided possible evidence of the QCD critical point. It has further narrowed the region in which to look for the critical point and has therefore provided a clear direction for the BES-II program of RHIC.

Appendix A

Error Calculation

A.1 Statistical Error Calculation

A.1.1 Sub Group Method

In Sub-group method, the whole sample divided randomly into several sub-groups with same statistics. Let's say there are N number of total statical events and we want to estimate the error for some observable X. Then for n number of sub-group, each sub-group contain $N' = \frac{N}{n}$ number of statistical events. Then the observable (x) is calculated from each sub-group to get a distribution of that observable. Finally, the width of the distribution of observables estimated from different sub-group represents the statistical error for that particular observable, i.e,

$$Var(X) = \frac{\langle (N'_i - \langle N' \rangle)^2 \rangle}{n-1} \tag{A.1}$$

where, $\langle N' \rangle$ is the average of all N' from all sub-group and define as,

$$\langle N' \rangle = \frac{1}{n} \sum_{i=1}^{n} N'_i \tag{A.2}$$

For a large number of statistical events sub-group method is a good. It is always better to use large number of sub-group in this method. For the higher moments analysis this method is not useful to calculate the errors for moments

higher then the 2^{nd} order.

A.1.2 Delta Theorem

The formulation of errors of the moments and the volume independent moment products from the Delta Theorem are shown in the following equations [121].

$$\begin{aligned} Var(\hat{\sigma}) &= (m_4 - 1)\sigma^2/(4n) \\ Var(\hat{S}) &= [9 - 6m_4 + m_3^2(35 + 9m_4)/4 - 3m_3m_5 + m_6]/n \\ Var(\hat{\kappa}) &= [-m_4^2 + 4m_3^3 + 16m_3^2(1 + m_4) - 8m_3m_5 - 4m_4m_6 + m_8]/n \end{aligned} \tag{A.3}$$

The errors in the volume independent moment products are also shown.

$$\begin{aligned} (\hat{S}\hat{\sigma}) =& [9 - 6m_4 + m_3^2(6 + m_4) - 2m_3m_5 + m_6]\sigma^2/n \\ (\hat{\kappa}\hat{\sigma}^2) =& [-9 + 6m_4^2 + m_4^3 + 8m_3^2(5 + m_4) - 8m_3m_5 + m_4(9 - 2m_6) - 6m_6 + m_8]\sigma^4/n \\ (\hat{\kappa}\hat{\sigma}/\hat{S}) =& [64m_3^4 - 8m_3^3m_5 - (-3 + m_4)^2(-9 + 6m_4 - m_6) + 2m_3(-3 + m_4)(9m_5 - m_7) \\ & + m_3^2(171 - 48m_4 + 8m_4^2 - 12m_6 + m_8)]\sigma^2/(n \times m_3^4) \end{aligned} \tag{A.4}$$

For this higher moments analysis the calculation of detector efficiency required up to 8^{th} order moments to calculate efficiency for 4^{th} order moment. The calculation of 8^{th} order moments using this method is very complicated and required huge time and computational work.

A.1.3 Bootstrap Method

The basic idea of bootstrap method is based on the repeated random sampling from sample data. Then the observable can be calculate from each set of the sample data. The root mean square of the estimated observable from each sample lead us to the final error for that particular observable. For example let's say for a sample N there are $x_1, x_2, x_3...x_n$ variables to calculate an observable O. Then for a random generator there will be n^n number of ways to make samples. For a

sample size A, the error for O, from the bootstrap method is given by,

$$Var(O) = \frac{\sum_{i=1}^{A}[O'(x_i) - s]^2}{A - 1} \tag{A.5}$$

where, O' represent the observable from each sample and s is given by,

$$s = \sum_{i=1}^{A} \frac{s(x_i)}{B} \tag{A.6}$$

The performance of this method is better with large ($\geq$ 200) number of bootstrap samples. This method required huge time and computational work for larger data set.

Bibliography

[1] Joseph Silk, "Horizons of Cosmology " *Templeton Press* , (2009) p. 208.

[2] Simon Singh, "Big Bang: The Origin of the Universe. Harper Perennial "*Harper Perennial* , (2005) p. 560.

[3] E. J. Wollack, "Cosmology: The Study of the Universe. Universe 101: Big Bang Theory. " , (2010, 2011).

[4] Joseph Silk, "Planck reveals an almost perfect universe " *Planck. ESA* , (2013).

[5] R. Oerter, "The Theory of Almost Everything: The Standard Model, the Unsung Triumph of Modern Physics (Kindle ed.). " *Penguin Group* , (2006) p. 2. ISBN 0-13-236678-9.

[6] E.D. Bloom *et al.*, "High-Energy Inelastic $e - p$ Scattering at 6^o and 10^o, " *Phys. Rev. Lett.* **23 (16)**, (1969) 930-934.

[7] M. Breidenbach *et al.*, "Observed Behavior of Highly Inelastic Electron-Proton Scattering, " *Phys. Rev. Lett.* **23 (16)**, (1969) 935-939.

[8] Encyclopdia Britannica, (1969). "Lepton (physics, " *Retrieved* , (2010).

[9] Sean Carroll, "Dark Matter, Dark Energy: The Dark Side of the Universe, Guidebook, " *Part* **2**, (2007) p. 43.

[10] John C. Wells, "Longman pronunciation dictionary, " *Harlow, England:* **Longman**, (1990).

[11] D. J. Gross and F. Wilczek , "Ultraviolet Behavior of Non-Abelian Gauge Theories, " *Phys. Rev. Lett.* **30 (26)**, (1973) 1343-1346.

[12] H. Fritzsch and M. Gell-Mann, "QCD: The theory of strong interactions, " *Proc. XVI Int. Conf. on High Energy Physics.* , (1972).

[13] H. Fritzsch, M. Gell-Mann and H. Leutwyler, "ADVANTAGES OF THE COLOR OCTET GLUON PICTURE, " *Phys. Lett. B.* **47**, (1973) 365.

[14] T. van Ritbergen, J.A.M. Vermaseren, S.A. Larin, "The four-loop beta-function in Quantum Chromodynamics, " *Phys. Lett. B.* **400**, (1997) 379.

[15] Siegfried Bethke, "Experimental Tests of Asymptotic Freedom, " *Prog. Part. Nucl. Phys.* **58**, (2007) 351-386.

[16] E. Fermi, "Notes on Termodynamics and Statistics, " (1953).

[17] I. Ya. Pomeranchuk, Doklady Akad. Nauk, "Experimental Tests of Asymptotic Freedom, " *Nauk. SSSR.* **78**, (1981) 889.

[18] R. Hagedorn, "Statistical thermodynamics of strong interaction at high energies, " *Nuovo Cim. Suppl.* **3**, (1965) 147.

[19] D.J. Gross and F. Wilczek, "Ultraviolet Behavior of Non-Abelian Gauge Theories, " *Phys. Rev. Lett.* **30 (26)**, (1973) 1343-1346.

[20] H.D. Politzer, "Reliable Perturbative Results for Strong Interactions, " *Phys. Rev. Lett.* **30**, (1973) 1346.

[21] Siegfried Bethke, "Experimental Tests of Asymptotic Freedom, " *Prog. Part. Nucl. Phys.* **58**, (2007) 351-386.

[22] K.G. Wilson, "Confinement of quarks, " *Phys. Rev. D.* **10**, (1974) 2445.

[23] A. M. Polyakov, "Confinement of quarks, " *Nucl. Phys. B.* **120**, (1977) 429.

[24] **STAR** Collaboration, M. M. Aggarwal, *et al* "An Experimental Exploration of the QCD Phase Diagram: The search for the Critical Point and the Onset of De-confinement, " *arXiv:nucl-ex/10072613.* (2010)

[25] **STAR** Collaboration, TC. Adler, *et al* "Centrality Dependence of High p_T Hadron Suppression in Au + Au Collisions at $\sqrt{s_{NN}}$ = 130 GeV, " *Phys. Rev. Lett* **89**, (2002) 202301.

[26] Michael L. Miller et al. Annu. Rev. Nucl. Part. Sci. 2007. 57:205; arXiv:0701025 [nucl-ex].

[27] **STAR** Collaboration, J. Adams, *et al* "Evidence from d+Au measurements for final-state suppression of high p_T hadrons in Au+Au collisions at RHIC , " *Phys. Rev. Lett* **91**, (2003) 072304.

[28] **PHENIX** Collaboration, S. S. Adler, *et al* "Common Suppression Pattern of η and π^0 Mesons at High Transverse Momentum in Au+Au Collisions at $\sqrt{s_{NN}}$ = 200 GeV" *Phys. Rev. Lett* **96**, (2006) 202301.

[29] W. Reisdorf and H. G Ritter, "Collective Flow in Heavy-Ion Collisions "*Annual Review of Nuclear and Particle Science* **47**, (1997) 663.

[30] W. Reisdorf and H. G Ritter, "Collective Flow in Heavy-Ion Collisions "*Annual Review of Nuclear and Particle Science* **47**, (1997) 663.

[31] J. Adams, *et al.*, "Experimental and Theoretical Challenges in the Search for the Quark Gluon Plasma: The STAR Collaboration's Critical Assessment of the Evidence from RHIC Collisions"*Nucl. Phys. A* **757**, (2005) 102.

[32] J. Y Ollitrault, *et al.*, "Anisotropy as a signature of transverse collective flow "*Phys. Rev. D* **46**, (1997) 229.

[33] J. Rafelski and B. Muller,"Strangeness Production in the Quark-Gluon Plasma" Phys. Rev. Lett. 48, (1982) 1066

[34] P. Koch, B. Muller and J. Rafelski, "Fast hadronization of a quark gluon plasma and meson production" Phy. Rep. 142 (1986) 167

[35] STAR Collaboration, "Strangeness Enhancement in Cu+Cu and Au+Au $\sqrt{s_{NN}}$ = 200 GeV Collisions"Phys. Rev. Lett. 108 (2012) 72301

[36] STAR Collaboration, "Energy and system size dependence of ϕ meson production in image and image collisions" Phys. Lett. B 673 (2009) 183

[37] J. Adams, *et al.*, "Experimental and Theoretical Challenges in the Search for the Quark Gluon Plasma: The STAR Collaboration's Critical Assessment of the Evidence from RHIC Collisions"*Nucl. Phys. A* **757**, (2005) 102.

[38] M. Stephanov, "QCD phase diagram: an overview" arXiv:hep-lat/0701002v1

[39] Cabibbo N. and Parisi G. "Exponential hadronic spectrum and quark liberation" Phys. Lett. B 59 (1975) 67

[40] R. Hagedorn, Nuovo Cimento Suppl. 3 (1965) 147

[41] R. Hagedorn and J. Ranft, Nuovo Cimento Suppl. 6 (1968) 169.

[42] R. D. Pisarski and F. Wilczek, "Remarks on the chiral phase transition in chromodynamics" Phys. Rev. D 29 (1984) 338.

[43] K. Szabo, "Twisted mass QCD thermodynamics: first results on apeNEXT" PoS(LAT2006)149.

[44] M. Cheng et al., "Baryon Number, Strangeness and Electric Charge Fluctuations in QCD at High Temperature" Phys. Rev. D 79, 074505 (2009); arXiv:0811.1006 [hep-lat].

[45] R.V. Gavai, S. Gupta, Phys. Rev. D 71 (2005) 114014, R. V. Gavai and S. Gupta, Phys. Rev. D 78, 114503 (2008).

[46] M. A. Stephanov, "Sign of Kurtosis near the QCD Critical Point" Phys. Rev. Lett. 107, 052301(2011).

[47] F. Karsch, , "Lattice results on QCD thermodynamics "*arXiv: 0103314 [hep-ph]* (2002) 199-208.

[48] S. Ejiri, *et al.*, "Lattice results on QCD thermodynamics "*Prog. Theor. Phys. Suppl.* **153** (2004) 118.

[49] P. de Forcrand, *et al.*, "The phase diagram of $N_f = 3$ QCD for small baryon densities "*Nucl. Phys. B* **673** (2004) 170.

[50] Z. Fodor, *et al.*, "Lattice determination of the critical point of QCD at finite T and μ "*JHEP* **0203** (2002) 014.

[51] N. G. Antoniou, *et al.*, "Bootstraping the QCD Critical Point "*Phys. Lett. B* **563** (2003) 165.

[52] A. Barducci, R. Casalbuoni, S. De Curtis, R. Gatto and G. Pettini, Phys. Lett. B 231 (1989) 463; Phys. Rev. D 41 (1990) 1610.

[53] A. Barducci, R. Casalbuoni, G. Pettini and R. Gatto, Phys. Rev. D 49 (1994) 426.

[54] J. Berges and K. Rajagopal, Nucl. Phys. B 538 (1999) 215 [arXiv:hep-ph/9804233].

[55] M. A. Halasz, A. D. Jackson, R. E. Shrock,M. A. Stephanov and J. J. M. Verbaarschot, Phys. Rev. D 58 (1998) 096007 [arXiv:hep-ph/9804290].

[56] Y. Hatta and T. Ikeda, Phys. Rev. D 67 (2003) 014028 [arXiv:hep-ph/0210284].

[57] S. Roessner, C. Ratti and W. Weise, arXiv:hep-ph/0609281.

[58] O. Scavenius, A. Mocsy, I. N. Mishustin and D. H. Rischke, Phys. Rev. C 64 (2001), 045202 [arXiv:nucl-th/0007030].

[59] A. Barducci, R. Casalbuoni, G. Pettini and L. Ravagli, Phys. Rev. D 72, 056002 (2005) [arXiv:hep-ph/0508117].

[60] M. Asakawa and K. Yazaki, Nucl. Phys. A 504 (1989) 668.

[61] M. Harrison, T. Ludlam, S. Ozaki, "RHIC project overview," *Nucl. Instrum. Meth.* **A 499** (2003) 235 - 244.

[62] $http://www.bnl.gov/rhic/RHIC\_complex.htm.$

[63] H. Hahn *et al.*, "The RHIC design overview," *Nucl. Instrum. Meth.* **A 499** (2003) 245 - 263.

[64] P. Braun-Munzinger, K. Redlich and J. Stachel, arXiv:nucl-th/0304013.

[65] M. A. Stephanov, Int.J.Mod.Phys.A20:4387-4392 (2005); arXiv:hepph/0402115

[66] **Wikipedia** Source, "Moments " http://en.wikipedia.org/wiki/Moment˙(mathematics)

[67] **Mathworld** Source, "Raw Moments at Math-world " http://mathworld.wolfram.com/RawMoment.html

[68] **Wikipedia** Source, "Skewness " http://en.wikipedia.org/wiki/Skewness

[69] **Wikipedia** Source, "Kurtosis " http://en.wikipedia.org/wiki/Kurtosis

[70] **Wikipedia** Source, "Cumulants " http://en.wikipedia.org/wiki/Cumulant

[71] K. Wilson, , "Confinement of quarks," *Phys. Rev. D* **10** (1974) 2445.

[72] **Wikipedia** Source, "Lattice QCD " http://en.wikipedia.org/wiki/Lattice˙QCD

[73] K. Wilson, , "Confinement of quarks," *arxiv.org: 9807028 [hep-lat]* (1998).

[74] G. N Lewis and M. Randall, , "Thermodynamics," *2nd Edition* (1961).

[75] **Wikipedia** Source, "Intensive and extensive properties " http://en.wikipedia.org/wiki/Intensive˙and˙extensive˙properties

[76] F. Karsch and K. Redlich, , "Probing freeze-out conditions in heavy ion collisions with moments of charge fluctuations," *Phys. Lett. B* **695** (2011) 136-142.

[77] S. Borsanyi, *et al.*, "Freeze-out parameters from electric charge and baryon number fluctuations: is there consistency?," *arXiv: 1403.4576v2 [hep-lat]* (2014).

[78] P. Braun-Munzinger *et al.*, "Particle Production in Heavy Ion Collisions," *arXiv: 0304013 [nucl-th]* (2003).

[79] M. Cheng *et al.*, "Baryon number, strangeness, and electric charge fluctuations in QCD at high temperature," *Phys. Rev. D* **79** (2009) 074505.

[80] Y. V. Kovchegov *et al.*, "Large Scale Rapidity Correlations in Heavy Ion Collisions," *Phys. Rev. C* **63** (2001) 024903.

[81] F. Karsch and K. Redlich, , "Probing freeze-out conditions in heavy ion collisions with moments of charge fluctuations," *Phys. Lett. B* **695** (2011) 136-142.

[82] R. V. Gavai and S. Gupta, , "Probing freeze-out conditions in heavy ion collisions with moments of charge fluctuations," *Phys. Lett. B* **696** (2011) 459.

[83] M. A. Stephanov, , "Non-Gaussian Fluctuations near the QCD Critical Point," *Phys. Rev. Lett* **102** (2009) 032301.

[84] S. Gupta, , "Finding the critical end point of QCD: lattice and experiment," *arXiv:0909.4630 [nucl-ex]* (2009).

[85] M. Asakawa *et al.*, "Third moments of conserved charges as probes of QCD phase structure," *Phys. Rev. Lett.* **103** (2009) 262301.

[86] M. Asakawa et al., Phys. Rev. Lett. 103, 262301 (2009).

[87] **STAR** Collaboration, K. H. Ackermann *et al.*, "STAR Detector Overview," *Nucl. Instrum. Meth.* **A 499** (2003) 624.

[88] **STAR** Collaboration, F. Bergsma *et al.*, "The STAR detector magnet subsystem," *Nucl. Instrum. Meth.* **A 499** (2003) 633 - 639.

[89] **STAR** Collaboration, M. Anderson *et al.*, "The STAR Time Projection Chamber: A Unique Tool for Studying High Multiplicity Events at RHIC," *Nucl. Instrum. Meth.* **A 499** (2003) 659.

[90] **STAR** Collaboration, G. Van Buren *et al.*, "Correcting for Distortions due to Ionization in the STAR TPC," *Nucl. Instrum. Meth.* **A 566**, (2006) 22.

[91] **STAR** Collaboration, G. Van Buren *et al.*, "Precision Calibration of the STAR TPC," *Nucl. Inst. and Meth.* **A 566** (2006) 22.

[92] W. R. Leo, "Techniques for Nuclear and Particle Physics Experiments."

[93] **STAR** Collaboration, M. Shao *et al.*, "Extensive Particle Identification with TPC and TOF at the STAR Experiment," *Nucl. Instrum. Meth.* **A 558** (2006) 419.

[94] W.J. Llope, *et al.*, "The TOFp/pVPD Time-Of-Flight System for STAR," *arXiv nucl-ex/0308022.* (2003).

[95] **STAR** Collaboration, "STAR Time Of Flight," *Winter Workshop.* (2008).

[96] **STAR** Collaboration, W.J. Llope, "Proposal for a Larhe Area Time Of Flight System for STAR," (2004). http://www.star.bnl.gov/ ruanlj/MTDreview2010/TOF˙20040524.pdf

[97] **STAR** Collaboration, R. Bellwied *et al.*, "The STAR Silicon Vertex Tracker: A large area Silicon Drift Detector," *Nucl. Instrum. Meth.* **A 439** (2000) 497.

[98] **STAR** Collaboration, L. Arnold *et al.*, "The STAR silicon strip detector (SSD)," *Nucl. Instrum. Meth.* **A 499** (2003) 652.

[99] **ALICE** Collaboration, L. Hebrard *et al.*, "A CMOS full custom ASIC for the readout of silicon strip detectors in the ALICE experiment," *3rd workshop on electronics for LHC experiments.* (1997).

[100] L. Hebrard et al., ALICE 128C : a CMOS full custom ASIC for the readout of silicon strip detectors in the ALICE experiment, proceeding of the 3rd workshop on electronics for LHC experiments, London, Sept. 1997

[101] **STAR** Collaboration, M.M. Aggarwal *et al.*, "The STAR Photon Multiplicity Detector," *Nucl. Instrum. Meth.* **A 499** (2003) 751.

[102] P. Tribedy, Ph.D thesis, VECC, 2015

[103] **STAR** Collaboration, M. Beddo *et al.*, "STAR Barrel Electromagnetic Calorimeter, " *Nucl. Instrum. Meth.* **A 499** (2003) 725.

[104] **STAR** Collaboration, C.E. Allgower *et al.*, "The forward time projection chamber in STAR," *Nucl. Instrum. Meth.* **A 499** (2003) 713.

[105] **STAR** Collaboration, K.H. Ackermann *et al.*, "The forward time projection chamber in STAR," *Nucl. Instrum. Meth.* **A 499** (2003) 713.

[106] **PHENIX** Collaboration, Astrid Morreale, "Recent Spin Results from the PHENIX Detector at RHIC " *Annu. Rev. Nucl. Part. Sci.* **50** (2000).

[107] **STAR** Collaboration, C.E. Allgower *et al.*, "The STAR endcap electromagnetic calorimeter," *Nucl. Instrum. Meth.* **A 499** (2003) 740.

[108] G. Bunce, N. Saito, J. Soffer and W. Vogelsang, "Physics with Polarized Beams " *Annu. Rev. Nucl. Part. Sci.* **50** (2000).

[109] **STAR** Collaboration, L.C. Bland *et al.*, "Spin Physics with the STAR detector " *arXiv:hep-ex/0002061.* (2000).

[110] **STAR** Collaboration, L.C. Bland *et al.*, "An Endcap Electromagnetic Calorimeter for Star: Conceptual Design Report " *STAR Note.* **A 401** (1999).

[111] **STAR** Collaboration, J.M. Landgraf *et al.*, "The STAR Level-3 trigger system " *Nucl. Instrum. Meth.* **A 499** (2003) 778.

[112] **STAR** Collaboration, J.M. Landgraf *et al.*, "The STAR trigger," *Nucl. Instrum. Meth.* **A 499** (2003) 766.

[113] **STAR** Collaboration, J.M. Landgraf *et al.*, "An overview of the STAR DAQ system," *Nucl. Instrum. Meth.* **A 499** (2003) 762.

[114] Grazyna Odyniec, Journal of Physics: Conference Series 455 (2013) 012037

[115] STAR Collaboration, "STAR Results from the RHIC Beam Energy Scan-I" http://arxiv.org/abs/1211.1350

[116] M. M. Aggarwal et al., arXiv:1007.2613, 2010.

[117] Yuting Bai, Anisotropic Flow Measurements in STAR at the Relativistic Heavy Ion Collider

[118] http://www.star.bnl.gov/cgi-bin/protected/cvsweb.cgi/offline/users/hmasui/StRefMultCor

[119] http://en.wikipedia.org/wiki/Errors˙and˙residuals˙in˙statistics

[120] X. Luo, J. Phys. G: Nucl. Part. Phys. 39, 025008 (2012).

[121] arXiv:1312.4574v1 [nucl-th] 16 Dec 2013

[122] http://en.wikipedia.org/wiki/Bootstrapping˙(statistics)

[123] Bradley Efron, Computers and the Theory of Statistics: Thinking the Unthinkable ; http://www.jstor.org/stable/2030104

[124] R. Hagedorn, in Quark Matter 84, Lecture Notes in Physics, Vol. 211 (Springer, Berlin 1985); R. Hagedorn, Riv. Nuovo Cim. 6, 1 (1983); R. Fiore, R. Hagedorn and F. DIsep Nuovo Cim. 88 A, 301 (1985).

[125] A. Andronic **et al.**,"Statistical hadronization of charm in heavy-ion collisions at SPS, RHIC and LHC " *Phys. Lett. B* **571** (2003) 36.

[126] J. Noronha-Hostler **et al.**,"Transport Coefficients of Hadronic Matter near T_c *Phys. Rev. Lett* **103** (2009) 172302.

[127] P. Braun-Munzinger **et al.**,"Chemical freeze-out and the QCD phase transition temperature " *Phys. Lett. B* **596** (2004) 61.

[128] F. Karsch **et al.**,"Hadron Resonance Mass Spectrum and Lattice QCD Thermodynamics " *Eur. Phys. J. C* **29** (2003) 549.

[129] F. Karsch and K. Redlich ,"Moments of charge fluctuations, pseudo-critical temperatures and freeze-out in heavy ion collisions " *Phys. Lett. B* **695** (2011).

[130] J. Cleymans **et al.**,"Comparison of chemical freeze-out criteria in heavy-ion collisions " *Phys. Rev. C* **73** (2006) 034905.

[131] P. Garg **et al.**,"Conserved number fluctuations in a hadron resonance gas model " *arXiv:1304.7133v2 [nucl-ex]* (2013).

[132] **Web** Source, "UrQMD " http://en.wikipedia.org/wiki/UrQMD

[133] **Web** Source, "UrQMD " http://urqmd.org/general

[134] **Web** Source, "UrQMD " https://sites.google.com/a/lbl.gov/relativistic-nuclear-collisions/home

[135] **Web** Source, "Geant 4 " http://en.wikipedia.org/wiki/Geant4

[136] H. Petersen **et al.**,"Fully integrated transport approach to heavy ion reactions with an intermediate hydrodynamic stage " *Phys. Rev. C* **78** (2008) 044901.

[137] S. A. Bass **et al.**,"Microscopic Models for Ultrarelativistic Heavy Ion Collisions " *Prog. Part. Nucl. Phys.* **41** (1998) 225-370.

[138] M. Bleicher **et al.**,"Relativistic Hadron-Hadron Collisions in the Ultra-Relativistic Quantum Molecular Dynamics Model " *J. Phys. G: Nucl. Part. Phys* **25** (1999) 1859-1896.

[139] N. R. Sahoo **et al.**,"Baseline study for higher moments of net-charge multiplicity distributions at RHIC energies " *Phys. Rev. C* **87** (2013) 044906.

[140] **Web** Source, "Poisson distribution " http://en.wikipedia.org/wiki/Poisson_distribution

[141] Frank A. Haight (1967). Handbook of the Poisson Distribution. New York: John Wiley Sons.

[142] **Web** Source, "Skellam distribution" http://en.wikipedia.org/wiki/Skellam_distribution

[143] **Web** Source, "Negative Binomial Distribution " http://en.wikipedia.org/wiki/Negative_binomial_distribution

[144] **Web** Source, "Central Limit Theorem " http://www.math.uah.edu/stat/sample/CLT.html

[145] **Web** Source, "The Central Limit Theorem " http://en.wikipedia.org/wiki/Central_limit_theorem

[146] N. Shao, Ph.D thesis, VECC, 2014

List of Publications

Publications:

- **Observation of Transverse Spin-Dependent Azimuthal Correlations of Charged Pion Pairs in $p + p$ at $\sqrt{s} =$ 200 GeV**
  L. Adamczyk *et al.*, (STAR Collaboration), Phys. Rev. Lett. 115 (2015) 242501
  e-Print Archives (1504.00415)
- **Azimuthal anisotropy in $U + U$ and $Au + Au$ collisions at RHIC**
  L. Adamczyk *et al.*, (STAR Collaboration), Phys. Rev. Lett. 115 (2015) 222301
  e-Print Archives (1505.07812)
- **Energy dependence of acceptance-corrected dielectron excess mass spectrum at mid-rapidity in $Au + Au$ collisions at $\sqrt{s_{NN}} = 19.6$ and 200 GeV**
  L. Adamczyk *et al.*, (STAR Collaboration), Phys. Lett. B 750 (2015) 64
  e-Print Archives (1501.05341)
- **Di-Hadron Correlations with Identified Leading Hadrons in 200 GeV $Au+Au$ and $d + Au$ Collisions at STAR**
  N. M. Abdelwahab *et al.*, (STAR Collaboration), Phys. Lett. B 751 (2015) 233
  e-Print Archives (1410.3524)
- **Measurement of interaction between antiprotons**
  L. Adamczyk *et al.*, (STAR Collaboration), Nature 527 (2015) 345
  e-Print Archives (1507.07158)
- **Precision Measurement of the Longitudinal Double-spin Asymmetry for Inclusive Jet Production in Polarized Proton Collisions at $\sqrt{s}$ = 200 GeV**
  L. Adamczyk *et al.*, (STAR Collaboration), Phys. Rev. Lett. 115 (2015) 92002
  e-Print Archives (1405.5134)
- **Measurements of Dielectron Production in $Au + Au$ Collisions at $\sqrt{s_{NN}} =$ 200 GeV from the STAR Experiment**
  L. Adamczyk *et al.*, (STAR Collaboration), Phys. Rev. C 92 (2015) 24912
  e-Print Archives (1504.01317)
- **Energy Dependence of K-pi, p-pi, and K-p Fluctuations in $Au + Au$ Collisions from $\sqrt{s_{NN}} =$ 7.7 to 200 GeV**
  N. M. Abdelwahab *et al.*, (STAR Collaboration), Phys. Rev. C 92 (2015) 21901
  e-Print Archives (1410.5375)

- **Long-range pseudo-rapidity dihadron correlations in d+Au collisions at $\sqrt{s_{NN}} =$ 200 GeV**
  L. Adamczyk $et\ al.$, (STAR Collaboration), Phys. Lett. B 747 (2015) 265
  e-Print Archives (1502.07652)
- **Beam energy dependent two-pion interferometry and the freeze-out eccentricity of pions in heavy ion collisions at STAR**
  L. Adamczyk $et\ al.$, (STAR Collaboration), Phys. Rev. C 92 (2015) 14904
  e-Print Archives (1403.4972)
- **Observation of charge asymmetry dependence of pion elliptic flow and the possible chiral magnetic wave in heavy-ion collisions**
  L. Adamczyk $et\ al.$, (STAR Collaboration), Phys. Rev. Lett. 114 (2015) 252302
  e-Print Archives (1504.02175)
- **Isolation of Flow and Nonflow Correlations by Two- and Four-Particle Cumulant Measurements of Azimuthal Harmonics in $\sqrt{s} =$ 200 GeV $Au + Au$ Collisions**
  N. M. Abdelwahab $et\ al.$, (STAR Collaboration), Phys. Lett. B 745 (2015) 40
  e-Print Archives (1409.2043)
- **Effect of event selection on jetlike correlation measurement in $d + Au$ collisions at 200 GeV**
  L. Adamczyk $et\ al.$, (STAR Collaboration), Phys. Lett. B 743 (2015) 333
  e-Print Archives (1412.8437)
- **Charged-to-neutral correlation at forward rapidity in $Au + Au$ collisions at 200 GeV**
  L. Adamczyk $et\ al.$, (STAR Collaboration), Phys. Rev. C 91 (2015) 34905
  e-Print Archives (1408.5017)
- **Cosmic Ray Test of Mini-drift Thick Gas Electron Multiplier Chamber for Transition Radiation Detector**
  Nucl. Instrum. Meth. A 785 (2015) 33
  e-Print Archives (1412.4769)
- **The Lambda Lambda Correlation Function in Au+Au collisions at $\sqrt{s_{NN}} =$ 200 GeV**
  L. Adamczyk $et\ al.$, (STAR Collaboration), Phys. Rev. Lett. 114 (2015) 22301
  e-Print Archives (1408.4360)
- **J/ψ polarization in $p + p$ collisions at $\sqrt{s}$ = 200 GeV in STAR**
  L. Adamczyk $et\ al.$, (STAR Collaboration), Phys. Lett. B 739 (2014) 180
  e-Print Archives (1311.1621)

- **Dielectron Azimuthal Anisotropy at mid-rapidity in $Au + Au$ collisions at $\sqrt{s_{NN}} = 200\ GeV$**
  L. Adamczyk *et al.*, (STAR Collaboration), Phys. Rev. C 90 (2014) 64904
  e-Print Archives (1402.1791)
- **Calibration and performance of the STAR Muon Telescope Detector using cosmic rays**
  L. Adamczyk *et al.*, (STAR Collaboration), Nucl. Instrum. Meth. A 762 (2014) 1
  e-Print Archives (1402.1078)
- **Observation of D^0 meson nuclear modifications in $Au + Au$ collisions at $\sqrt{s_{NN}}$ = 200 GeV**
  L. Adamczyk *et al.*, (STAR Collaboration), Phys. Rev. Lett. 113 (2014) 142301
  e-Print Archives (1404.6185)
- **Beam-energy dependence of charge separation along the magnetic field in $Au + Au$ collisions at RHIC**
  L. Adamczyk *et al.*, (STAR Collaboration), Phys. Rev. Lett. 113 (2014) 52302
  e-Print Archives (1404.1433)
- **Measurement of longitudinal spin asymmetries for weak boson production in polarized proton-proton collisions at RHIC**
  L. Adamczyk *et al.*, (STAR Collaboration), Phys. Rev. Lett. 113 (2014) 72301
  e-Print Archives (1404.6880)
- **J/ψ production at low p_T in $Au + Au$ and Cu+Cu collisions at $\sqrt{s_{NN}}$ = 200 GeV at STAR**
  L. Adamczyk *et al.*, (STAR Collaboration), Phys. Rev. C 90 (2014) 24906
  e-Print Archives (1310.3563)
- **Beam energy dependence of moments of the net-charge multiplicity distributions in $Au + Au$ collisions at RHIC**
  L. Adamczyk *et al.*, (STAR Collaboration), Phys. Rev. Lett. 113 (2014) 92301
  e-Print Archives (1402.1558)
- **Beam-Energy Dependence of Directed Flow of Protons, Antiprotons and Pions in $Au + Au$ Collisions**
  L. Adamczyk *et al.*, (STAR Collaboration), Phys. Rev. Lett. 112 (2014) 162301
  e-Print Archives (1401.3043)
- **Dielectron Mass Spectra from $Au + Au$ Collisions at $\sqrt{s_{NN}}$ = 200 GeV**
  L. Adamczyk *et al.*, (STAR Collaboration), Phys. Rev. Lett. 113 (2014) 22301
  e-Print Archives (1312.7397)

- **Suppression of Upsilon Production in d+Au and $Au + Au$ Collisions at $\sqrt{s_{NN}}$ = 200 GeV**
  L. Adamczyk *et al.*, (STAR Collaboration), Phys. Lett. B 735 (2014) 127
  e-Print Archives (1312.3675)
- **Thermal neutron flux measurements in the STAR experimental hall**
  L. Adamczyk *et al.*, (STAR Collaboration), Nucl. Instrum. Meth. A 756 (2014) 68
  e-Print Archives (arXiv:1310.2495)
- **Energy dependence of moments of net-proton multiplicity distributions at RHIC**
  L. Adamczyk *et al.*, (STAR Collaboration), Phys. Rev. Lett. 112 (2014) 32302
  e-Print Archives (1309.5681)
- **Neutral pion cross section and spin asymmetries at intermediate pseudorapidity in polarized proton collisions at $\sqrt{s}$=200 GeV**
  L. Adamczyk *et al.*, (STAR Collaboration), Phys. Rev. D 89 (2014) 12001
  e-Print Archives (1309.1800)
- **Measurement of Charge Multiplicity Asymmetry Correlations in High Energy Nucleus-Nucleus Collisions at 200 GeV**
  L. Adamczyk *et al.*, (STAR Collaboration), Phys. Rev. C 89 (2014) 44908
  e-Print Archives (1303.0901)
- **Jet-Hadron Correlations in $\sqrt{s_{NN}}$ = 200 GeV $Au + Au$ and p+p Collisions**
  L. Adamczyk *et al.*, (STAR Collaboration), Phys. Rev. Lett. 112 (2014) 122301
  e-Print Archives (1302.6184)
- **Fluctuations of charge separation perpendicular to the event plane and local parity violation in $\sqrt{s_{NN}}$=200 GeV $Au + Au$ collisions at RHIC**
  L. Adamczyk *et al.*, (STAR Collaboration), Phys. Rev. C 88 (2013) 64911
  e-Print Archives (1302.3802)
- **Freeze-out Dynamics via Charged Kaon Femtoscopy in $\sqrt{s_{NN}}$=200 GeV Central $Au + Au$ Collisions**
  L. Adamczyk *et al.*, (STAR Collaboration), Phys. Rev. C 88 (2013) 34906
  e-Print Archives (1302.3168)
- **System Size Dependence of Transverse Momentum Correlations at RHIC**
  L. Adamczyk *et al.*, (STAR Collaboration), Phys. Rev. C 87 (2013) 64902
  e-Print Archives (arXiv:1301.6633)
- **Third Harmonic Flow of Charged Particles in $Au + Au$ Collisions at $\sqrt{s_{NN}}$ = 200 GeV**

L. Adamczyk *et al.*, (STAR Collaboration), Phys. Rev. C 88 (2013) 14904
e-Print Archives (1301.2187)

- **Observation of an energy-dependent difference in elliptic flow between particles and antiparticles in relativistic heavy ion collisions**
  L. Adamczyk *et al.*, (STAR Collaboration), Phys. Rev. Lett. 110 (2013) 142301
  e-Print Archives (1301.2347)
- **Elliptic flow of identified hadrons in $Au+Au$ collisions at $\sqrt{s_{NN}} =$ 7.7–62.4 GeV**
  L. Adamczyk *et al.*, (STAR Collaboration), Phys. Rev. C 88 (2013) 14902
  e-Print Archives (1301.2348)
- **Measurement of J/psi Azimuthal Anisotropy in $Au+Au$ Collisions at $\sqrt{s_{NN}}$= 200 GeV**
  L. Adamczyk *et al.*, (STAR Collaboration), Phys. Rev. Lett. 111 (2013) 52301
  e-Print Archives (arXiv:1212.3304)
- **Studies of di-jets in $Au + Au$ collisions using angular correlations with respect to back-to-back leading hadrons**
  L. Adamczyk *et al.*, (STAR Collaboration), Phys. Rev. C 87 (2013) 44903
  e-Print Archives (arXiv:1212.1653)
- **J/ψ production at high transverse momenta in p+p and $Au + Au$ collisions at $\sqrt{s_{NN}}$ = 200 GeV**
  L. Adamczyk *et al.*, (STAR Collaboration), Phys. Lett. B 722 (2013) 55
  e-Print Archives (1208.2736)
- **Inclusive charged hadron elliptic flow in Au + Au collisions at $\sqrt{s_{NN}}$ = 7.7 - 39 GeV**
  L. Adamczyk *et al.*, (STAR Collaboration), Phys. Rev. C 86 (2012) 54908
  e-Print Archives (arXiv:1206.5528)
- **Single Spin Asymmetry A_N in Polarized Proton-Proton Elastic Scattering at $\sqrt{s} = 200$ GeV**
  L. Adamczyk *et al.*, (STAR Collaboration), Phys. Lett. B 719 (2013) 62
  e-Print Archives (1206.1928)
- **Transverse Single-Spin Asymmetry and Cross-Section for π^0 and η Mesons at Large Feynman-x in Polarized p+p Collisions at $\sqrt{s}$ = 200 GeV**
  L. Adamczyk *et al.*, (STAR Collaboration), Phys. Rev. D 86 (2012) 51101
  e-Print Archives (1205.6826)
- **Longitudinal and transverse spin asymmetries for inclusive jet production at mid-rapidity in polarized p+p collisions at $sqrts$=200 GeV**

L. Adamczyk *et al.*, (STAR Collaboration), Phys. Rev. D 86 (2012) 32006
e-Print Archives (1205.2735)

- **Measurements of D^0 and D^* Production in p + p Collisions at $\sqrt{s}$ = 200 GeV**
  L. Adamczyk *et al.*, (STAR Collaboration), Phys. Rev. D 86 (2012) 72013
  e-Print Archives (1204.4244)
- **Di-electron spectrum at mid-rapidity in $p + p$ collisions at $\sqrt{s} = 200$ GeV**
  L. Adamczyk *et al.*, (STAR Collaboration), Phys. Rev. C 86 (2012) 24906
  e-Print Archives (1204.1890)
- **Directed Flow of Identified Particles in Au + Au Collisions at $\sqrt{s_{NN}} = 200$ GeV at RHIC**
  L. Adamczyk *et al.*, (STAR Collaboration), Phys. Rev. Lett. 108 (2012) 202301
  e-Print Archives (1112.3930)
- **Measurement of the $W \to e\nu$ and $Z/\gamma^* \to e^+e^-$ Production Cross Sections at Mid-rapidity in Proton-Proton Collisions at $\sqrt{s}$ = 500 GeV**
  G. Agakishiev *et al.*, (STAR Collaboration), Phys. Rev. D 85 (2012) 92010
  e-Print Archives (1112.2980)
- **Energy and system-size dependence of two- and four-particle v_2 measurements in heavy-ion collisions at 62.4 and 200 GeV and their implications on flow fluctuations and nonflow**
  G. Agakishiev *et al.*, (STAR Collaboration), Phys. Rev. C 86 (2012) 14904
  e-Print Archives (arXiv:1111.5637v1)
- **System size and energy dependence of near-side di-hadron correlation**
  G. Agakishiev *et al.*, (STAR Collaboration), Phys. Rev. C 85 (2012) 14903
  e-Print Archives (nucl-ex/1110.5800)
- **Identified hadron compositions in p+p and $Au + Au$ collisions at high transverse momenta at $\sqrt{s_{NN}} = 200$ GeV**
  G. Agakishiev *et al.*, (STAR Collaboration), Phys. Rev. Lett. 108 (2012) 72302
  e-Print Archives (1110.0579)
- **Directed and elliptic flow of charged particles in Cu+Cu collisions at $\sqrt{s_{NN}} =$ 22.4 GeV**
  G. Agakishiev *et al.*, (STAR Collaboration), Phys. Rev. C 85 (2012) 14901
  e-Print Archives (1109.5446)
- **Anomalous centrality evolution of two-particle angular correlations from Au-Au collisions at $\sqrt{s_{\rm NN}}$ = 62 and 200 GeV**

G. Agakishiev *et al.*, (STAR Collaboration), Phys. Rev. C 86 (2012) 64902
e-Print Archives (1109.4380)

- rho^0 **Photoproduction in AuAu Collisions at $\sqrt{s_{NN}}$=62.4 GeV with STAR**
  G. Agakishiev *et al.*, (STAR Collaboration), Phys. Rev. C 85 (2012) 14910
  e-Print Archives (arXiv:1107.4630)
- **Strangeness Enhancement in Cu+Cu and $Au + Au$ $\sqrt{s_{NN}}$ 200 GeV Collisions**
  G. Agakishiev *et al.*, (STAR Collaboration), Phys. Rev. Lett. 108 (2012) 72301
  e-Print Archives (1107.2955)
- **Evolution of the differential transverse momentum correlation function with centrality in $Au + Au$ collisions at $\sqrt{s_{NN}} = 200$ GeV**
  H. Agakishiev *et al.*, (STAR Collaboration), Phys. Lett. B 704 (2011) 467
  e-Print Archives (1106.4334)
- **Observation of the antimatter helium-4 nucleus**
  H. Agakishiev *et al.*, (STAR Collaboration), Nature 473 (2011) 353
  e-Print Archives (1103.3312)
- **Experimental studies of di-jet survival and surface emission bias in $Au + Au$ collisions via angular correlations with respect to back-to-back leading hadrons**
  H. Agakishiev *et al.*, (STAR Collaboration), Phys. Rev. C 83 (2011) 061901
  e-Print Archives (1102.2669)
- **High p_T non-photonic electron production in p+p collisions at $\sqrt{s}$ = 200 GeV**
  H. Agakishiev *et al.*, (STAR Collaboration), Phys. Rev. D 83 (2011) 52006
  e-Print Archives (arXiv:1102.2611)

Submitted for publication

- **Measurement of the transverse single-spin asymmetry in $p+p \rightarrow W\pm/Z0$ at RHIC**
  L. Adamczyk *et al.*, (for the STAR Collaboration)
  e-Print Archives (1511.06003)
- **Centrality dependence of identified particle elliptic flow in relativistic heavy ion collisions at $\sqrt{s_{NN}} =$ 7.7-62.4 GeV**
  L. Adamczyk *et al.*, (for the STAR Collaboration)
  e-Print Archives (1509.08397)

- **Centrality and transverse momentum dependence of elliptic flow of multi-strange hadrons and phi meson in Au+Au collisions at $\sqrt{s_{NN}} = 200\ GeV$**
  L. Adamczyk $et\ al.$, (for the STAR Collaboration)
  e-Print Archives (1507.05247)
- **Beam-Energy Dependence of Charge Balance Functions from Au+Au Collisions at RHIC**
  L. Adamczyk $et\ al.$, (for the STAR Collaboration)
  e-Print Archives (1507.03539)
- **Probing Parton Dynamics of QCD Matter with Omega and Phi Production**
  L. Adamczyk $et\ al.$, (for the STAR Collaboration)
  e-Print Archives (1506.07605)
- **Leptonic decay the phi(1020) meson in Au+Au collisions at sqrt(sNN)= 200 GeV measured with the STAR experiment**
  L. Adamczyk $et\ al.$, (for the STAR Collaboration)
  e-Print Archives (1503.04217)
- **Elliptic flow of non-photonic electrons in $Au + Au$ collisions at $\sqrt{s_{NN}}$ = 200, 62.4 and 39 GeV**
  L. Adamczyk $et\ al.$, (for the STAR Collaboration)
  e-Print Archives (1405.6348)
- **Calibration and performance of the STAR Muon Telescope Detector using cosmic rays**
  L. Adamczyk $et\ al.$, (for the STAR Collaboration)
  e-Print Archives (1402.1078)

Refereed Conference Papers

- **Higher moments of net-kaon multiplicity distributions at RHIC energies for the search of QCD Critical Point**
  A. Sarkar, (for the STAR Collaboration), PoS: CPOD 061 (2013)
- **Higher moments of net-kaon multiplicity distributions at RHIC energies for the search of QCD Critical Point at STAR**
  A. Sarkar, (for the STAR Collaboration), EPJ: Conf. 60 (2013) 13013
  DOI: 10.1051/epjconf/20136013013
- **Higher moments of net-kaon multiplicity distributions at RHIC energies for the search of QCD Critical Point at STAR**

A. Sarkar, (for the STAR Collaboration), $J.Phys.$: Conf. Ser. 509 (2014) 012069
DOI: 10.1088/1742-6596/509/1/012069

- **Higher-moment measurements of net-kaon, net-charge and net-proton multiplicity distributions at STAR**
  A. Sarkar, (for the STAR Collaboration), $NuclearPhysics\ A$ 931 (2014) 796-801
  DOI: 10.1016/j.nuclphysa.2014.10.042

Acknowledgements

I am very thankful and want to revere my respect to the Almighty for giving me the strength, determination and to showing my path of my life. I would like to venerate the Almighty for guiding me through many people during the entire period of my studies and make it a success. There are many people without whom this thesis would not have been written. I am thankful to all of my family members, friends and teachers who has always inspired, supported and helped me during my graduation.

Foremost, I would like to express my sincere gratitude to my thesis supervisor Prof. Raghava Varma, for his guidance and supervision on my work during this entire period. His wide and deep knowledge help me to understand each problem I faced during this period. His nice personality made him not only my supervisor but also a very good friend of mine. His guidance, support and advice to my life is not forgettable. He always treated me as a family member and cared for me in every aspect during this period. His kindness and caring behavior will keep him alive in my heart throughout my life. I do not have any word to express my respect, sincerity and thanks to him. Thank you Sir, thank you for everything you have done for me, I owe the success to you.

I wish to express my sincere thanks to Prof. Basant Kr. Nandi and Prof. Sadhana Dash for their invaluable advice and constructive criticism. Their invaluable advice and discussion throughout this period increases my knowledge of understanding on this field. I am very thankful for their cooperation and support.

I am very glad for having an opportunity to work with Dr. Gen Van Buren from BNL in the beginning of my graduation. I would like to express my sincere thanks to him for his help, kindness and for all the useful discussions. I express my warm and sincere thanks to Prof. Nu Xu, Prof. Huan Huang, Prof. Frithjof Karsch, Prof. Sourendu Gupta, Prof. M.M Aggarwal, Prof. Tapan Nayak, Prof. Bedanga Das Mohanty, Prof. W.J. Llope, Prof. Mike Lisa, Dr. Brijesh Srivastava, Dr Hiroshi Masui, Dr. Zhangbu Xu, Dr. James Dunlop, Dr. Paul Sorensen and Dr. Premomoy Ghosh for their invaluable advice and encouragement for this work. I had a great pleasure to discuss physics with all of them. It is my great pleasure to thank all the STAR collaborators for their support, help and many useful physics discussions. It was a very friendly and memorable experience to work with all of them. I am thankful to Dr. Sayan Gupta, Dr. Desigan Kumaran,

Dr. Shankhamala Kundu, Dr. Rhijuta D'Mello, Dr. Prithis Tribedy, Dr. Mriganka M Mondal, Dr. Chanaka De Silva and Arindam Roy for such a wonderful time during my stay at BNL.

I am very glad to have seniors and friends like Dr. Ankhi Roy, Dr. Prabhat R. Pujahari, Dr. Neha Shah, Dr. Himani Bhatt, Dr. Kavita Lalwani, Dr. Xiaofeng Luo, Dr. Nihar R. Shaoo, Dr. Nirbhay Kr. Behera and Dr. Anitha Nyatha. I will be grateful for their constant support and help through out my graduation. I express my heartily thanks to my colleagues Manoj B Jadav, Greeshma periyat, Siddesh Sawant, Jitendra Kr. Nogia, Shyam Kumar and Divyash Pant for all their love and support.

I am very thankful to the Department of Science and Technology (DST), India and PMD collaboration for giving me the opportunity to work on this project. I express my sincere thanks to all seniors and warm love to my friends and juniors from PMD collaboration for all their support, help and encouragement.

I express my sincere respect to Amitava Das and Bishnu Roy for their encouragement, support and help through out my student life. I am very thankful to them, without their help and support it would have been very difficult for me to chose this career path.

I am very thankful to my teachers Jahar Kr. Saha, Mrintunjoy Sarkar, Kamanamoy Das, Anil Das, Soumen Dutta, Subhendu Mondal, and many others who has always supported me and encouraged me to chose this field. Their guidance, support and love will always keep them in my heart.

After all these years IIT Bombay feel second home to me. During my stay I have been blessed with a very friendly and cheerful groups. I express my thanks and love to Shashank Pandey, Suman G Das, Dr. Kulveer Sing, Dr. Tanmoy Chakrabarty, Dr. Debtanu De, Dr. Bijay Kr. Aggarwal, Rajarshi Pal, Dr. Abhishek Sen, Arnab Ghosh, Dr. Amit Goel, Dr. Dipjyoti Das and all other Master and Ph.D classmates. I also express my thanks and love to Dr. Santidan Biswas, Arijit Mitra, Dr. Surya Ghosh and Dr. Swarup Panda for their valuable guidance. I have been blessed with very good friends like Nabin Kr. Ram, Dr. Siddhart Dwivedi, Dr. Reetanjali Moharana, Dr. Suprabh Prakash, Pintu Ghosh, Ravi Swarnkar, Cijy Mathai, Lata Kh Joshi, Cini Sobha, Ushak Rahaman, Gouri Saha, Dithi Bhattacharya, Minakshi Roy and many others. I thank to all of them for their support and providing me such a wonderful friendly environment.

I would like to express my thanks to Almighty to give me such wonderful friends in my life without whom it would have been very difficult for me to reach this point. I wish to express my love and thanks to my childhood friends Para-

mananada Biswas, Shubhajit Biswas, Shubhankar Das, Shiben Mondal, Shovon Mondal, Soumen Chackraborty, Modidipa Mondal, Krishna Biswas, Mummun Mondal, Lily Sinha, Gourav Biswas, Tamal Ghosh, Subhamoy Biswas, Kripashankar Aggarwal, Arka Prabha Das and many others for their constant encouragement and support during my student life.

Most importantly, I would like to express my due respect and love to my parents for their immense patience, support and encouragement. Without their love and support, this thesis would not have been possible. I am very greatful to them for giving me the freedom to choose my career. I am very thankful to my elder brothers Anusan Sarkar and Anup Sarkar and their wives Rupa Sarkar and Poulomi Das Sarkar for their moral support and blessing. I am very thankful to my in laws specially Palas Das, Malati Das, Ajay Das, Atoshi Mondal and Partha Das for their constant support and encouragements. I am very thankful to my loving wife Moumita Das for her moral support to me throughout during my Ph.D. It is only because of their love, affection and blessing that I could complete this thesis.